Façonnage d'impulsions optiques et sources ultra-brèves

Nicolas Forget

Manuscript

en vue de l'obtention de

l'habilitation à diriger des recherches (HDR)
délivrée par l'Université de la Côte d'Azur

Discipline : Physique

École doctorale Sciences Fondamentales et Appliquées (ED SFA)

Présentée et soutenue publiquement le 25 mars 2022
par **Nicolas FORGET**

Façonnage d'impulsions optiques et sources ultra-brèves

Devant la commission d'examen formée de :

Mme	Aurélie Jullien	*CNRS*	Examinatrice
M.	Frédéric Druon	*CNRS*	Rapporteur
M.	Manuel Joffre	*École Polytechnique*	Rapporteur
M.	Eric Cormier	*Université de Bordeaux*	Rapporteur
M.	Hervé Rigneault	*CNRS*	Examinateur
M.	Daniel Kaplan	*Fastlite*	Examinateur

Remerciements

Je tiens tout d'abord à remercier les membres de mon jury d'habilitation et, en particulier, à mes trois rapporteurs : Frédéric Druon, Manuel Joffre et Éric Cormier. Je vous remercie d'avoir pris du temps, sur un emploi du temps chargé, pour lire mon manuscrit. C'est un grand honneur que vous ayez accepté d'être rapporteurs de mon HDR. Chacun d'entre vous a été à un modèle et/ou une source d'inspiration un moment ou à un autre de ma carrière. J'adresse également mes sincères remerciements à Hervé Rigneault, grâce à qui j'ai plongé avec délice dans le monde de la microscopie Raman. Notre collaboration sur la microscopie Raman est aujourd'hui, et pour mon plus grand plaisir, au cœur de l'un de mes principaux axes de recherche. Je remercie également du fond du cœur Aurélie Jullien, avec qui j'anime le laboratoire commun Softlite, un autre grand pilier de mes travaux actuels. Sans Aurélie ce laboratoire n'aurait sans doute pas son succès actuel et je me dois ici de lui exprimer toute ma reconnaissance pour sa créativité, son dynamisme, son enthousiasme, mais aussi ses grandes qualités scientifiques, pédagogiques et humaines. J'en profite pour mentionner le soutien sans faille de l'Institut de Physique de Nice et de son directeur, Guillaume Huyet, à Softlite.

Enfin, j'exprime toute ma gratitude à Daniel Kaplan, qui m'a convaincu de tenter l'aventure Fastlite et avec qui j'ai beaucoup appris et continue toujours à apprendre. J'ai, bien entendu, une pensée pour mon mentor Pierre Tournois, qui nous a quitté en 2017, et que j'aurai aimé inclure dans ce jury. Je remercie bien évidemment Pascal Tournois qui dirige aujourd'hui la société Fastlite et qui m'accorde sa confiance depuis de nombreuses années. Je tiens, plus largement, à exprimer ma reconnaissance à toutes celles et à tous ceux avec qui ont partagé avec moi ou continuent à partager l'aventure scientifique, industrielle et humaine « Fastlite ». Ils sont trop nombreux pour être tous cités ici mais chacun a apporté sa pierre à l'édifice, et je les en remercie individuellement. Sans mes collègues la très grande majorité des travaux décrits dans ce manuscrit n'auraient pas abouti. C'est notamment le cas des sources paramétriques optiques qui ont demandé des développements concertés en optique, en mécanique et en électronique/logiciel. Je n'oublie pas les étudiants en thèse que j'ai co-encadrés ou co-encadre aujourd'hui, ainsi que les étudiants dont j'ai dirigé les stages.

Je ne peux évidemment pas terminer ces remerciements sans un mot pour ma merveilleuse épouse. Nous avons traversé ensemble d'innombrables épreuves et, sans elle, rien de tout ceci n'aurait été possible, pas même notre famille et notre merveilleuse fille. Celle-ci (8 ans

à l'heure où j'écris ces lignes) m'a demandé hier soir ce que c'était que la physique... j'avoue que j'ai été pris de court. Alors je lui réponds ici : c'est la science qui essaie de comprendre, de modéliser et d'expliquer les phénomènes naturels de l'univers. Et merci pour cette question, toute simple, qui rappelle que l'humilité est une vertu.

Table des matières

Chapitre 1

Introduction

1.1 Contexte scientifique

Les travaux que j'ai menés ou dirigés depuis 2005 s'articulent autour de deux thématiques : l'optique non linéaire et la physique ultra-rapide. Si l'optique non linéaire est une discipline clairement établie en optique, la physique ultra-rapide l'est moins – du moins en langue française. Le terme anglo-saxon d'« ultrafast technologies » est plus explicite et englobe les aspects théoriques, technologiques, métrologiques et applicatifs des impulsions ultra-brèves [1].

Pour se conformer à l'usage en vigueur, on caractérise d'ultra-brève une source optique pulsée dont la durée d'impulsion est comprise entre quelques femtosecondes (10^{-12} s) et quelques picosecondes (10^{-12} s). Cette plage correspond à deux limites physiques : d'une part celle de la période du cycle optique (2.7 fs à 800 nm), de l'autre celle du temps caractéristique de propagation des phonons acoustiques sur une distance inter-atomique dans un solide [1]. Ces deux bornes délimitent un régime d'interaction dans lequel on peut, en première approximation, tout à la fois réduire l'impulsion optique à un paquet d'onde de porteuse bien définie, et négliger les déplacements atomiques lors de l'interaction lumière-matière.

Résumer l'histoire des sources ultra-brèves en quelques lignes est probablement impossible mais on peut néanmoins en citer les grandes étapes de développement [2].

1. **Sources de première génération**. Dans les années 1970, le blocage de modes dans les lasers à colorant produit les premières impulsions de durée sub-picoseconde [3] puis de quelques dizaines de femtoscondes [4–6]. Cependant, la très faible fluence de saturation de ces lasers limitent l'amplification de ces impulsions à des énergies de l'ordre de quelques microjoules et à des puissances crêtes de quelques MW [7, 8].
2. **Sources ultra-brèves de seconde génération**. L'énergie par impulsion augmente significativement à la fin des années 1980 grâce aux milieux laser solides [9, 10], caractérisés par une fluence de saturation supérieure mais aussi par de meilleures

1. La vitesse du son dans un solide étant de l'ordre de $1\,000\,\mathrm{m}\cdot\mathrm{s}^{-1}$, le temps caractéristique de propagation sur 1 pm est de 1 ps

propriétés thermo-opto-mécaniques (milieux cristallins). La mise en place de l'amplification à dérive de fréquence ou « chirped pulse amplification » (CPA, [11]), notamment dans les chaînes d'amplification à base de laser saphir dopé au Titane (Ti:Saphir, ≃800 nm), ouvre la voie à des domaines de recherche nouveaux, tels que la science attoseconde [12], l'accélération de particules par laser [13] ou la physique nucléaire par laser [14]. Parmi les exemples les plus spectaculaires et les plus récents de ces sources de seconde génération (Ti :Saphir) on peut citer le 4 PW (83 J, 19.4 fs) du GIST en Corée du sud [15], le 10 PW (339 J, 21 fs) du SIOM en Chine [16], ou encore le 2x10 PW d'ELI-NP en construction en Roumanie. En raison de la limitation en puissance moyenne du Ti:Saphir [2], les lasers solides dopés Ytterbium [3] se développent en parallèle, notamment sous l'impulsion des applications industrielles. Les lasers fibrés dopés Ytterbium ainsi que les lasers solides Yb:KGW et Yb:CaF_2 voient le jour. Les lasers picosecondes Yb:YAG de type « thin-disk » et « slab » atteignent des puissances moyennes de plusieurs centaines de W voire de quelques kW.

3. Au début des années 2000 commencent à apparaître les sources ultra-brèves de **troisième génération**. Ces dernières ne sont plus seulement des lasers mais une combinaison de lasers et d'optique non linéaire. Deux tendances se dessinent :
   - d'une part, les techniques de post-compression (filamentation, fibres photoniques, fibres creuses, passages multiples dans des lames ou des cellules de gaz, plasma...) qui permettent de raccourcir les impulsions tout en conservant la même porteuse optique,
   - d'autre part, l'amplification paramétrique optique à dérive de fréquence (OPCPA pour Optical Parametric Chirped Pulse Amplification), qui permet de convertir un laser picoseconde/nanoseconde en une source femtoseconde. Cette conversion de fréquence s'accompagne, en général, de propriétés émergentes que ne possède pas le laser de « pompe » : accordabilité en longueur d'onde, contraste temporel élevé, relation de phase constante entre l'enveloppe de l'impulsion et la porteuse optique. Deux critères distinctifs des sources de troisième génération sont la durée picoseconde du laser de pompe (un laser de forte énergie et/ou de forte puissance moyenne) et le mécanisme de génération des nouvelles longueurs d'onde (via élargissement spectral du laser de pompe).

Mon activité scientifique, à laquelle est consacrée cette synthèse, s'inscrit dans ce vaste contexte, notamment à la charnière entre les sources de seconde et de troisième génération.

1.2 Contexte industriel

Une particularité du travail exposé dans ce mémoire est son contexte industriel et commercial. L'ensemble des travaux décrits dans ce mémoire ont été réalisés au sein de l'entreprise Fastlite entre 2005 et 2022.

La société Fastlite a été créée en 1999 par Daniel Kaplan et Pierre Tournois, tous deux alors retraités du groupe Thales [4]. Lorsque j'ai rejoint la société après ma thèse en 2005,

2. caractérisé par un défaut quantique relativement large (laser à quatre niveaux)
3. caractérisés par un très faible défaut quantique (lasers à « quasi » trois niveaux)
4. Thompson, à l'époque

la société comptait quatre salariés. Elle emploie aujourd'hui vingt-trois salariés, dont neuf docteurs en physique, cinq ingénieurs et trois doctorants. J'anime l'équipe de R&D optique de Fastlite depuis 2012 et suis directeur adjoint de la société depuis 2016. Fastlite conçoit, développe et commercialise des instruments et des sources ultra-brèves pour la communauté scientifique nationale et internationale. Son marché est presque exclusivement scientifique et ses clients sont des laboratoires de recherche ou des industriels. Le portfolio commercial compte aujourd'hui quatre principales lignes de produits, que l'on retrouve plus ou moins directement dans les thèmes de recherche développés dans ce document :

- des façonneurs d'impulsions (« pulse shapers ») acousto-optiques (Dazzler™)
- des spectromètres infrarouges (Mozza™)
- des instruments de caractérisation du profil temporel de ces impulsions (Wizzler™)
- des sources ultra-brèves de troisième génération (Starzz™ et twinStarzz™)

Il m'est difficile de conclure cette partie sans commenter qu'elle a été ma perception de la recherche en entreprise - à Fastlite tout du moins. A la différence de la recherche académique, la recherche en milieu industriel est une recherche que je qualifierai : :

- *d'opportuniste*[5] : à l'exception des contrats d'étude subventionnés et des collaborations informelles avec des laboratoires académiques, le financement de la recherche est financé sur affaire, c'est à dire par la vente d'un produit spécifiquement développée pour un client particulier - donc sans filet de sécurité autre que la marge de manœuvre commerciale,
- *de contrainte* : les délais sont nécessairement courts, soit pour honorer les délais de livraison annoncés, soit pour des raisons économiques[6]. Par ailleurs, le secret industriel ou les délais imposés par la mise en place d'une propriété intellectuelle/industrielle décalent souvent les recherches de leur publication,
- *appliquée/polyvalente* : le temps du chercheur est pris sur celui de l'ingénieur et l'arbitrage n'est pas toujours favorable au premier.

Certains diront sans doute qu'il n'y là rien de très spécifique et que la recherche publique actuelle évolue dans un contexte similaire, ou, en tout cas, en voie de le devenir. C'est probablement vrai en raison de la contractualisation croissante de la recherche publique. A ce jour, des différences demeurent. Je me risquerais à attribuer à la recherche en entreprise une forme d'équation d'état à trois variables, les trois variables d'état étant :

- une pression interne : la performance collective, l'exigence de retour sur investissement, la stratégie de l'entreprise,
- une température : le contexte réglementaire national (fiscalité, crédit impôt-recherche), les taux d'emprunts bancaires, la concurrence des autres entreprises et, parfois, des laboratoires,
- un volume : les effets cumulés des modalités et de l'ampleur du financement de la recherche publique, les politiques internationales (restrictions aux frontières en

5. Opportunisme : attitude consistant à régler sa conduite selon les circonstances du moment, que l'on cherche à utiliser toujours au mieux de ses intérêts. L'opportunisme désigne aussi la politique de prudence et de réalisme prônée par Gambetta, Jules Ferry et les républicains modérés entre 1879 et 1895.

6. Un retour sur investissement minimum est requis.

temps de Covid-19 par exemple), les évolutions des besoins de la communauté scientifique...

La recherche en entreprise bénéficie aussi d'avantages indéniables : une grande souplesse administrative (au regard de la recherche publique), des procédures simples pour les achats, un accès simple et direct à des bureaux d'étude (mécanique, électronique ou logiciel), une large palette de sujets de recherche dans des domaines très variés. Le crédit impôt recherche (CIR) français tempère également l'exigence de retour sur investissement des dépenses de R&D[7]. La liberté de pouvoir « piocher » dans un large stock de matériel disponible facilite aussi la mise en œuvre d'expériences. Enfin, l'exposition à des laboratoires et de chercheurs de tous horizons et sur tous les continents est une vraie richesse.

Toutes ces caractéristiques de la recherche en entreprise ont, d'une façon ou d'une autre, structuré mes travaux de recherche. Ces derniers sont sans doute moins approfondis et plus morcelés que s'ils avaient été menés dans un cadre académique mais probablement, aussi, plus variés. Ce manuscrit n'est d'ailleurs pas exhaustif et je n'ai sélectionné qu'une partie des thèmes de recherche : ceux impliquant des collaborations et/ou des situations de direction ou d'encadrement. J'ai, par exemple, écarté la métrologie d'impulsions courtes (Wizzler™ [17, 18], chirp scan [19], Phazzler™ [20]) ainsi que les extensions à l'infrarouge thermique des twinStarzz™.

1.3 Guide de lecture

Le chapitre 2 est dédié au façonnage d'impulsions courtes soit par filtre acousto-optique dispersif programmable (AOPDF), soit par des assemblages de réseaux et de prismes (grismes). Le chapitre 3 présente les applications des AOPDF à la spectroscopie ultra-rapide, par des méthodes linéaires ou non linéaires. Le chapitre suivant décrit l'étude et le développement de sources optiques ultra-brèves relevant de la technologie d'amplification paramétrique optique à dérive de fréquence. Enfin, le dernier chapitre aborde une thématique de recherche plus récente : les cristaux liquides pour l'optique ultra-rapide.

Chaque chapitre est organisé de la manière suivante : après une brève introduction, je rappelle les collaborations, contrats et étudiants liés à cette thématique. Je résume ensuite les principaux résultats scientifiques obtenus. Les publications les plus significatives sont incluses en fin de section ou de chapitre.

7. Peut-être au détriment de la recherche publique mais c'est un autre débat.

Chapitre 2

Façonnage d'impulsions optiques ultra-brèves

2.1 Le filtre acousto-optique programmable

Le façonnage d'impulsions optiques par filtre acousto-optique dispersif programmable (AOPDF pour « Acousto-Optic Programmable Dispersive Filter »), inventé et breveté par Pierre Tournois en 1996, est à l'origine du succès de la société Fastlite. Les usages de ce filtre sont multiples [21] mais sa principale application demeure la compression d'impulsions dans le contexte du CPA. Je détaille ici brièvement la physique de ce filtre auquel il est fait référence de nombreuses fois dans ce manuscrit.

Les collaborations auxquelles j'ai pris part sont indiquée dans le tableau 2.1, ainsi les contrats pour lesquels j'ai été en situation de responsabilité. Le tableau 2.2 synthétise les stages encadrés et les thèses co-encadrées.

Type	Acronyme	Laboratoire/entreprise	Rôle	Date
Contrat ASTRE	-	LOA (PCO)	Participant	2010-2012
Collaboration	informelle	MPQ	Participant	2006
Collaboration	informelle	TUW	Participant	2009
Collaboration	informelle	LOA-PCO	Participant	2008
Collaboration	commerciale	Femtolasers	Participant	2014

Table 2.1 – Contrats et collaborations.

Cadre	Type	Nom	Date	Direction	Laboratoire
Thèse	CIFRE	Stéphanie Grabielle	2007-2011	Olivier Gobert	CEA
Stage	M2	Romain Lavalard	2011	Nicolas Forget	Fastlite

Table 2.2 – Thèses que j'ai co-encadrées et stages dirigés.

2.1.1 Principe et propriétés

Un fitre acousto-optique dispersif programmable repose sur une interaction acousto-optique particulière :

- le cristal acousto-optique est anisotrope (il est biréfringent optiquement et acoustiquement)
- l'onde optique incidente est polarisée linéairement suivant l'une des deux directions principales de polarisation (polarisation ordinaire ou polarisation extraordinaire)
- l'onde acoustique est une onde de cisaillement,
- la coupe du cristal est telle que les vecteurs de Pointing optiques et acoustiques sont colinéaires (ou quasi-colinéaires).

2.1.2 Équations des ondes couplées

Soit E_m les amplitudes complexes d'un ensemble d'ondes électromagnétiques planes progressives de pulsations ω_m et de vecteurs d'onde k_m se propageant dans un cristal biréfringent en présence d'une onde acoustique intense. On note $\mathbf{e}_m$ les polarisations associées à ces ondes. Le champ électrique total est :

$$\mathbf{E}(\mathbf{r},t) = \sum_m E_m \exp i\left(\omega_m t - \mathbf{k}_m.\mathbf{r}\right)\mathbf{e}_m + \text{c.c.} \tag{2.1}$$

L'onde acoustique est, elle, représentée par un champ de déformation, c'est-à-dire un tenseur de rang 2 :

$$\mathbf{S}(\mathbf{r},t) = S \exp i\left(\Omega_m t - \mathbf{K}.\mathbf{r}\right)\mathbf{s} + \text{c.c.} \tag{2.2}$$

Cette onde de déformation induit une polarisation nonlinéaire microscopique $\mathbf{P}^{\text{NL}}$ telle que :

$$\mathbf{P}^{\text{NL}} = \epsilon_0 \chi^{(4)} : \mathbf{S}.\mathbf{E} = \epsilon_0 \mathbf{\Delta}\chi.\mathbf{E} \tag{2.3}$$

Le tenseur $\chi^{(4)}$, de range 4, est le tenseur nonlinéaire de susceptibilité acousto-optique. Il couple chaque composante du champ de déformation avec chacune des polarisations électriques. $\mathbf{\Delta}\chi = \chi^{(4)} : \mathbf{S}$ est le tenseur de rang 2 obtenu par contraction de $\chi^{(4)}$ et de $\mathbf{S}$. D'un point de vue formel, la réponse non linéaire acousto-optique prend donc la même forme que la réponse linéaire du matériau sous l'effet du champ $\mathbf{E}$. On comprend donc que le champ de contrainte $\mathbf{S}$ induit une modification de la surface des indices et donc, en général, ne préserve pas les directions propres de polarisation. ce qui a pour effet de coupler les ondes, même si leurs polarisations d'origine sont différentes. Tous calculs faits, pour une propagation paraxiale suivant une direction z quelconque et avec une seule onde non nulle à l'entrée du cristal ($E_m = 0$ pour $m \neq 0$), on arrive à l'équation des modes couplés, qui, comme son nom l'indique couple l'onde m aux ondes $m-1$ et $m+1$ [22] :

$$\begin{cases} \dfrac{dE_m}{dz} - i\Delta k_m E_m(z) = \dfrac{k_m^2}{4k'_{mz}} pS\left[n_{m-1}^2 E_{m-1}(z) - n_{m+1}^2 E_{m+1}(z)\right] \\ E_0(0) = E_0,\ E_{m\neq 0}(0) = 0 \end{cases} \tag{2.4}$$

où $\mathbf{k}' = k_0 + m\mathbf{K}$ est le vecteur d'onde diffracté d'ordre m. k'_{mz} est la projection de ce vecteur d'onde suivant z et n_m l'indice de réfraction associé. Le nombre p, qui dépend de $\mathbf{\Delta}\chi$ et des polarisations $\mathbf{e}_m$ est le coefficient acousto-optique effectif. Ces équations

couplées font intervenir le terme de désaccord de phase *longitudinal* $\Delta k_m = \Delta k_{mz} = k'_{mz} - k_{mz}$, lequel vient déphaser le terme source (membre de droite de 2.4) de la propagation. Le désaccord de phase transverse est, lui, nécessairement nul, ce qui complète la description vectorielle. Le désaccord de phase longitudinal est en général non nul car $\mathbf{k}'$ ne vérifie pas nécessairement la relation de dispersion $|\mathbf{k}|^2 = n(\omega_m, \mathbf{e})^2\omega^2/c^2$. En pratique, l'accord de phase exact ou approché $\Delta k_m L \ll 1$ ne peut être réalisé que pour deux champs, par exemple, $\mathbf{E}_0$ et $\mathbf{E}_1$ (ou, de manière équivalente, $\mathbf{E}_0$ et $\mathbf{E}_{-1}$), si bien que seules ces deux ondes vont être couplées efficacement dans un cristal épais. C'est le régime de diffraction de Bragg (un seul ordre de diffraction), par opposition au régime de Raman-Nath (multiples diffractions). Tous calculs faits [22], dans la limite des ondes planes monochromatiques et des conditions de Bragg, l'efficacité de diffraction η varie comme [1] :

$$\eta = |E_1(L)|^2/|E_0(0)|^2 = \left(\frac{v}{2}\right)^2 \mathrm{sinc}^2\sqrt{\zeta^2 + \left(\frac{v}{2}\right)^2} \tag{2.5}$$

$$v = \frac{2\pi}{\lambda\cos\theta}\sqrt{\frac{M_2}{2}P_a}L \tag{2.6}$$

$$\zeta = \Delta k_1 L/2 \tag{2.7}$$

$$\Delta k_1 = (\mathbf{k}_1 - \mathbf{k}_0 - \mathbf{k})\,.\mathbf{u}_z \tag{2.8}$$

où P_a est la densité surfacique de puissance acoustique dans la colonne acoustique, L est l'épaisseur du cristal, et où M_2 ne dépend que des caractéristiques du matériau acousto-optique. Le terme M_2 fait intervenir l'inverse de la densité du cristal ainsi que l'inverse de la vitesse acoustique. Des matériaux denses et des ondes acoustiques à faible vélocité, comme les ondes de cisaillement, maximisent donc le facteur de mérite M_2 et donc l'efficacité de diffraction. La formule 2.5 indique que l'efficacité de diffraction est maximale à l'accord de phase ($\Delta k_1 L \ll 1$). On peut également retenir que pour $\eta \ll 1$ on a simplement :

$$\eta \propto \ \mathrm{sinc}^2\left(\frac{\Delta k_1 L}{2}\right) P_a L^2 \tag{2.9}$$

2.1.3 Accord de phase acousto-optique

Il est intéressant de développer le terme de désaccord de phase $\Delta k_1 = \Delta k$ au voisinage de l'accord de phase. Au premier ordre en $\Delta\omega = \omega - \omega_0$ et $\Delta\Omega = \Omega - \Omega_0$ on obtient :

$$\Delta k(\Delta\omega, \Delta\Omega) = \frac{\partial\Delta k}{\partial\Omega}\Delta\Omega + \frac{\partial\Delta k}{\partial\omega}\Delta\omega \tag{2.10}$$

Comme l'efficacité de diffraction chute sensiblement lorsque $\Delta k L \simeq 1$ pour un cristal d'épaisseur L, on peut définir des valeurs limites $\Delta\Omega_m$ et $\Delta\omega_m$ pour lesquelles ce désaccord maximal est atteint indépendamment. On trouve ainsi :

$$1/\Delta\Omega_m = L\left(\frac{\partial k_1}{\partial\omega} - \frac{\partial K}{\partial\Omega}\right).u_z = \left(\frac{1}{v_g} - \frac{1}{V}\right)L \tag{2.11}$$

où v_g et V sont, respectivement, la vitesse de groupe optique et acoustique suivant la direction de diffraction z. En réalité les dérivées partielles sont des gradients que l'on

1. $\mathrm{sinc}(x) = \sin x/x$ dans ce document.

peut relier aux vecteurs de Pointing, lequels sont colinéaires dans les AOPDFs. La vitesse acoustique étant beaucoup plus lente que la vitesse de la lumière, l'expression de $\Delta\Omega_m$ est simplement :

$$\Delta\Omega_m = \frac{V}{L}$$

Autrement dit, pour une fréquence optique donnée, la résolution spectrale acoustique est égale à l'inverse du temps de propagation. Pour un cristal de TeO_2 de 25 mm, la résolution spectrale acoustique est de l'ordre de quelques dizaines de kHz, soit une valeur très faible devant la porteuse acoustique (entre 30 MHz et 100 MHz typiquement). Le même type d'analyse conduit à :

$$\Delta\omega_m = \frac{c}{|\Delta n_g| L}$$

où Δn_g est la différence entre la vitesse de groupe extraordinaire et la vitesse de groupe ordinaire suivant la direction de diffraction. Pour un cristal de TeO_2 de 25 mm, on trouve une résolution spectrale optique de l'ordre de 0.1 THz.

Les résolutions optiques et acoustiques sont reliées par :

$$\alpha = \frac{\Delta\Omega_m}{\Delta\omega_m} = |\Delta n_g| \frac{V}{c}$$

Comme la vitesse acoustique est indépendante de la fréquence acoustique entre 10 MHz et quelques centaines de MHz, le ratio α ne varie que faiblement avec la longueur d'onde optique et il peut être considéré, en première approximation, comme une constante qui ne dépend que du matériau et de la direction des vecteurs de Poynting. Pris ensemble, ces trois résultats indiquent que la diffraction acousto-optique induit une relation linéaire et quasi-bijective entre fréquence acoustique et fréquence optique diffractée. Bien que non démontré ici, il en va de même angulairement.

2.1.4 Diffraction d'un paquet d'ondes

Le dernier point de la démonstration prend en compte des paquets d'onde (en optique et en acoustique). En raison du réservoir gigantesque de phonons disponibles, la diffraction acousto-optique ne modifie pas l'onde acoustique et la diffraction acousto-optique est linéaire du point de vue optique. Dans la limite d'une diffraction faible (paquet d'onde optique incident « non déplété »), le paquet d'onde diffracté s'écrit simplement, par linéarité [2] :

$$E_1(\omega_1, L) \propto \int S(\Omega) E_0(\omega_0) \ \mathrm{sinc}\left(\frac{\Delta k_1(\omega_0, \omega_1, \Omega) L}{2}\right) \delta(\omega_1 - \omega_0 - \Omega) d\Omega d\omega_0 \qquad (2.12)$$

Les fréquences acoustiques (typiquement <1 GHz) étant négligeables devant les fréquences optiques (typiquement dans la gamme THz-PHz), le décalage Doppler $\omega_d - \omega = \Omega$ est négligeable et l'on peut faire l'approximation $\omega_1 \simeq \omega_0 \simeq \omega$). Comme, de plus, l'accord de phase est très étroit [3] par rapport aux largeurs spectrales optiques et acoustiques

2. et d'un changement de phase à l'origine.
3. du fait de la grande longueur d'interaction L

impliquées, on peut également faire l'approximation que le terme en sinc^2 se réduit à $\delta(\omega - \alpha\Omega)$, ce qui permet de simplifier l'équation précédente en :

$$E_1(\omega, L) \propto S(\alpha\omega) E_0(\omega) \tag{2.13}$$

Autrement dit, dans le domaine temporel, l'AOPDF opère une simple convolution entre l'onde optique incidente et l'onde acoustique, à une mise à l'échelle temporelle de l'onde acoustique par le facteur α près :

$$E_1(t, L) \propto S(t/\alpha) * E_0(t) \tag{2.14}$$

Une prise en compte un peu moins simpliste du terme de désaccord de phase consiste à réduire celui à une dépendance en $\omega - \alpha\Omega$ au voisinage de l'accord de phase exact $\Delta k_1 \simeq -(\omega - \alpha\Omega)/V$. Il vient alors :

$$E_1(\omega, L) \propto E_0(\omega) \int S(\Omega) \mathrm{sinc}\left[\frac{\omega - \alpha\Omega}{2}\frac{L}{V}\right] d\Omega \tag{2.15}$$

La transformée de l'expression précédente est alors :

$$E_1(t, L) \propto \hat{S}(t/\alpha) * E_0(t) \tag{2.16}$$

où $\hat{S}(t)$ est l'amplitude (complexe) de l'onde acoustique dont le support est limité à une fenêtre de largeur totale $T = L/V$: $\hat{S}(t) = S(t)\Pi(t/T)$ où Π est la fonction porte valant 1 entre $-1/2$ et $1/2$ et zéro ailleurs. Une prise en compte plus détaillée de ce terme de désaccord de phase met en évidence un certain nombre d'effets fins : variation de la résolution spectrale avec la longueur d'onde, dispersion différentielle avec le temps de groupe moyen etc.

Les publications de référence sur les AOPDF sont celles de Frédéric Verluise [23] et de Daniel Kaplan [24] pour le TeO_2 (visible et proche infrarouge), de Sébastien Coudreau [25] pour le KDP (ultra-violet) et de Raman Maksimenka [26] pour le Calomel (infrarouge moyen).

2.2 Précision du façonnage

La calibration d'un AOPDF, c'est-à-dire la correspondance entre fréquence acoustique et fréquence optique, dépend de trois facteurs : la coupe cristalline choisie, l'orientation relative du composant et du faisceau optique incident et la connaissance des propriétés optiques du matériau. Cette dernière se résume, pour l'essentiel, à celle de la biréfringence et de sa dépendance en longueur d'onde. L'orientation cristallographique du cristal ainsi que la réalisation du composant font appel à des techniques de grande précision (rayons X) et la direction de propagation acoustique est un excellent critère [4] de vérification de la coupe cristalline. L'orientation du composant par rapport au faisceau incident est ajustée expérimentalement par autocollimation sur la face d'entrée. Paradoxalement, la plus

4. la propagation acoustique dans certains plans est extrêmement anisotrope dans un cristal comme la paratellurite.

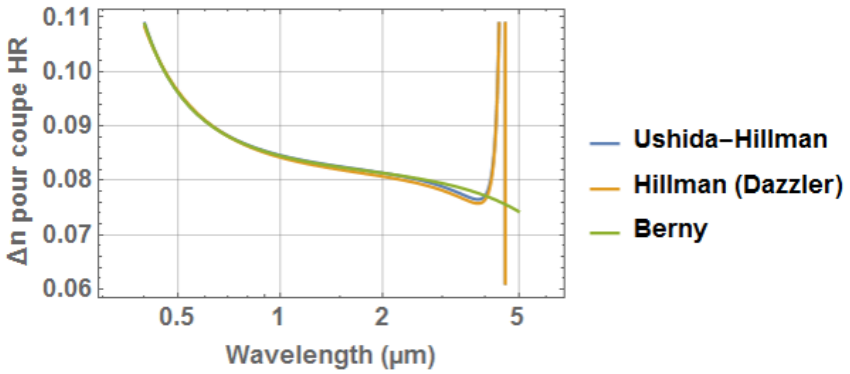

FIGURE 2.1 – Comparatif des formules de Sellmeier pour le TeO_2.

grande incertitude est celle des indices de réfraction. En effet, les formules de Sellmeier des matériaux acousto-optiques comme TeO_2 ne sont pas nécessairement connues avec une précision suffisante dans le visible ou le proche infrarouge, ni même bien déterminées dans l'infrarouge moyen. Les formules publiées pour la paratellurite [27–29] présentent ainsi des écarts et/ou ne sont pas établies sur les mêmes plages spectrales. La publication de Berny de 1972 [29] avait été initialement ignorée par Fastlite car peu référencée et uniquement publiée en français. La littérature cite principalement les travaux d'Uchida [27] et Hillman [28]. Cette dernière est celle utilisée par Fastlite depuis une quinzaine d'année pour ses logiciels commerciaux. Les différentes formules donnent des résultats proches, notamment d'Uchida et Hillman, mais non identiques - et en particulier au-delà de 1 µm.

Dans son travail de thèse [30] (CIFRE), dirigé par Olivier Gobert (CEA, Saclay) et que j'ai contribué à co-encadrer, Stéphanie Grabielle a mené une étude précise de la fidélité du façonnage spectral à 800 nm. Un AOPDF de 25 mm en coupe HR est placé dans le bras test d'un interféromètre de type Mach-Zhender et la phase spectrale de l'onde diffractée est déterminée par interférométrie spectrale. Le résultat principal de l'étude est qu'après calibration, il subsiste une erreur systématique de $\simeq$0.5% entre les temps de groupe programmés et mesurés. Cet écart ne peut s'expliquer que par une erreur sur les formules de Sellmeier. La dispersion des valeurs de biréfringence publiées est d'ailleurs de cet ordre de grandeur. Une erreur systématique aussi faible peut paraître dérisoire mais elle conduit à des erreurs parfois non négligeables en spectre large compte tenu de la grande dispersion optique (passive) d'un AOPDF de 25 mm. Le calcul de cette dispersion est requise pour auto-compenser l'insertion du cristal dans une source femtoseconde. Ce calcul de dispersion étant basé sur les dérivées premières et secondes des indices optiques, ce calcul est extrêmement sensible à la formule utilisée. Plus généralement, certaines applications métrologiques comme la spectroscopie 2D ou la caractérisation temporelle d'impulsions par la technique SPIDER nécessitent une précision meilleure que 0.1% pour des temps de groupe de $\simeq$1 ps.

L'ambiguïté sur les Sellmeier est aggravée dans l'infrarouge moyen car la formule donnée par Hillman diverge vers 4.2 µm. Néanmoins la formule d'Uchida, proche de Hillman mais non divergente, ne reproduit pas non plus fidèlement les résultats expérimentaux. La solution retenue initialement avait été de simplement tabuler la correspondance entre

fréquence acoustique et fréquence optique à partir d'une connaissance a priori de la réponse spectrale d'un étalon Fabry-Pérot en Silicium vers 2 µm. Cette approche pragmatique est néanmoins insatisfaisante car elle présuppose une parfaite connaissance de l'épaisseur et de l'indice du Silicium. De plus, la difficulté de ce travail repose sur le fait que l'orientation du filtre acousto-optique est un paramètre critique dont l'effet est d'ajouter ou retrancher une constante sur les courbes de correspondance entre fréquence acoustique et optique. Il est donc nécessaire de comparer non les valeurs mais les variations des valeurs et ainsi, pour être suffisamment précis, de réaliser des mesures sur une plage spectrale la plus large possible.

Des mesures systématiques sur un corps noir ont été entreprises sur TeO_2 dans le cadre du stage de M2 de Romain Lavalard (Paris-Sud) que j'ai encadré en 2011. J'ai ensuite complété ces données à Antibes en 2017 avec un analyseur de spectre optique (OSA) de façon à couvrir l'ensemble de la plage 650-1700 nm. Ces mesures ont confirmé que la formule de Berny conduit à une bien meilleure conformité entre théorie et expérience qu'Uchida ou Hillman (écart réduit d'un facteur 4), et ce de 0.5 µm à 5 µm. Le détail de ces résultats n'a pas été rendu public et est toujours considéré comme un secret industriel.

2.3 Compression d'impulsions

La durée minimale d'une impulsion est classiquement limitée par son support spectral. En pratique, la relation de phase entre les différentes composantes spectrales - la phase spectrale - ne permet pas toujours d'atteindre cette durée minimale. Cette phase spectrale, qui joue un rôle équivalent aux aberrations optiques en imagerie (aberration sphérique, coma...), résulte le plus souvent d'imperfections dans les systèmes lasers produisant ces impulsions. C'est en particulier le cas dans les systèmes laser exploitant le concept d'amplification à dérive de fréquence (CPA). Les composants et systèmes permettant de manipuler ou de corriger la phase spectrale sont cruciaux dans ce contexte et les AOPDFs sont appréciés pour leur compacité et leur simplicité d'utilisation. Les AOPDFs ne font cependant, en général, pas partie intégrante du CPA et sont insérés postérieurement à la construction du système laser.

Le problème se pose différemment dans les amplificateurs paramétriques optiques à dérive de fréquence (OPCPA) infrarouges où les étapes d'étirement et de compression sont moins évidentes que dans le proche infrarouge. La raison principale de cette difficulté est, qu'à durée constante, le nombre de cycles optiques sous l'enveloppe diminue lorsque la longueur d'onde augmente. Dit autrement, la bande spectrale relative $\Delta\omega/\omega_0$ augmente, ce qui implique de considérer des phases de plus en plus complexes. Par ailleurs, les réseaux de diffraction et les miroirs dispersifs sont d'autant plus inefficaces que la bande spectrale s'approche de l'octave ($\Delta\omega \simeq \omega_0$). Pour ces raisons, un étirement et/ou une compression par des matériaux massifs est souvent recherchée. En 2006 j'ai collaboré avec le MPQ (Garching, Allemagne) à un OPCPA à 2 µm [31] conçu autour de ce concept. Puis, avec le TUW (Vienne, Autriche), j'ai prolongé ce travail dans le cadre des techniques de post-compression à 1.5 µm [32–37]. Pour ces deux collaborations, l'AOPDF était inséré dans en début de chaîne OPCPA et était utilisé pour précompenser la dispersion des matériaux et/ou comprimer finement les impulsions en sortie de système. L'usage de l'AOPDF dans le système à 2 µm [31] est particulièrement intéressant car celui-ci joue un double rôle :

celui d'étireur et de façonneur d'impulsion. De plus, cette publication est la première démonstration que l'AOPDF préserve la phase porteuse-enveloppe (CEP). A bien des égards, l'OPCPA décrit dans [31] peut être considéré comme un précurseur des sources femtosecondes infrarouges de troisième génération [2], dont les AOPDFs constituent aujourd'hui l'une des pierres angulaires.

Parametric amplification of few-cycle carrier-envelope phase-stable pulses at 2.1 μm

T. Fuji, N. Ishii, C. Y. Teisset, X. Gu, Th. Metzger, and A. Baltuška
Max-Planck-Institut für Quantenoptik, Hans-Kopfermann-Strasse 1, D-85748 Garching, Germany

N. Forget and D. Kaplan
Fastlite, Bâtiment 403, Ecole Polytechnique, 91128 Palaiseau, France

A. Galvanauskas
Department of Electrical Engineering and Computer Science, College of Engineering, University of Michigan, 1301 Beal Avenue, Ann Arbor, Michigan 48109-2122

F. Krausz*
Ludwig-Maximilians-Universität München, Am Coulombwall 1, D-85748 Garching, Germany

Received December 9, 2005; accepted December 23, 2005; posted January 27, 2006 (Doc. ID 66564)

We demonstrate an optical parametric chirped-pulse amplifier producing infrared 20 fs (3-optical-cycle) pulses with a stable carrier-envelope phase. The amplifier is seeded with self-phase-stabilized pulses obtained by optical rectification of the output of an ultrabroadband Ti:sapphire oscillator. Energies of ~80 μJ with a well-suppressed background of parametric superfluorescence and up to 400 μJ with a superfluorescence background are obtained from a two-stage parametric amplifier based on periodically poled $LiNbO_3$ and $LiTaO_3$ crystals. The parametric amplifier is pumped by an optically synchronized 1 kHz, 30 ps, 1053 nm Nd:YLF amplifier seeded by the same Ti:sapphire oscillator. © 2006 Optical Society of America

OCIS codes: 190.4970, 320.5520, 140.3070.

Rapid advances in high-field physics have been achieved in recent years, particularly in the reproducible generation of isolated soft-x-ray attosecond pulses,[1] as a result of the development of drive lasers with specialized pulse properties. These properties include ultrahigh peak intensity, quasi-monocycle duration, and reliable control over the carrier-envelope phase (CEP).[2] While existing drive lasers operate near 0.8 μm, in the gain region of the Ti:sapphire, operating at longer, infrared wavelengths would be advantageous because the ponderomotive energy scales with λ^2. Therefore, the intensity of driving laser pulses needed to attain higher-order harmonic generation at a given x-ray photon energy can be substantially lower in comparison with the 0.8 μm case.[3–5] The use of IR drive pulses should extend the cutoff energy of x-ray photons and yield even shorter attosecond x-ray pulses. From the standpoint of laser technology, the longer duration of the IR optical period reduces the number of cycles for a given pulse envelope and, therefore, relaxes the requirement for amplifier gain bandwidth.

The concept of optical parametric chirped-pulse amplification[6,7] (OPCPA) could be ideal for future development of intense ultrashort-pulse higher-harmonic generation drive sources. Recently, several OPCPA systems delivering few-cycle 0.8 μm pulses were reported.[8–11] Femtosecond IR OPCPA systems have also been demonstrated,[12–14] but not in the few-cycle pulse range. In this Letter we describe a prototype few-cycle CEP-stabilized IR OPCPA based on periodically poled crystals.

A schematic of our two-stage OPCPA is presented in Fig. 1. The pump laser consists of a home-built 30 ps, 1053 nm Nd:YLF regenerative amplifier and a 4-pass postamplifier, delivering pulses up to 10 mJ at 1 kHz repetition rate. The pump pulses are optically synchronized with the seed pulses of OPCPA by injection seeding from a broadband Ti:sapphire oscillator.[15] The output spectrum of the 5 nJ, 6 fs all-chirped-mirror Ti:sapphire oscillator is given elsewhere.[16] The oscillator pulse energy within the fluorescence bandwidth of Nd:YLF at 1053 nm, diverted for optical seeding of the regenerative amplifier, is ~2 pJ.

IR seed pulses for the OPCPA are produced by difference-frequency generation (DFG) of the output of the Ti:sapphire oscillator in a 1 mm long MgO-doped periodically poled $LiNbO_3$ crystal (PPLN) with a quasi-phase-matching period of $\Lambda_{QPM}=13.9$ μm. The resultant DFG spectrum is shown as a dashed curve in Fig. 2. The estimated energy in the IR seed pulse is 4 pJ without heating the DFG crystal. The three-wave mixing process in DFG is identical to op-

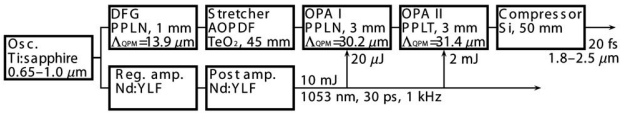

Fig. 1. Schematic of the IR OPCPA. AOPDF, acousto-optic programmable dispersive filter (Dazzler; Fastlite, Ltd.); PPLN, periodically poled $LiNbO_3$ crystal; PPLT, periodically poled $LiTaO_3$ crystal. All periodically poled crystals were obtained from HC Photonics, Ltd.

0146-9592/06/081103-3/$15.00

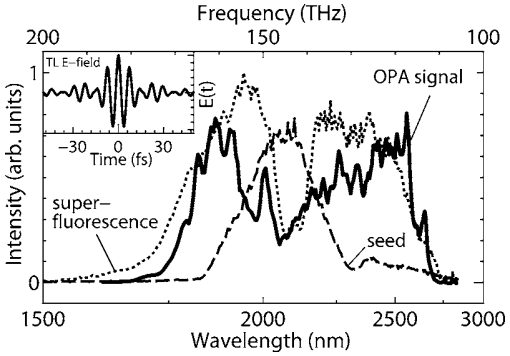

Fig. 2. Summary of spectral properties of the IR OPCPA. Solid curve, amplified signal spectrum after the second OPA stage; dashed curve, spectrum of the seed pulse generated by difference-frequency mixing; dotted curve, superfluorescence spectrum in a 3 mm thick PPLN. Inset, electric field of the pulse calculated for the solid curve assuming ideal pulse compression.

tical rectification, therefore, the pulses generated via DFG carry a constant CEP offset.[17–19] Unlike DFG schemes that mix two frequency-shifted pulses,[19] DFG between short- and long-wavelength components of a single broadband pulse removes the necessity to maintain a constant time delay between the mixing pulses. Consequently, there is no delay-related source of CEP jitter in our system.

Our optical parametric amplifier (OPA) operates near the degeneracy point of the three-wave mixing to ensure the broadest possible gain[20] in periodically poled nonlinear crystals. The first stage of the two-stage amplifier employs a 3 mm thick periodically poled MgO-doped $LiNbO_3$ crystal (PPLN OPA I in Fig. 1, $\Lambda_{QPM}=30.2\ \mu m$). The crystal is heated to 200°C to minimize the parasitic photorefractive effect. In the second-stage amplifier we use a periodically poled MgO-doped $LiTaO_3$ crystal (PPLT OPA II in Fig. 1, $\Lambda_{QPM}=31.4\ \mu m$). Compared with PPLN, the PPLT crystal has a lower nonlinear coefficient and, for the same crystal thickness, a slightly narrower phase-matching bandwidth. However, PPLT exhibits a higher damage threshold and has considerably smaller photorefractivity. The ultimate gain bandwidth potentially obtainable in our system is illustrated by the spectrum of parametric superfluorescence (dotted curve in Fig. 2) measured behind OPA I. For this measurement, the external OPA seed was blocked and a higher pump intensity was applied to switch to the regime of the optical parametric generator. The Fourier-limited pulse duration of this spectrum is ~12 fs.

In both OPA stages we introduced a 1.5° noncollinearity angle (internal) between the pump and the seed beams. A small crossing angle is required for spatial separation of the otherwise degenerate signal and idler waves and to prevent their mutual interference. The $1/e^2$ pump beam diameters are ~150 and ~350 μm for the first and the second OPA stages, respectively. In OPA I, the signal pulse is amplified to 1.35 μJ with a 40 μJ pump. In OPA II, the signal energy is boosted to 0.4 mJ using a 5 mJ pump pulse. The pump energy in this case is limited by optical damage to the PPLT crystal. The stability of the amplified pulse energy is 5% rms. Prior to amplification, the seed pulse was stretched to ~10 ps in a 50 mm long antireflection-coated silicon block to maximize the efficiency of the pump energy conversion. The corresponding amplified spectrum is shown in Fig. 2 (solid curve). Gain saturation causes substantial broadening of the injected seed spectrum. A single-pass parametric gain in excess of 10^6 can be easily obtained in our system. However, this amplification regime corresponds to a nonnegligible amount of superfluorescence that competes with the injected seed pulse. Therefore, for further amplification, the signal has to be injected into subsequent parametric amplifier stages with correspondingly increased pump pulse energies.

Several options for the pulse stretcher–compressor pair can be considered. Both the pulse stretcher and the compressor of an IR chirped-pulse amplifier could be based on bulk-dispersion materials,[21] because several types of glass (fused silica, fluoride glass, etc.) exhibit negative dispersion in this spectral range. However, it is impossible for compression from ~10 ps to <20 fs, which is a few cycles for IR pulses, since the sign of the third-order dispersion is the same for the materials with both positive and negative linear dispersion. To achieve few-cycle operation in this work, we employ an IR acousto-optic programmable dispersive filter Dazzler (Fastlite, Ltd.) as a pulse stretcher in front of the OPA and recompress the pulse in the above-mentioned 50 mm thick Si block. Because of the low material dispersion in the IR in comparison with the typically used near-IR spectral range, our 1.3–2.5 μm Dazzler can fully compensate for both the internal dispersion of a 45 -mm TeO_2 crystal and its dispersion of the Si block. The diffraction efficiency of the broadband Dazzler is ~10%, which dramatically reduces the seed energy supplied to the OPA. Therefore, the pump energies of both OPA stages have to be reduced correspondingly to suppress amplification of superfluorescence. As a result, the usable signal energy at the output of OPA II is decreased to ~80 μJ.

The amplified pulse is compressed in the Si block without significant loss. The pulse width is measured with an autocorrelator based on two-photon-induced photocurrent[22] in an InGaAs photodetector. The measured interferometric autocorrelation trace is shown in Fig. 3. The pulse appears to be compressed nearly to its theoretical limit, i.e., ~20 fs, or 3 cycles at FWHM. Since the wavelength range supported by the Dazzler is blueshifted with respect to the OPA gain bandwidth, the resultant amplified spectrum (Fig. 3, inset) is clipped around 2.5 μm. Therefore, further reduction of the pulse duration is expected with a modified Dazzler that will cover the entire bandwidth of interest.

To characterize the CEP stability of the OPCPA system, we measured f-to-3f spectral interferograms in a specially designed nonlinear interferometer. A 1 mm thick type I phase-matching β-barium borate crystal for third-harmonic generation[23] was placed in one arm of the interferometer, and a 2-mm-thick sap-

phire window for white-light generation in the other. The resultant spectral fringes, observed around 680 nm, are depicted in Fig. 4. The CEP dependence was verified by varying the glass thickness in front of the nonlinear interferometer. The residual phase excursions, seen in Fig. 4(b), are attributed to the amplitude–phase noise coupling in the white-light generator of the nonlinear interferometer.

In summary, we have demonstrated what is to our knowledge the first CEP-stable chirped-pulse parametric amplifier that currently produces 3-cycle pulses at the central wavelength of 2.1 μm. The laser output is directly scalable with pump pulse energy and crystal size.[24] This scheme presents a promising route toward constructing a high-peak-power IR drive laser for high-field and attosecond applications.

This work was supported by the LaserLab Europe and XTRA European networks. We thank HC Photonics for fruitful discussions on periodically poled crystals. This research was greatly motivated by a proposal of L. DiMauro from Ohio State University for improved attosecond high-harmonic generation with an IR driver. T. Fuji's e-mail address is tkf@mpq.mpg.de.

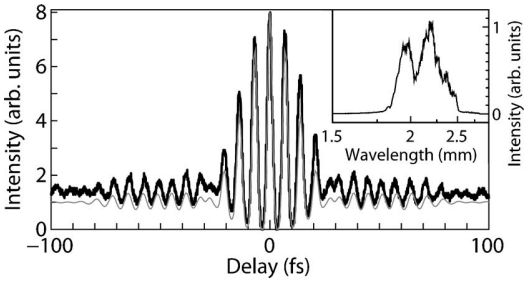

Fig. 3. Adaptive pulse compression using a Dazzler. Thick curve, measured interferometric autocorrelation based on the two-photon-induced photocurrent in an InGaAs photodiode; thin curve, calculated autocorrelation trace assuming ideal pulse compression. Inset, signal pulse spectrum.

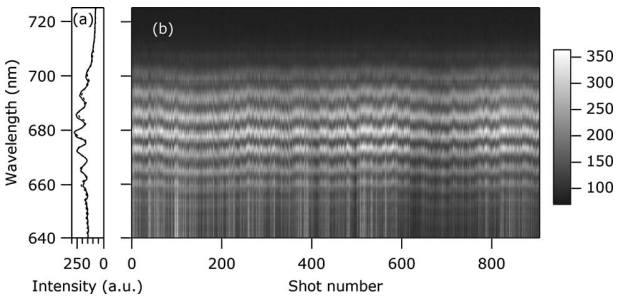

Fig. 4. Examination of CEP stability by nonlinear spectral interferometry. (a) Single-shot f-to-3f interferogram (solid curve) and an average over 1 s (dashed curve). (b) Single-shot interferograms for successive laser shots. See text for details.

*Also with the Max Planck Institute of Quantum Optics, Hans-Kopfermann-Strasse 1, D-85748 Garching, Germany, and the Photonics Institute, Vienna University of Technology, Gusshausstrasse 27/387, A-1040 Vienna, Austria.

References

1. R. Kienberger, E. Goulielmakis, M. Uiberacker, A. Baltuška, V. S. Yakovlev, F. Bammer, A. Scrinzi, T. Westerwalbesloh, U. Kleineberg, U. Heinzmann, M. Drescher, and F. Krausz, Nature **427**, 817 (2004).
2. A. Baltuška, T. Udem, M. Uiberacker, M. Hentschel, E. Goulielmakis, C. Gohle, R. Holzwarth, V. S. Yakovlev, A. Scrinzi, T. W. Hänsch, and F. Krausz, Nature **421**, 611 (2003).
3. P. Agostini and L. F. DiMauro, Rep. Prog. Phys. **67**, 1 (2004).
4. M. Lewenstein, P. Balcou, M. Y. Ivanov, A. L'Huillier, and P. B. Corkum, Phys. Rev. A **49**, 2117 (1994).
5. A. Gordon and F. X. Kärtner, Opt. Express **13**, 2941 (2005).
6. A. Dubietis, G. Jonušauskas, and A. Piskarskas, Opt. Commun. **88**, 437 (1992).
7. I. N. Ross, P. Matousek, M. Towrie, A. J. Langley, and J. L. Collier, Opt. Commun. **144**, 125 (1997).
8. C. P. Hauri, P. Schlup, G. Arisholm, J. Biegert, and U. Keller, Opt. Lett. **29**, 1369 (2004).
9. R. T. Zinkstok, S. Witte, W. Hogervorst, and K. S. E. Eikema, Opt. Lett. **30**, 78 (2005).
10. N. Ishii, L. Turi, V. S. Yakovlev, T. Fuji, F. Krausz, A. Baltuška, R. Butkus, G. Veitas, V. Smilgevičius, R. Danielius, and A. Piskarskas, Opt. Lett. **30**, 567 (2005).
11. S. Witte, R. T. Zinkstok, W. Hogervorst, and K. S. E. Eikema, Opt. Express **13**, 4903 (2005).
12. A. Galvanauskas, A. Hariharan, D. Harter, M. A. Arbore, and M. M. Fejer, Opt. Lett. **23**, 210 (1998).
13. F. Rotermund, C. J. Yoon, V. Petrov, F. Noack, S. Kurimura, N.-E. Yu, and K. Kitamura, Opt. Express **12**, 6421 (2004).
14. J. V. Rudd, R. J. Law, T. S. Luk, and S. M. Cameron, Opt. Lett. **30**, 1974 (2005).
15. N. Ishii, C. Y. Teisset, T. Fuji, S. Köhler, K. Schmid, L. Veisz, A. Baltuška, and F. Krausz, "Seeding of the 11-fs OPCPA and its Nd^{3+} picosecond pump laser from a single broadband Ti:sapphire oscillator," IEEE Sel. Top. Quantum Electron (to be published).
16. T. Fuji, J. Rauschenberger, C. Gohle, A. Apolonski, T. Udem, V. S. Yakovlev, G. Tempea, T. W. Hänsch, and F. Krausz, New J. Phys. **7**, 116 (2005).
17. A. Baltuška, T. Fuji, and T. Kobayashi, Phys. Rev. Lett. **88**, 133901 (2002).
18. T. Fuji, A. Apolonski, and F. Krausz, Opt. Lett. **29**, 632 (2004).
19. C. Manzoni, G. Cerullo, and S. D. Silvestri, Opt. Lett. **29**, 2668 (2004).
20. J. Limpert, C. Aguergaray, S. Montant, I. Manek-Hönninger, S. Petit, D. Descamps, E. Cormier, and F. Salin, Opt. Express **13**, 7386 (2005).
21. N. Demirdöven, M. Khalil, O. Golonzka, and A. Tokmakoff, Opt. Lett. **27**, 433 (2002).
22. J. K. Ranka, A. L. Gaeta, A. Baltuška, M. S. Pshenichnikov, and D. A. Wiersma, Opt. Lett. **22**, 1344 (1997).
23. P. S. Banks, M. D. Feit, and M. D. Perry, Opt. Lett. **24**, 4 (1999).
24. H. Ishizuki and T. Taira, Opt. Lett. **30**, 2918 (2005).

2.4 Contrôle et stabilisation de la phase enveloppe-porteuse

Si la plupart des interactions lumière-matière ne sont sensibles qu'à l'éclairement optique (ie au flux de puissance surfacique instantané), certains phénomènes comme la génération d'harmoniques élevées dépendent directement du champ électrique. L'étude de ces phénomènes requiert donc des sources ultra-brèves dont le champ électrique est contrôlé et reproductible d'une impulsion optique à l'autre. Il s'agit donc non seulement de produire des impulsions optiques de même énergie, de même durée et de même profil temporel/spatial, mais aussi avec la même relation de phase entre le champ électrique et son enveloppe. Cette phase enveloppe-porteuse – CEP pour « carrier-envelope phase » - n'est pas triviale à caractériser ni même à stabiliser. L'amplification laser étant insensible à la CEP, les lasers ne produisent pas naturellement des impulsions de CEP stable. Plusieurs solutions techniques sont possibles pour contourner cette difficulté. L'une d'elle consiste à exploiter le fait que la dispersion optique induit un glissement de l'enveloppe par rapport à la porteuse. En contrôlant avec précision la dispersion intracavité d'un oscillateur femtoseconde (via une contre-réaction sur la puissance de pompe par exemple) celle-ci peut être réglée de manière suffisamment précise pour que la CEP varie périodiquement et qu'un large sous-ensemble d'impulsions partagent une même valeur de CEP. Par sélection électro-optique (par exemple) on forme ainsi un train d'impulsions de même CEP. En pratique, cette opération de décimation n'est pas sans conséquence et tend à « replier » le bruit haute fréquence vers les basses fréquences. De plus, les variations de chemin optique induits lors de la propagation ou de l'amplification réintroduisent des fluctuations de CEP. La stabilité thermique et/ou mécanique des étireurs et des compresseurs dans les CPA, qui sont nécessairement très dispersifs, est une cause majeure de dérive lente de la CEP. Une boucle de rétroaction « lente » est donc nécessaire pour maintenir la stabilité de la CEP.

Les AOPDFs fournissent, là encore, une solution élégante à ce problème pour contrôler et stabiliser la CEP. La phase absolue acoustique étant transférée à l'onde diffraction, le contrôle de la première permet celui de la seconde. Or, la phase de l'onde RF (qui induit l'onde acoustique via un transducteur) est générée point par point de manière arbitraire. Les AOPDF autorisent donc un contrôle indépendant de l'enveloppe temporelle et de la phase de la porteuse optique. Une quantité quelconque de CEP peut être ajoutée ou retranchée sur l'onde diffractée. Cette propriété est d'autant plus intéressante que ce contrôle de phase n'est pas borné, à la différence des systèmes de correction dispersifs : une dérive monotone de la CEP peut être continûment corrigée sans limitation de durée. Enfin, le contrôle de CEP est complètement découplé de celui de l'enveloppe temporelle. Une mesure de la dérive de CEP, par un interféromètre f-2f par exemple, reste néanmoins nécessaire pour bâtir une boucle de stabilisation.

Les premières démonstrations de stabilisation de CEP ont été menées en collaboration avec l'équipe PCO au LOA (ENSTA, Palaiseau) d'abord sur une chaîne Ti:Saphir [38, 39] en 2008-2009 puis dans le cadre du développement d'un double CPA de classe 10 mJ, à la fois stable en CEP et à haut contraste temporel. Le développement des grismes de compression (section 2.5) a également permis de réduire la dérive de CEP par construction [40]. La collaboration avec le LOA sur la stabilisation de la CEP s'est étendue sur plusieurs thèses :

celles de Lorenzo Canova [41], Aurélien Ricci [42] et de Hermance Jacqmin [43]. Bien que n'ayant pas encadrer ces thèses au quotidien, j'ai eu l'occasion de travailler fréquemment avec eux et notamment avec Lorenzo Canova.

L'application des AOPDFs à la stabilisation de CEP s'est poursuivie avec une collaboration industrielle avec Femtolasers (Vienne, Autriche). Grâce à une mesure rapide (10 kHz) de la dérive de CEP, j'ai pu démontrer avec Vincent Crozatier (Fastlite), et Fabian Lücking (doctorant à Femtolasers à l'époque) que les AOPDFs permettent d'atteindre des valeurs records de stabilité de CEP (non moyennée) dans les systèmes laser Ti:Saphir en 2014 : 100 mrad rms sur 1 mn [44]. Le principe de la mesure rapide et l'asservissement sont détaillées dans un chapitre de revue [45]. Une très large part des sources femtosecondes de 3ème génération, qu'elles soient commerciales ou construites par des laboratoires de recherche, intègre aujourd'hui une stabilisation active de la CEP via un AOPDF.

2.5 Grismes

Dans un contexte connexe, nous avons proposé, avec Pierre Tournois et Vincent Crozatier, un nouveau type de compresseur : les « grismes de Bragg » [46, 47]. Cet assemblage de prismes et de réseaux en transmission permet de comprimer efficacement (moins de 30% de pertes) des impulsions ultra-brèves tout en combinant dispersion quadratique négative (GVD [5] négative) et dispersion cubique également négative (TOD [6] négative) - une combinaison habituellement impossible à atteindre avec des réseaux seuls. Les compresseurs à grismes sont ainsi bien adaptés à la compensation de la dispersion de matériaux massifs (caractérisés par un chirp positif et un troisième ordre positif). Une extension aux phases quartiques à également été démontrée [48] en collaboration avec Laszlo Weisz au Max-Planck-Institut für Quantenoptik (MPQ, Garching, Allemagne) puis au Département de Physique de l'Université d'Umeå (Umeå, Suède).

Les grismes ont été principalement développés avec le groupe PCO du LOA, dans le cadre du contrat ASTRE 2010 coordonnée par Rodrigo Lopez-Martens (programme du Conseil Général de l'Essonne). Ce contrat a permis l'étude détaillée d'une nouvelle configuration d'étirement-compression pour les lasers femtosecondes dont la CEP est stabilisée. Ce schéma, basé sur la combinaison d'un étireur verre (SF57, géométrie en « billard ») et d'un compresseur composé de prismes en SF57 et de réseaux en transmission a permis l'étirement à 50 ps puis la compression à 20 fs d'impulsions de 10 mJ, 1 kHz. Le dispositif préserve la CEP [40,49]. Ma contribution a porté sur les calculs de dispersion, la conception de l'étireur et des grismes et la coordination de la partie Fastlite de ce programme de recherche.

5. Group Velocity Dispersion
6. Third Order Dispersion

Appl. Phys. B (2012) 109:121–125
DOI 10.1007/s00340-012-5126-2

Applied Physics B
Lasers and Optics

Transmission Bragg-grating grisms for pulse compression

Nicolas Forget · Vincent Crozatier · Pierre Tournois

Received: 1 December 2011 / Revised: 18 May 2012 / Published online: 16 September 2012

Abstract We design a grism compressor based on transmission gratings and high refractive index prisms to compensate for both the second- and third-order dispersions of SF57 glass at 800 nm. The use of transmission gratings eases the geometrical constraints, allows a final recombination of the spectral components out of the bulk of the prisms and suggests a potential application of these grims to high-energy pulse compression. The dispersion law of this grism compressor is measured in double-pass configuration and negative third-order dispersion is achieved. We demonstrate efficient operation with an overall throughput >60% over a 100 nm bandwidth.

1 Introduction

Chirped-pulse amplification (CPA) requires optical devices characterized by large group delay dispersions (GDD) to stretch/compress the ultrashort pulses before/after the amplification stage. In the first embodiment of CPA [1] in 1985, the laser pulses were stretched in a fused silica fiber with positive GDD and compressed by a pair of reflective gratings arranged to provide negative GDD (Treacy configuration [2, 3]). However, as both fused silica and grating pairs introduce a high level of positive third-order dispersion (TOD) in the near infrared, the dispersion of the grating pair was not perfectly opposite to the dispersion of the fiber [4] and the pulses could not be recompressed to their Fourier-transform limit. To solve this issue and achieve a perfect matching between stretcher and compressor, an open-space stretcher combining reflective gratings and an imaging afocal telescope of magnification -1, introduced by Martinez [5] in 1987, can be used. Since then, Treacy compressors and Martinez/Öffner stretchers [6] have been extensively used in CPA laser systems.

The use of bulk stretchers made of highly dispersive glass rods simplifies the overall design of CPA sources and improves their long-term stability. These devices are indeed immune to vibrations, mechanical or thermal drifts and offer the highest throughput and bandwidth. If grating-based stretchers have been favored in the earlier years of CPA because of their larger GDD, the recent spread of ultrabroadband sources (>50–100 nm) brings a renewed attention to bulk stretchers and to the issue of TOD compensation. In 1969 [7], it was already pointed that TOD could be canceled or inversed by replacing reflective gratings by a combination of gratings and prisms [8].

However, these very first grisms were designed far from the Littrow incidence and suffered from low diffraction efficiency. Besides, the highest peak power was reached in the bulk of the prisms which induced a high level of nonlinear effects such as self-focusing and self-phase-modulation. In practice, these drawbacks prevented the practical use of these grisms as pulse compressors. Since then several other grism designs based on reflective gratings have been proposed and demonstrated [9–13]. By working closer to the Littrow angle, the diffraction efficiency of the gratings could be enhanced to that of conventional grating compressors [14]. Yet, the issue of nonlinear effects was not solved, which limited the applications of grisms to low-energy pulse compression in up-chirped CPAs [15] or pulse stretching in down-chirped CPAs [9]. Although out of the scope of this paper, grisms have also found applications in research fields such as pulse-shaping devices [16, 17], achromatic phase-matching schemes in nonlinear optics

N. Forget (✉) · V. Crozatier · P. Tournois
FASTLITE, Centre scientifique d'Orsay - Bât.503,
Plateau du Moulon, 91401, Orsay, France
e-mail: forget@fastlite.com

[18], confocal microscopy [19] or nonlinear endomicroscopy [20].

In this letter, we study a grism compressor comprising two parallel Bragg gratings between which two anti-parallel, right-angle, high-index prisms are placed (Fig. 1). As opposed to designs based on reflective gratings, the use of transmission gratings simplifies the geometrical constraints and allows to work at the exact Littrow angle, where the diffraction efficiency and bandwidth are optimal. With this geometry, the distance between the optical components can also be varied arbitrarily and the resulting GDD and TOD can be continuously tuned from 0 to a value only bounded by the transverse dimension of the optics. Last, an air gap can be introduced between the first grating and the first prism, which enables a final recombination of the spectral components out of the bulk of the prisms. This key feature could considerably reduce the level of nonlinear effects and suggest a potential application of these grisms to high-energy pulse compression. As a proof of concept, we experimentally characterize a grism compressor designed to compensate for both the GDD and TOD of an SF57 glass rod at 800 nm.

2 Principle

Let σ be the groove density of the gratings and α be the apex angle of the prisms of refractive index n. The prisms are inserted between the gratings with the outer faces parallel to the grating surfaces. Let L be the distance between the outer faces of the prisms, $G = G_1 + G_2$ be the total air gap between the grating and the prisms, H be the perpendicular distance between the prism apices, measured as the projection of the segment linking the apices along the grating surface. The distance between the inner surfaces of the prisms is $d = L\cos(\alpha) - H\sin(\alpha)$. The total length of the device is $G + L$. Light propagates from left to right and the input beam direction is θ_i with respect to the normal to the grating surfaces. The first Bragg order is diffracted in air with a positive angle θ_d given by the grating rule:

$$\sin(\theta_d) - \sin(\theta_i) = c\frac{\sigma}{\nu} \tag{1}$$

where ν is the optical frequency and c is the velocity of light in vacuum. The diffracted beam is then refracted by the first air–glass interface and propagates in glass with an angle r_1 with respect to the input face. Let r_2 be the incidence angle at the output glass–air interface and i_2 be the propagation direction in air after the second refraction with respect to the normal to the glass–air surface. The angles θ_d, r_1, r_2, i_2 and α are linked by

$$\begin{cases} n\sin(r_1) = \sin(\theta_d) \\ r_2 = r_1 - \alpha \\ n\sin(r_2) = \sin(i_2) \end{cases} \tag{2}$$

The beam travels in air the distance $d/\cos(i_2)$, is refracted by the second prism, diffracted by the second grating and exits parallel to the input beam direction. We now consider the total group delay τ_p added by the grism pair to a plane wave propagating between the reference planes defined by the two prisms apices and the direction θ_i. Let N be the group delay index of the prisms. All interfaces being two-by-two parallel, it is clear that the total group delay depends neither on the incident position of the input beam nor on the repartition of the air gaps between the gratings and the prisms. For the sake of simplicity, it is therefore convenient to assume, without any loss of generality, that the first grating is engraved on the first prism and that the input light ray hits the first prism at the apex. The absolute group delay τ_p is then equal to the sum of the group delays of the three consecutive propagating segments, in air (d), glass (second prism) and air again:

$$\begin{aligned} c.\tau_p = {} & \frac{d}{\cos(i_2)} + \frac{L}{\cos(r_1)}\left[N - \sin(\theta_i)\frac{\cos(r_2)}{\sin(\alpha)}\right] \\ & \times \left[1 - \frac{d}{L}\frac{\cos(\alpha + i_2)}{cos(i_2)}\right] + G\frac{1 - \cos(\theta_i - \theta_d)}{\cos(\theta_d)} \end{aligned} \tag{3}$$

It is easy to check that these three terms are always positive, as can be expected for absolute group delays. As can be shown by numerical investigation, the total third-order dispersion of a grism pair becomes negative when r_2 is close to the critical angle for total internal reflection. As a general trend, for given G, H and L values, large apex angles correspond to negative TOD, whereas small apex angles correspond to positive TOD. From a design point of view, once the groove density and the optical indices have been defined, the dispersion law of the grism compressor depends on five independent geometrical variables. However, since θ_i has to be equal to the Bragg incidence ($2\sin\theta_i = -c\sigma/\nu_0$) there remains, in fact, only four independent geometrical parameters: the apex angle α, the

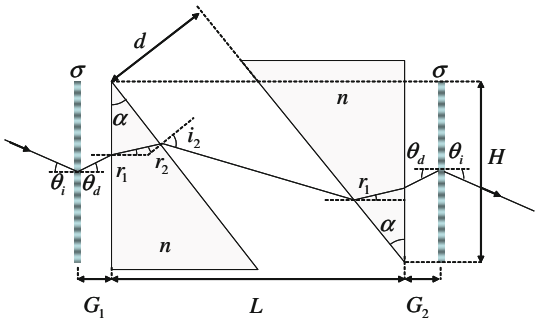

Fig. 1 Single-pass grism setup

geometrical parameters $g = G/L$, $h = H/L$ and the scaling length L. It is also worth noting that the contribution of the air gap G (last term of Eq. 3) to the total dispersion is minor when compared with the other terms and that negative TOD values can also be reached if $G = 0$. As for pairs of prisms or gratings, a pair of grism exhibits in single pass a lateral chromatism since all the optical rays exit the grism pair with the same direction but at frequency-dependent location. In the experiments described below, a roof-top mirror was used to double-pass the grism pair and compensate for this effect.

3 Experimental results

A grism compressor was assembled from 10×20 mm^2 fused-silica gratings with a groove density of 1,250 g/mm (Ibsen Photonics, damage threshold >40 GW/cm^2 http://www.ibsen.dk/highpower) and 25×25 mm^2 SF57 prisms with a apex angle of 42.5°. Broadband anti-reflection coatings were deposited on the substrate sides of the gratings as well as on the three facets of the prisms. The apex angle $\alpha = 42.5°$ and the geometrical parameters $g = 0.32$ and $h = 0.8$ were chosen. For practical reasons, the selected geometrical parameters were $G \simeq 10$ mm, $H \simeq 25$ mm and $L \simeq 31$ mm. The dispersion law of the corresponding compressor in double-pass configuration is shown in Fig. 2 together with a sketch of the compressor. the The total size of the compressor was 25×40 mm^2, which is a little smaller than a grating compressor with the same GDD. The dispersion law of the grism pair was measured, in double-pass configuration, by spectral interferometry: the grism compressor was inserted in one arm of a dispersion balanced Michelson interferometer and the interference pattern was recorded with a spectrometer (AvaSpec2048L from Avantes, spectral resolution of 0.1 nm). However, given the large dispersion of the grism compressor and the finite resolution of the spectrometer, it was not possible to resolve the interference pattern over the complete spectral range. Rather than retrieving the spectral phase piecewise, we measured directly the group delay as a function of frequency, using the method described by [9]: due to the high dispersion of the grisms, the interferogram

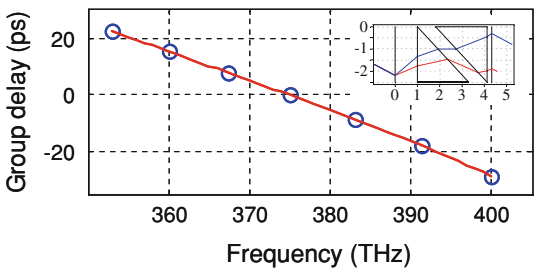

Fig. 2 Theoretical group delay in double-pass configuration as a function of frequency computed from Eq. (*solid line*) and from a ray tracing algorithm (*dots*). *Inset*: *ray* tracing *plot* showing the optical propagation at 750 and 850 nm. Units are cm

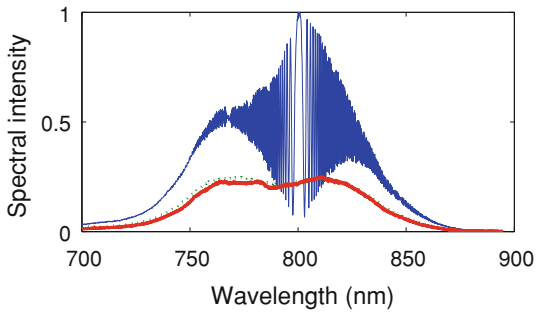

Fig. 3 Example of experimental interference pattern (*solid line*) between the input spectrum (*dots*), the output of the grism compressor (*dashed line*)

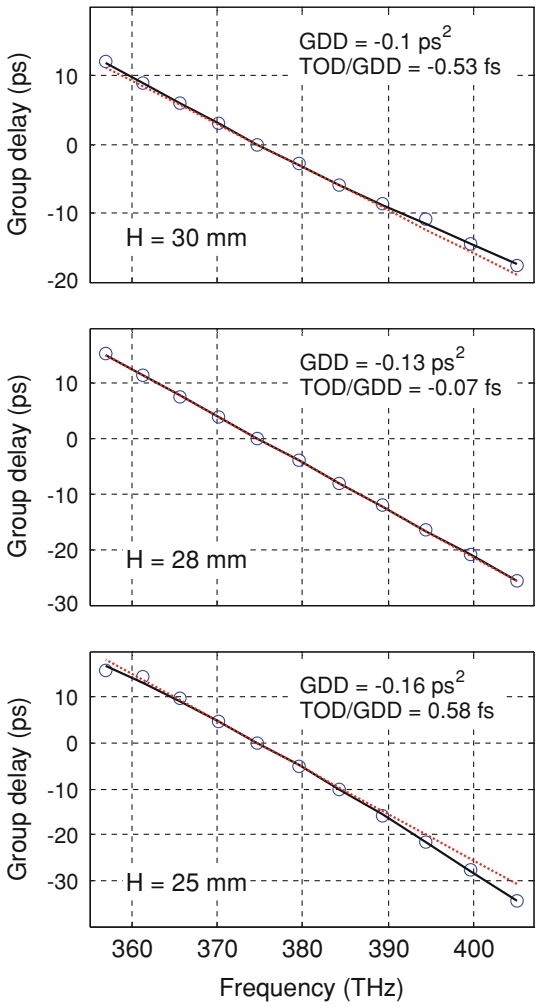

Fig. 4 Group delay as a function of frequency for three settings. *Blue dots*: experimental points. *Blue solid line*: parabolic fit. *Red dashed line*: linear fit

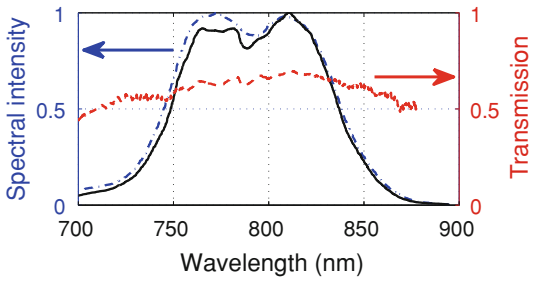

Fig. 5 Transmission of the double-pass grism compressor as function of wavelength. *Blue dash-doted line*: normalized input spectrum. *Solid dark line*: output spectrum. *Red dots*: transmission

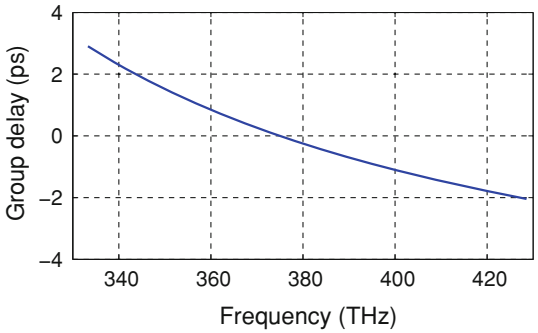

Fig. 6 Calculated group delay added by the last air interval

exhibits chirped fringes with a flat fringe localized at the wavelength for which the group delay is equal on both arms (Fig. 3). By varying the length of the reference arm and recording the coincidence wavelength, the group delay of the grism compressor could be retrieved with ±60 fs and ±0.3 THz accuracies over the full bandwidth of a ≃12 fs mode-locked oscillator (740–840 nm).

A polynomial fit of the group delay as a function of angular frequency was then used to extract the GDD and TOD values. As shown in Fig. 4, for the experimental parameters $G1 + G2 \simeq 8$ mm, $H \simeq 25$ mm, $L \simeq 31$ mm and $\theta_i \simeq -32.5°$ the measured GDD and TOD were equal to -1.62×10^5 fs^2 and -0.94×10^5 fs^3, in good agreement with the theoretical values (-1.64×10^5 fs^2 and -0.91×10^5 fs^3) given the fit accuracy ($\pm 0.03 \times 10^5$ fs^2 and $\pm 0.18 \times 10^5$ fs^3). The corresponding experimental TOD/GDD ratio was comprised between +0.47 and +0.69 fs and the corresponding chirp ratio was of ≃0.5 ps/nm. Although not demonstrated here, such GDD values would be large enough to compensate for the dispersion of an SF57 rod of approximately 73 cm. By translating one of the prism parallel to the gratings it was possible to vary the TOD/GDD ratio from −0.5 fs to +0.7 fs, encompassing the value of +0.63 fs necessary to compensate for the TOD/GDD ratio of SF57. As shown in Fig. 4, the curvature of the group delay as a function of frequency decreases from positive to negative as H is decreased. For $H \simeq 28$ mm, the TOD nearly vanishes and the dispersion of the grims compressor is almost completely linear with frequency.

The total throughput of the grism compressor was ≃ 65% at 800 nm, >60 % over the 740–840 nm bandwidth and >50 % over the 710–875 nm bandwidth (Fig. 5). As it can be noticed, the latter bandwidth (≃165 nm at 790 nm) is large enough to sustain Gaussian pulses of ≃12 fs FWHM. Assuming a perfect compression at the output of the grism compressor, the group delay function at the output of the last prism (first prism in double-pass configuration) is given by the last term of Eq. 3 for $G = G1$. For the experimental parameters, the calculated group delay spreads from −2.0 to +2.9 ps over the 700–900 nm bandwidth and indicates that for ≃12 fs pulses, the shortest pulse duration in the bulk of the prism would be about 1.8 ps FWHM (Fig. 6). With $G1 = 8$ mm and $G2 = 0$, this value could even reach 3.6 ps FWHM.

4 Conclusion

Grism compressors based on Bragg transmission gratings and high refractive index prisms open the path to efficient and broadband compression scheme with adjustable third-order dispersion phase. Such compressors could be designed to match and compensate for the GDD and TOD of bulk stretchers, with chirp ratii large enough to sustain <15 fs, mJ-level, amplified pulses.

References

1. D. Strickland, G. Mourou, Opt. Commun. **55**, 447–449 (1985)
2. E.B. Treacy, Phys. Lett. A **28**, 34–35 (1968)
3. E. Treacy, IEEE J. Quantum Electron. **5**, 454–458 (1969)
4. P. Maine, D. Strickland, P. Bado, M. Pessot, G. Mourou, IEEE J. Quantum Electron. **24**, 398–403 (1988)
5. O. Martinez, IEEE J. Quantum Electron. **23**, 59–64 (1987)
6. G. Cheriaux, P. Rousseau, F. Salin, J.P. Chambaret, B. Walker, L.F. Dimauro, Opt. Lett. **21**, 414–416 (1996)
7. P. Tournois, C.R. Acad. Sc. Paris **269**, 455–458 (1969)
8. P. Tournois, Electron. Lett. **29**, 1414–1415 (1993)
9. T.H. Dou, R. Tautz, X. Gu, G. Marcus, T. Feurer, F. Krausz, L. Veisz, Opt. Express **18**, 27900–27909 (2010)
10. F. Tavella, Y. Nomura, L. Veisz, V. Pervak, A. Marcinkevičius, F. Krausz, Opt. Lett. **32**, 2227–2229 (2007)
11. J. Zheng, H. Zacharias, Appl. Phys. B Lasers Opt. **96**, 445–452 (2009)
12. V. Chauhan, P. Bowlan, J. Cohen, R. Trebino, J. Opt. Soc. Am. B **27**, 619–624 (2010)
13. R. Fork, C. Cruz, P. Becker, C. Shank, Opt. Lett. **12**, 483–485 (1987)
14. S. Kane, J. Squier, J. Opt. Soc. Am. B **14**, 661–665 (1997)
15. E.A. Gibson, D.M. Gaudiosi, H.C. Kapteyn, R. Jimenez, S. Kane, R. Huff, C. Durfee, J. Squier, Opt. Lett. **31**, 3363–3365 (2006)
16. M.S. Kirchner, S.A. Diddams, Opt. Lett. **35**, 3264–3266 (2010)

Carrier-envelope-phase stable, high-contrast, double chirped-pulse-amplification laser system

Aurélie Jullien,[1,*] Aurélien Ricci,[1,2] Frederik Böhle,[1] Jean-Philippe Rousseau,[1] Stéphanie Grabielle,[3] Nicolas Forget,[3] Hermance Jacqmin,[1,2] Brigitte Mercier,[1] and Rodrigo Lopez-Martens[1]

[1]*Laboratoire d'Optique Appliquée, École Nationale Supérieure de Techniques Avancées—Paristech, École Polytechnique, CNRS, 91762 Palaiseau Cedex, France*

[2]*Thales Optronique SA, Laser Solutions Unit, 2 Avenue Gay-Lussac, 78995 Elancourt, France*

[3]*Fastlite, Les Collines de Sophia, 1900 Route des Cretes, 06560 Valbonne, France*

**Corresponding author: aurelie.jullien@ensta-paristech.fr*

Received March 28, 2014; accepted May 8, 2014;
posted May 16, 2014 (Doc. ID 208929); published June 19, 2014

We present the first carrier-envelope-phase stable chirped-pulse amplifier (CPA) featuring high temporal contrast for relativistic intensity laser–plasma interactions at 1 kHz repetition rate. The laser is based on a double-CPA architecture including cross-polarized wave (XPW) filtering technique and a high-energy grism-based compressor. The 8 mJ, 22 fs pulses feature 10^{-11} temporal contrast at –20 ps and a carrier-envelope-phase drift of 240 mrad root mean square.

OCIS codes: (320.7090) Ultrafast lasers; (320.5520) Pulse compression; (190.7110) Ultrafast nonlinear optics.
http://dx.doi.org/10.1364/OL.39.003774

Relativistic optics has opened the way to compact plasma-based particle accelerators and extreme ultraviolet (XUV) and x-ray sources [1–4]. Currently, several trends can be recognized in experimental facilities dedicated to intense laser–matter interactions. On the one hand, multiterawatt femtosecond lasers with ultrahigh intensity can be used to drive compact plasma-based particle accelerators [1,2]. On the other hand, the ability to generate waveform-controlled few-cycle light pulses has provided brand new tools for investigating ultrafast electronic processes in atoms, molecules, or solids [4]. More recently, few-cycle pulses with relativistic intensity, but without carrier-envelope-phase (CEP) control, have been used to study electron-bunch acceleration from gas jets or high-harmonic generation from solid targets [5,6]. At Laboratoire d'Optique Appliquée (LOA), a pioneering experimental platform has been developed (Salle Noire) that merges these two trends and is dedicated to the study of laser–plasma interactions in the few-cycle regime at 1 kHz repetition rate. Until now, the waveform-controlled laser source delivered 1.2 mJ, 5 fs pulses with a relative CEP drift of 250 mrad root mean square (RMS) and a temporal contrast of 10^{-7} [7]. It was based on a Ti:Sa CPA system followed by postcompression in a gas-filled hollow-core fiber. When focused down to a spot size of 2 μm FWHM, the laser pulses could reach typical intensities on the solid target just below 10^{18} W/cm^2. Recent results obtained with this system include attosecond control of collective electron motion in plasmas, the generation of synchronized isolated attosecond pulses from plasma mirrors and the acceleration of energetic ions [8–10].

In this Letter, we present the upgrade of the Salle Noire laser system to pass into the relativistic intensity regime, i.e., with intensities on target well above 10^{18} W/cm^2 at 800 nm wavelength. It involves increasing both the pulse energy as well as the temporal contrast by several orders of magnitude, while maintaining high repetition rate and full waveform control. Two major techniques are now widely used to decrease the intensity of the amplified spontaneous emission (ASE) background of existing chirped-pulse-amplifier (CPA) systems. Plasma mirrors can efficiently clean the pulse at the output of the laser chain at the expense of the available energy [11,12]. Another option is to insert a temporal filter inside the laser chain, with subsequent reamplification enabling recovery of the energy losses. In this case, efficient temporal cleaning is provided by a nonlinear effect, which calls for a double-CPA architecture [13]. At LOA, we have developed and qualified a nonlinear filter relying on cross-polarized wave (XPW) generation [14]. XPW generation is an achromatic and degenerated four-wave mixing process relying on the anisotropy of the χ^3 tensor in isotropic crystals. A linearly polarized input beam is focused onto a nonlinear crystal placed between crossed polarizers and generates an orthogonally polarized wave. The cubic dependence between output and input intensities improves temporal contrast that is limited only by the extinction ratio of the crossed polarizers (3–4 orders of magnitude). Currently, XPW filters have become widespread in high-peak-power laser systems [12,15–17].

Therefore, we modified the laser system to a double-CPA architecture with an XPW filter. Another challenge was associated with this upgrade. As the final goal is to postcompress the laser pulses down to the few-cycle regime, CEP stability is needed. Consequently, the increase of the output energy requires specific dispersion management in the second CPA to reduce B integral during amplification while preserving the CEP stability.

As a result, we demonstrate the realization of the first double-CPA CEP-stable laser system featuring 8 mJ, 22 fs, 1 kHz pulses with a temporal contrast of 10^{-11}. The overall layout of the laser system appears in Fig. 1.

A detailed description and characterization of the high-contrast injector can be found in [18]. It consists of a commercial 1 kHz CEP-stabilized CPA (CPA1, Femtopower Compact Pro CE Phase, Femtolasers GmbH) followed by an XPW contrast filter. The oscillator pulses (Rainbow) are CEP-locked via pump-laser amplitude modulation and stretched in a 20-cm-long SF57 block

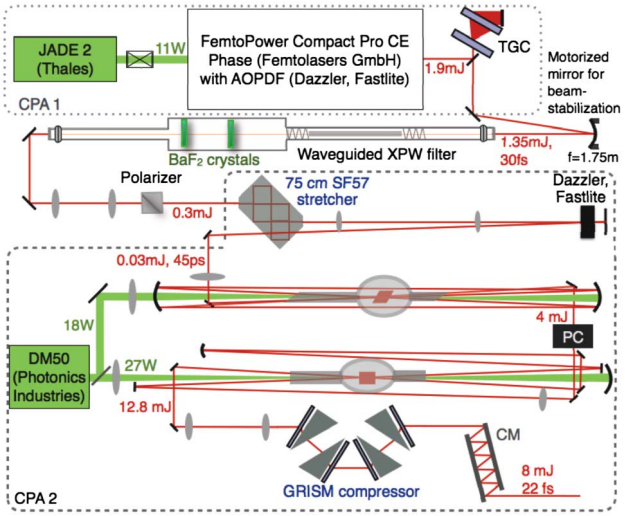

Fig. 1. Experimental scheme of high-contrast, 8 mJ, 22 fs, 1 kHz CEP-stable double-CPA system. (TGC, transmission gratings compressor; PC, Pockels cell; CM, chirped mirrors).

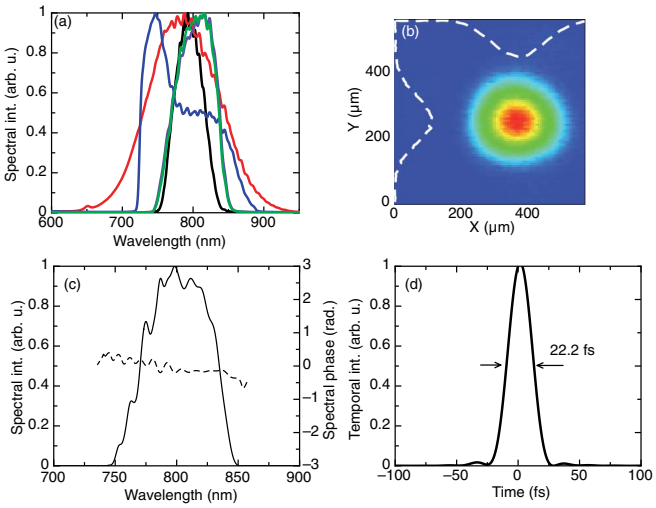

Fig. 2. (a) Evolution of the spectrum along the laser chain: after the FemtoPower (black), after XPW (red), after stretcher (bulk and Dazzler) of CPA2 (blue), after power amplifier (purple), and after the compressor (green). (b) Far-field spatial quality of the compressed pulse. Temporal measurement of the compressed 8 mJ pulse (Wizzler), (c) spectral amplitude and phase, and (d) temporal intensity profile.

before amplification up to 1.9 mJ in a 10-pass Ti:Sa amplifier including an acousto-optic programmable dispersive filter (AOPDF) (low-jitter Dazzler HR800, Fastlite). The amplification stage is pumped by 11 W from a 1 kHz frequency-doubled Q-switched Nd:YLF laser (JADE, Thales). The 7-ps-long amplified pulses are then compressed through a transmission-grating compressor (TGC) with an overall efficiency of 85%. The TGC consists of a pair of 1280 l/mm gratings used at the Littrow incidence angle (30.8°) and separated by 10 mm. The compressed-pulse duration is 28 fs.

The pulses are then sent to the XPW filter which is an optimized version of the energy-scalable device described in [19]. It consists of a 47 cm, 250 μm inner-diameter hollow-core waveguide providing efficient spatial filtering (75% transmission), followed by two thin, 1.5-mm-thick, BaF_2 crystals with holographic crystallographic orientation, all under vacuum. The beam is then expanded to go through the output Glan polarizer enabling XPW pulse selection, with an extinction ratio of 3–4 orders of magnitude. Pulses of 300 μJ are routinely generated, corresponding to an XPW internal efficiency of 33% (fiber transmission and reflection losses on crystals deducted) and a global energy transmission of 22%. At this stage, the spectral bandwidth supports sub-10-fs duration [Fig. 2(a)]; the pulse presents a good spatio-temporal quality; the energy stability is ~2% RMS over several hours; and the CEP drift can be kept below 200 mrad RMS [18].

For the second CPA (CPA2), the issue of dispersion management must be carefully addressed. So far, in order to minimize the CEP drift, a compact stretcher (e.g., bulk) and compressor are preferred [20,21]. The compressor has to present minimum optical-beam path while an AOPDF can help to compensate for the spectral phase of the stretcher and amplifier material. The stretching factor should give a moderate B-integral value during amplification and nonlinear effects in the compressor should be avoided. The solution applied to CPA1 consists in a bulk stretcher and a TGC, whose chromatic dispersions do not match [the third-order dispersion/group-delay dispersion (TOD/GDD) ratios are of the opposite sign]. Consequently, the finite pulse-shaping capability of the AOPDF limits the stretching factor to about 0.1 ps/nm, thus preventing efficient amplification beyond a few millijoules. Recently, we proposed an efficient and compact grism compressor design (combination of prisms and TG) able to match the first orders of the chromatic dispersion introduced by the bulk stretcher and amplifier and therefore relaxing the constraints on the AOPDF [22]. CEP stability was also demonstrated. The use of transmission gratings eases the geometrical constraints and the position of the prism pair between the two can be used to tune the TOD/GDD ratio [23]. An air space between the prism and TG avoids final wavelength recombination inside the bulk and thus limits nonlinear effects. Here, we present a grism design optimized for high-energy pulses and a larger stretching factor. An unfolded configuration is implemented to use smaller gratings, with a total footprint of 40 cm × 27 cm. The arrangement is shown in Fig. 3(a). It consists of 35 mm × 30 mm and 70 mm × 30 mm, 1282 l/mm TG used at Littrow incidence, coupled to AR-coated SF57 prisms (70 mm × 50 mm, apex 43.5°). Transmission of 78% is measured over 750–850 nm spectral bandwidth. The introduced group delay was measured by inserting the grism into the arm of a Michelson interferometer [Fig. 3(b)]. The stretching factor is 0.75 ps/nm, seven times larger than in CPA1, with a TOD/GDD ratio of 0.3 fs. The chromatic dispersion can be decomposed as follows: $-260,000\ \text{fs}^2$, $-80,000\ \text{fs}^3$, and $-1.6e6\ \text{fs}^4$. This huge amount of fourth-order dispersion (FOD) has to be compensated by the AOPDF and is the limit of the current design.

The amplifier stages were first bypassed to check the validity of the compression without any amplification. The XPW beam is sent to the stretcher, a 75-cm-long SF57 bulk with a snooker design (117.8 mm× 151.5 mm × 25 mm, six total internal reflections) with

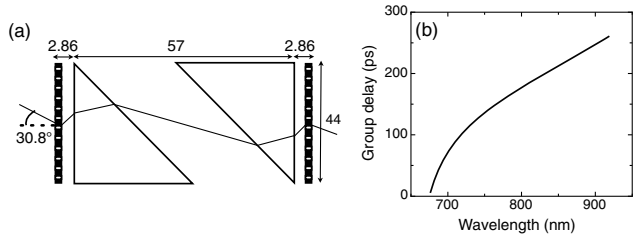

Fig. 3. (a) Grism design (distances are in millimeters). (b) Measured group delay introduced by two identical grism pairs in an unfolded version.

70% transmission. The XPW beam diameter (20 mm) is sufficient to avoid any nonlinearity. The bulk is followed by a double-pass AOPDF (low-jitter Dazzler HR45, Fastlite). Although the Dazzler is able to transmit the full XPW spectral bandwidth, the FOD amount needed for compression imposes significant spectral clipping, as can be seen in Fig. 2(a). The overall transmission (bulk + Dazzler) is then 10% and the stretched-pulse duration is about 45 ps FWHM. The pulse was then compressed in the grism to its Fourier limit of 18 fs.

Stretched-pulse amplification in CPA2 is achieved in two stages. Both amplifiers are pumped by a 50 W, 1 kHz frequency-doubled *Q*-switched Nd:YLF laser (DM50, Photonics Industries) split into two arms and are cryogenically cooled under vacuum to 180 K. The 30 μJ seed pulses are first boosted up to 4 mJ after six-pass amplification in an 8 mm Ti:Sa crystal pumped by 18 W. This booster stage (Femtolasers GmbH) is a confocal multipass configuration. At this stage, gain narrowing reduces the spectral bandwidth [Fig. 2(a)]. The final power amplifier consists in a homemade, image-relayed two-pass in a 3 mm Ti:Sa crystal, cut at Brewster angle for S polarization. With 27 W pump power and both seed and pump beam diameter at 650 μm ($1/e^2$), the seed pulses are typically amplified to 9 and 12.8 mJ, respectively, after each pass. A third pass can provide higher energy (14 mJ) but at the expense of the spatial beam quality (spatial modulations inherited from the pump beam profile), and this last pass is not implemented yet. In any case, gain saturation is nearly reached with the second pass, and energy stability is then 1% RMS over hours.

For compression in the grism, the beam size is then expanded to 22 mm ($1/e^2$), limited by the gratings size. To avoid nonlinearity in the last grating substrate, final compression is achieved by 10 bounces on highly dispersive chirped mirrors (−2000 fs^2). Therefore, no spectral modifications occur during compression [Fig. 2(a)]. The overall transmission of the compressor is then 67%. Compressed-pulse energy is 8 mJ. Self-referenced spectral interferometry (Wizzler, Fastlite) enables accurate spectral phase compensation via a feedback loop on the Dazzler. We measure a pulse duration of 22 fs [Fig. 2(d)] (FT limited).

Far-field spatial quality is shown in Fig. 2(b), and a beam Strehl ratio better than 0.7 is measured (limited by astigmatism).

The temporal contrast of the 8 mJ, 22 fs pulses is measured thanks to a homemade high-dynamic range third-order autocorrelator. The energy is reduced to 2 mJ before entering the device. The incoherent contrast between −100 ps and −15 ps is 10^{-11}, limited by the

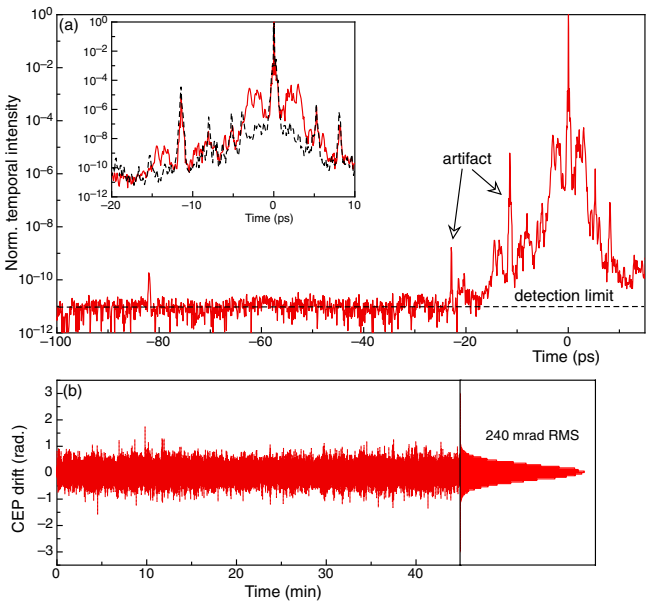

Fig. 4. (a) Measured temporal contrast of the 8 mJ, 22 fs pulses. The inset presents a zoom of the −20 ps/10 ps temporal window. The dashed black line is the temporal contrast measured when applying a spectral Gaussian apodization. (b) Relative CEP drift with feedback control on the oscillator.

detection [Fig. 4(a)]. The improvement of three orders of magnitude compared to CPA1 laser corresponds to the extinction ratio of the output polarizer of the XPW setup. One can notice that the main pulse is surrounded by a pedestal culminating at 10^{-5} relative intensity. We found that these coherent structures are due to a severe clipping of the spectral bandwidth in the Dazzler of CPA2. When applying a Gaussian apodization of the Dazzler acoustic wave to smooth the edges of the spectrum at the expense of the final pulse duration (28 fs instead of 22 fs), the symmetric shoulders (±2.5 ps) are decreased to 10^{-8} [see inset of Fig. 4(a)]. Same contrast measurements have been obtained using a commercial device (Sequoia, Amplitude Technologies).

CEP stability of the whole system is the last critical feature to be characterized. To implement it, a few microjoules of the compressed pulse are split off and sent into a collinear *f*-to-2*f* interferometer (APS800, Menlo Systems). The slow CEP drift of the output pulses at 1 kHz is precompensated by a feedback loop to the oscillator-locking electronics. Results are shown in Fig. 4(b). The RMS phase error is 240 mrad over 45 min. This behavior is not affected by the apodization of the spectrum, nor by the energy level sent into the compressor.

To conclude, we have demonstrated a prototype laser source for driving relativistic optics at 1 kHz. We have shown CEP stabilization of a double-CPA laser system and demonstrated a compact grism-based compression design suited to the compression of multi-millijoule energy pulses. In a next step, postcompression in hollow-core fiber will be implemented to produce TW peak-power (4 mJ, 4 fs) controlled few-cycle light waveforms [24]. In this postcompression stage, CEP control is expected to be preserved, if specific care is devoted to keeping a good spectral and energy stability.

Financial support from the Conseil Général de l'Essonne (ASTRE 2010 program), the Agence Nationale pour la Recherche (grants ANR-09-JCJC-0063 and ANR-11-EQPX-005-ATTOLAB), and Triangle de la Physique (RTRA, SOURCELAB-2012-057T) is gratefully acknowledged.

References

1. E. Esarey, C. B. Schroeder, and W. P. Leemans, Rev. Mod. Phys. **81**, 1229 (2009).
2. C. Thaury, F. Quéré, J. P. Geindre, A. Levy, T. Ceccotti, P. Monot, M. Bougeard, F. Rau, P. D'Oliveira, P. Audebert, R. Marjoribanks, and P. Martin, Nat. Phys. **3**, 424 (2007).
3. K. Ta Phuoc, S. Corde, C. Thaury, V. Malka, A. Tafzi, J. P. Goddet, R. C. Shah, S. Sebban, and A. Rousse, Nat. Photonics **6**, 308 (2012).
4. F. Krausz and M. Ivanov, Rev. Mod. Phys. **81**, 163 (2009).
5. A. Buck, M. Nicolai, K. Schmid, C. M. S. Sears, A. Savert, J. M. Mikhailova, F. Krausz, M. C. Kaulza, and L. Veisz, Nat. Phys. **7**, 543 (2011).
6. P. Heissler, R. Hörlein, J. M. Mikhailova, L. Waldecker, P. Tzallas, A. Buck, K. Schmid, C. M. S. Sears, F. Krausz, L. Veisz, M. Zepf, and G. D. Tsakiris, Phys. Rev. Lett. **108**, 235003 (2012).
7. X. Chen, A. Malvache, A. Ricci, A. Jullien, and R. Lopez-Martens, Laser Phys. **21**, 1 (2011).
8. A. Borot, A. Malvache, X. Chen, A. Jullien, J.-P. Geindre, P. Audebert, G. Mourou, F. Quéré, and R. Lopez-Martens, Nat. Phys. **8**, 416 (2012).
9. J. A. Wheeler, A. Borot, S. Monchoce, H. Vincenti, A. Ricci, A. Malvache, R. Lopez-Martens, and F. Quéré, Nat. Photonics **6**, 829 (2012).
10. M. Veltcheva, A. Borot, C. Thaury, A. Malvache, E. Lefebvre, A. Flacco, R. Lopez-Martens, and V. Malka, Phys. Rev. Lett. **108**, 075004 (2012).
11. G. Doumy, F. Quéré, O. Gobert, M. Perdrix, P. Martin, P. Audebert, J. C. Gauthier, J.-P. Geindre, and T. Wittmann, Phys. Rev. E **69**, 026402 (2004).
12. J. M. Mikhailova, A. Buck, A. Borot, K. Schmid, C. Sears, G. D. Tsakiris, F. Krausz, and L. Veisz, Opt. Lett. **36**, 3145 (2011).
13. M. P. Kalashnikov, E. Risse, H. Schönagel, and W. Sandner, Opt. Lett. **30**, 923 (2005).
14. A. Jullien, O. Albert, F. Burgy, G. Hamoniaux, J.-P. Rousseau, J.-P. Chambaret, F. Augé-Rochereau, G. Chériaux, J. Etchepare, N. Minkovski, and S. M. Saltiel, Opt. Lett. **30**, 920 (2005).
15. A. Flacco, F. Sylla, M. Veltcheva, M. Carrié, R. Nuter, E. Lefebvre, D. Batani, and V. Malka, Phys. Rev. E **81**, 036405 (2010).
16. W. P. Leemans and C. Simon-Boisson, "The BELLA system and facility," presented at the Conference of the International Committee on Ultra-High Intensity Lasers, 2012.
17. G. Matras, F. Lureau, S. Laux, O. Casagrande, C. Radier, O. Chalus, F. Caradec, L. Boudjemaa, C. Simon-Boisson, R. Dabu, F. Jipa, L. Neagu, I. Dancus, D. Sporea, C. Fenic, and C. Grigoriu, "First sub-25fs PetaWatt laser system," presented at the Advanced Solid-State Lasers, 2013.
18. A. Ricci, A. Jullien, J. P. Rousseau, and R. Lopez-Martens, Appl. Sci. **3**, 314 (2013).
19. A. Ricci, A. Jullien, J. P. Rousseau, Y. Liu, A. Houard, P. Ramirez, D. Papadopoulos, A. Pellegrina, P. Georges, F. Druon, N. Forget, and R. Lopez-Martens, Rev. Sci. Instrum. **84**, 043106 (2013).
20. Z. Chang, Appl. Opt. **45**, 8350 (2006).
21. L. Canova, X. Chen, A. Trisorio, A. Jullien, A. Assion, G. Tempea, N. Forget, T. Oksenhendler, and R. Lopez-Martens, Opt. Lett. **34**, 1333 (2009).
22. A. Ricci, A. Jullien, N. Forget, V. Crozatier, P. Tournois, and R. Lopez-Martens, Opt. Lett. **37**, 1196 (2012).
23. N. Forget, V. Crozatier, and P. Tournois, Appl. Phys. B **109**, 121 (2012).
24. F. Böhle, M. Kretschmar, A. Jullien, M. Kovacs, M. Miranda, R. Romero, H. Crespo, P. Simon, R. Lopez-Martens, and T. Nagy, "Compression of CEP-stable multi-mJ laser pulses down to 4 fs in long hollow fibers," Laser Phys. Lett. (in press).

Approaching the limits of carrier-envelope phase stability in a millijoule-class amplifier

Fabian Lücking,[1,2,*] Vincent Crozatier,[3] Nicolas Forget,[3] Andreas Assion,[1] and Ferenc Krausz[2,4]

[1]*Femtolasers Produktions GmbH, Fernkorngasse 10, 1100 Vienna, Austria*

[2]*Institut für Experimentalphysik, Ludwig-Maximilians-Universität München, Am Coulombwall 1, 85748 Garching, Germany*

[3]*Fastlite, Centre Scientifique d'Orsay, Bâtiment 503, Plateau du Moulon, 91401 Orsay, France*

[4]*Max-Planck-Institut für Quantenoptik, Hans-Kopfermann-Straße 1, 85748 Garching Germany*

**Corresponding author: fabian.luecking@femtolasers.com*

Received April 3, 2014; revised May 26, 2014; accepted May 26, 2014;
posted May 27, 2014 (Doc. ID 209534); published June 24, 2014

The demand for ever shorter light pulses presents a challenge to the detection and stabilization of the carrier-envelope phase (CEP) in amplifier systems. Here we present a combination of single-shot detection and a fast actuator that is capable of measuring and correcting the CEP in every single shot emitted by a millijoule-scale, multi-kHz femtosecond laser amplifier. The residual CEP noise within 50 s amounts to 98 mrad rms in-loop (fast detection, $5 \cdot 10^5$ shots) and 140 mrad out-of-loop (slow detection, 6250 shots), approaching the noise floor of the f-to-2f measurement. Both values represent a twofold improvement of the CEP stability over previously published results in comparable systems.

OCIS codes: (320.7090) Ultrafast lasers; (140.3280) Laser amplifiers; (320.7160) Ultrafast technology.
http://dx.doi.org/10.1364/OL.39.003884

The last decade has seen tremendous progress in the investigation of the fastest processes occurring in the microcosm. Few-cycle laser pulses with constant carrier-envelope phase (CEP) constitute a primary tool for accessing the highly nonlinear interactions underlying these processes. In order to achieve higher temporal resolution as well as higher field strengths, much effort is undertaken to confine the interaction to a single half-cycle of the driving laser field. Thanks to advancements in hollow-fiber compression, the duration of pulses used for attosecond experiments is approaching a single optical cycle. These developments place rising demands on the CEP stability of the laser at the front end of the experimental chain.

Several factors contribute to the overall CEP noise measured at the output of an amplifier. First, the oscillator CEP noise integrated over the temporal interval between two consecutive amplified pulses sets a lower limit to the pulse-to-pulse variation of the CEP of the amplified pulses. This CEP noise floor commonly amounts to about 100–140 mrad rms (when referring to statistical deviations from a constant value, rms values are given in this Letter unless otherwise noted) for stabilization using feedback [1], and has been shown to reach below 50 mrad using cavity-external frequency shifting in the so-called feed-forward scheme [2].

However, this limit set by the seed oscillator has remained a theoretical issue up to now. Rather, the overall CEP performance of millijoule-class sources has so far been dominated by CEP noise added during the amplification process. These secondary sources of CEP noise fall into one of two categories. On the one hand CEP can be affected by changes in dispersion through mechanical vibration of components (such as large grating stretchers and compressors) as well as variation of beam pointing and/or ambient conditions. These effects dominate at frequencies up to 1 kHz, often occurring in narrow frequency bands, or with $1/f$-like noise behavior. On the other hand are effects coupling pulse intensity to CEP through self-phase modulation (SPM). Intensity noise can be caused by pulse-switching electronics or pump power fluctuations. Beam pointing drifts can also act in this fashion by varying the overlap of the pump and seed beams. Except for the latter, these effects generate stochastic or high-frequency noise.

The impact of CEP noise sources from both categories can be reduced through careful design of the amplifier, e.g., by using bulk material for pulse stretching, low-vibration cooling systems, and keeping the accumulated nonlinear phase low. Furthermore, feedback correction loops can, in principle, be employed to cancel noise up to half the amplifier repetition rate. In practice, however, other limitations come into effect much earlier in both measurement and actuation. For instance, conventional CEP detection in a single-shot f-to-2f interferometer relies on the processing of a spectrogram [3], the acquisition and analysis of which typically takes milliseconds. This reduces the bandwidth of stabilization loops to typically a few hundred hertz. Only within the last decade have methods been invented to determine the shot-to-shot CEP fluctuations of amplified pulses at a repetition rate above the kilohertz range. These schemes either replace the time-consuming spectrogram evaluation in an f-to-2f interferometer [4,5] or directly measure a phase-sensitive effect [6].

Faster means of CEP detection also call for faster actuators. Suitable mechanisms include adding an offset to the seed oscillator stabilization [7], and shifting the phase in an acousto-optical programmable dispersive filter (AOPDF) [8] or an electro-optic crystal [9]. However, neither fast detection [10], fast actuation [7], nor their combination [11] have succeeded in reducing the system CEP noise to less than 250 mrad measured in-loop [4,7] and 294 mrad out-of-loop [10] on a single-shot basis. In what follows, we present a 10 kHz, millijoule-class amplifier whose CEP stability approaches the limit set by the seed oscillator.

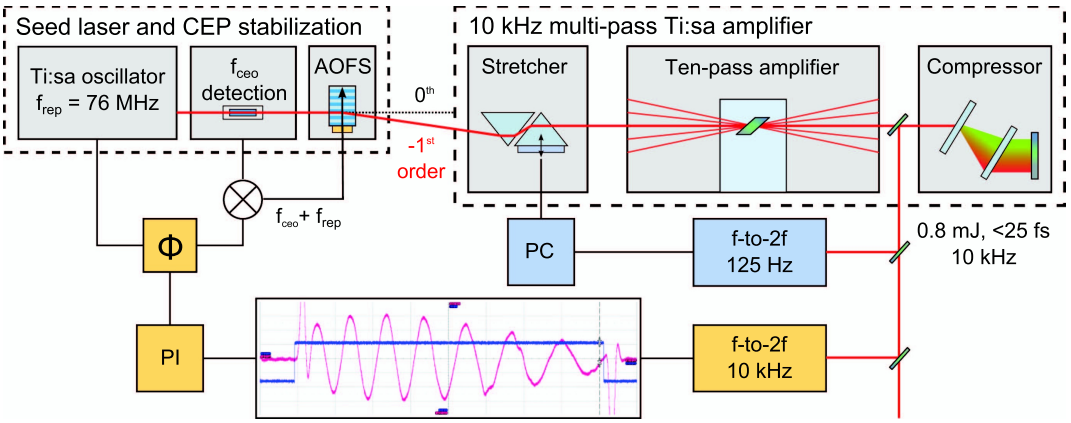

Fig. 1. Schematic layout of the experiment. A Ti:sapphire oscillator is CEP stabilized by frequency-shifting. Multi-pass amplification at 10 kHz yields pulses with 0.8 mJ energy and a duration of 25 fs. The CEP of the amplified pulses is measured by two collinear f-to-2f interferometers at 125 and 10 kHz acquisition rate, respectively. Feedback correction can be applied by varying either the stretcher dispersion or the RF phase of the AOFS driver signal. Φ, RF phase shifter; PI, proportional-integral controller; PC, personal computer. Inset, oscilloscope screen-shot of an interferogram acquired by the fast f-to-2f.

The layout of our experiment is depicted in Fig. 1. The seed oscillator (rainbow CEP4, Femtolasers) is CEP-stabilized by frequency-shifting all lines in the laser output spectrum by the measured carrier-envelope offset frequency f_{ceo}. This is accomplished using an acousto-optic frequency shifter (AOFS), imparting a Doppler frequency shift equal to its driving frequency to the diffracted light. As f_{ceo} cannot be conveniently filtered to reach the AOFS drive band of 85 MHz, the sum of f_{ceo} and the repetition rate f_{rep} is used instead. This equally results in a zero-offset comb in the −1st diffraction order. The seed laser CEP stability is estimated to be on the order of 50 mrad based on the previous characterization of an essentially identical system [12].

About 70 mW of average power within a 100 nm band centered around 800 nm is used to seed a single-stage multipass amplifier (Femtopower 10 kHz, Femtolasers). Bulk SF57 glass is used to stretch the pulses, and an AOPDF (low-jitter Dazzler HR, Fastlite) provides spectral shaping and compensation of higher-order dispersion. Mechanical construction and cooling of the gain medium were optimized to achieve minimal mechanical vibration. After 10 passes, the pulses are re-compressed by transmission gratings, resulting in 0.8 mJ pulses of 25 fs duration.

Beam splitters direct a small fraction of the output to two collinear f-to-2f interferometers [3]. One of the devices uses a commercial USB spectrometer running at 125 Hz, whereas the other is equipped with a prototype device capable of extracting CEP fluctuations from interferograms at the full amplifier repetition rate [13]. The integration times of both allow only one amplifier shot to contribute to each CEP measurement.

The prototype is based on a typical grating spectrometer. It is built in Czerny–Turner configuration with an arm length of 75 mm and an entrance slit width of 25 μm. The detector is a 512 pixel CMOS array with fast-readout capability (line reading scan time <85 μs) receiving a 30 nm band centered at 520 nm. The f-to-2f interference pattern is converted into an electronic signal by the CMOS array. After filtering it appears as a pseudo-sine wave. Such a signal is easily processed to extract the phase deviation as an analog voltage. The acquisition is triggered synchronously with the q-switch of the amplifier pump laser. The maximum acquisition rate exceeds 10 kHz and is limited by the detector read-out and phase extraction process.

In order to correct the CEP jitter induced during amplification, feedback can be applied in two ways. First, the error signal provided by the slow conventional measurement is fed to a Piezo stage, changing the insertion of a prism into the stretcher. The bandwidth of this feedback loop is limited to half the acquisition rate (62.5 Hz). The second method exploits both the fast acquisition device and the acoustic grating phase, a free parameter previously unused in the CEP stabilization technique employed here.

In addition to modifying the frequency of the diffracted light, the acoustic-wave imprints its phase on that of the optical wave. Thus, by changing the phase of the acoustic wave, the AOFS can be employed not only to produce pulses with constant CEP, but also to arbitrarily set its value. This effect does not rely on material dispersion and hence does not modify the pulse temporal envelope. The drawbacks of using material dispersion to influence the CEP, aggravated with decreasing pulse duration, can thus be circumvented. In practice, the phase of the AOFS driving signal is controlled by a standard voltage-controlled radio frequency (RF) phase shifter (Sigatek), allowing 360° of electronic phase shift with linear voltage-to-phase response and a specified modulation bandwidth of 1 MHz.

In order to test the open-loop performance of both the fast phase measurement and the actuator, a triggered square wave at half the amplifier repetition rate was applied to the RF phase shifter, its amplitude chosen such as to produce phase jumps of roughly π. The CEP of every single shot in the output beam was measured using the fast f-to-2f. The results are depicted in Fig. 2 (red trace). The experiment illustrates that the method can be used to choose an arbitrary CEP of the output pulse from one pulse to the next. One possible application is lock-in detection of CEP-sensitive effects, scalable to a much higher repetition rate depending on the amplifier being seeded. Providing fast CEP control

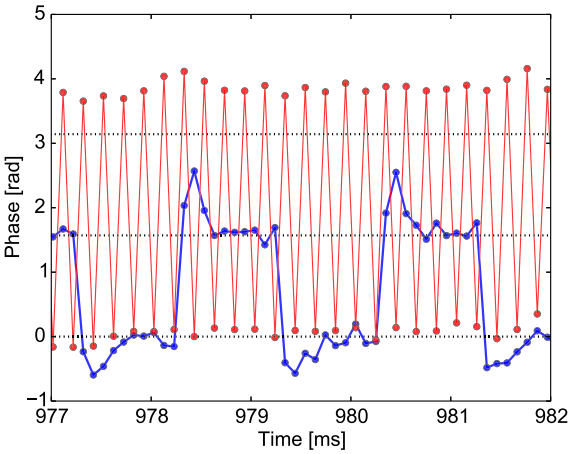

Fig. 2. Acoustic grating phase actuator in open and closed loop operation, recorded by fast f-to-2f. Red trace, amplified pulse CEP switched by 1.2π from shot-to-shot by triggered square wave applied to RF shifter. Blue trace, closed-loop operation, target phase switched by $\pi/2$ every 10 shots.

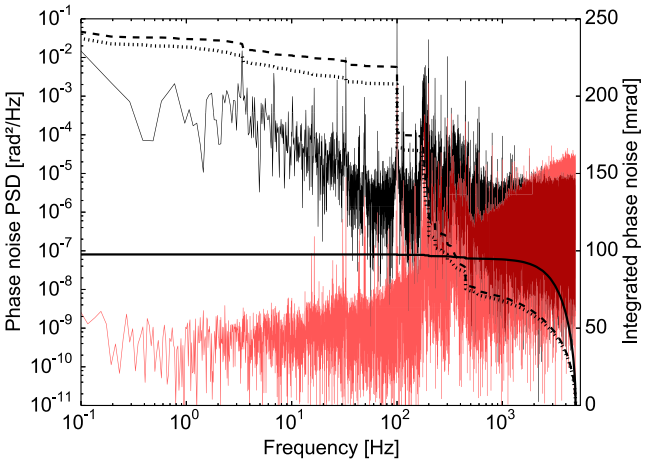

Fig. 3. Fourier transform of the CEP data collected using the fast f-to-2f device. Black/dashed trace, open loop PSD/IPN; Dotted trace, IPN of loop closed using 125 Hz f-to-2f and prism actuator; red/solid trace, PSD/IPN of loop closed using 10 kHz f-to-2f and grating phase actuator.

without changing the pulse envelope or introducing additional losses, this actuator renders the use of dispersive elements for CEP control obsolete.

Next, the fast control loop was closed using the measurement provided by the fast spectrometer. The error was processed by a proportional–integral (PI) controller (integration time constant $\tau_i = 0.2$ ms) before being fed back to the RF phase shifter. For this test the target phase was switched by $\pi/2$ every 10 shots. The blue trace in Fig. 2 shows the CEP data acquired during the lock for optimized servo gain. At this setting the closed loop step response is fast enough to lock to the new target within 3–4 shots. The response speed indicates a large feedback bandwidth at the expense of a low damping factor, as indicated by the overshoot. The deviation of the CEP from the upper and lower target amounted to 246 and 217 mrad ($2 \cdot 10^4$ shots, 2 s).

We then characterized the CEP stability of the amplified pulses for different configurations of measurement and actuator. First, the amplifier feedback loop was left open, yielding the noise power spectral density (PSD) of the overall system as measured by the fast f-to-2f (Fig. 3, black trace). The integrated phase noise (IPN) amounts to 242 mrad within 10 s. As can be seen from the step-like features of the IPN curve (dashed trace), the dominant contributions stem from two narrow-band spikes at 100 and 200 Hz as well as from a broad continuum spanning from 100 to 500 Hz. These correspond to mains leakage and acoustic vibration of the mechanical components inside the amplifier, respectively.

Second, the loop is closed using the 125 Hz measurement and the prism actuator, with the fast f-to-2f providing an out-of-loop measurement. As most of the CEP error accumulates at frequencies beyond that of the in-loop detection, the difference between open- and closed-loop performance is marginal. The resulting IPN of 237 mrad (10 s, dotted trace in Fig. 3, PSD trace not shown) agrees with the in-loop value to within 10% and can typically be maintained over tens of hours in everyday operation. The main purpose of such a low bandwidth loop is to avoid slow drifts and a long time-scale.

In a third experiment, feedback was applied using the full repetition rate CEP measurement and the grating phase actuator. Exceeding 2.5 kHz the estimated loop bandwidth is sufficient to cancel a significant part of the CEP fluctuations occurring during amplification. This is clearly demonstrated by the PSD (red trace) and IPN (solid black trace) plotted in Fig. 3. Within 50 s, evaluation and correction of the CEP of $5 \cdot 10^5$ shots resulted in a residual phase error of 98 mrad. No notable steps occur in the IPN curve in this case. The base level of the PSD keeps falling from high to low frequency, meaning that the control bandwidth spans the entire measurement range. In the absence of a second fast-acquisition system, no equivalent out-of-loop comparison could be performed. Still, using the slow-detection apparatus, CEP fluctuations were simultaneously measured to be below 140 mrad. Even for hours-scale datasets, out-of-loop noise did not exceed 150 mrad. Note that this figure, although markedly higher than the in-loop value, still represents a 100 mrad improvement over the residual noise obtained with the conventional loop.

A closer look at Fig. 3 suggests that the loop still offers room for optimization. Clearly, the fast-loop PSD level exceeds that of the free-running system upward of 2 kHz, meaning that the stabilization system actually adds noise not present in the other cases, which can be explained as follows. Stochastic shot-to-shot fluctuations of the amplifier-pump laser energy cause intensity jitter on the femtosecond output. In an f-to-2f measurement this jitter is translated to the CEP via SPM [14]. The measured CEP noise spectrum therefore contains a white-noise background at high frequency that sets the measurement noise floor. In the present amplifier, the shot-to-shot intensity fluctuations were measured to 0.5% rms. Assuming the coupling constant of 160 mrad/% given in [14], the stochastic noise background of the measurement can be estimated to 80 mrad, which is in excellent agreement with the open loop IPN at high frequencies (Fig. 3). A feedback loop acting on such a stochastic error adds noise instead of suppressing it, and the high-frequency integration stage ($\tau_i = 0.2$ ms)

used in our experiment provided gain at a region where the f-to-2f signal was already dominated by such noise. Tailoring the loop-filter high-frequency response to the crossover point of the two PSD curves in Fig. 3 could result in modest reduction of the CEP jitter. Eventually, a measurement with a lower noise floor would enable the use of the fast loop at its full potential, likely pushing the residual CEP noise closer to the oscillator limit.

Recent analysis of the CEP noise added in hollow fiber compression [15,16] suggests that further benefit could result from including these in a fast correction loop.

In conclusion, we have presented a millijoule-scale femtosecond amplifier system in which fast feedback elements almost completely compensate for the CEP noise emerging in the amplification process. It relies on an f-to-2f device capable of measuring the CEP of pulses at an acquisition rate exceeding 10 kHz. The cavity-external CEP stabilization technique was augmented to allow fast CEP modulation, providing arbitrary CEP shift from one amplifier shot to the next. The resulting integrated CEP noise of 98 mrad constitutes a substantially improved performance as compared to previous CEP-stabilized systems. Our results indicate that there is room for further reduction of the CEP jitter.

The authors would like to thank the group of M. Kling at LMU for kindly providing equipment and support during the experiment. The presented work was partially funded by the European Research Council (grant agreement no. 238362-ATTOFEL) and the Munich Center for Advanced Photonics.

References

1. T. Fuji, J. Rauschenberger, C. Gohle, A. Apolonski, T. Udem, V. S. Yakovlev, G. Tempea, T. W. Hänsch, and F. Krausz, New J. Phys. **7**, 116 (2005).
2. S. Koke, C. Grebing, H. Frei, A. Anderson, A. Assion, and G. Steinmeyer, Nat. Photonics **4**, 462 (2010).
3. M. Kakehata, H. Takada, Y. Kobayashi, K. Torizuka, Y. Fujihira, T. Homma, and H. Takahashi, Opt. Lett. **26**, 1436 (2001).
4. S. Koke, C. Grebing, B. Manschwetus, and G. Steinmeyer, Opt. Lett. **33**, 2545 (2008).
5. T. Fordell, M. Miranda, C. L. Arnold, and A. L'Huillier, Opt. Express **19**, 23652 (2011).
6. M. Möller, A. M. Sayler, T. Rathje, M. Chini, Z. Chang, and G. G. Paulus, Appl. Phys. Lett. **99**, 121108 (2011).
7. L. Canova, X. Chen, A. Trisorio, A. Jullien, A. Assion, G. Tempea, N. Forget, T. Oksenhendler, and R. Lopez-Martens, Opt. Lett. **34**, 1333 (2009).
8. N. Forget, L. Canova, X. Chen, A. Jullien, and R. Lopez-Martens, Opt. Lett. **34**, 3647 (2009).
9. O. Gobert, P. Paul, J. Hergott, O. Tcherbakoff, F. Lepetit, P. d'Oliveira, F. Viala, and M. Comte, Opt. Express **19**, 5410 (2011).
10. D. Adolph, A. M. Sayler, T. Rathje, K. Rühle, and G. G. Paulus, Opt. Lett. **36**, 3639 (2011).
11. C. Feng, J.-F. Hergott, P.-M. Paul, X. Chen, O. Tcherbakoff, M. Comte, O. Gobert, M. Reduzzi, F. Calegari, C. Manzoni, M. Nisoli, and G. Sansone, Opt. Express **21**, 25248 (2013).
12. F. Lücking, A. Assion, A. Apolonski, F. Krausz, and G. Steinmeyer, Opt. Lett. **37**, 2076 (2012).
13. V. Crozatier, N. Forget, and T. Oksenhendler, in *CLEO/Europe and EQEC 2011 Conference Digest* (Optical Society of America, 2011), paper CF1-4.
14. C. Li, E. Moon, H. Mashiko, H. Wang, C. M. Nakamura, J. Tackett, and Z. Chang, Appl. Opt. **48**, 1303 (2009).
15. W. A. Okell, T. Witting, D. Fabris, D. Austin, M. Bocoum, F. Frank, A. Ricci, A. Jullien, D. Walke, J. P. Marangos, R. Lopez-Martens, and J. W. G. Tisch, Opt. Lett. **38**, 3918 (2013).
16. F. Lücking, A. Trabattoni, S. Anumula, G. Sansone, F. Calegari, M. Nisoli, T. Oksenhendler, and G. Tempea, Opt. Lett. **39**, 2302 (2014).

Chapitre 3

Spectroscopie rapide et ultra-rapide

3.1 Introduction

Les lasers femtocondes à haute cadence (>10 kHz) trouvent un nombre toujours croissant d'applications et ouvrent de nouveaux thèmes de recherche en métrologie et notamment en spectroscopie. Deux de ces thématiques sont décrites ici :

- la spectroscopie dans l'infrarouge moyen et thermique
- la spectroscopie ultra-rapide (>10 kHz)

Le premier thème de recherche correspond à la spectroscopie de sources optiques pulsées de longueur d'onde supérieure à 1 µm. Ces sources sont, en général, « secondaires » au sens où elles sont basées sur la modification, via des effets non linéaires (génération de continuum, de différence de fréquence etc) d'impulsions optiques « primaires » produites par des lasers commerciaux dans le proche infrarouge (≃0.8 µm ou ≃1 µm pour l'essentiel). Ces sources secondaires infrarouges sont caractérisées par une largeur de bande spectrale pouvant dépasser l'octave, une forte brillance et des cadences souvent élevées. Or, les spectromètres classiques ne sont pas toujours adaptés à ce type de sources. Le second thème de recherche est la spectroscopie non linéaire à très haute cadence : spectroscopie multi-dimensionnelle, échantillonnage électro-optique et imagerie hyperspectrale par diffusion Raman stimulée.

Cadre	Type	Nom	Date	Direction	Laboratoire
Stage	Corps de Mines	Antoine Bourget	2012	Nicolas Forget	Fastlite
Stage	2A/M1	Raymond Santoso	2012	Nicolas Forget	Fastlite
Stage	M2	Varvara Chiliaeva	2019	Nicolas Forget	Fastlite
Stage	M1	Marie Skaljac	2020	Nicolas Forget	Fastlite
Thèse	CIFRE	Ines Martin	>2022	Hervé Rigneault	Institut Fresnel

Table 3.1 – Thèses co-encadrées et stages dirigés.

Type	Acronyme	Laboratoire/entreprise	Rôle	Date
Contrat RAPID	FASOR	Fastlite	PI	2011-2013
Contrat Eurostars	RESPIRE	TUW (Autriche)	PI	2012-2015
Contrat FEDER	SAVOIRS	Fastlite	Lancement	2021-2022
Collaboration	informelle	Univ. Regensburg	Participant	2013
Collaboration	informelle	MPQ	Participant	2013
Collaboration	informelle	Institut Fresnel	Participant	2018
Collaboration	CIFRE	Institut Fresnel	Encadrant	2022

TABLE 3.2 – Contrats et collaborations.

3.2 Spectromètres rapides

Il est d'usage de distinguer les spectromètres « dispersifs » ou « sélectifs », reposant sur un élément permettant de sélectionner les longueurs d'onde, des spectromètres à transformée de Fourier. Il est également d'usage de distinguer les spectromètres optiques basés sur des détecteurs ponctuels (mono-canal) de ceux basés sur des détecteurs linéaires ou matriciels (multi-canaux). Ces derniers sont nettement avantageux par rapport aux premiers car l'acquisition des composantes spectrales est simultanée (monocoup) et non séquentielle. Malheureusement, les détecteurs matriciels avec un nombre élevé de capteurs élémentaires ne sont pas commercialement disponibles dans l'infrarouge moyen – ou à des prix prohibitifs - de telle sorte que les détecteurs ponctuels sont encore largement utilisés dans cette gamme spectrale. C'est dans ce contexte que se placent les études décrites ici. Un grand nombre de solutions techniques ont été proposées pour l'acquisition séquentielle :

- spectromètres dispersifs ou sélectifs : rotation d'un prisme, d'un réseau ou d'un assemblage de ces derniers, ou mouvement équivalent (rotation d'un miroir, déplacement du capteur ponctuel derrière un prisme, un réseau etc), filtre acousto-optique (AOTF)...
- spectromètres à transformée de Fourier, basés sur un interféromètre : déplacement mécanique d'un miroir ou d'une membrane, d'un miroir en toit, d'un prisme à réflexion totale interne, rotation d'un miroir en toit , galvanomètre dans le plan de Fourier d'une ligne à dispersion nulle...

Dans le contexte des sources pulsées et de la mesure temps-réel, certaines de ces solutions ne conviennent pas, soit en raison de l'inertie des éléments mobiles, soit en raison de la résolution spectrale et/ou des contraintes d'alignement et de calibration.

3.2.1 L'AOPDF comme monochromateur

L'idée est ici d'utiliser un AOPDF pour réaliser un filtrage spectral rapidement accordable en longueur d'onde pour l'analyse spectrale à la façon d'un monochromateur. J'ai coordonné et pris part à deux programmes de recherche sur les monochromateurs acousto-optiques :

- 2011-2014 : RAPID FASOR ()« Filtres Acousto-optiques pour l'analyse et imagerie Spectrale à haute Résolution »), financé par la DGA.
- 2012-2015 : Eurostars RESPIRE (« REal time acousto-optic based SPectrometer

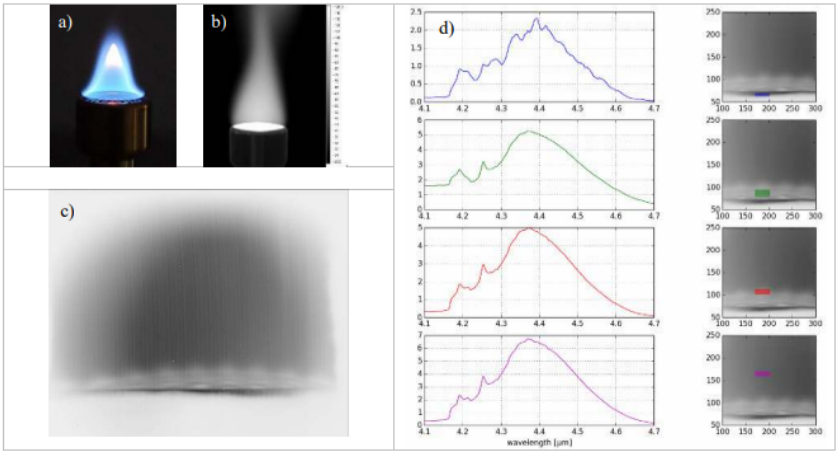

FIGURE 3.1 – Imagerie hyperspectrale d'une flamme de butane-propane. a) et b) Images visible et thermique de la flamme. c) Image de la base de la flamme à 4.4 µm (émission du CO2 chaud). d) Spectres mesurés en différents points de la flamme.

for femtosceonde broadband and/or tunable mid-InfraEDd laser sources » [1]) avec le TUW (Vienne) et, en particulier, Audrius Pugzlys et Andrius Baltuska.

La majeure partie du travail expérimental correspondant a été réalisée par deux docteurs de Fastlite : Raman Maksimenka (FASOR) et Grégory Gitzinger (RESPIRE).

L'étude FASOR se place dans un double contexte : l'imagerie hyperspectrale à haute résolution (quelques cm^{-1}) sur la bande 0.4-2.5 µm et l'imagerie hyperspectrale infrarouge en bande II (3-5.5 µm) et bande III (8-12 µm). Quatre approches novatrices ont été explorées :

- l'utilisation de géométries colinéaires permettant d'augmenter d'un ordre de grandeur la résolution spectrale et d'améliorer la qualité d'image,
- une configuration d'imageur à détecteur matriciel et une procédure d'extraction de l'image permettant de s'affranchir de la dépendance angulaire de la longueur d'onde filtrée, dans les configurations où cette dépendance est un facteur limitant,
- l'utilisation, dans la gamme de longueur d'ondes du visible, d'un matériau (Niobate de Lithium) permettant de combiner ouverture angulaire et géométrie colinéaire sans nécessiter de procédure d'extraction,
- l'utilisation d'un matériau (Calomel, Hg_2Cl_2) adapté au domaine spectral de l'infrarouge moyen [26]jusqu'à 20 µm en principe

Le programme RESPIRE est la déclinaison adaptée aux sources pulsées de FASOR [50].

Ces deux programmes m'ont amené à encadrer plusieurs stages. Le stage en entreprise d'un an d'Antoine Bourget (« Imagerie hyperspectrale par filtrage acousto-optique », Corps des Mines, 2012) et celui de 3 mois de Raymond Santoso (Ecole Polytechnique, 2012). Ces travaux de recherche n'ont pas donné lieu à publication hormis une présentation de conférence [50]. Le produit commercial Mozza™ en est cependant l'un des aboutissements, avec la commercialisation temporaire des AOPDFs en Calomel.

1. On n'est pas toujours inspiré...

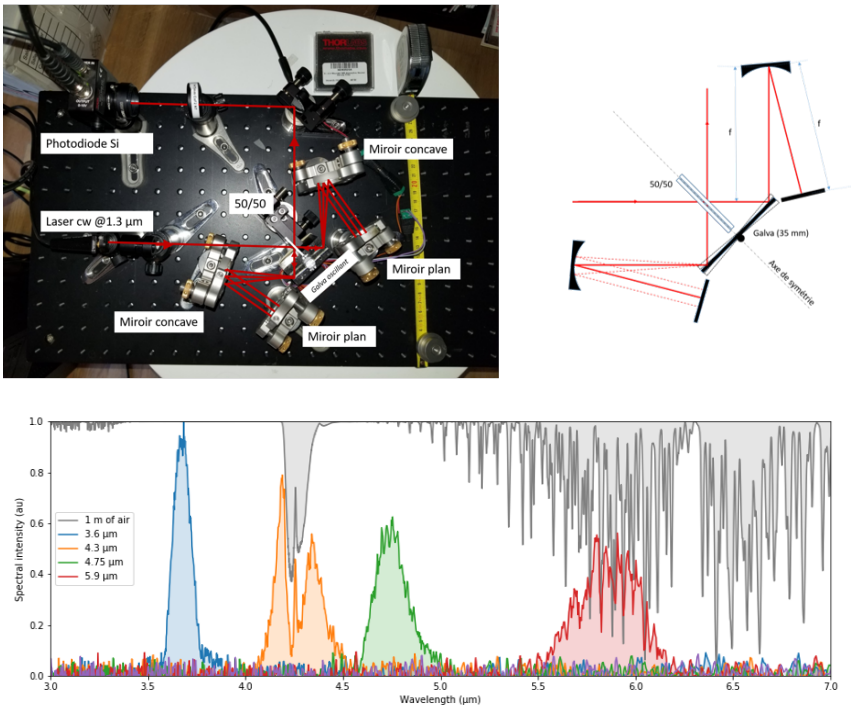

FIGURE 3.2 – En haut : vue du montage de Varvara Chiliaeva et schéma de principe de l'interféromètre. En bas : exemple de spectres mesurés sur un OPA accordable.

3.2.2 Spectromètres à transformée de Fourier

L'extension des dispositifs acousto-optique à l'infrarouge moyen au-delà de 5 µm s'étant heurtée à des problèmes techniques récurrents depuis 2015 (disponibilité des cristaux de Calomel, inhomogénéité des cristaux, difficulté d'alignement) et fondamentaux (faible efficacité de diffraction, sensibilité à la polarisation, niveau de bruit des détecteurs), une solution alternative a été recherchée. Ainsi que mentionné précédemment, la spectroscopie par transformée de Fourier (FTS pour « Fourier-transform spectrometry ») est une solution technique potentielle au problème posé : la spectroscopie large bande temps-réel dans le contexte des sources pulsées à haute cadence. La FTS présente des avantages indéniables dans l'infrarouge : les avantages de Gellgett (pas de fente) et de Jacquinot (pas de filtrage spectral).

J'ai entamé un programme de recherche en proposant une solution inventive reposant sur des miroirs oscillants (galvanomètres). J'ai encadré deux stages sur ce sujet :

- le stage de M2 de Varvara Chiliaeva (« Spectromètre à transformée de Fourier pour des lasers pulsés dans l'infrarouge moyen », 2019, Université Côte d'Azur)
- le stage de M1 de Marie Skaljac (« Spectromètre à transformée de Fourier », Polytec Nice-Sophia, Université Côte d'Azur, 2020)

Le projet s'est ensuite poursuivi en entreprise et a débouché sur un produit commercialisé en 2021. Le principe du système de mesure, de synchronisation et de calibration par un laser monomode continu ont cependant pu être validé expérimentalement durant ces stages sur des sources pulsées représentatives (100 kHz) à 1.4-1.5 µm et 5 µm.

3.3 Lignes à retard AOPDF

3.3.1 Spectroscopie bidimensionnelle

Une forme particulière de façonnage par AOPDF consiste à moduler simultanément l'amplitude et la phase afin de produire deux répliques temporelles de l'impulsion d'entrée (quelle que soit cette dernière). L'intérêt est ici que l'AOPDF se comporte comme un interféromètre parfaitement stable, avec un contrôle fin de la phase relative entre les deux répliques. Ce type de paires d'impulsions (« phase-locked ») est non triviale avec des composants optiques usuels, et des systèmes d'asservissement avancés sont nécessaires pour garantir une stabilité de phase suffisante, notamment dans le domaine visible. Le recours aux façonneurs d'impulsions, et aux AOPDFs en particulier, simplifie grandement l'implémentation des techniques de mesures nécessitant de telles paires d'impulsions. C'est en particulier le cas de la spectroscopie bidimensionnelle électronique [51] et infrarouge [52] et plus généralement celui de la spectroscopie multidimensionnelle.

Combiner deux AOPDFs travaillant chacun sur une polarisation donnée offre la possibilité d'étendre cette technique à des paires d'impulsions avec des états de polarisation arbitraires. C'est dans ce contexte que j'ai travaillé avec Pooja Tyagi, puis Hélène Seiler et enfin Samuel Palato, trois doctorants de l'Université de McGill (Montréal, Canada) dirigés par Patanjali Kambhampati. J'ai eu, en particulier, l'occasion d'encadrer le travail d'Hélène Seiler durant son séjour de 6 mois à Fastlite en 2012-2013. Ce travail de collaboration a mis en évidence, dans le visible, une stabilité de phase relative de l'ordre de $\lambda/300$ entre impulsions produites par un AOPDF et de $\lambda/100$ entre deux AOPDFs [53,54] (cf publication jointe).

JOURNAL OF APPLIED PHYSICS **118**, 103110 (2015)

Kilohertz generation of high contrast polarization states for visible femtosecond pulses via phase-locked acousto-optic pulse shapers

Hélène Seiler,[1] Brenna Walsh,[1] Samuel Palato,[1] Alexandre Thai,[2] Vincent Crozatier,[3] Nicolas Forget,[2] and Patanjali Kambhampati[1,a)]
[1]*Department of Chemistry, McGill University, Montreal, Quebec H3A 0B8, Canada*
[2]*Fastlite, 1900 route des Crêtes, 06560 Valbonne, France*
[3]*Fastlite, Centre Scientifique d'Orsay, Bât.503, Plateau du Moulon, BP 45 Orsay, France*

(Received 13 July 2015; accepted 20 August 2015; published online 14 September 2015)

We present a detailed analysis of a setup capable of arbitrary amplitude, phase, and polarization shaping of broadband visible femtosecond pulses at 1 kHz via a pair of actively phase stabilized acousto-optic programmable dispersive filters arranged in a Mach-Zehnder interferometer geometry. The setup features phase stability values around $\lambda/225$ at 580 nm as well as degrees of polarization of at least 0.9 for any polarization state. Both numbers are important metrics to evaluate a setup's potential for applications based on polarization-shaped femtosecond pulses, such as fully coherent multi-dimensional electronic spectroscopy. © *2015 AIP Publishing LLC*.
[http://dx.doi.org/10.1063/1.4929954]

I. INTRODUCTION

In ultrafast optics, the ability to control all degrees of freedom of optical pulses independently and in a versatile way hinges on active pulse shaping technology. So far, pulse shapers such as spatial light modulators (SLMs) or acousto-optic programmable dispersive filters (AOPDFs) have been most commonly employed for controlling the spectral phase and amplitude of femtosecond pulses in chirped-pulse amplification (CPA) laser systems.[1] However, shaping the polarization degrees of freedom in addition to phase and amplitude opens a new realm of possibilities in the fields of coherent control, high-harmonic generation and in coherent multi-dimensional spectroscopy experiments.[2] In the latter case, for example, there is a strong rationale for adding full electric field shaping to the existing capabilities of pulse shapers to generate multiple pulse sequences with well-defined and controllable phase relationships. This goal is especially relevant for the observation of multi-quantum coherences, which can provide information on the many-body interactions in a system.[3] More generally, any multi-dimensional spectroscopy experiment would benefit from polarization shaping of each pulse as a flexible tool to highlight couplings between quantum states.

The most general polarization state of polarized monochromatic light is elliptical and can be completely specified by the ellipse parameters describing the field. Drawing from this limiting case, polarization shaping of femtosecond pulses refers to the process of manipulating the ellipse parameters for the individual wavelength components present in the pulse. This process requires controlling at least two degrees of freedom, namely, the ellipticity and orientation of the field. Polarization control of femtosecond pulses was pioneered by Brixner and coworkers in the early 2000s.[4] By placing a double array of SLMs in the Fourier plane of a compressor folded in a 4f geometry, they were able to shape the spectral phase and ellipticity of 800 nm pulses. However, this initial design did not allow for the control of amplitude or the orientation of the ellipse's major axis, meaning that no linear states other than vertical and horizontal could be created. Since then, other groups have shown partial or complete polarization control of femtosecond pulses.[2,5–8]

This paper expands on the ideas presented in a previous contribution by our group.[9] Here, we provide a detailed analysis of our polarization shaping setup that builds upon our initial work,[9] including a description of the calibration steps required to obtain full polarization control. In addition, we also introduce two major technical improvements with respect to the initial setup. The first improvement relates to the polarization contrast, or degree of polarization, defined as the fraction of the pulse's total intensity which has the desired polarization state.[10] It is an essential metric when considering the potential of a polarization shaping setup for applications. In Ref. 9, the polarization contrasts obtained were never higher than 50%. This made the setup impracticable to use in multi-dimensional spectroscopy experiments featuring polarization-shaped pulses. Thanks to a fully automatized calibration of our setup, we have now solved this issue and are able to obtain contrasts above 90% for any polarization state with minimal user effort. The second improvement concerns a fast refresh rate of the AOPDFs, up to 25 kHz. Previously, only 1024 radio-frequency (RF) waveforms could be stored in the memory of the pulse shapers and the loading time for these waves could take up to 2 or 3 min. In the new system, the pulse shapers are equipped with an additional first in, first out (FIFO) memory able to play sequentially several tens of waveforms. The transfer time from the pulse shapers' static random access memory (SRAM) to FIFO is on the order of 200 μs. In this improved setup, a pattern contained in the FIFO is repeated N times while the next pattern is being uploaded in the driver SRAM. This allows the user to "stream" sequences of pulses,

a)Author to whom correspondence should be addressed. Electronic mail: pat.kambhampati@mcgill.ca

the length of which is only limited by the RAM size of the computer in which the waveforms are calculated. This results in a significant increase of the data acquisition speed, therefore minimizing the influence of laser drifts. The new streaming mode enables arbitrary screening at 1 kHz of any controllable physical parameter of the shaped electric field, be it polarization, delay or phase between a pair of pulses, over a set of tens of thousands pulse combinations. The maximal delay between pulses in a sequence depends on their spectral bandwidth, as the larger the spectral bandwidth to be diffracted the larger portion of the photo-elastic crystal is required. When pre-compensation for the dispersion coming from the pulse shapers' crystal is performed, one is typically able to achieve 5 ps maximal time delay with a 70 nm bandwidth pulse. Combined with its compactness on the optical table ($<30 \times 30\,\mathrm{cm}^2$), its easiness to align compared to SLMs and its broadband capabilities in the visible, the improved setup now forms a reliable building block that can readily be integrated into more complex experiments such as fully coherent multi-dimensional electronic spectroscopy.

II. EXPERIMENTAL SETUP

A scheme of the setup can be seen in Figure 1. The incoming beam first travels through an achromatic quarter wavelength waveplate (B-Halle, air-spaced, flat retardance over 480 nm–700 nm) before being split by a polarizing cube (B-Halle, extinction ratio $>1{:}10^4$). A half waveplate is introduced in the horizontally polarized arm of the interferometer, so that the beam has the desired entrance polarization of the pulse shaper. The beams are then independently shaped in amplitude and phase by two AOPDFs (WR25 Dazzlers, Fastlite, 480 nm–700 nm (Ref. 11)). We refer the reader to previous publications on the functioning of the pulse shapers.[11,12] A second half waveplate is introduced in the arm of AOPDF 1 to rotate the shaped beam's polarization from horizontal to vertical. Finally, the two orthogonally polarized shaped beams are recombined in a broadband polarizing cube. A pair of wedges is inserted in the arm of AOPDF 2 to compensate for the delay introduced by the waveplates in the other arm as well as compensate for residual delay. The transmission of the interferometer is around 30%.

A. Active phase stabilization

Because of small air currents and ambient acoustics, the relative carrier envelope offset phase of the pulses travelling optical path lengths of the two arms independently drift over time. This is undesired since polarization states can only be formed if there is a fixed, controlled, phase relationship between the vertical and horizontal components. To remedy this issue, an active feedback loop based on spectral interferometry was implemented. A delay of a couple of hundreds of femtoseconds is periodically programmed in one of the shapers and the spectral interference fringes obtained from the delayed pulses are used to recover the absolute phase difference. The value is then fed back to a phase shifter on the RF wave to be diffracted by AOPDF 1 in such a way that it compensates for the phase drift, defined as the difference between the measured phase and a user defined phase. A useful quantity to assess the phase stability is given by $2\pi/\varphi_{RMS}$, where φ_{RMS} is the root mean square value of the phase. The literature often refers to λ over this ratio, where λ is the wavelength.

To test the stabilization loop, we use Non-collinear Optical Parametric Amplifier (NOPA) pulses centered at 517 THz (580 nm) derived from a S-Pulse HP^2 laser from Amplitude Systèmes. The energy of the pulses is roughly 3 μJ/pulse at 1 kHz and the beam size 1 mm at the full-width at half maximum. Fig. 2(a) shows the relative phase between the two arms as a function of time. Without active phase stabilization feedback and without a box around the setup, the phase stability of the interferometer is around $\lambda/30$ (190 mrad) over several minutes (black curve in Fig. 2(a)). Simply covering the setup improves phase stability to $\lambda/80$ (78 mrad) over the same period of time (blue curve in Fig. 2(a)). Actively stabilizing at 30 Hz gets rid of the slow drift and leads to a phase stability of $\lambda/225$ (28 mrad) over a time only defined by the experimenters' needs. When active stabilization is performed, removing the box does not seem to have a major impact on the phase stability values. The hardware limit to the phase correction is given by the 8-bits resolution of the digital stabilization module, which is equivalent to $\lambda/256$. Fig. 2(b) shows the phase noise power spectral density (PSD).[13] The PSD is a useful quantity as it enables noise content analysis per unit frequency. As can be seen, most of the noise in the no-stabilization case originates from slow variations and phase drift up to 1 Hz, with a 1/f behavior. When the feedback loop is activated, this low frequency noise is reduced down to the white noise level. However, the white noise level is increased when the loop is active because of the limited phase resolution of the feedback loop.

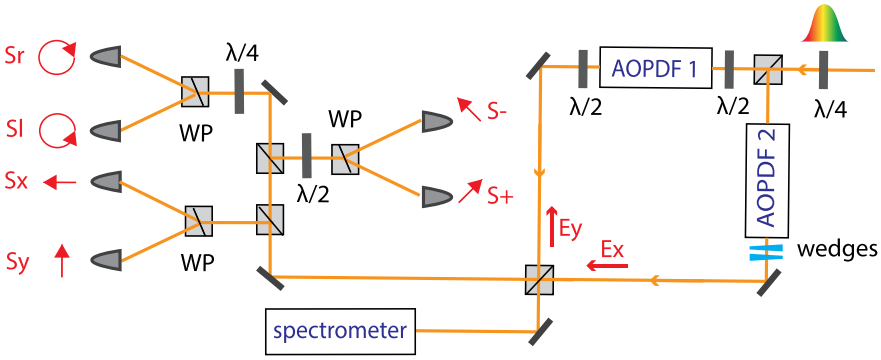

FIG. 1. The setup consists in two AOPDFs arranged in a Mach-Zehnder interferometer. A small part of the outgoing beam is used to carry out spectral interferometry for active phase stabilization. The remaining part of the beam is used to analyze the polarization states in a Müller Ellipsometer built from a series of non-polarizing beamsplitter cubes (Thorlabs), achromatic waveplates, and Wollaston polarizers (WP).

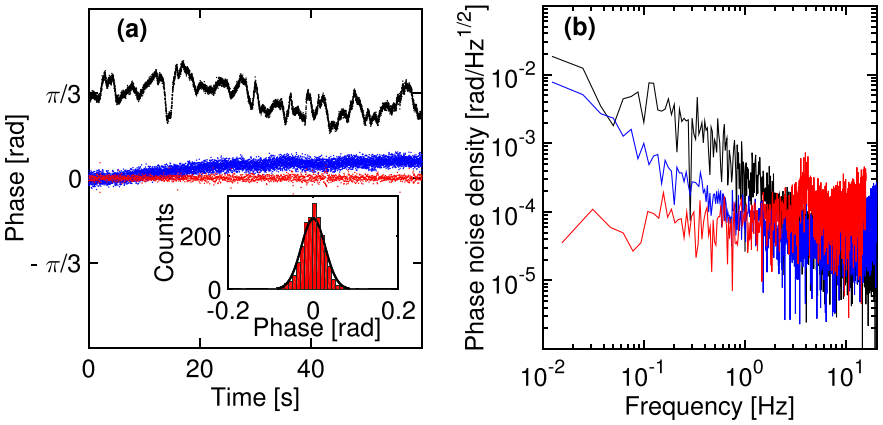

FIG. 2. Demonstration of the active phase stabilization loop (a) phase as a function of time for the cases of non-actively stabilized without box (black), non-actively stabilized with box (blue), and actively stabilized with box (red). The inset is a histogram of the phase values obtained when active phase stabilization is performed. (b) Phase noise power spectral density for the three cases (matching colors), displaying the noise content per unit frequency.

B. Interferometer calibration

Beyond maintaining phase stability in the interferometer, the main challenge of any interferometric-based polarization shaping setup is to balance the pulses in the two arms of the interferometer with respect to their energies, spectra, spectral phases, and beam profiles. In the present case, the energies can be easily tuned by fine adjustments of the quarter wave-plate at the entrance of the interferometer (see Fig. 1).

To balance the spectra, a common target spectrum is defined by the user, typically of Gaussian shape. Corrective amplitude masks are then successively applied in AOPDF 1 and AOPDF 2 until both spectra match the target. The correction is defined as the ratio $T_i(\omega)$ between the target spectrum and the initially diffracted spectrum. The new amplitude mask is then $\alpha \times T_i(\omega) \times A_i(\omega)$, where $\alpha \in [0, 1]$ regulates the feedback strength. An example of this amplitude shaping process is shown in Figure 3(a). In order to match the spectral phases, a spectral interferometry experiment is performed, from which the spectral phase difference between the two arms is extracted. This difference is then subtracted from the phase mask of AOPDF 1. This operation is carried out until the spectral phase difference is flat over the bandwidth of our pulses, as can be seen in Fig. 3(b). Through this operation, the group delay between the two arms is also cancelled. At this stage, the pulses should thus be overlapped in time. A crucial step in the interferometer calibration is the spatial beam overlap, for which we use a small camera (Thorlabs DCC1240M).

Several tests were carried out to assess the calibration of the interferometer. A first visual test consists in creating an interferogram and looking at the fringe contrast. An example of interferogram obtained when energies, spectra, spectral phase difference, and beam overlap are optimized is shown in Fig. 4(a). A more quantitative test consists in placing a linear polarizer at +45° in front of a spectrometer and subsequently generating +45°, −45°, 90°, and 0° linearly polarized states in the interferometer, the result of which can be seen in Fig. 4(b). The ratio of the areas between the constructive interference case (+45° state) and the case where one of the interferometer arms is blocked (90° or 0° sates) is 3.98, close to the expected value of 4. Indeed, the +45 state is twice as intense as the 0° and 90° states, which are further projected onto the +45 linear polarizer leading to the overall 4:1 intensity ratio. Similarly, the ratio of the areas between the completely destructive and constructive cases is 0.001. In a third test, the spectrometer is replaced by the camera set on maximum gain. When a −45° state is created, totally destructive interference should be observed, an example of which can be seen in Fig. 4(e). Any residual small angle between the recombining beams will lead to a fringe pattern on the camera, which proves extremely useful for fine alignment purposes. Those three calibration metrics provide a strong indication that our setup is capable of generating polarization states with high contrast.

C. Polarization states detection

To analyze the polarization states, we choose the Stokes vector description.[10] In this formalism, the polarization of a

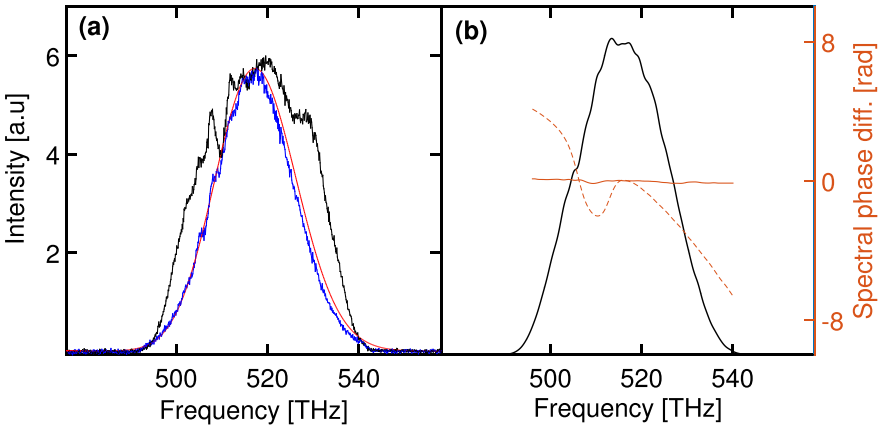

FIG. 3. Calibration of the interferometer (a) a corrective amplitude mask is applied in each pulse shaper to ensure matching between spectra. Following this feedback, the initially diffracted spectrum (black) is matched (blue) to a user-defined target spectrum (red) (b) similarly, a corrective phase mask is applied to AOPDF 1 to reduce the initial spectral phase difference between the two arms (dotted) to close to zero (plain). The phase jump at 510 THz originates from a coating layer inside the recombining cube.

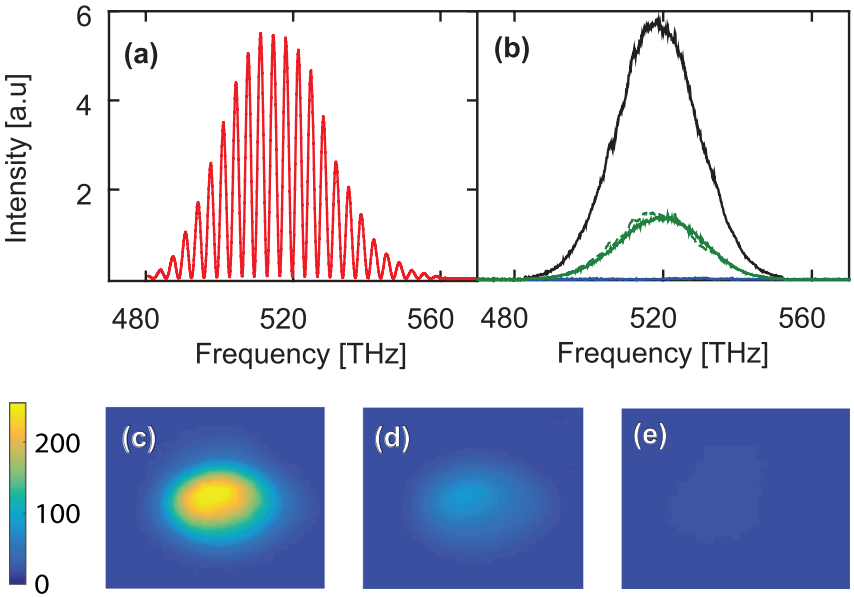

FIG. 4. Interferometer calibration metrics (a) a balanced interferogram (b) spectra collected after a linear polarizer at +45° for the cases of linearly polarized states at +45° (black), 90° (green, plain), 0° (green, dotted), and −45° (blue) (c)–(e) camera images collected after a linear polarizer at +45° for the cases of +45° (c), 0° (d), and −45° (e) states.

monochromatic electric field is represented by four real numbers with the dimension of intensities

$$\begin{pmatrix} S_0(\omega) \\ S_1(\omega) \\ S_2(\omega) \\ S_3(\omega) \end{pmatrix} = \begin{pmatrix} E_x^2(\omega) + E_y^2(\omega) \\ E_x^2(\omega) - E_y^2(\omega) \\ 2E_x(\omega)E_y(\omega)\cos\left(\delta_x(\omega) - \delta_y(\omega)\right) \\ 2E_x(\omega)E_y(\omega)\sin\left(\delta_x(\omega) - \delta_y(\omega)\right) \end{pmatrix},$$

where $E_x(\omega)$ and $E_y(\omega)$ are the amplitudes and $\delta_x(\omega)$ and $\delta_y(\omega)$ are the phases of the electric fields in, respectively, the first and second arms of the interferometer. From this representation, it is trivial to recover the standard ellipse parameters.[10] Our polarization state detection method consists of a Müller Ellipsometer, which can be seen in Figure 1. The polarization states are projected onto pairs of polarization bases: a linear horizontal/vertical basis (S_x, S_y), a circular left/ circular right basis (S_r, S_l) and a +45 and −45 linearly polarized basis (S_+, S_-). The beams in each of those six states are then sent onto high gain, large area photodiodes, which signals are sampled by a USB oscilloscope (Picoscope 4824) and subsequently integrated. From the projections, the Stokes parameters can readily be obtained. For example, $S_2 = S_r - S_l$ and $S_3 = S_+ - S_-$. The drawback of this ellipsometer is that it is limited to detecting polarization states where all the wavelengths in the pulse are shaped in a similar fashion. However, this case is the most demanding one as any misalignment, spurious dephasing, spectral imbalance, or difference in the spatial mode of the diffracted beams will decrease significantly the polarization contrast.

III. POLARIZATION STATES SEQUENCES

To demonstrate the capabilities of the setup, the Poincaré's sphere is sampled using two simple polarization sequences played at 1 kHz. One stabilization wave is also sent at the beginning of each sequence to maintain phase stability in the interferometer. In the first sequence, a series of linear polarization states ranging from vertical to +45° is created by varying the amplitude of $E_x(\omega) \in [0, E_y(\omega)]$ but maintaining the relative phase $\delta_x(\omega)$ - $\delta_y(\omega)$ to zero. In the second sequence, a series of polarization states with fixed relative amplitudes but varying relative phases is generated. An example of the Stokes components obtained from the ellipsometer is shown in Fig. 5(a) for the case of the second sequence. Within the Stokes formalism, the degree of polarization is readily expressed as $P = (S_1^2+S_2^2+S_3^2)^{1/2}/S^0$.[10] Contrasts of 10^{-5} are achieved for vertical and horizontal

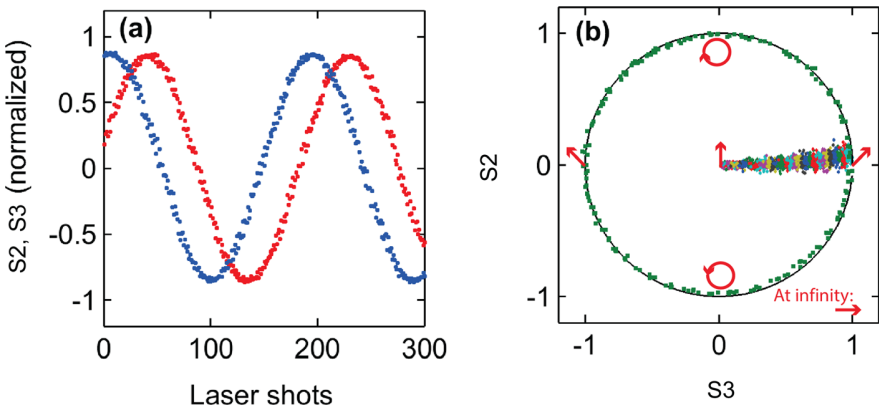

FIG. 5. (a) Stokes components S_2 and S_3 as a function of laser shots when $E_x(\omega) = E_y(\omega)$ and $\delta_x(\omega) - \delta_y(\omega)$ is varied between 0 and 2π. S_2 and S_3 are normalized with respect to the total energy going into each pair of photodiodes, S_r+S_l and S_++S_-, respectively. (b) Two simple polarization sequences are used to sample the Poincaré sphere. Results are normalized, corrected for the phase shift mentioned in (a), shown on a 2D projection. Green squares correspond to the sequence shown in (a). Diamonds of various colors represent a sequence spanning vertical to +45° linearly polarized states.

linearly polarized sates, and of 0.95 for ±45 linearly polarized states as well as left and right circular states. These polarization contrasts, obtained for broadband visible pulses, are on par if not better than those obtained in previous setups using near-IR Titanium Sapphire oscillator pulses.

It is worth noting that the phase shift between S_2 and S_3 as shown in Fig. 5(a) is not exactly $\pi/2$ (here $3\pi/8$). We attribute this to a phase shift of the S and P components occurring due to imperfect optical components or reflections on metallic surfaces in the ellipsometer. The observed phase shift was different for different mirror coatings or beamsplitters but could not be suppressed. If that phase shift was present in the pulse before the ellipsometer, this would have shown as reduced contrast in Fig. 4.

IV. CONCLUSION

In summary, we have demonstrated a setup capable of completely shaping the electric field of broadband visible femtosecond pulses by combining two orthogonally polarized electric fields diffracted in acousto-optic pulse shapers. In addition to the high contrasts, the compactness of the setup on the optical table, its easiness to align, and ability to perform single-shot large data set acquisition in the kilohertz range make it a flexible tool that will facilitate its integration as a building block of more complex experiments, such as fully collinear multi-dimensional spectroscopy.

ACKNOWLEDGMENTS

Hélène Seiler acknowledges the Swiss National Science Foundation for their scholarship. The authors acknowledge funding from CFI, NSERC, FQRNT, and McGill University.

[1]N. Forget, L. Canova, X. Chen, A. Julien, and R. Lopez-Martens, "Closed-loop carrier-envelope phase stabilization with an acousto-optic programmable dispersive filter," Opt. Lett. **34**(23), 3647–3649 (2009).
[2]M. Plewicki, S. M. Weber, F. Weise, and A. Lindinger, "Independent control over the amplitude, phase, and polarization of femtosecond pulses," Appl. Phys. B **86**, 259–263 (2007).
[3]K. W. Stone, D. B. Turner, K. Gundogdu, S. T. Cundiff, and K. A. Nelson, "Exciton-exciton correlations revealed by two quantum two-dimensional Fourier transform optical spectroscopy," Acc. Chem. Res. **42**(9), 1452–1461 (2009).
[4]T. Brixner and G. Gerber, "Femtosecond polarization pulse shaping," Opt. Lett. **26**(8), 557–559 (2001).
[5]F. Weise and A. Lindinger, "Full control over the electric field using four liquid crystal arrays," Opt. Lett. **34**(8), 1258–1260 (2009).
[6]L. Polachek, D. Oron, and Y. Silberberg, "Full control of the spectral polarization of ultrashort pulses," Opt. Lett. **31**(5), 631–633 (2006).
[7]M. Ninck, A. Galler, T. Feurer, and T. Brixner, "Programmable common-path vector field synthesizer for femtosecond pulses," Opt. Lett. **32**(23), 3379–3381 (2007).
[8]C. T. Middleton, D. B. Strasfeld, and M. T. Zanni, "Polarization-shaping in the mid-IR and polarization-based balanced hereodyne detection with application to 2D IR spectroscopy," Opt. Express **17**(17), 14526–14533 (2009).
[9]P. Tyagi, J. I. Saari, B. Walsh, A. Kabir, V. Crozatier, N. Forget, and P. Kambhampati, "Two-color two-dimensional electronic spectroscopy using dual acousto-optic pulse shapers for complete amplitude, phase, and polarization control of femtosecond laser pulses," J. Phys. Chem. A **117**(29), 6264–6269 (2013).
[10]R. M. A Azzam and N. M. Bashara, *Ellipsometry and Polarized Light* (North-Holland Publishing Company, 1977).
[11]A. Monmayrant, A. Arbouet, B. Girard, B. Chatel, A. Barman, B. J. Whitaker, and D. Kaplan, "AOPDF-shaped optical parametric amplifier output in the visible," Appl. Phys. B **81**(2–3), 177–180 (2005).
[12]F. Verluise, V. Laude, Z. Cheng, Ch. Spielmann, and P. Tournois, "Amplitude and phase control of ultrashort pulses by use of an acousto-optic programmable dispersive filter: Pulse compression and shaping," Opt. Lett. **25**(8), 575–577 (2000).
[13]V. Crozatier, "Carrier- envelope phase stabilization," in *Attoscience and XUV Science*, edited by T. Schultz and M. Vrakking (Wiley, 2011).

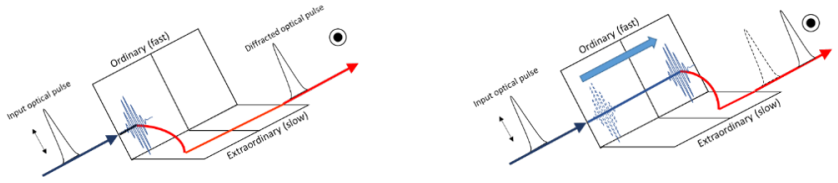

FIGURE 3.3 – Schéma illustrant l'effet de la propagation acoustique. Au premier ordre le retard acoustique induit un simple retard optique.

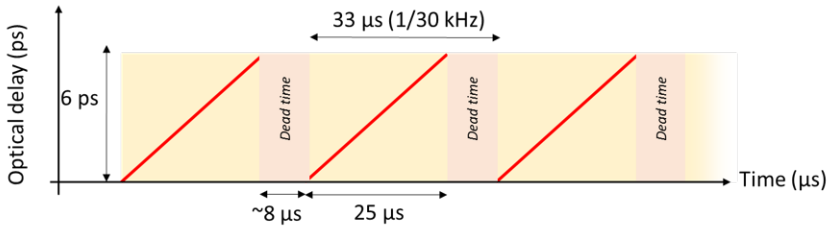

FIGURE 3.4 – Schématisation de l'effet de ligne à retard rapide induit par un AOPDF

3.3.2 Pompe-sonde

Une autre propriété intéressante des AOPDFs tient au caractère transitoire (et non statique) du façonnage. Étant donné que l'onde acoustique se propage, il est nécessaire de rafraichir celle-ci à la cadence du laser pour façonner chacune des impulsions de manière identique. Comme le temps de propagation dans le cristal est de l'ordre de 33 µs dans un cristal de TeO_2 de 25 mm (coupe HR), il semble impossible de façonner des sources pulsées de très haute cadence (>100 kHz). Ce n'est pas tout à fait le cas. En réalité, pour une source à haute cadence comme un train d'impulsions 80 MHz, plusieurs impulsions optiques interagissent avec la même onde acoustique mais à différents instants. Du fait de la propagation acoustique, la diffraction se produit à différentes profondeurs, ce qui se traduit par un délai de groupe optique variable d'une impulsion à l'autre : pour un AOPDF de 25 mm en TeO_2 (coupe HR), le délai de groupe varie de 8 ps en 25 µs, soit l'équivalent d'un miroir se déplaçant à 260 km/h environ.

Une première application de ce type de ligne à retard ultra-rapide est la réalisation d'expériences de type pompe-sonde à très haute cadence. Une collaboration avec le groupe de Rupert Huber de l'Université de Regensburg (Allemagne) a permis de vérifier la vitesse de balayage mais aussi d'en évaluer la reproductibilité et la précision. L'expérience menée avec Olaf Schubert [55] consiste à partager en deux bras la sortie d'un oscillateur Erbium à 1.55 µm puis à amplifier chaque bras au moyen d'un EDFA et à les recombiner colinéairement sur une photodiode en InGaAs. L'AOPDF est inséré sur l'un des bras avant l'EDFA. Le générateur RF de l'AOPDF est synchronisé sur la cadence de l'oscillateur (mode « low jitter ») de même que l'échantillonneur. On observe une figure d'interférence extrêmement reproductible avec une gigue temporelle d'une quinzaine d'attosecondes rms et de 0.8 fs à long terme (5 h). L'expérience est reproduite avec une fibre non linéaire en aval de l'EDFA, montrant ainsi que la ligne à retard rapide est compatible de ce type de post-compression.

Aucune des expériences précédentes n'ayant pu réellement exploiter les avantages inhé-

rents à la cadence de mesure offerte par une ligne à retard rapide, une nouvelle expérience a été mise en place en collaboration avec le groupe de Regensburg. Dans cette étude [56], le numériseur est capable de stocker un grand nombre de mesures et de moyenner en temps réel les mesures. Le montage permet ici de mesurer, par échantillonnage électro-optique, le spectre d'impulsions électromagnétiques dans le domaine térahertz (environ 2 THz). Le montage reprend celui d'Olaf Schubert et le complète par une génération d'impulsions THz par rectification optique (bras retardé) et une détection electro-optique dans un cristal de ZnTe (voie de référence). L'expérience met en évidence le bénéfice de la spectroscopie à haute cadence : le rapport signal-à-bruit de la mesure peut être amélioré de plusieurs ordres de grandeur par rapport à une mesure à basse cadence.

L'étude menée avec Olaf Schubert [57] peut également se comprendre dans le domaine spectral en termes de peignes de fréquences. En effet, comme précisé dans le chapitre 2.1, le faisceau diffracté subit un décalage Doppler égal à la porteuse de l'onde acoustique, soit quelques dizaines de MHz. On peut donc considérer que le train d'impulsions diffracté est spectralement décalé par rapport au train incident et que la combinaison du faisceau incident et du faisceau diffracté forme un double peigne de fréquence. Cette analyse n'est pas tout à fait exacte car le rafraichissement de l'onde acoustique recrée des coïncidences toutes les 33 µs. C'est cependant la formulation choisie par Irina Znakovskaya dans l'étude [58] que nous avons menée au MPQ (Garching, Allemagne) sur un oscillateur Ytterbium de forte puissance moyenne (thin-disk). Par simple analyse de la figure d'interférence avec un analyseur de spectre RF, le spectre d'absorption de l'acétylène au voisinage de 1030 nm a été mesuré. Bien que l'expérience soit formellement équivalente à celle d'Olaf Schubert, l'usage d'un simple analyseur de spectre RF (non synchronisé sur le laser) simplifie grandement la détection et rend ce type de spectroscopie extrêmement simple à réaliser.

Rapid-scan acousto-optical delay line with 34 kHz scan rate and 15 as precision

O. Schubert,[1,*] M. Eisele,[1] V. Crozatier,[2] N. Forget,[2] D. Kaplan,[2] and R. Huber[1]

[1]*Department of Physics, University of Regensburg, 93040 Regensburg, Germany*

[2]*Fastlite, 1900 route des crêtes, 06560 Valbonne, France*

**Corresponding author: olaf.schubert@physik.uni-regensburg.de*

Received June 14, 2013; revised July 6, 2013; accepted July 8, 2013;
posted July 8, 2013 (Doc. ID 192287); published August 1, 2013

An optical fast scan delay exploiting the near-collinear interaction between a train of ultrashort optical pulses and an acoustic wave propagating in a birefringent crystal is introduced. In combination with a femtosecond Er:fiber laser, the scheme is shown to delay few femtosecond pulses by up to 6 ps with a precision of 15 as. A resolution of 5 fs is obtained for a single sweep at a repetition rate of 34 kHz. This value can be improved to 39 as for multiple scans at a total rate of 0.3 kHz. © 2013 Optical Society of America

OCIS codes: (320.7100) Ultrafast measurements; (230.1040) Acousto-optical devices; (320.7160) Ultrafast technology; (320.7080) Ultrafast devices.

http://dx.doi.org/10.1364/OL.38.002907

Ultrashort laser pulses are now routinely employed in a rich variety of powerful analytical tools in physics, chemistry, and biology. Time-resolved pump-probe studies [1], nonlinear optical frequency mixing [2], optical coherence tomography [3], or broadband and ultrabroadband THz time-domain spectroscopy [4–6] are but a few examples of popular concepts. Temporal or spatial resolution is commonly achieved with the aid of a controllable optical delay line: A laser pulse is shifted in time with respect to a reference, and the experiment is repeated for different temporal offsets. The adjustable delay is usually implemented by mounting a retroreflector assembly on a mechanical stage and exploiting the geometric path difference for different positions of the stage.

Fast scan rates are desirable in order to reach sufficient recording speeds for multidimensional spectroscopy, to minimize the impact of thermal drifts of complex optical setups, or to monitor rapidly evolving systems, such as live biological tissue. In the case of mechanical delay lines, the inertia of the mirrors mounted on motor- or piezo-driven stages limits the maximal scan rates to a few tens of Hertz. Fast scan delays based on loudspeaker diaphragms or rotating mirrors [7,8] have reached higher repetition rates up to tens of kilohertz, yet with limited precision. A conceptually different route has been taken recently by asynchronous optical sampling (ASOPS) [9,10]. Two mode-locked lasers have been electronically stabilized to slightly mismatched repetition rates thus causing a shot-to-shot increase of the temporal offset between two pulse trains. For ASOPS, the scan window is fixed by the repetition rate of the laser f_{rep} to $1/f_{\mathrm{rep}}$, which amounts to typical values between 100 ps and several nanoseconds. Active electronic stabilization of the oscillators has been sophisticated enough to allow for a temporal precision as good as 50 fs [9]. This technique has opened exciting possibilities, e.g., in high-resolution spectroscopy [11].

Nonetheless many experiments call for delay concepts reaching a higher temporal precision and shorter scan ranges. In condensed matter physics, for example, ultrafast electron and lattice dynamics typically occur in the energy range of few millielectron volts to electron volts, corresponding to time scales of the order of a few femtoseconds to picoseconds [1,2]. Furthermore pump-probe experiments employing single-cycle [12] or even subcycle temporal resolution [4–7] are now possible. In this context a precision better than one femtosecond and a scan window of no more than a few picoseconds would be optimal. The ultimate scan rate f_{scan} is given by $f_{\mathrm{scan}} = f_{\mathrm{rep}}/N$, where N denotes the number of sample points. In this case, each laser pulse creates exactly one data point. Typical values $N = 1000$ and $f_{\mathrm{rep}} = 40$ MHz suggest an optimal scan rate of $f_{\mathrm{scan}} = 40$ kHz.

Here we introduce an acousto-optical fast scan delay capable of scanning a temporal window of 6 ps with a precision of 15 as and a repetition rate of 34 kHz. The novel scanning concept is based on an acousto-optic programmable dispersive filter (AOPDF) [13]. It exploits the propagation of the acoustic signal between successive optical pulses: An acoustic shear wave and an optical pulse train from a femtosecond laser oscillator copropagate in an anisotropic dielectric. The acoustic wave appears stationary to each optical pulse because the acoustic group velocity v_{sound} is several orders of magnitude lower than the speed of light. As a laser pulse reaches the acoustic wave, the polarization of the diffracted electromagnetic wave is switched from the ordinary to the extraordinary axis of the crystal (Fig. 1), by acousto-optic interaction. Consequently the velocity of the diffracted optical pulse is changed from c/n_o to c/n_e, where c, n_o, and n_e are the speed of light and the group refractive indices for ordinary and extraordinary polarizations, respectively. Depending on the position x_i of interaction, an optical delay,

$$t_i = (n_e - n_o) \times (L - x_i)/c, \tag{1}$$

is introduced between the diffracted and the nondiffracted pulse. L denotes the length of the crystal. During the time interval between successive laser pulses, the acoustic wave propagates by a small distance $\Delta x = v_{\mathrm{sound}}/f_{\mathrm{rep}}$, leading to a variation of the positions x_1, x_2, x_3 etc. of acousto-optic interaction from shot to

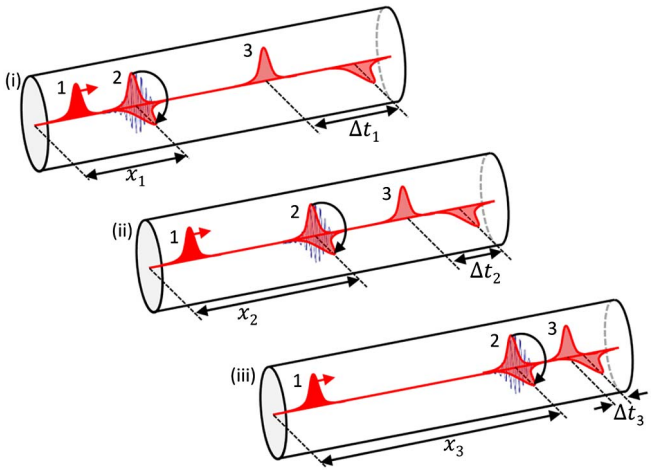

Fig. 1. Principle of operation of the acousto-optical fast scan delay: for laser pulses (red) entering a birefringent crystal (1), a propagating acoustic wave (blue) appears as a quasi-stationary modulation of the refractive index. Acousto-optic interaction rotates the polarization of the optical pulse by 90°, from the ordinary to the extraordinary axis (2). While the diffracted pulse proceeds at speed c/n_e, the velocity of the nondiffracted pulse amounts to c/n_o, leading to a time delay Δt_i (3). Subsequent optical pulses from a high-repetition-rate laser system catch up with the propagating acoustic wave at different positions x_i, thus imposing different optical delays Δt_i [(i)–(iii)].

shot. In this way, the optical delay imposed on each diffracted laser pulse shifts in small increments of

$$\Delta t = (n_e - n_o) \times (v_{\text{sound}}/c) \times f_{\text{rep}}^{-1}. \quad (2)$$

For a standard TeO_2 AOPDF and near-infrared wavelengths, one finds $v_{\text{sound}}/c = 2.6 \times 10^{-6}$ and $n_e - n_o \leq 0.14$, depending on the cut of the crystal. With $f_{\text{rep}} = 40$ MHz, we may choose a delay step Δt between 5 and 9 fs. In other words, the large velocity mismatch between acoustic and optical waves allows us to convert the laser pulse-to-pulse temporal separation of 25 ns into an optical delay on the femtosecond scale. Note that this acousto-optic device requires neither moving parts nor active electronic feedback loops. Therefore, our concept circumvents problems of beam-pointing fluctuations typically encountered in mechanical scanning systems. Furthermore, the time increment Δt [Eq. (2)] depends only on material constants and the repetition rate of the laser source, which makes the device intrinsically precise in the attosecond regime, as shown below.

In our implementation, we employ an Er:fiber-laser system operating at a repetition rate of $f_{\text{rep}} = 40$ MHz. After the oscillator the pulse train is split into two copies (Fig. 2). One part is directly amplified in a diode-pumped Er:fiber (branch A), while the other one is sent through a TeO_2 AOPDF crystal of a length of $L = 25$ mm (HR25, Fastlite). An acoustic wave is launched by a piezo transducer at a repetition rate of $f_{\text{scan}} = 34$ kHz and propagates nearly collinearly with the optical beam. The diffracted femtosecond pulse is coupled into a second Er:fiber stage (branch B). After amplification, the pulses in each branch carry energies of more than 8 nJ with pulse durations below 100 fs. For the current crystal length of 25 mm, the theoretical maximum of discrete

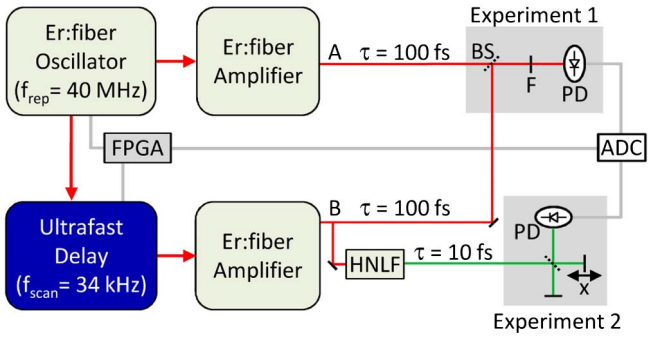

Fig. 2. Acousto-optic fast scan delay incorporated in a femtosecond Er:fiber-amplifier system. Seed pulses from an Er:fiber oscillator are split into two branches, one of which is acousto-optically delayed. In experiment 1, we combine pulse trains A and B after amplification with a beam splitter (BS), filter them spectrally (F), and superpose them on a photodiode (PD). In experiment 2, we characterize pulses compressed in a highly nonlinear fiber (HNLF) via a nonlinear autocorrelator, exploiting two-photon absorption and an interferometer with a moveable mirror (x). Electronic synchronization signals are derived directly from the oscillator pulse train and processed by a field programmable gate array (FPGA).

delay positions t_i per scan is $f_{\text{rep}}/f_{\text{scan}} \approx 1200$. The total delay corresponds to 6 ps, which is scanned with a resolution of 5 fs. These parameters are ideally suited, e.g., for femtosecond pump-probe experiments or electro-optic detection of ultrabroadband THz transients [1,4–6,11].

In order to put the precision of the delay to an ultimate test, we study interferometric cross-correlation between pulse trains derived from the two amplifier branches. A well-defined frequency of the signal is ensured by passing the pulses through a narrowband filter (center wavelength $\lambda_0 = 1560$ nm, full-width at half-maximum $\Delta\lambda = 12$ nm). Afterward, the collinear superposition of both pulses is detected on an InGaAs photodiode (PD). We digitize the signals with a standard analog-to-digital converter (ADC) and integrate the PD signal corresponding to individual laser pulses on a computer. For lowest jitter and noise, a reference clock is obtained from a PD monitoring the pulse train from the laser oscillator. Subsequently, the clock rate is divided using a field programmable gate array (FPGA) to provide synchronization signals for the ADC and the AOPDF. We subtract the reference signals, obtained by blocking the beam of either branch A or branch B, from the recorded voltage, which yields a bipolar linear cross-correlation signal (Fig. 3). Figure 3(a) depicts the trace recorded in a single sweep of the delay stage, with a total acquisition time of only 29 μs. Clear indications of interference fringes can be identified. Since the natural increment of the delay line of $\Delta t = 5$ fs is comparable to the oscillation period of the optical carrier wave of 5.2 fs, the optical interference fringes remain undersampled in this scan. The excellent stability and repeatability of the delay, however, allow us to readily increase the effective resolution by means of multiple scans. Following the operating principle of a sampling oscilloscope in electronics, we delay the starting time of the acoustic wave between successive scanning cycles by an integer fraction of the inverse

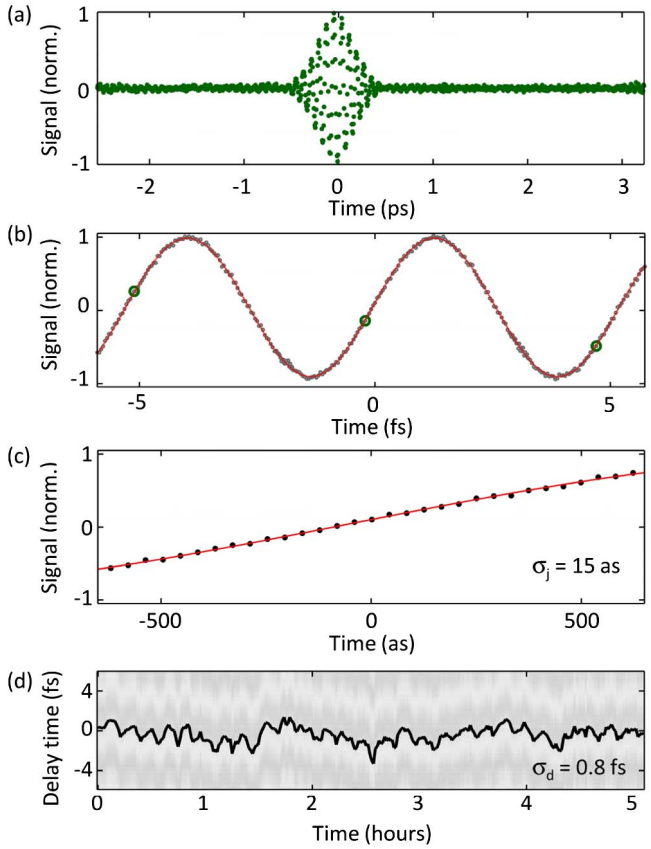

Fig. 3. (a) Linear cross-correlation between two spectrally degenerate pulse trains ($\lambda_0 = 1560$ nm, $\Delta\lambda = 12$ nm), as recorded with one laser shot per data point (acquisition time: 29 μs). (b) Close-up with improved time resolution. Green circles indicate the scan from (a), gray dots correspond to data obtained from 128 consecutive, time-offset scans (148,000 data points, acquisition time: 4 ms), red line: fit of sine function to data. (c) Zoom into data from (b), σ_j is the rms jitter. (d) Long-term drift of the delay time leading to an rms deviation of $\sigma_d = 0.8$ fs.

repetition rate, i.e. by $1/(f_{\mathrm{rep}} \times m)$. This translates, via Eq. (2), to an additional optical delay $\Delta\tau = \Delta t/m$ for each interleaved scanning cycle with m scans. The number of acquisitions, and thus the effective scan rate and the temporal resolution, can be conveniently selected with a computer interface. A phase-locked loop warrants precise synchronization of the launch event of the acoustic wave and the laser pulse train. The electronic timing jitter of this feedback loop of 30 ps corresponds to an optical jitter of 9 as.

With 128 consecutive scans, with an acquisition time of 29 μs each, we record a cross-correlation trace comprising a total number of 148,000 data points within 4 ms. The central part of this signal is shown in Fig. 3(b) on a femtosecond scale. Green circles indicate the data obtained with one scan. Gray dots correspond to the signal of individual laser shots during the collection of 128 scans. Featuring an interlaced time increment of $\Delta\tau = 39$ as, the measured data sharply resolve the oscillations due to the near-infrared carrier wave. All data points closely follow a sine function (red curve), demonstrating the extremely high precision as well as the linearity of the delay. This can be seen even better in Fig. 3(c), where a close-up of the cross-correlation signal is displayed with a total delay window of only 1.3 fs. Even on this scale, the data points line up precisely.

To quantify the precision of the delay, we fit two cycles of the signal at the center of the cross-correlation trace with a sine function [red line in Figs. 3(b) and 3(c)]. The variance between the measured data points and the fit curve close to the zero crossing is taken as an upper limit of the timing jitter. Besides the actual limitation of the delay line, this value includes mutual timing and intensity fluctuations of the two laser arms during the measurement [14]. The rms value of this jitter is found to be as low as 15 as. This result attests to the excellent stability of the acousto-optic delay and the laser system on time scales up to the acquisition time of 4 ms.

For a test of the long-term timing drift, we repeatedly record linear cross-correlation traces for more than 5 h. For each scan, we extract the center of the interference fringes. This analysis yields an rms timing drift of the complete system as low as 0.8 fs [Fig. 3(d)]. No active stabilization, e.g. by additional delay stages or feedback loops, was employed during this measurement. In fact, the long-term jitter is limited by thermal drift of the laser system [14], rather than fluctuations of the acousto-optical delay line itself. If considered necessary, the launch time of the acoustic wave may even be reprogrammed for each scan to compensate for laser drift.

Straightforward estimates confirm that the inherent precision of the delay is expected to be even better than 15 as. According to Eq. (2), the temporal increment Δt is given by the product of a material factor of order 10^{-7}, and the laser pulse-to-pulse spacing given by $1/f_{\mathrm{rep}}$. During the duration of 29 μs, required for one scan, thermal drifts are negligible, and the material parameters are strictly constant. In addition, the temperature dependence of the refractive indices n_o and n_e cancels to first order because only their difference enters. Thus the pulse-to-pulse timing jitter of the laser system, which typically remains well below 1 fs [6,14], is the dominating factor. From these considerations, we estimate the delay precision during one scan to be well below 1 as. Note that we may safely neglect the finite length of the interaction region in Eq. (2) because the acousto-optic interaction remains identical for all positions x_i. For an interleaved scanning cycle, the electronic synchronization becomes the limiting factor, if laser drift can be neglected. As shown above, the expected precision in this case is 9 as for our current implementation.

One of the outstanding advantages of telecom-compatible Er:fiber femtosecond lasers is their versatility to compress 100 fs optical pulses close to their ultimate single-cycle limit by means of highly nonlinear germanosilica optical fibers (HNLF) [12,15]. For these ultrabroadband pulses, it is particularly important to ensure that the dispersion does not change significantly during a full delay scan. In order to test the compatibility of our fast scan device with such applications, we couple the 100 fs pulses from amplifier B into a dispersion-tailored HNLF assembly (see Fig. 2) to generate a supercontinuum spanning more than one optical octave [12]. A prism sequence is used to compress the short-wavelength part of the spectrum (wavelength range 950–1500 nm) close to Fourier-limited pulse duration. Since the spectrum results from a subtle interplay of linear propagation and

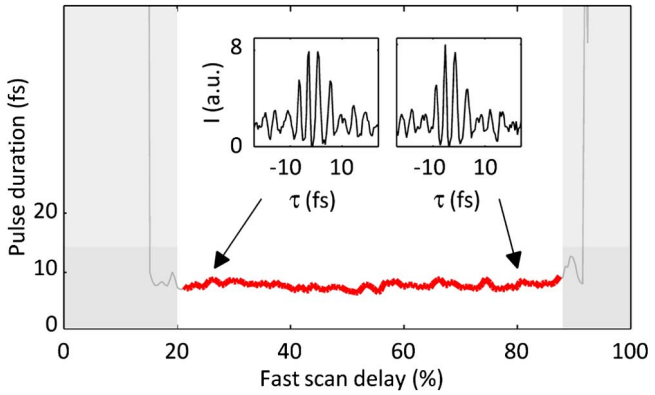

Fig. 4. Compatibility test of the acousto-optic fast-scan delay with 8 fs pulses. Duration of pulses derived from a highly nonlinear optical fiber as a function of delay position, as extracted from nonlinear auto-correlation traces assuming a Gaussian pulse shape (red line). The gray area indicates dead time, associated with launching a new acoustic wave. Insets: typical auto-correlation traces for two different delay positions (arrows) of the fast scan delay at the start and the end of the scan, respectively.

nonlinear effects [15], the duration of the compressed pulses after the HNLF may sensitively depend on the dispersion imposed on the 100 fs input pulses by the fast-scan delay.

We determine the actual duration of the pulses after the prism sequence as a function of the position of the fast scan delay with nonlinear auto-correlation measurements. To this end, the pulses are guided into a Michelson interferometer with a standard mechanical delay stage and focused tightly onto a GaAsP PD. The two-photon absorption signal is then recorded as a function of the positions of both the fast-scan delay and the mechanical delay. For each position of the fast scan delay, we extract the approximate pulse duration from the respective auto-correlation trace assuming a Gaussian envelope. The pulse duration of 8 fs is, indeed, constant within the measurement accuracy of ± 1 fs, for a duty cycle of about 70% (Fig. 4). This finding underpins the low variation of the dispersion induced by the delay. The remaining dead time associated with the launch of a new acoustic wave will be eliminated in a future implementation of the concept.

In conclusion, we demonstrate an ultrastable acousto-optical delay line with 34 kHz scan rate and a few attosecond precision. By translating the repetition rate of the laser into a femtosecond optical delay, our novel concept permits fast and flexible electronic control of sub-optical-cycle delays via precisely adjustable radio-frequency signals. Relying on intrinsic material parameters of the acousto-optic cell, such as refractive index and sound velocity, the compact device reaches unsurpassed short- and long-term stability. Since sophisticated acousto-optic pulse shaping has been well established in a different context [13], we are convinced that the new idea is fully compatible with a broad range of femtosecond lasers, including Er:fiber and Ti:sapphire technology. The novel scheme offers exciting perspectives for a wide field of applications in ultrafast optics, ranging from pump-probe spectroscopy, via THz photonics and OCT to attosecond experiments. More specifically, rapid pump-probe measurements with real-time recording cycles of tens of microsecond are anticipated to facilitate, for instance, *in situ* pump-probe measurements of biological matter. Further work toward extremely sensitive electro-optic sampling of multi-THz transients down to the few photon sensitivity level [16] and multidimensional spectroscopy is under way.

Support by the German Research Foundation (DFG) via the Emmy Noether Program (HU1598/1-1) and the European Research Council via ERC Starting Grant QUANTUMsubCYCLE is acknowledged.

References

1. M. Chergui, A. Taylor, S. Cundiff, R. de Vivie-Riedle, and K. Yamagouchi, eds., *Proceedings of the XVIIIth International Conference on Ultrafast Phenomena*, *EPJ Web of Conferences*, Lausanne, Switzerland, July 8–13 2013, Vol. **41**.
2. S. Mukamel, Annu. Rev. Phys. Chem. **51**, 691 (2000).
3. J. Fujimoto, Nat. Biotechnol. **21**, 1361 (2003).
4. E. Matsubara, M. Nagai, and M. Ashida, Appl. Phys. Lett. **101**, 011105 (2012).
5. A. Sell, R. Scheu, A. Leitenstorfer, and R. Huber, Appl. Phys. Lett. **93**, 251107 (2008).
6. R. Ulbricht, E. Hendry, J. Shan, T. Heinz, and M. Bonn, Rev. Mod. Phys. **83**, 543 (2011).
7. D. Molter, F. Ellrich, T. Weinland, S. George, M. Goiran, F. Keilmann, R. Beigang, and J. Léotin, Opt. Express **18**, 26163 (2010).
8. N. Chen and Q. Zhu, Opt. Lett. **27**, 607 (2002).
9. R. Gebs, G. Klatt, C. Janke, T. Dekorsy, and A. Bartels, Opt. Express **18**, 5974 (2010).
10. S. Kray, F. Spöler, T. Hellerer, and H. Kurz, Opt. Express **18**, 9976 (2010).
11. T. Yasui, K. Kawamoto, Y.-D. Hsieh, Y. Sakaguchi, M. Jewariya, H. Inaba, K. Minoshima, F. Hindle, and T. Araki, Opt. Express **20**, 15071 (2012).
12. G. Krauss, S. Lohss, T. Hanke, A. Sell, S. Eggert, R. Huber, and A. Leitenstorfer, Nat. Photonics **4**, 33 (2010).
13. P. Tournois, Opt. Commun. **140**, 245 (1997).
14. F. Adler, A. Sell, F. Sotier, R. Huber, and A. Leitenstorfer, Opt. Lett. **32**, 3504 (2007).
15. A. Sell, G. Krauss, R. Scheu, R. Huber, and A. Leitenstorfer, Opt. Express **17**, 1070 (2009).
16. G. Günter, A. A. Anappara, J. Hees, A. Sell, G. Biasiol, L. Sorba, S. De Liberato, C. Ciuti, A. Tredicucci, A. Leitenstorfer, and R. Huber, Nature **458**, 178 (2009).

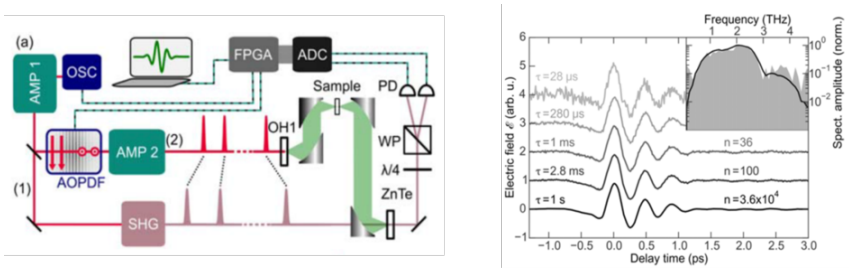

FIGURE 3.5 – A gauche montage expérimental tiré de la publication [56]. A droite : effet du moyennage sur le rapport signal-à-bruit de mesure.

3.3.3 Spectral focusing, imagerie par diffusion Raman stimulée

Deux applications biologiques récentes des lignes à retard AOPDF sont l'imagerie hyperspectrale par diffusion Raman stimulée [59–61] via la technique de « spectral focusing » et l'imagerie Raman de basse fréquence via une mesure pompe-sonde rapide [62]. Dans les deux cas, la ligne à retard rapide permet une acquisition « temps réel », compatible avec des objectifs de diagnostics biomédicaux.

La microscopie de fluorescence est une (sinon la) technique de référence dans les laboratoires de recherche évoluant dans le domaine de l'imagerie cellulaire. Bien que très impressionnantes, les avancées permises par la microscopie de fluorescence présupposent la présence de colorants ou marqueurs fluorescents au sein des échantillons à analyser, rendant l'analyse in-vivo de tissus cellulaires impossible. Plus généralement, la microscopie par fluorescence fait face à des limites fondamentales telles que :

- un faible nombre (typiquement <5) d'indicateurs fluorescents utilisables simultanément et une profondeur maximale d'imagerie limitée (≃100 µm) dans les tissus ou les échantillons ;
- une complexité de mise en œuvre liée à l'utilisation des marqueurs fluorescents (micro-injections, interactions moléculaires, toxicité, blanchiment, cinétique...) ou le recours à des techniques d'encodage génétique.

Ces limites rendent la transposition de ces techniques à l'homme soit difficilement envisageable, soit confinée aux analyses ex-vivo (i.e. aux biopsies). A l'inverse, la microscopie par diffusion Raman stimulée (SRS, Stimulated Raman Scattering) ne nécessite pas de marquage et offre des contrastes et des informations comparables à l'imagerie par fluorescence (membranes, noyaux, ions...) en y ajoutant une sélectivité chimique. Le SRS a déjà démontré sa pertinence en histologie (détection de cancers), l'étude dynamique de l'efficacité médicamenteuse sur les tissus cellulaires et la détermination de groupes chimiques au sein des tissus cellulaires. A titre d'exemple, l'histopathologie par SRS est actuellement évaluée au sein même de certains blocs opératoires outre-Atlantique (société Invenio Imaging Inc, start-up émulée par Harvard University).

La diffusion Raman stimulée est un processus non linéaire bien connu pour sa capacité à révéler, dans un échantillon, la présence de liaisons chimiques caractérisées par une énergie de liaison spécifique. Néanmoins, lorsque plusieurs types de liaisons sont présents il est nécessaire de balayer la plage spectrale de détection afin de pouvoir les distinguer. Lorsqu'elle est appliquée à la microscopie, cette technique pose un problème de vitesse car

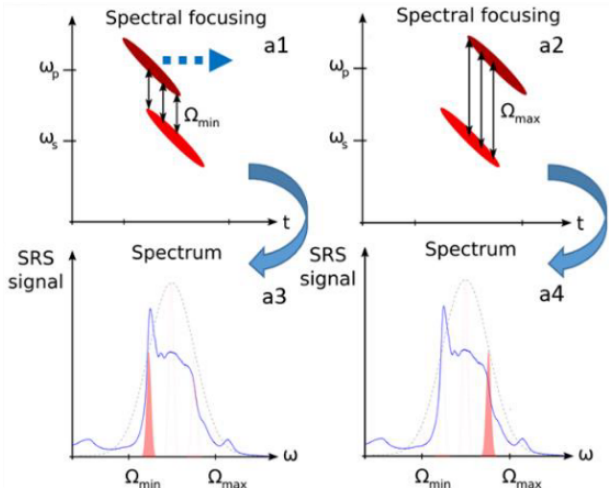

FIGURE 3.6 – Principe du spectral focusing. Image empruntée à Hervé Rigneault.

les faisceaux optiques doivent être focalisés sur l'échantillon et l'image est nécessairement reconstruite point par point. Il faut alors balayer trois paramètres : deux coordonnées spatiales et une coordonnée spectrale. Grâce une grande vitesse de balayage spectrale, une image hyperspectrale est réalisable en quelques minutes seulement. Ici le balayage spectral est réalisé au moyen d'un balayage temporel via la méthode de « spectral focusing » par variation du retard optique entre deux impulsions à dérive de fréquence. L'étude et l'adaptation des AOPDFs à l'imagerie hyperspectrale par SRS a été menée en collaboration avec le groupe MOSAIC de l'Institut Fresnel sous l'impulsion d'Hervé Rigneault. J'ai notamment eu l'occasion de travailler avec Xavier Audier dans le cadre de sa thèse [63]. Nous avons, en particulier, étudié l'effet de la ligne à retard acousto-optique et l'effet de son insertion sur les fluctuations d'intensité (RIN pour Relative Intensity Noise). Cette étude a mis en évidence :

- l'existence de rétro-diffusions multiples du faisceau acoustique au sein du cristal acousto-optique (dues à amortissement insuffisant),
- un mécanisme original et jamais rapporté (à notre connaissance du moins) expliquant comment ces rétro-diffusions causent une modulation de la lumière diffractée à une fréquence égale au double de la fréquence de la porteuse acoustique.

Le mécanisme découvert est le suivant : en présence d'hétérogénéités volumiques et/ou de surfaces diffusantes localisées après la zone d'interaction acousto-optique, une fraction du faisceau acoustique contra-propage jusqu'à la zone de l'interaction acousto-optique primaire et provoque une diffraction acousto-optique secondaire. Cette diffraction secondaire est indistinguable de l'interaction primaire du point de vue de ses propriétés géométriques (même direction, même accord de phase). Néanmoins, en raison de son caractère contra-propagatif, cette diffraction secondaire s'accompagne d'un décalage Doppler de signe opposé à celui de la diffraction primaire. L'interférence entre les faisceaux optiques issus des interactions primaire et secondaire crée alors un battement au double du décalage Doppler, c'est-à-dire à deux fois la fréquence de la porteuse acoustique. De par sa nature interférométrique, l'amplitude de battement est directement proportionnelle à la racine carrée de l'amplitude de la rétrodiffusion. Une rétrodiffusion de l'ordre de 10^{-4} est donc largement suffisante pour augmenter significativement le RIN de la source laser incidente.

Il est remarquable que ce phénomène soit passé inaperçu aussi longtemps étant donné le nombre de systèmes Dazzler commerciaux installés à travers le monde. Ce paradoxe s'explique par la nature retardée de la diffraction secondaire : ce phénomène ne s'observe qu'avec des sources laser continues (comme pour l'étude) ou pulsées à très haute cadence (>10 kHz).

La collaboration avec l'Institut Fresnel sur l'application d'une ligne à retard acousto-optique à la microscopie SRS s'est poursuivie en 2019. Les obstacles découverts en 2018 ont été résolus et la technique a pu être non seulement validée sur des échantillons de référence mais également appliquée à des échantillons de tissus humains congelés. Les résultats, en termes de contraste d'image et de vitesse d'acquisition, sont des résultats record et ont fait l'objet d'une publication en 2020 [61].

En 2021-2022 la collaboration s'approfondit avec le début de la thèse CIFRE d'Ines Martin, dirigée par Hervé Rigneault et que j'encadre du côté entreprise. Par ailleurs, Fastlite vient de débuter le développement de sources optiques dédiées à l'imagerie non linéaire et à l'imagerie SRS en particulier, grâce à un financement FEDER (programme SAVOIRS : Source Accordable et Versatile Optique pour l'Imagerie par diffusion Raman Stimulée).

Research Article | Vol. 28, No. 10 / 11 May 2020 / Optics Express 15505
Optics EXPRESS

High-speed chemical imaging of dynamic and histological samples with stimulated Raman micro-spectroscopy

XAVIER AUDIER,[1] NICOLAS FORGET,[2] AND HERVÉ RIGNEAULT[1,*]

[1] Aix Marseille Univ, CNRS, Centrale Marseille, Institut Fresnel, 13013 Marseille, France
[2] FASTLITE, 06560 Valbonne, France
[*] herve.rigneault@fresnel.fr

Abstract: We report a shot noise limited high-speed stimulated Raman microscopy platform allowing to acquire molecular vibrational spectra over 200 cm^{-1} in 12 µs at a scan rate of 40kHz. Using spectral focusing together with optimized acousto-optics programmable dispersive filters, the designed low noise imaging platform performs chemical imaging of dynamical processes such as Mannitol crystal hydration and reaches a signal to noise ratio sufficient to perform label free histological imaging on frozen human colon tissue slides.

1. Introduction

Stimulated Raman scattering (SRS) [1] imaging has gain tremendous interest over the last decade due to its ability to perform label free chemical imaging in biological sample [2,3]. In SRS microscopy two laser pulses, a pump at frequency ω_p and a Stokes at frequency ω_s, are focused on a sample to generate an image by point scanning. If the frequency difference $\omega_p - \omega_s$ equals a molecular vibrational frequency Ω_R an energy transfer occurs between the pump and the Stokes beam [4] that can be detected using dedicated modulation schemes. Since SRS imaging first demonstrations [5,6], efforts have been pursue to perform fast images [7], but also to acquire a complete vibrational spectrum at each pixel [8–16]. The fastest approaches to acquire a full spectrum [11,12] use the SRS spectral focusing scheme that allow to retrieve spectral resolution by adding dispersion on the femtosecond pulses [17,18]. When the pump and Stokes pulses are identically chirped, a narrow wavenumber range can be probed within the spectral bandwidth allowed by the pulses (Fig. 1(d)). Not only is spectral resolution recovered, but the probed wavenumber can easily be tuned by adjusting the time delay between the two pulses, allowing for spectral scanning without the need to change the lasers center wavelengths or fast spectrometer. Recently, acousto-optic programmable dispersive filters (AOPDF) have been used as ultrafast delay lines in different applications, such as transient absorption and terahertz spectroscopy [19,20]. Contemporary to this work, spectral focusing and AOPDF has been combined to rapidly sweep the delay between two chirped femtosecond pulses in an SRS microscope [21]. Raman spectra covering the full lipid band (2800 to 3050 cm^{-1}) were acquired at 33 µs per pixel, with a 25 cm^{-1} resolution. Although it showed impressive results, this study did not fully explore the possibilities offered by the technique. In particular, the noise brought by the AOPDF was not studied, the sensitivity was not showcased on biological tissues, and the increased acquisition rate was not applied to the study of chemically dynamic behaviors, while those two aspects are essential for applications.

Here, we report hyperspectral SRS imaging over 200 cm^{-1} in 12 µs at a scan rate of 40kHz with shot noise limited sensitivity. By characterizing the noise in our system and engineering the optimal laser pulses, we have designed an SRS imaging platform combining spectral focusing together with a faster AOPDF delay line to surpass the acquisition speed and sensitivity

#390850 https://doi.org/10.1364/OE.390850
Journal © 2020 Received 3 Mar 2020; revised 23 Apr 2020; accepted 28 Apr 2020; published 7 May 2020

Optics EXPRESS

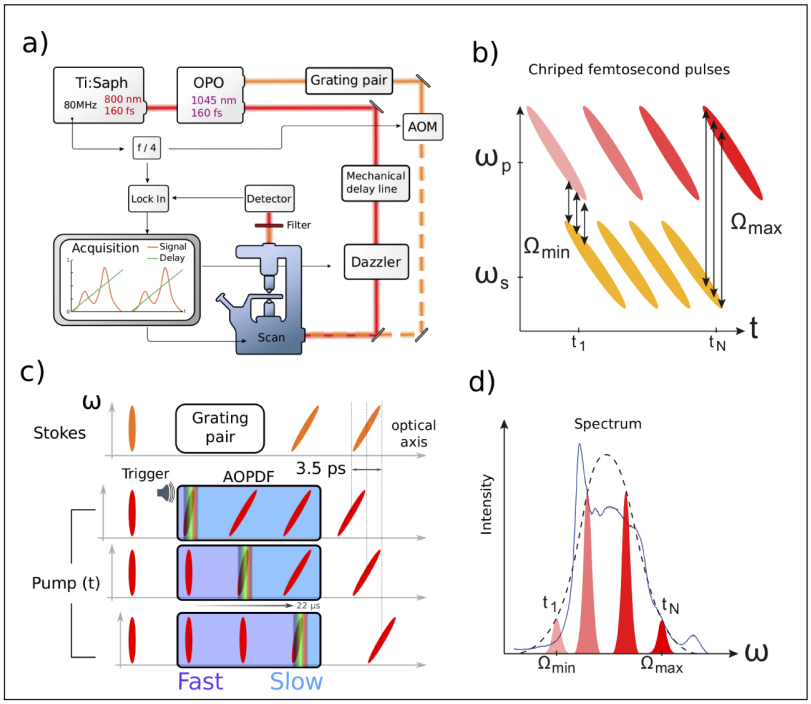

Fig. 1. a) Setup schematics, OPO: optical parametric oscillator, AOM: acousto-optic modulator. b) Spectral focusing scheme: the instantaneous frequency difference between the pulses is a function of the pulses relative delay. c) Acousto-optic programmable dispersive filter (AOPDF): the acoustic wave propagating inside the crystal imprints both negative dispersion, and a delay that changes linearly with the acoustic wave propagation time. d) Schematic of a typical spectrum (solid line) and the spectral bands (red gaussians) probed by the successive chirped pulses illustrated in b). The dashed line represent their relative signal amplitude, and consequently the bandwidth of the system.

demonstrated previously. We demonstrate optimized speed and sensitivity by targeting two major applications that are dynamic chemical imaging and label-free histology on human tissue samples.

2. Setup description

The SRS pump and Stokes beams are generated by a commercial femtosecond laser system (Chameleon OPO-VIS, Coherent) working at 80 MHz repetition rate. (Fig. 1(a)) The pump (800 nm) and Stokes (1045 nm) optical pulses are synchronized, and both can be modeled as Gaussian pulses with temporal full widths at half maximum of 160 fs. The pump laser is sent to an AOPDF (HR or WB Dazzler, Fastlite) which acts as both a tunable dispersive medium and an ultra fast delay line (see details below). The Stokes laser is sent through an acousto-optic modulator (MT200-A0.2-1064, AA optoelectronics) driven by a sinusoidal modulation at one fourth of the laser repetition rate (20 MHz). The first diffraction order of the Stokes beam is collected and sent through a double pass grating pair (custom gratings, Wasatch Photonics) where it undergoes negative dispersion. The modulated and negatively chirped Stokes beam is then recombined with the pump beam by means of a dichroic mirror before being sent to an inverted scanning microscope (TiU, Nikon). The two lasers are focused in the sample using a 20x air objective (0.75NA, CFI Plan Apo Lambda, Nikon) and collected with the same objective in the forward

Optics EXPRESS

direction. The Stokes beam is filtered out using an optical short pass filter (FES0900, Thorlabs), and the pump is collected using a photodiode who's output is then fed to a lock-in amplifier module. The photodiode, the lock-in amplifier and frequency divider are commercial systems optimized to work at 20 MHz (SRS Lockin Module, APE). The lock-in amplifier bandwidth was reduced to 1.35 MHz using an electronic lowpass filter (EF508 Thorlabs, 5th order). The signal from the lock-in was sent to a data acquisition card (ATS460, AlazarTech) and acquired with a sampling rate of 20 MHz. Simultaneously to SRS, and to address biological applications, second harmonic generation (SHG) was recorded at 400 nm in the epi direction, using a dichroic mirror (770dcxr, Chroma) band-pass filter (HQ400/40, Chroma), and photomultiplier tube (R9110 tube and C7950 data socket, Hamamatsu). Average laser powers at the sample plane were 15 mW and 20 mW for the pump and Stokes beams, respectively.

3. AOPDF description

The AOPDF consists of a birefringent crystal in which an acoustic shearing wave co-propagates with an ordinary-polarized optical beam (fast axis). Each acoustic frequency interacts with a specific optical frequency (acousto-optic phase-matching relationship) and gives rise to an extraordinary-polarized diffracted beam (slow axis). Therefore, using the proper acoustic waveform, one can imprint an arbitrary phase profile on incoming optical pulses [22]. In addition to this tunable phase profile, the propagation of the acoustic wave inside the crystal effectively imprints a delay on successive optical pulses that increases linearly over time (Fig. 1(c)). Using both of these properties, one can address the two requirements for spectral focusing SRS: chirped optical pulses and fast delay scanning. Two different AOPDF, the High-Resolution (HR) and Wide-Band (WB), have been used in this study. They are based on the same concept, but have different working parameters, reported in Table 1. In particular, the WB model has a higher repetition rate, a higher diffraction efficiency, and a shorter delay range, making it better suited for the present application. The transmission efficiency of the AOPDF depends on many parameters such as the amount of dispersion added or pulse bandwidth, but ranges from 30% to 60%.

Table 1. Characteristics of the two AOPDF types. Both models consist of a 25-mm-long TeO_2 crystal, but the cut angle is different for each, to allow for different acoustic propagation speed. The repetition rate is the maximum rate at which successive acoustic wave can be sent inside the crystal. The range is the maximum delay allowed by the optical index difference between the fast and slow axis, the values are given for 800 nm light. The time ratio gives the amount of delay added per microsecond of acoustic propagation.

Model	Rep. rate (kHz)	Range (ps)	Ratio (fs/ µs)
HR	30.6	8.5	260
WB	40	3.5	161

4. Noise levels

The laser system used in this study is shot noise limited for electronic frequencies around 20 MHz and average laser intensities at least up to 70 mW [23]. However, to investigate if the AOPDF introduces additional noise, we measure the laser noise in the presence of the AOPDF, at the detector plane, using 5 mW of average laser power and a commercial photodiode (Det10A, 350 MHz bandwidth, Thorlabs). The photodiode was loaded with a 50 Ω resistor and the resulting voltage was filtered with a 5.6 MHz high-pass filter (EF515, 6th order, Thorlabs). The purpose of this filter is to damp the repetition rate and harmonics of the AOPDF (Table 1). The filtered photodiode output was sent to a spectrum analyzer (HF2LI, Zurich instrument) and its electrical power spectral density was acquired between 8 MHz and 40 MHz (Fig. 2(a)).

The power spectral density associated with shot noise is estimated at -191 dB W Hz^{-1}, which is below the detection limit of our spectrum analyzer (-180 dB W Hz^{-1}). However, the laser

Optics EXPRESS

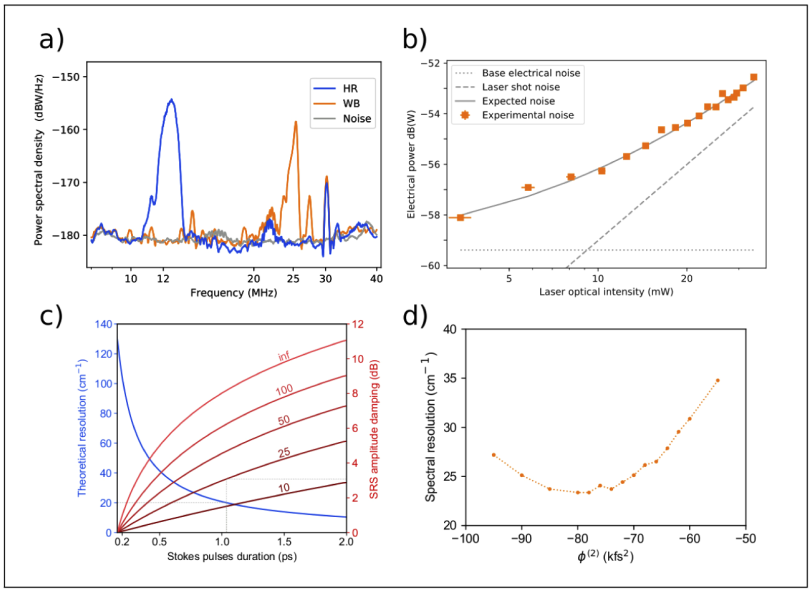

Fig. 2. a) Laser intensity noise for the HR and WB AOPDF. b) System output noise power compared to shot noise and electronic noise, for increasing laser power. c) SRS signal loss and resolution gain as a function of the chirped Stokes pulse duration. The different losses (red lines) corresponds to different linewidths for the probed molecular vibration, indicated in red in cm^{-1}. d) Achieved spectral resolution as a function of the dispersion (second order phase) applied using the AOPDF.

intensity noise introduced by the AOPDF was high enough to be measured without amplification. The laser intensity noise is particularly high around 12 MHz for the HR AOPDF, and around 25 MHz for the WB AOPDF. This point has not been addressed in previous studies, and may have limited the sensitivity of previous systems using these devices. It is suspected that the amplitude noise imprinted on the laser by the AOPDF results from the interference of successive acoustic waves by reflection and diffusion inside the crystal. The carrier frequency for the HR and WB crystals are around 86 MHz and 52.5 MHz respectively. Interactions of the light pulse with co-propagating and counter-propagating acoustic waves may result in optical modulation at double the carrier frequency. Combined with the repetition rate of the laser 80 MHz, this may result in optical modulation at $2 \times 86 - 2 \times 80 = 12$ MHz and $2 \times 52.5 - 80 = 25$ MHz for the HR and WB crystal respectively. To support this hypothesis we mitigated the spatio-temporal overlap of co-propagating and counter-propagating acoustic waves by adding 1 to 5 µs of delay between successive acoustic waves. This did not affect the diffraction efficiency by a significant amount but decreased the recorded noise level to a negligible amount. Although further investigation would be required to fully confirm the origin of the noise, its strong timing sensitivity strongly supports an interaction with counter-propagating acoustic waves, and a 3 µs delay was found enough to decrease the noise to a negligible level.

It is also possible to avoid the excess noise introduced by the AOPDF by selecting a suitable modulation frequency and lock-in bandwidth. Using the lock-in system described previously, with a modulation frequency of 20 MHz and a 1.35 MHz bandwidth, the measured noise from this system matches exactly the expected shot noise from the laser (Fig. 2(b)). For average laser intensities above 9 mW, detector electronic noise becomes negligible compared to the laser shot noise.

Optics EXPRESS

5. Resolution and signal level

Spectral focusing is used to recover spectral resolution when performing SRS with two femtosecond pulses, as illustrated in Fig. 1(b). The spectral resolution that can be achieved using spectral focusing is only a function of the dispersion added to the optical pulses (Fig. 2(c)), and can be improved to less than 5 cm^{-1} with pulses stretched to more than 5 ps. While high spectral resolution may be required for specific applications or in the Raman fingerprint region, the spectral features of interest in dilute samples such as biological tissues that are typically larger than 20 cm^{-1} in the C-H region. Any excessive dispersion does not contribute to significantly improve the resolution of those features, but greatly diminish the amplitude of the SRS signal. As shown in Fig. 2(c), the damping of the SRS signal increases significantly with higher resolution, and a trade-off needs to be made between resolution and signal power. The associated mathematical derivations can be found in the work of Su and collaborators [24].

To optimize the signal/resolution trade-off when imaging biological sample, both pump and Stokes pulses were chirped to 1 ps, by adding negative dispersion with the AOPDF and grating pair, respectively. Such pulse dispersion corresponds to a theoretical value of 22 cm^{-1} for the SRS spectral resolution, and a 3 dB drop in SRS signal assuming sample linewidths of 25 cm^{-1} (Fig. 2(c)).

The AOPDF working range (Table 1) sets the limit on how much dispersion and dispersion can be applied with the device. The acoustic wave needs to be fully formed inside the crystal to achieve the expected resolution, and then propagate to apply the expected delay. As a result, when using the AOPDF for both dispersion and delay, the maximum duration of the pulse allowed by the device is around half of its working range.

The resolution of the spectral measurement was quantified using the Raman line of DMSO at 2913 cm^{-1} (Fig. 2(d)). The amount of dispersion applied on the Stokes pulse with the grating pair was fixed to achieve a 1 ps pulse at the sample plane, measured with an optical autocorrelator (pulseCheck, APE). The amount of added second order phase imprinted on the pump pulse by the AOPDF was optimized (Fig. 2(d)) to match that of the pump pulse, and a resolution of 23 cm^{-1} was achieved. The resulting total negative dispersion is consistent with the optics in the system. The −77 kfs2 second order phase added by the AOPDF includes the −59 kfs2 required to negatively chirp the pulses at the sample plane, the −13 kfs2 required to compensate the dispersion introduced by the AOPDF crystal, and the −5 kfs2 compensating the rest of the optics on the optical path. Higher order dispersion on the pump pulse can be controlled with the AOPDF as well, but the optimal values found were similar to the factory settings for compensating the dispersion inside the AOPDF crystal. We suspect that the 1 cm^{-1} discrepancy between theoretical and experimental resolution may instead be due to the third order dispersion on the Stokes pulse coming from the AOM, grating pair, and lenses.

6. Chemical imaging of multiple species

Figure 3(a) shows the SRS spectra acquired for 5 pure species: melamine (Resin, bead 5um), polystyrene (PS, bead 20um), polymethylmethacrylate (PMMA, bead 10um), bovine serum albumin (BSA) crystals an olive oil solution. An artificial sample composed of these 5 species was prepared and imaged using the WB AOPDF using a pixel dwell time of 25 µs that allowed to record the full Raman spectrum between 2850 cm^{-1} and 3000 cm^{-1} with a resolution ≈23 cm^{-1}. The recorded hyperspectral image was projected over the known pure spectra using linear decomposition that allowed to map the 5 species (Fig. 3(b)). The different components are easily distinguishable without further averaging.

Optics EXPRESS

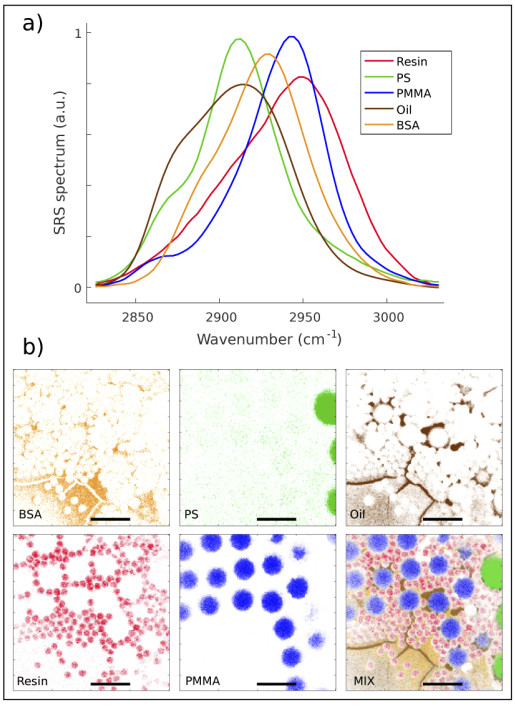

Fig. 3. a) SRS spectra of pure species acquired with the AOPDF delay line (Resin: melamine, PS: polystyrene, PMMA: polymethylmethacrylate, Oil: olive oil, BSA: bovine serum albumin). b) Image components associated with each pure species, as extracted from the hyperspectral image. MIX represents the summed image of all components. Pixel dwell time 25 µs, scale bar: 25 µm, total image acquisition time: 1s

7. Dynamic imaging of chemical reactions

We use here our fast SRS imaging platform to monitor the dynamic of chemical reactions. We concentrate on Mannitol, a common excipient used in pharmaceutical industry, that can crystallize in several polymorphic forms: α, β, and δ. The δ polymorph can change into β upon hydration, and both forms can be identified through their Raman spectra in the lipid band. Understanding how a pharmaceutical compound evolves after ingestion (change in pH and hydration) is key for proper drug delivery. Additionally, the signal levels obtained on Mannitol crystals are comparable to that of lipids in biological samples. The polymorphism of Mannitol is therefore a convenient proxy to the study lipid metabolism, while providing more experimental control than an *in vivo* experiment.

Pure δ-Mannitol crystals were prepared between a microscope slide and a coverslip and imaged over twenty minutes during the introduction of water vapor. Snapshots of the user interface during the acquisition are displayed in Fig. 4.(a-d), while the full video recording is available (Visualization 1). Another example is shown in Visualization 2. δ-Mannitol (red) transforms in β-Mannitol (blue) over time upon water hydratation. We used the HR AOPDF with a frame rate of 1 image every 1.6 second (two successive images were averaged to increase the signal to noise ratio). The hyperspectral images were processed on the fly by projecting them on the components corresponding to pure β and δ-Mannitol (Fig. 4.e), therefore providing live feedback on the crystal transformation process. Because of the dynamic nature of the process, image

Optics EXPRESS

refocusing and tracking of the relevant feature was necessary, and was made possible with live two color rendering.

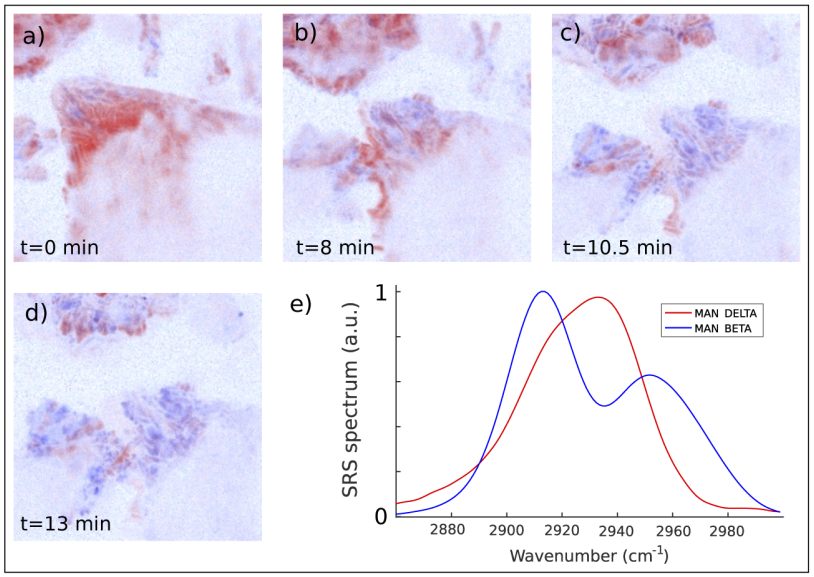

Fig. 4. a)-d) Timelapse of a δ-Mannitol (red) crystal transforming into β-Mannitol (blue) in the contact of water vapour. The field of view is 100 micron large, pixel dwell time 40 µs, e) SRS spectra of pure δ-Mannitol (red) and β-Mannitol (blue).

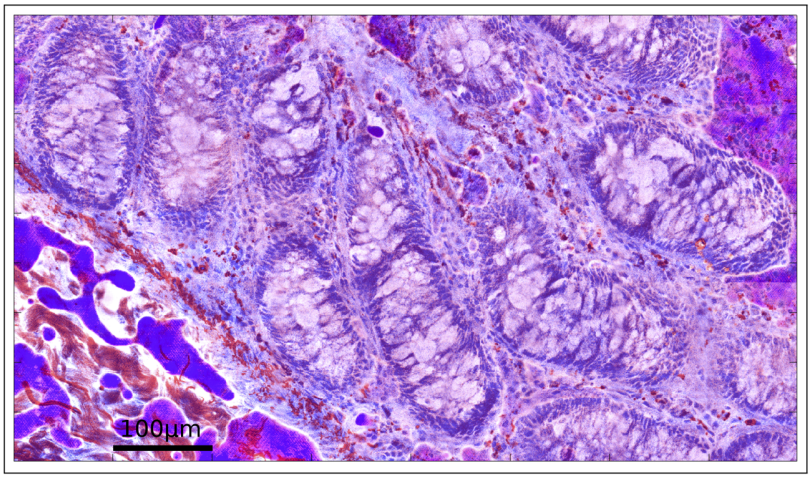

Fig. 5. Frozen section of healthy human colon imaged using fast SRS and SHG. The spatial map of proteins (blue) and lipids (pink), were retrieved using the spectra of BSA and Oil for projection. The SHG signal, characteristic of collagen fibers is shown in red. Image total acquisition time 15 minutes.

Optics EXPRESS

8. Label-free histological recordings

Fast label free imaging of biopsy sections is a major application of coherent Raman imaging that can potentially revolutionize the field of histology by increasing diagnosis speed, lowering hospital costs, and improving patient care [25]. Frozen sections of human cancer colon tissues were imaged with our fast SRS imaging platform, using the WB AOPDF with a pixel time of 25 µs. 8 by 10 adjacent fields of views (100 µm x 100 µm) were acquired separately and stitched together to reconstruct a wider image (Fig. 5). The total acquisition time was 15 minutes. Second harmonic generation at 400 nm was recorded in the epi direction, to provide an additional contrast mechanism specific to collagen fibers. As previously for each pixel, the recorded hyperspectral images were projected on the spectra corresponding to pure BSA (protein) and oil (lipid) to highlight the nuclei and cell bodies, respectively. For rendering look up tables were adjusted to mimic eosin, saffron and haematoxylin staining [26–28].

9. Discussion

Our SRS imaging platform acquires a full vibrational spectra over the [2850 cm^{-1}, 3050 cm^{-1}] spectral range in 12.5 µs, this corresponds to the time during which the chirped pump and Stokes pulses overlapped, while the pump pulse delay is swept by the AOPDF. However the minimum total time per pixel is 25 µs when using the WB AOPDF corresponding to a duty cycle of 50 percent. This figure could be increased by designing a shorter AODPF delay line optimized for lower delay range and higher repetition rate. Using a crystal of only half of the WB crystal length would satisfy both requirements. By applying the second order dispersion with a grating pair, and using the AOPDF solely as a delay line, a 80 kHz pixel acquisition rate should be achievable while maintaining a linear delay sweep. Although such AOPDF hasn't been manufactured, for lack of market application so far, there is not technological barrier to achieving such repetition rate.

The spectral window covered by the system is 200 cm^{-1}, limited by the spectral of the pulses used, which is sufficient to record most of the C-H stretch region. Larger bandwidth could be used by using shorter pulses. We expect the lower limit would be pulses of around 50 µs (at 800 nm). This limit would be set by the difficulty in maintaining phase control and beam wave-front with the dispersive optics used, including the AOPDF, but also the AOM, gratings, and lenses. This limitation is common to most spectral focusing schemes.

Imaging biological tissues (Fig. 5), image-wise averaging had to be performed to achieve signal to noise ratios (SNR) compatible with imaging (SNR > 3 dB). With our shot noise limited system, the SNR achieved on this sample without averaging (pixel dwell time 25 µs) is on the order of 1, corresponding to an associated SRS modulation. $\Delta I/I \approx 2 \times 10^{-5}$.

We limited our investigation to the lipid band but the proposed approach can be easily extended to the fingerprint spectral range using appropriate AOPDF and large bandwidth tunable fs sources. While covering the full fingerprint region using spectral focusing would not be possible due to the dispersive limit detailed above, a window of several hundreds of wave-numbers can still be covered. The narrower features in the fingerprint region would call for pulses dispersed to two or more picosecond. The HR crystal can readily be used for such dispersion and delay scanning. The smaller Raman cross section may limit the acquisition speed significantly, in which case higher Raman signal must be achieved.

This higher signal could be obtained by red-shifting the SRS pump and Stokes wavelength. Using near-infrared light such as 940 nm pump and 1310 nm Stokes, one may significantly increase the average laser power on the sample, while keeping photo-damage low. Such near-IR scheme would allow for an increase of both laser powers by a factor of 2 to 3, which would be sufficient to improve the SNR by a factor of 10, therefore allowing for single SRS spectral measurements per pixel, even on dilute samples or in the Raman fingerprint.

Optics EXPRESS

Other improvements may include the use of spatial multiplexing, provided higher laser powers are available. Using multiple foci has been demonstrated as a method to scale up the acquisition rate [29] in SRS. Another possible strategy would be to use our fast spectral acquisition scheme while under-sampling the image through matrix completion scheme [30]. The amount of data generated by hyperspectral Coherent Raman microscopy can be large, with several hundreds of megabytes per second. The linear delay sweep allowed by the AOPDF simplifies greatly the data processing, which can easily be performed on the fly.

10. Conclusion

We demonstrated fast hyperspectral SRS imaging by combining spectral focusing with an acousto-optic delay line working at 40 kHz. Our system is at the shot noise level for 15 mW of laser probe power, and a bandwidth of 1.3 MHz. The achieved resolution is 23 cm^{-1} over a bandwidth of 130 cm^{-1} full width at half maximum. SRS spectra in the lipid band were acquired with 12.5 µs recordings per pixel corresponding to a duty cycle of 50 percent. Samples containing up to 5 different chemical species have been imaged, and individual component maps were retrieved with no visible cross-talk. Time-resolved imaging of a chemical transformation (δ-Mannitol to β-Mannitol) was made possible, opening the door to other studies requiring fast chemical imaging. Finally, the sensitivity of the system was sufficient to perform stimulated Raman imaging of human frozen tissue sections, demonstrating the applicability of this measurement system for label-free and live histology.

Funding

Agence Nationale de la Recherche (ANR- 10-INSB-04-01, ANR-11-INSB-0006); Institut National de la Santé et de la Recherche Médicale (18CP128-00, PC201508); Aix-Marseille Université (A-M-AAP-ID-17-13-170228-15.22-RIGNEAULT, ANR-11-IDEX-0001-02).

Acknowledgments

The authors thank Barbara Sarri (Institut Fresnel) and Flora Poizat (Institut Paoli-Calmettes) for providing and helping with the frozen tissue sections.

Disclosures

Nicolas Forget has financial interest in FASTLITE.

References

1. N. Bloembergen, "The stimulated Raman effect," Am. J. Phys. **35**(11), 989–1023 (1967).
2. J. X. Cheng and X. S. Xie, "Vibrational spectroscopic imaging of living systems: An emerging platform for biology and medicine," Science **350**(6264), aaa8870 (2015).
3. C. Zhang and J. X. Cheng, "Perspective: Coherent Raman scattering microscopy, the future is bright," APL Photonics **3**(9), 090901 (2018).
4. H. Rigneault and P. Berto, "Tutorial: Coherent Raman light matter interaction processes," APL Photonics **3**(9), 091101 (2018).
5. C. W. Freudiger, W. Min, G. B. Saar, S. Lu, G. R. Holtom, C. He, J. C. Tsai, J. X. Kang, and X. S. Xie, "Label-Free Biomedical Imaging with High Sensitivity by Stimulated Raman Scattering Microscopy," Science **322**(5909), 1857–1861 (2008).
6. P. Nandakumar, A. Kovalev, and A. Volkmer, "Vibrational imaging based on stimulated Raman scattering microscopy," New J. Phys. **11**(3), 033026 (2009).
7. B. G. Saar, C. W. Freudiger, J. Reichman, C. M. Stanley, G. R. Holtom, and X. S. Xie, "Video-Rate Molecular Imaging in Vivo with Stimulated Raman Scattering," Science **330**(6009), 1368–1370 (2010).
8. K. Seto, Y. Okuda, E. Tokunaga, and T. Kobayashi, "Development of a multiplex stimulated raman microscope for spectral imaging through multi-channel lock-in detection," Rev. Sci. Instrum. **84**(8), 083705 (2013).
9. W. Rock, M. Bonn, and S. H. Parekh, "Near shot-noise limited hyperspectral stimulated Raman scattering spectroscopy using low energy lasers and a fast CMOS array," Opt. Express **21**(13), 15113 (2013).

Optics EXPRESS

10. C. S. Liao, M. N. Slipchenko, P. Wang, J. Li, S. Y. Lee, R. A. Oglesbee, and J. X. Cheng, "Microsecond scale vibrational spectroscopic imaging by multiplex stimulated Raman scattering microscopy," Light: Sci. Appl. **4**(3), e265 (2015).
11. C.-S. Liao and J.-X. Cheng, "In Situ and In Vivo Molecular Analysis by Coherent Raman Scattering Microscopy," Annu. Rev. Anal. Chem. **9**(1), 69–93 (2016).
12. R. He, H. Ma, M. Ji, Y. Xu, W. Huang, Z. Liu, R. He, W. Huang, Y. Xu, and Z. Liu, "Stimulated Raman scattering microscopy and spectroscopy with a rapid scanning optical delay line," Opt. Lett. **42**(4), 659–662 (2017).
13. V. Kumar, A. De La Cadena, A. Perri, F. Preda, N. Coluccelli, G. Cerullo, and D. Polli, "Invited Article: Complex vibrational susceptibility by interferometric Fourier transform stimulated Raman scattering," APL Photonics **3**(9), 092403 (2018).
14. B. Figueroa, W. Fu, T. Nguyen, K. Shin, B. Manifold, F. Wise, and D. Fu, "Broadband hyperspectral stimulated raman scattering microscopy with a parabolic fiber amplifier source," Biomed. Opt. Express **9**(12), 6116–6131 (2018).
15. A. Ragni, G. Sciortino, M. Sampietro, G. Ferrari, and D. Polli, "Multi-channel lock-in based differential front-end for broadband raman spectroscopy," Integration **67**, 44–49 (2019).
16. Y. Ozeki, T. Asai, J. Shou, and H. Yoshimi, "Multicolor stimulated raman scattering microscopy with fast wavelength-tunable yb fiber laser," IEEE J. Sel. Top. Quantum Electron. **25**(1), 1–11 (2019).
17. E. Gershgoren, R. Bartels, J. Fourkas, R. Tobey, M. Murnane, and H. Kapteyn, "Simplified setup for high-resolution spectroscopy that uses ultrashort pulses," Opt. Lett. **28**(5), 361–363 (2003).
18. T. Hellerer, A. M. Enejder, and A. Zumbusch, "Spectral focusing: High spectral resolution spectroscopy with broad-bandwidth laser pulses," Appl. Phys. Lett. **85**(1), 25–27 (2004).
19. B. Urbanek, R. Huber, C. Lange, M. Möller, M. Eisele, D. Kaplan, and S. Baierl, "Femtosecond terahertz time-domain spectroscopy at 36 kHz scan rate using an acousto-optic delay," Appl. Phys. Lett. **108**(12), 121101 (2016).
20. X. Audier, N. Balla, and H. Rigneault, "Pump-probe micro-spectroscopy by means of an ultra-fast acousto-optics delay line," Opt. Lett. **42**(2), 294 (2017).
21. M. S. Alshaykh, C.-S. Liao, O. E. Sandoval, G. Gitzinger, N. Forget, D. E. Leaird, J.-X. Cheng, and A. M. Weiner, "High-speed stimulated hyperspectral raman imaging using rapid acousto-optic delay lines," Opt. Lett. **42**(8), 1548–1551 (2017).
22. F. Verluise, V. Laude, J.-P. Huignard, P. Tournois, and A. Migus, "Arbitrary dispersion control of ultrashort optical pulses with acoustic waves," J. Opt. Soc. Am. B **17**(1), 138–145 (2000).
23. X. Audier, S. Heuke, P. Volz, I. Rimke, and H. Rigneault, "Noise in stimulated raman scattering measurement: From basics to practice," APL Photonics **5**(1), 011101 (2020).
24. J. Su, R. Xie, C. K. Johnson, and R. Hui, "Single-fiber-laser-based wavelength tunable excitation for coherent Raman spectroscopy," J. Opt. Soc. Am. B **30**(6), 1671 (2013).
25. M. T. Cicerone and C. H. Camp, "Histological coherent Raman imaging: A prognostic review," Analyst **143**(1), 33–59 (2018).
26. D. A. Orringer, B. Pandian, Y. S. Niknafs, T. C. Hollon, J. Boyle, S. Lewis, M. Garrard, S. L. Hervey-Jumper, H. J. L. Garton, C. O. Maher, J. A. Heth, O. Sagher, D. A. Wilkinson, M. Snuderl, S. Venneti, S. H. Ramkissoon, K. A. McFadden, A. Fisher-Hubbard, A. P. Lieberman, T. D. Johnson, X. S. Xie, J. K. Trautman, C. W. Freudiger, and S. Camelo-Piragua, "Rapid intraoperative histology of unprocessed surgical specimens via fibre-laser-based stimulated raman scattering microscopy," Nat. Biomed. Eng. **1**(2), 0027 (2017).
27. B. Sarri, R. Canonge, X. Audier, E. Simon, J. Wojak, F. Caillol, C. Cador, D. Marguet, F. Poizat, M. Giovannini, and H. Rigneault, "Fast stimulated raman and second harmonic generation imaging for intraoperative gastro-intestinal cancer detection," Sci. Rep. **9**(1), 10052 (2019).
28. B. Sarri, F. Poizat, S. Heuke, J. Wojak, F. Franchi, F. Caillol, M. Giovannini, and H. Rigneault, "Stimulated raman histology: one to one comparison with standard hematoxylin and eosin staining," Biomed. Opt. Express **10**(10), 5378 (2019).
29. H. Rigneault, X. Audier, S. Heuke, B. Sarri, and A. Lombardini, "Dual-focus stimulated Raman scattering microscopy: a concept for multi-focus scaling," Opt. Lett. **43**(19), 4763 (2018).
30. H. Lin, C. S. Liao, P. Wang, N. Kong, and J. X. Cheng, "Spectroscopic stimulated Raman scattering imaging of highly dynamic specimens through matrix completion," Light: Sci. Appl. **7**(5), 17179 (2018).

Chapitre 4

Sources ultra-brèves de 3^{e} génération

4.1 Introduction

A partir de 2012, j'ai orienté ma thématique de recherche principale vers un sujet proche de celui de ma thèse : l'amplification paramétrique optique à dérive de fréquence (OPCPA, pour Optical Parametric Chirped-Pulse Amplification). Ce regain d'intérêt tient à l'essor extraordinaire des lasers Ytterbium :YAG picosecondes de forte puissance moyenne (jusqu'à quelques kW). Bien qu'initialement développés pour l'industrie, ces lasers trouvent aujourd'hui des applications multiples. Leur usage scientifique requiert, le plus souvent, d'augmenter leur puissance crête soit par un mécanisme de post-compression dans les gaz ou les solides, soit par OPCPA. L'OPCPA permet, en outre, de convertir ces lasers de « pompe » en sources infrarouges stables en CEP. A l'heure actuelle, les OPCPA infrarouges entre $\simeq$1.5 et $\simeq$3.2 µm sont devenus les principaux « drivers » pour la génération de rayonnements X-UV intenses par génération d'harmoniques élevées dans les gaz. Les OPCPAs sont également utilisés comme préamplificateurs à haut contraste pour les chaînes laser de très forte intensité (systèmes 100 TW voire pétawatt).

Il est intéressant de comparer les situations de 2002, quand j'ai commencé ma thèse, avec celle de 2012. Les OPCPAs avaient déjà été identifiés à la fin des années 90 [64,65] comme une alternative intéressante à l'amplification laser en bande large. Parmi les avantages cités : des bandes de gain extrêmement larges dans certaines configurations (accords de phase « magiques » dans BBO, LBO ou KDP par exemple), une faible charge thermique, la possibilité de multiplexer plusieurs lasers de pompe et un contraste temporel élevé. La première génération d'OPCPA s'est ainsi appuyée sur les principaux lasers de puissance de l'époque : les lasers Nd:YAG de durée nanoseconde (1-10 ns typiquement à 1064 nm). Sans aller jusqu'à dire que cette première génération d'OPCPA a connu un échec, on peut tout de même pas crier à la réussite. Pourquoi ? Principalement à cause de la difficulté à synchroniser deux lasers indépendants (le laser de pompe et celui produisant les impulsions à amplifier, en général un Nd:YAG et un Ti ::Saphir) avec une gigue temporelle suffisamment faible - mais pas seulement. La structure spatio-temporelle complexe des lasers Nd:YAG à cavité instable n'est pas appropriée au pompage d'OPA (structure en balle de fusil). Le contraste d'injection de ces lasers n'est pas non plus suffisant pour ga-

rantir un fonctionnement réellement monomode (longitudinalement). Des lasers Nd:YAG adaptés ont été développés (amplificateurs régénératifs injectés par l'aile infrarouge d'un oscillateur Ti:Saphir par exemple) mais la complexité de l'ensemble reste décourageante et forme un système difficile à maintenir dans la durée. Les lasers Yb de durée picoseconde ou sub-picoseconde - et dans une moindre mesure les laser Erbium couplés à des fibres non linéaires - ont radicalement changé la donne. Il est désormais possible, avec un seul laser amplifié, d'injecter correctement un amplificateur de puissance tout en disposant de mécanismes robustes et cohérents d'élargissement spectral pour former les longueurs d'onde à amplifier. Le pompage diode des lasers Yb, leur compacité (liée à la forte fluence de saturation des milieux dopés Yb) et un investissement industriel massif ont permis des gains spectaculaires de stabilité et de robustesse. Enfin, les architectures d'amplification par « thin disks » et « slabs » ont décuplé la puissance moyenne des Yb:YAG.

Les OPCPAs de 2022 sont également assez différents de ceux de 2002 car le régime picoseconde a de multiples conséquences :

- le seuil de dommage en intensité des diélectriques variant avec l'inverse de la racine carrée de l'intensité de pompe [1], soit en $1/\sqrt{I_p}$, un OPA picoseconde peut travailler à des intensités beaucoup plus importantes qu'en régime nanoseconde : typiquement 50-100 GW/cm^2 tant que l'on peut ignorer l'absorption à deux photons, soit au moins un ordre de grandeur au dessus des intensités habituelles à 1-10 ns.
- le même gain paramétrique est atteint sur une longueur d'interaction beaucoup plus courte et l'épaisseur typique des cristaux non linéaires en régime picoseconde n'est que de quelques mm (vs des dizaines de mm en nanoseconde),
- la bande de gain des OPAs variant avec l'inverse des épaisseurs, la bande de gain en régime picoseconde est beaucoup plus large qu'en régime nanoseconde,
- les facteurs d'étirement et de compression sont réduits, si bien que des solutions d'étirement/compression par miroirs dispersifs ou par des matériaux massifs sont envisageables (en remplacement des étireurs/compresseurs à réseaux),
- la génération d'impulsions stables en CEP est également une conséquence indirecte de ce régime d'interaction.

L'originalité des OPCPA développés par Fastlite et des travaux de recherche que je développe ici tiennent en cinq points :

- un étirement et une gestion de la dispersion par un AOPDF,
- des cristaux de MgO:PPLN courts pompés à 1030 nm pour les OPAs à fort gain et à faible puissance/énergie,
- des cristaux massifs de $LiNbO_3$ pour les OPAs à faible gain et à forte puissance/énergie,
- une métrologie embarquée conséquente : mesures à 100 kHz, mesure de CEP...,
- une accordabilité en longueur d'onde, réalisée au moyen de l'AOPDF (pour l'adaptation de la dispersion), de PPLNs en géométrie fanout (bande de gain variable) et d'un compresseur large bande (un ensemble de miroirs dispersifs).

J'ai conduit différents programmes de recherche (FUI « STAR », Eurostars « CURE ») et participé à des collaborations qui ont aboutis à plusieurs publications [66–70] et brevets [71] dans le domaine. Le point d'orgue de ces travaux est la source MIR [70] d'ELI-

1. En régime ps-ns.

Cadre	Type	Nom	Date	Direction	Laboratoire
Thèse	CIFRE	Aymeric Van de Walle	2013-2016	Marc Hanna	LCF
Thèse	CIFRE	Gaëtan Jargot	2016-2019	Marc Hanna	LCF
Thèse	ITN Smart-X	Benjamin Maingot	2019-	Aurélie Jullien	InPhyNi
Stage	M2	Eric Chea	2013	Nicolas Forget	Fastlite
Stage	M1	Thibault Seyrat	2017	Nicolas Forget	Fastlite
Stage	2A/M1	Quang Anh Nguyen	2021	Nicolas Forget	Fastlite

TABLE 4.1 – Thèses co-encadrées et stage dirigés.

ALPS en Hongrie, aujourd'hui opérée comme serveur laser. Cette source est l'un des tous premiers OPCPAs à haute cadence (100 kHz) délivrant des impulsions courtes (40 fs) dans l'infrarouge (≃3.2 µm) et rassemblant quatre caractéristiques : une cadence élevée (100 kHz), une forte puissance moyenne (15 W à 3.2 µm, 200 W de pompe à 1030 nm), une stabilité extrême (en énergie, spectre et pointé) et une phase enveloppe-porteuse record (65 mrad rms). Ce système appartient aux sources ultra-brèves dites de 3ème génération : l'ensemble des caractéristiques de la source (longueur d'onde, durée, phase porteuse-enveloppe) est obtenu à partir d'un laser Ytterbium picoseconde à 1030 nm au moyen d'effets non linéaires (filamentation, différence de fréquence, diffraction acousto-optique, amplification paramétrique).

Des variantes de cette source ont ensuite été développées pour différents grands instruments et/ou serveurs lasers : RAL (UK), Max-Born Institute (Allemagne), Helmholtz-Zentrum Berlin (Allemagne), INRS (Canada), SPring-8 (Japon). Ces réalisations ont mobilisé toutes les équipes de développement de Fastlite et, en particulier, le groupe de R&D optique qui a grandi au fil du temps et dont j'assure encore le suivi : Raman Maksimenka, Alexandre Thai [2], Olivier Albert, Nicolas Thiré, Yoann Pertot, Simone Bux, Vincent Femy, Maxim Neradovskiy et Cyril Vaneph. Je ne peux pas ne pas mentionner ici le rôle clé de nos géniaux ingénieurs opto-mécaniques (Thomas Pinoteau, Clément Ferchaud [3]) et de l'équipe d'instrumentation (Sébastien Coudreau, Grégory Gitzinger [4], Simon Pomarède, José Villanueva, Ivan Jelicic, Didier Fousset). Le travail de recherche a porté sur la génération de continuum [72], les architectures d'amplification [68, 69], la gestion de la dispersion optique dans des systèmes accordables, les effets linéaires (absorption, thermique) et non-linéaires (effets Kerr, auto-modulation de phase, effets parasites) dans les étages d'amplification mais aussi la métrologie à cadence élevée [70]. C'est dans ce contexte que j'ai notamment co-encadré avec Marc Hanna (LCF, Palaiseau) les thèses d'Aymeric van de Walle et de Gaëtan Jargot. Je co-encadre actuellement, avec Aurélie Jullien (InPhyNi), la thèse de Benjamin Maingot qui cherche à établir l'origine du bruit de CEP dans les chaînes OPCPA.

2. Maintenant chez Amplitude
3. Maintenant à Imperial College
4. Maintenant chez HGH.

Type	Acronyme	Laboratoire/entreprise	Rôle	Date
Contrat FUI	STAR	Amplitude Technologies	PI	2015-2018
Contrat Eurostars	CURE	HZB, Ultrafast Innovations	PI	2019-2022
ITN	Smart-X	-	PI	2019-2022

TABLE 4.2 – Contrats et collaborations où j'ai pris une part active.

4.2 FUI STAR

Le FUI « STAR » porte sur la réalisation d'un prototype d'OPCPA à 800 nm délivrant des impulsions courtes (20 fs) à haut contraste temporel ($>10^{12}$) et de CEP stable. L'idée sous-jacente est de remplacer les systèmes laser du type oscillateur + amplificateur régénératif. Le prototype se compose d'un laser de pompe (S-pulse HP2, Amplitude Systèmes, 550 fs, 1.6 mJ, 2 kHz à 1028 nm) et de 6 sous-modules : génération de super-continuum, différence de fréquences, génération de seconde harmonique, deuxième étage d'amplification, mise en forme spectrale et conjugaison de phase par AOPDF, troisième étage d'amplification, compression par matériaux et génération de seconde harmonique finale. Le prototype permet de générer environ des impulsions de 9 µJ à 780 nm. La largeur spectrale est de 63 nm et les impulsions ont pu être recomprimées à moins de 20 fs. En terme de stabilité, la sortie à 800 nm affichait 0.95% RMS de fluctuations pour une pompe 0.34% RMS de fluctuations (mesures à la photodiode sur quelques minutes). La CEP est mesurée après compression mais avant SHG sur la voie à $\simeq$1.6 µm. L'appareil de mesure est un f-2f colinéaire combiné à un spectromètre rapide. Les dérives jusqu'à 2 kHz sont compensées par une boucle en utilisant le module de contrôle CEP du Dazzler de la chaîne. Les variations de tir à tir sont de 80 mrad avec une mesure à 4 kHz (100 000 tirs). La figure 4.1 montre le contraste temporel mesuré après ré-amplification par un CPA Ti:Saphir (mesure réalisée par la société Amplitude). Un contraste $>10^{12}$ est atteint une cinquantaine de ps avant l'impulsion principale (cette mesure inclue la contribution de l'amplificateur régénératif). Le système OPCPA est aujourd'hui installé sur le laser 500 TW d'ELI-ALPS, le pilier hongrois de l'Extreme Light Infrastructure européen.

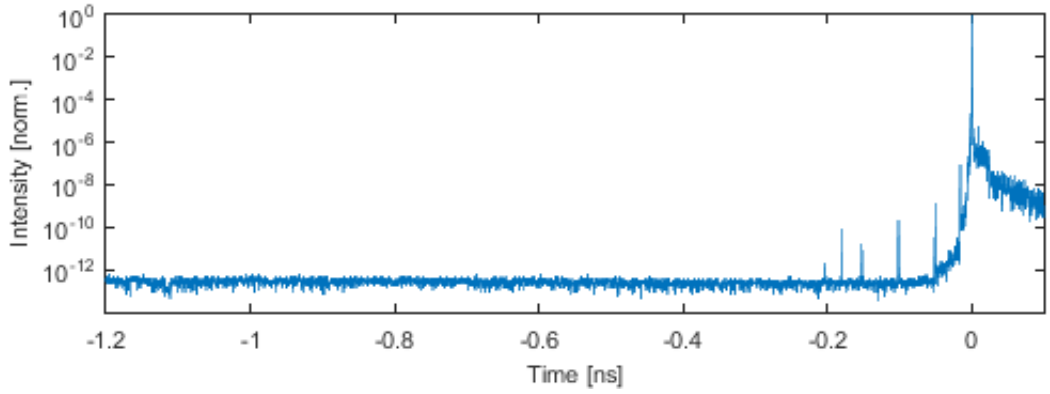

FIGURE 4.1 – Contraste de l'OPCPA mesuré après amplification (amplificateur régénératif Ti:Saphir). Source : Amplitude.

4.3 ELI-ALPS

Une autre étape importante été franchie avec le contrat de recherche et développement porté par ELI-ALPS. Les spécifications visées étaient : 100 kHz, 15 W, 40 fs, accordable entre 2.5 et 4 µm, stabilité CEP <150 mrad. Par rapport à l'état de l'art en 2018, cette source se distingue des précédentes par son laser de pompe Ytterbium (1 ps, 2 mJ à 100 kHz, soit une puissance moyenne de 200 W), sa puissance moyenne de sortie et une extrême stabilité (en énergie et en CEP). Techniquement elle se différentie par : (1) une génération de signal à $\simeq$3 µm par filamentation dans un cristal épais puis différence de fréquence, (2) une amplification dans des cristaux de MgO :PPLN courts (1 mm) et de grande ouverture (3 mm) en géométrie d'éventail (« fanout »), (3) une gestion de la dispersion par des matériaux massifs et (4) par un mécanisme de façonnage spectral et de contrôle de la CEP via un schéma « indirect » (ie avant la différence de fréquence). L'instrumentation développée spécifiquement pour cette source est également originale : mesure de la CEP à 10 kHz, caractérisation des fluctuations d'énergie à 100 kHz. A l'exception de l'accordabilité, l'ensemble des spécifications visées ont été atteintes.

Cette source est aujourd'hui opérée en serveur laser par ELI-ALPS. Elle est notamment utilisée dans le cadre de la génération d'harmoniques élevées dans le domaine X-UV. Ce projet de recherche de 3 ans a non seulement permis de valider l'approche des sources de troisième génération mais aussi démontré des valeurs record de stabilité phase-enveloppe. A titre personnel, elle est un exemple de développement que j'ai pu mener dans le cadre d'un grand instrument, avec les contraintes inhérentes à ce type d'environnement : planification, « reporting » mensuel, interfaces multiples et contexte international très compétitif

4.4 Simulations 3D

Afin de mieux appréhender certains des phénomènes observés dans les OPA/OPCPA comme les effets de cascade, j'ai débuté en 2020 à travailler sur un code de simulation 3D prenant en compte les effets non-linéaires d'ordres 2 et 3 sans connaissance *a priori* des processus majoritaires. Afin de disposer d'un outil de simulation adapté, un travail de recherche numérique a été entrepris. L'originalité de l'approche choisie repose sur les particularités suivantes :

- Code 3D (deux coordonnées spatiales, une coordonnée temporelle) ou 2D (avec symétrie cylindrique via une transformée de Hankel)
- Uniquement deux champs électriques, l'un pour la polarisation ordinaire et l'autre pour la polarisation extraordinaire : les ondes ne sont pas séparées en fonction de leurs porteuses optiques *a priori*
- Milieux de propagation généraux : tenseurs $\chi^{(1)}$, $\chi^{(2)}$ et $\chi^{(3)}$ génériques (absorption et anisotropie incluses). Tous les paramètres du matériau (orientation, température etc) sont contenus dans les éléments de tenseurs
- Modèle de propagation général : diffraction, dispersion, effets non-linéaires etc. Aucune hypothèses sinon celle d'une propagation paraxiale et celle des ondes co-propagatives

La première étape de ce travail de recherche a fait l'objet du stage de Nguyen Quang Anh

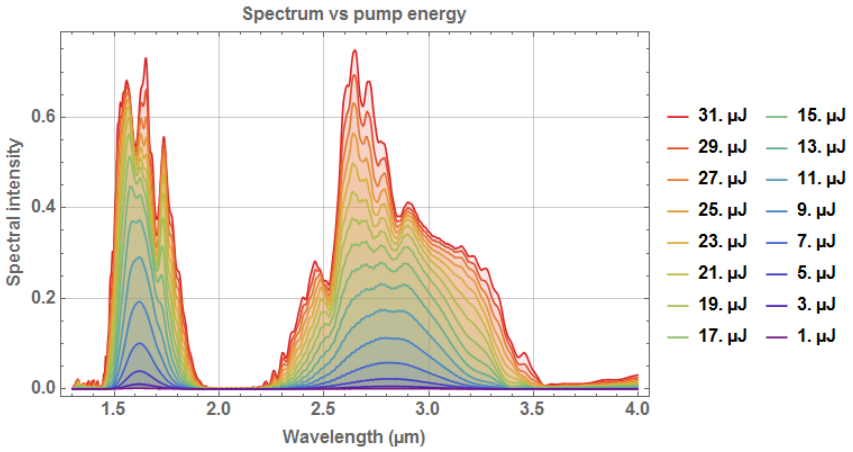

FIGURE 4.2 – Spectres signal et idler simulés dans un PPLN en fonction de l'énergie de pompe - géométrie colinéaire.

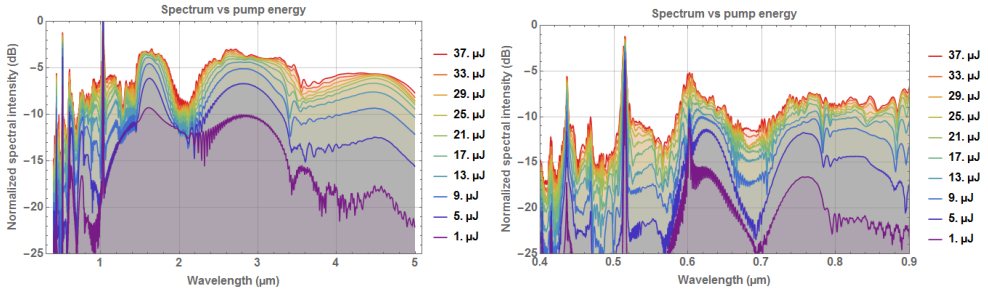

FIGURE 4.3 – Mêmes résultats présentés en échelle logarithmique. A gauche : partie visible. A droite : partie infrarouge.

(Ecole Polytechnique, stage 2A). Il s'agit d'un développement toujours en court. L'intérêt de ce type de simulation est de prendre en compte l'ensemble des effets non linéaires simultanément, ce qui est particulièrement important lorsque l'OPA est un cristal retourné périodiquement. Le quasi-accord de phase est paradoxalement moins sélectif qu'un accord de phase par biréfringence car plusieurs ordres de quasi-accord de phase sont possibles. Dans les OPA en PPLN pompés à 1030 nm par exemple, le quasi-accord de phase d'ordre 1 pour une amplification à $\simeq$1.7-1.8 µm correspond à un quasi-accord de phase d'ordre 3 pour une seconde harmonique à 1030 nm. Les phénomènes d'OPA et de SH se produisent donc simultanément, ce qui pose problème expérimentalement à cause des effets photo-réfractifs induits à 515 nm. En pratique, la structure du cristal autorise un grand nombre de combinaisons de longueurs d'onde qui sont difficiles à prévoir à l'avance - et d'autant plus en spectre large et/ou que le système est accordable en longueur d'onde. Ces effets de cascade sont illustrés en figure 4.2 (échelle linéaire) et figure 4.3 (échelle logarithmique sur une plage spectrale plus large) pour un PPLN de 1 mm d'épaisseur et de période 30.16 µm. L'effet principal d'amplification paramétrique à 1.5 µm s'accompagne d'une seconde harmonique parasite de la pompe mais aussi d'une troisième harmonique et d'une somme de fréquence pompe+signal etc. L'objectif de ce code de simulation est également de modéliser correctement l'automodulation de phase et la modulation de phase croisée dans les OPAs complexes.

4.5 Eurostars CURE

Une autre action de recherche, dédiée à la montée en énergie des OPCPA à ≃2 µm, a débuté en 2020 dans le cadre du programme de recherche franco-allemand CURE (Eurostars E113566, « Compact Ultrafast-X-ray-source REvolution »). Les objectifs du programme CURE et des trois partenaires (Fastlite, Helmholtz-Zentrum Berlin (HZB) et Ultrafast Innovations) sont de mettre au point : (i) un OPCPA capable de produire des impulsions à ≃2 µm de 1 mJ/20 fs à 50 kHz avec une stabilité en CEP inférieur à 250 mrad et (ii) une chambre de génération d'harmoniques élevées (HHG) produisant un rayonnement X-UV jusqu'à 500 eV. La conception globale de l'OPCPA 1mJ/20 fs/50 kHz, correspondant à une puissance moyenne délivrée de 50 W à ≃2 µm, a été entamée en 2020. L'OPCPA se compose des même briques technologiques que celles développées par Fastlite précédemment mais à des niveaux d'énergie et de puissance moyenne très supérieurs : une énergie 10 fois supérieure et une puissance moyenne 5 fois supérieure à ce qui a été obtenu à/par Fastlite précédemment. Ce changement d'échelle a nécessité de revisiter les composants, matériaux et architectures utilisées jusque-là.

La première phase du projet CURE a permis de reproduire et de confirmer la génération d'impulsions stables en CEP à 2 µm, avec une haute qualité (spatiale, spectrale) et une excellente stabilité court/long terme. CURE a permis d'augmenter l'énergie de 30 µJ (obtenus en 2019) à 100 µJ par impulsion (en 2020). Une amélioration très sensible de la stabilité en CEP a été observée après un filtrage spatial situé en amont de la DFG. Cet effet du profil spatial sur la stabilité en CEP n'a, à notre connaissance, jamais été rapportée.

La thèse de Benjamin Maingot, financée via l'ITN Smart-X et dirigée par Aurélie Jullien (InPhyNi) porte notamment sur ce sujet, et plus généralement sur l'origine du bruit de CEP dans les OPCPA. Les premiers résultats de son travail (soumis à Optics Letters en 2022) indiquent qu'une source probable est une perte partielle de cohérence lors de la génération de continuum. L'influence de la phase spatiale sur la génération de continuum et sur la stabilité de la CEP est en cours d'étude.

Research Article | Vol. 25, No. 2 | 23 Jan 2017 | OPTICS EXPRESS 1505

Optics EXPRESS

4-W, 100-kHz, few-cycle mid-infrared source with sub-100-mrad carrier-envelope phase noise

NICOLAS THIRÉ,[1,*] RAMAN MAKSIMENKA,[1] BÁLINT KISS,[2] CLÉMENT FERCHAUD,[1] PIERRE BIZOUARD,[1] ERIC CORMIER,[2] KÁROLY OSVAY,[2] AND NICOLAS FORGET[1]

[1]*Fastlite, 1900 route des Crêtes, Les Collines de Sophia, Bât. D1, 06560, Valbonne, France*
[2]*ELI-HU Non-Profit Ltd, Dugonics tér 1, 6720 Szeged, Hungary*
[*]*nicolas.thire@fastlite.com*

Abstract: We demonstrate an optical parametric chirped-pulse amplifier delivering 4-cycles (38-fs) pulses centered around 3.1 µm at 100-kHz repetition rate with an average power of 4 W and an undersampled single-shot carrier-envelope phase noise of 81 mrad recorded over 25 min. The amplifier is pumped by a ~1.1 ps, Yb-YAG, thin-disk regenerative amplifier and seeded with a supercontinuum generated in bulk YAG from the same pump pulses. Carrier-envelope phase stability is passively achieved through difference-frequency generation between pump and seed pulses. An additional active stabilization at 10 kHz combining 2f-to-f interferometry and a $LiNbO_3$ acousto-optic programmable dispersive filter achieves a record low phase noise.

OCIS codes: (320.7090) Ultrafast lasers; (190.4360) Nonlinear optics, devices; (190.4970) Parametric oscillators and amplifiers; (140.3070) Infrared and far-infrared lasers.

References and links

1. P. B. Corkum, "Plasma perspective on strong field multiphoton ionization," Phys. Rev. Lett. **71**(13), 1994–1997 (1993).
2. Ch. Spielmann, N. H. Burnett, S. Sartania, R. Koppitsch, M. Schnürer, C. Kan, M. Lenzner, P. Wobrauschek, and F. Krausz, "Generation of coherent X-rays in the water window using 5-femtosecond laser pulses," Science **278**(5338), 661–664 (1997).
3. E. J. Takahashi, T. Kanai, K. L. Ishikawa, Y. Nabekawa, and K. Midorikawa, "Coherent water window x ray by phase-matched high-order harmonic generation in neutral media," Phys. Rev. Lett. **101**(25), 253901 (2008).
4. T. Popmintchev, M.-C. Chen, D. Popmintchev, P. Arpin, S. Brown, S. Ališauskas, G. Andriukaitis, T. Balčiunas, O. D. Mücke, A. Pugzlys, A. Baltuška, B. Shim, S. E. Schrauth, A. Gaeta, C. Hernández-García, L. Plaja, A. Becker, A. Jaron-Becker, M. M. Murnane, and H. C. Kapteyn, "Bright coherent ultrahigh harmonics in the keV x-ray regime from mid-infrared femtosecond lasers," Science **336**(6086), 1287–1291 (2012).
5. M. Zürch, C. Kern, and C. Spielmann, "XUV coherent diffraction imaging in reflection geometry with low numerical aperture," Opt. Express **21**(18), 21131–21147 (2013).
6. H. Tomizawa, T. Sato, K. Ogawa, K. Togawa, T. Tanaka, T. Hara, M. Yabashi, H. Tanaka, T. Ishikawa, T. Togashi, S. Matsubara, Y. Okayasu, T. Watanabe, E. J. Takahashi, K. Midorikawa, M. Aoyama, K. Yamakawa, S. Owada, A. Iwasaki, and K. Yamanouchi, "Stabilization of a high-order harmonic generation seeded extreme ultraviolet free electron laser by time-synchronization control with electro-optic sampling," High Power Laser Sci. Eng. **3**, e14 (2015).
7. N. G. Johnson, O. Herrwerth, A. Wirth, S. De, I. Ben-Itzhak, M. Lezius, B. Bergues, M. F. Kling, A. Senftleben, C. D. Schröter, R. Moshammer, J. Ullrich, K. J. Betsch, R. R. Jones, A. M. Sayler, T. Rathje, K. Rühle, W. Müller, and G. G. Paulus, "Single-shot carrier-envelope-phase-tagged ion-momentum imaging of nonsequential double ionization of argon in intense 4-fs laser fields," Phys. Rev. A **83**(1), 013412 (2011).
8. A. D. Shiner, C. Trallero-Herrero, N. Kajumba, H.-C. Bandulet, D. Comtois, F. Légaré, M. Giguère, J.-C. Kieffer, P. B. Corkum, and D. M. Villeneuve, "Wavelength scaling of high harmonic generation efficiency," Phys. Rev. Lett. **103**(7), 073902 (2009).
9. B. M. Luther, K. M. Tracy, M. Gerrity, S. Brown, and A. T. Krummel, "2D IR spectroscopy at 100 kHz utilizing a Mid-IR OPCPA laser source," Opt. Express **24**(4), 4117–4127 (2016).
10. A. Thai, M. Hemmer, P. K. Bates, O. Chalus, and J. Biegert, "Sub-250-mrad, passively carrier-envelope-phase-stable mid-infrared OPCPA source at high repetition rate," Opt. Lett. **36**(19), 3918–3920 (2011).

#280369 http://dx.doi.org/10.1364/OE.25.001505
Journal © 2017 Received 11 Nov 2016; revised 13 Jan 2017; accepted 13 Jan 2017; published 19 Jan 2017

Optics EXPRESS

11. B. W. Mayer, C. R. Phillips, L. Gallmann, and U. Keller, "Mid-infrared pulse generation via achromatic quasi-phase-matched OPCPA," Opt. Express **22**(17), 20798–20808 (2014).
12. M. Baudisch, H. Pires, U. Elu, H. Ishizuki, T. Taira, and J. Biegert, "44 μJ, 160 kHz, few-cycle mid-IR OPCPA with chirp reversal," in Proceedings of CLEO OSA Technical Digest, paper STu3I.5 (2016).
13. B. W. Mayer, C. R. Phillips, L. Gallmann, M. M. Fejer, and U. Keller, "Sub-four-cycle laser pulses directly from a high-repetition-rate optical parametric chirped-pulse amplifier at 3.4 μm," Opt. Lett. **38**(21), 4265–4268 (2013).
14. M. Mero, F. Noack, F. Bach, V. Petrov, and M. J. J. Vrakking, "High-average-power, 50-fs parametric amplifier front-end at 1.55 μm," Opt. Express **23**(26), 33157–33163 (2015).
15. P. Rigaud, A. Van de Walle, M. Hanna, N. Forget, F. Guichard, Y. Zaouter, K. Guesmi, F. Druon, and P. Georges, "Supercontinuum-seeded few-cycle mid-infrared OPCPA system," Opt. Express **24**(23), 26494–26502 (2016).
16. H. Fattahi, H. G. Barros, M. Gorjan, T. Nubbemeyer, B. Alsaif, C. Y. Teisset, M. Schultze, S. Prinz, M. Haefner, M. Ueffing, A. Alismail, L. Vámos, A. Schwarz, O. Pronin, J. Brons, X. T. Geng, G. Arisholm, M. Ciappina, V. S. Yakovlev, D.-E. Kim, A. M. Azzeer, N. Karpowicz, D. Sutter, Z. Major, T. Metzger, and F. Krausz, "Third-generation femtosecond technology," Optica **1**(1), 45–63 (2014).
17. R. R. Alfano, *The supercontinuum laser source*, (Springer, 2016).
18. H. Fattahi, H. Wang, A. Alismail, G. Arisholm, V. Pervak, A. M. Azzeer, and F. Krausz, "Near-PHz-bandwidth, phase-stable continua generated from a Yb:YAG thin-disk amplifier," Opt. Express **24**(21), 24337–24346 (2016).
19. A. van de Walle, M. Hanna, F. Guichard, Y. Zaouter, A. Thai, N. Forget, and P. Georges, "Spectral and spatial full-bandwidth correlation analysis of bulk-generated supercontinuum in the mid-infrared," Opt. Lett. **40**(4), 673–676 (2015).
20. M. Bradler and E. Riedle, "Temporal and spectral correlations in bulk continua and improved use in transient spectroscopy," J. Opt. Soc. Am. B **31**(7), 1465–1475 (2014).
21. D. Majus and A. Dubietis, "Statistical properties of ultrafast supercontinuum generated by femtosecond Gaussian and Bessel beams: a comparative study," J. Opt. Soc. Am. B **30**(4), 994–999 (2013).
22. I. Gražulevičiūtė, M. Skeivytė, E. Keblytė, J. Galinis, G. Tamošauskas, and A. Dubietis, "Supercontinuum generation in YAG and sapphire with picosecond laser pulses," Lith. J. Phys. **55**(2), 110–116 (2015).
23. A.-L. Calendron, H. Çankaya, G. Cirmi, and F. X. Kärtner, "White-light generation with sub-ps pulses," Opt. Express **23**(11), 13866–13879 (2015).
24. A. Baltuska, M. Uiberacker, E. Goulielmakis, R. Kienberger, V. S. Yakovlev, T. Udem, T. W. Hansch, and F. Krausz, "Phase-controlled amplification of few-cycle laser pulses," IEEE J. Sel. Top. Quantum Electron. **9**(4), 972–989 (2003).
25. F. Lücking, V. Crozatier, N. Forget, A. Assion, and F. Krausz, "Approaching the limits of carrier-envelope phase stability in a millijoule-class amplifier," Opt. Lett. **39**(13), 3884–3887 (2014).
26. G. Gitzinger, V. Crozatier, R. Maksimenka, S. Grabielle, N. Forget, S. Alisauskas, A. Pugzlys, A. Baltuska, B. Monoszlai, C. Vicario, and C. P. Hauri, "Multi-octave acousto-optic spectrum analyzer for mid-infrared pulsed sources," in *CLEO: 2014*, paper STh1N.5, OSA Technical Digest (2014).
27. M. Baudisch, M. Hemmer, H. Pires, and J. Biegert, "Performance of MgO:PPLN, KTA, and $KNbO_3$ for mid-wave infrared broadband parametric amplification at high average power," Opt. Lett. **39**(20), 5802–5805 (2014).

1. Introduction

High-harmonic generation (HHG) [1] has become a routine technique to generate extreme-ultraviolet (XUV) radiation with full spatial and temporal coherence. The extension of HHG into the K-band water window (2.3 nm < λ < 4.4 nm) [2,3] and up to the keV photon energy regime [4] shows that fully coherent soft-x-ray beams/pulses could be produced from table-top ultrafast sources, promising probing and imaging [5] capabilities with unmatched tempo-spatial resolution. HHG sources have also been identified as potential seeders for free-electron lasers [6] to replace the current seeding schemes based on self-amplified spontaneous emission.

This extension towards XUV and up to soft-x-rays results from the recent development of driving sources with specific properties: mid-infrared wavelength, few-cycle pulses, high peak intensity, carrier-envelope phase stability and control, high energy and/or high-repetition rates. While long wavelength optical carriers extend the cutoff energy through the λ^2 dependency of the ponderomotive energy, shortening the pulses to few cycles increases the peak intensity and enhances the HHG conversion yield. Additionally, few-cycle pulses reduce the number of attosecond bursts up to, ideally, a single isolated attosecond pulse. In that case, CEP stability and control is paramount but also ensure a shot-to-shot reproducibility of the driving electric field as well as the HHG yield and spectra (especially for few-cycle pulses).

Optics EXPRESS

Besides, although phase-tagging [7] may be used for data post-processing, precise stabilization offers the unparalleled advantage of direct data averaging and/or heterodyning. Last, high pulse energy and/or repetition rate helps mitigating the λ^{-6}-λ^{-7} scaling law of the HHG yield [8] for an optimized XUV flux.

These requirements have triggered the development of a number of high-repetition-rate sources [9–15] combining nonlinear effects such as difference-frequency generation (DFG) and optical parametric amplification (OPA) to, respectively, generate and amplify broadband mid-infrared pulses within the 3-5 µm range. In both cases, energy is transferred, via local and instantaneous three-wave-mixing process, from a "pump" wave of angular frequency ω_p to a "signal" wave of angular frequency $\omega_s < \omega_p$. An "idler" wave at ω_i is generated as a by-product of parametric amplification to satisfy the energy conservation relationship $\hbar\omega_p = \hbar\omega_s + \hbar\omega_i$. For efficient operation when phase-matching conditions are fulfilled (momentum conservation), the phases of the three waves also satisfy φ_p-φ_s-$\varphi_i = \pi/2$. Finally, the Manley-Rowe relationship binds together the photon fluxes of the three waves and limits the maximum conversion yield from pump to signal wave to ω_s/ω_p. Therefore, it is clearly advantageous to pump OPAs with a pump wavelength as close as possible to the signal wavelength. The recent advent of scalable, picosecond, high-average-power infrared sources based on Yb:YAG has set these laser sources as the main work horses for broadband OPAs which are now described as "third-generation femtosecond technology" [16].

Previously demonstrated mid-IR DFG/OPA systems [9–15] differ in the characteristics of the pump laser (wavelength and pulse duration) but mostly in the way the signal and pump pulses are synchronized. Systems pumped by multi-ps (1-10 ps), 0.1-1 mJ pulses at repetition rates greater than 100 kHz are seeded by either optical parametric oscillators [9], or erbium-doped fiber-based femtosecond sources [10,11]. Although these solutions all lead to the generation of large optical spectra around either 1550 nm or 3 µm, they involve rather complex setups requiring active electronic locking of independent laser systems [9], or additional nonlinear effects to derive the pump seed from a signal oscillator [9–11]. In the latter case, the amplification process of the pump pulses introduces long optical delay which necessitates complex active stabilization to reduce delay jitter and drift between pump and signal pulses.

An alternative, which greatly simplifies the global architecture and provides robust passive optical synchronization between pump and seed pulses, is to use a small fraction of the pump laser energy to generate a supercontinuum (SC) via filamentation in a bulk material [17]. It is now well-known that, within the single-filament limit, the high- and low- frequency parts of a SC provide broadband, coherent [18] and stable [19–21] spectral content, even when driven by ~1 ps pulses at ~1 µm [22,23]. Additionally, the properties of the carrier-envelope phase of the SC essentially follow that of the pump pulse, a stupendous feature at the very heart of f-2f interferometry [24] and of the passive CEP-stabilization of idler pulses generated in self-seeded OPAs through a DFG process.

In this paper, we demonstrate and study a supercontinuum-seeded optical chirped-pulse parametric amplifier (OPCPA) generating few cycle pulses around 3.1 µm and optimized for CEP-stability. This source delivers 40-µJ, 40-fs pulses at 100 kHz repetition rate, which corresponds to a peak power of ~0.4 GW, an average power of 4 W and a pulse duration slightly under four optical cycles. Compared to former publications, and in particular to references [11,15], our source provides important novel features:

(i) It is the first 100-kHz-class OPCPA pumped with a diode-pumped solid-state laser delivering 1-ps pulses and self-seeded with an infrared supercontinuum generated in a bulk crystal,

(ii) Combines chirp-reversal with acousto-optic pulse shaping at 100 kHz and delivers, to date, the shortest pulses at this wavelength (3.1 µm) and average power (4W),

Optics EXPRESS

(iii) Achieves a non-averaged CEP stability with a phase noise as low as 81 mrad rms over more than $150 \cdot 10^6$ pulses (25 min at 100 kHz). To date this is the best recorded non-averaged CEP stability for an amplified system, independently of the wavelength, pulse duration or repetition rate [25].

2. Source description

The OPCPA is pumped by a fraction of an industrial Yb-YAG, thin-disk, regenerative amplifier (Dira-200 from TRUMPF Scientific Lasers) generating 2-mJ pulses at 1030 nm at the repetition rate of 100 kHz (average power of 200 W). The pulse duration at full-width half-maximum (FWHM) is 1.1 ps. The beam profile is close to Gaussian (measured $M^2<1.3$) and the typical pulse-to-pulse energy stability is <1% rms. About 55 W of pump power is used to pump the OPCPA in its current configuration (Fig. 1). The remaining 145 W is saved for a future upgrade of the system.

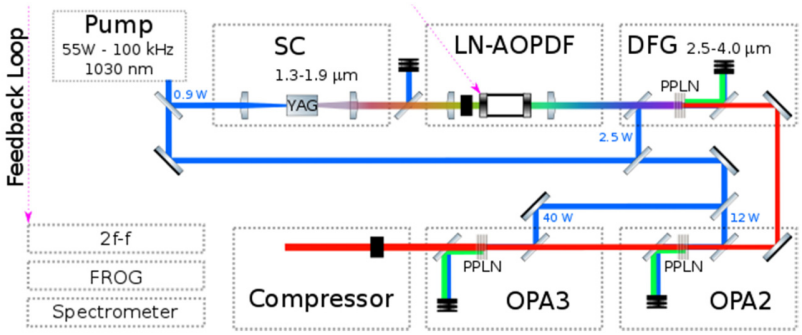

Fig. 1. Optical setup. SC: supercontinuum generation. DFG: difference-frequency generation. OPA: optical parametric amplifier. LN-AOPDF: $LiNbO_3$ acousto-optic programmable dispersive filter.

A small fraction (9 µJ) of the pump energy is used to generate a supercontinuum in a 10-mm YAG crystal mounted on a continuously moving translation stage. The crystal is translated transversally along a single direction, over 3 mm with a period of 10 min. A stable single-filament is formed in the bulk of the crystal and maintained for months without any visible permanent damage. A noticeable temperature elevation of the crystal is observed and stabilized around 10°C above ambient temperature by passive cooling. Filament instabilities and spectral modulation are noted above 12 µJ pump energy and immediate damage is observed for pump energies exceeding 14 µJ. These observations are in agreement with the previously reported data for both the SC threshold and nonlinear absorption of YAG [22,23]. At the output of the filament, the SC spectrum extends to ~2 µm (Fig. 2).

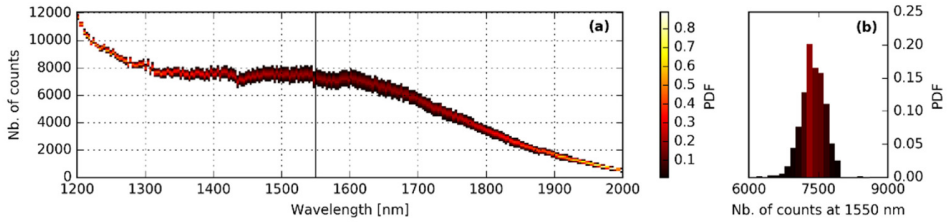

Fig. 2. (a) Supercontinuum spectra (red part) recorded by an InGaAs spectrometer (NIRQuest-2.5, Ocean Optics) with an integration time of 1 ms. Shown here is the probability density function (PDF) computed from 1000 successive acquisitions. (b) Cut at 1550 nm of the PDF showing a histogram with 5.7% rms.

Optics EXPRESS

The infrared part of the SC is filtered and temporally stretched by an AR-coated, 18-mm-long Silicon rod and a Lithium Niobate ($LiNbO_3$) acousto-optic programmable dispersive filter (LN-AOPDF, Fastlite), specifically developed for this application. Compared to TeO_2-based AOPDFs, LN-AOPDFs are capable of refresh rates exceeding 100 kHz and have large angular acceptance (~6°) and ultra-low spatial walk-off. This device is at the heart of the spectral/dispersion management and performs: phase shaping of the SC pulses to match the pump pulse duration; bandwidth selection and amplitude shaping of the SC spectrum; pre-compensation of the high-order spectral phase introduced by the optics; and last but not least, active CEP stabilization with a feedback from a 2f-to-f interferometer.

Shaped seed pulses are focused in a 12x3x1-mm^3 MgO-doped periodically poled Lithium Niobate crystal (MgO-PPLN) AR-coated at 1030 nm and from 1.3 to 4.2 µm. The crystal is heated to 120°C to limit photorefractive effects. The poling period varies across the 12-mm direction (so-called "fanout" poling geometry) to fulfill type-0 quasi-phase-matching conditions from 1.3 µm to 1.9 µm (for the signal) and 2.5 µm to 4.0 µm (for the idler). The MgO-PPLN of the DFG stage is pumped with 2.5 W (25 µJ) at 1030 nm and the calculated peak intensity is ~50 GW/cm^2 (3D Gaussian). Pump, signal and/or idler beams are combined and separated before and after the MgO-PPLN by pairs of dichroic mirrors. The spectrum of CEP-stable idler pulses produced by DFG is optimally centered at 3.1 µm and extends from 2.7 µm to 3.6 µm. The FWHM spectral bandwidth is 0.44 µm and the pulse energy is 0.9 µJ.

The generated mid-infrared pulses are successively amplified in two travelling-wave OPA stages (OPA2 and OPA3 on Fig. 1). Both stages use MgO-PPLN crystals as nonlinear medium and crystals are identical to the one of the DFG stage but for the thickness of the poled area: 0.5 mm for OPA2 and 0.7 mm for OPA3, instead of 1 mm for DFG. The pump power (and calculated peak intensity) in OPA2 and OPA3 is respectively 12.5 W (~35 GW/cm^2) and 40 W (~25 GW/cm^2). The output power at 3.1 µm, measured behind the dichroic mirrors, is respectively 0.8 W and 4 W. The output spectrum is measured by a scanning acousto-optic spectrum analyzer (Mozza, Fastlite) [26]. Figure 3(a) shows the output spectra after DFG (FWHM = 503 nm, 4σ = 706 nm), OPA2 (FWHM = 455 nm, 4σ = 681 nm) and OPA3 (FWHM = 480 nm, 4σ = 651 nm). The conversion efficiency, calculated as $(P_{s,out} - P_{s,in} + P_{i,out})/P_{p,in}$ where $P_{s,in}$, $P_{s,out}$,$P_{i,out}$,$P_{p,in}$ are the average powers of, respectively, output signal, input signal, output idler and input pump beams is ~17% for OPA2 and ~24% for OPA3. This calculation does not take into account the optical losses on the faces of the MgO-PPLN crystals, the losses on the dichroic mirrors (4 interfaces) and the parasitic effects in the nonlinear crystals (non-phase-matched SHG at the pump wavelength for example). The pump-to-idler conversion efficiency thus reads 6.4% for OPA2 and 10% for OPA3. The overall efficiency to generate 3.1 µm is 4W/55W = 7.2%.

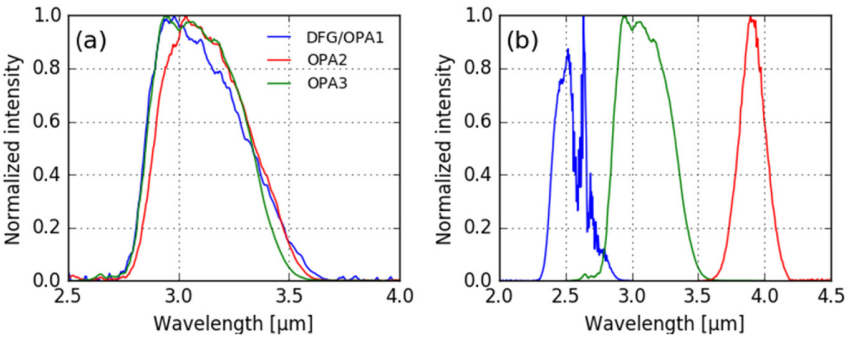

Fig. 3. (a) Spectra after DFG (blue), OPA2 (red) and OPA3 (green). (b) Output spectra at 2.5 µm (blue), 3.1 µm (green) and 3.9 µm (red) obtained by adjusting AOPDF settings, delays and PPLN period of the different stages.

Optics EXPRESS

The output beam is expanded by a reflective telescope and compressed in a set of AR-coated silicon flats corresponding to a total thickness of 14 mm.

3. Dispersion management and tunability

Durations of pump and signal pulses are simultaneously matched in all OPAs by means of the AOPDF and by combining materials having positive (Silicon) and negative (CaF_2) group velocity dispersions (GVD) in the 2.5-4 µm range. The thicknesses of the optics (dichroic mirrors, lenses…) were selected to achieve a near perfect GVD balance at 3 µm between the DFG and OPA2 stages but also the OPA2 and OPA3 stages. When the wavelength is tuned, this balance is partly lost and the pump-signal duration match cannot be perfectly maintained in all OPAs simultaneously (without adding CaF_2 or Silicon windows, which was not done here). Indeed, once the AOPDF is set to match the pulse duration in OPA3, there is no additional available degree of freedom to control the durations of the seed pulse in the DFG and OPA2 stages. This duration mismatch results in spectral narrowing or a reduced conversion efficiency depending on the seed duration which respect to that of the pump pulse.

The OPCPA output spectrum can be tuned by translating the MgO-PPLN crystals transversally and by adjusting the settings of the AOPDF and the delay lines. Tunability from ~2.5 µm to ~3.9 µm (central wavelength) has been demonstrated. Figure 3(b) shows the spectra obtained for three different settings and for the same pump power. The output powers at 2.5 µm, 3.1 µm and 3.9 µm are 1.5 W, 4W and 0.5 W respectively. The spectral structures on the spectrum centered at ~2.5 µm result from absorption in ambient water vapor. Since the gain bandwidth for type-0 phase-matching is maximum close to degeneracy at 2.06 µm, broader spectra could have been expected at around 2.5 µm. The observed result can be explained by the lower seed level available at 1.75 µm for the DFG, and also, as explained above, by a mismatch between the durations of the pump and signal pulses.

4. Output energy stability

An average output power of ~4W was measured by a powermeter (UP25N-40S, Gentec) over 25 min.

In order to monitor the pulse-to-pulse stability of the pump, SC and output pulses, fractions of these beams are sampled out and sent to amplified photodiodes: InGaAs photodiode for the pump pulses, extended-InGaAs photodiode for the SC pulses, HgCdTe photodiode for the output pulses. The output signals are simultaneously recorded at 100 kHz (synchronous acquisition) and the resulting data are stored and processed. For 100 successive shots, recorded data show an output pulse-to-pulse energy variations of ~1.3% rms, while the energy variations of the pump pulses are ~0.9% rms. Remarkably, the energy stability improves from DFG (~4.7% rms) to OPA3 (~1.3% rms) indicating the increasing level of saturation within the successive nonlinear stages. In order to demonstrate long-term pulse energy trends (power drift), the data averaged over $2 \cdot 10^5$ pulses at each point are presented on Fig. 4.

Optics EXPRESS

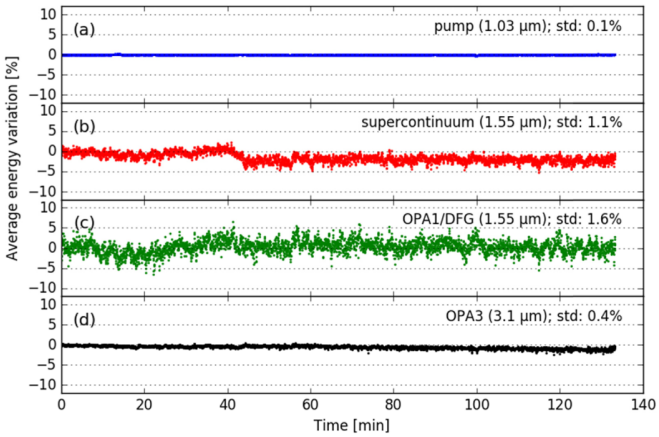

Fig. 4. Average energy variation as a function of time. Each point is an average over 2 sec ($2 \cdot 10^5$ shots). (a) pump (0.1% rms), (b) supercontinuum after a high-pass filter with a cut-off at 1.3 μm (~1.1% rms), (c) DFG (amplified seed, ~1.6%) and (d) output (OPA3) (~0.4% rms).

As in [11,15,27], we report the onset of nonlinear and/or thermal effects limiting the output power of the OPAs and, in particular, of OPA3, where the pump and idler powers are the highest. The parameters of the last OPA stage are intermediate between those given in [15] and in [27] and essentially differ by: the thickness of the MgO-PPLN crystals (with respect to [26]), the pump pulse duration (with respect to [15,27]) and the contrast of the pump pulses (with respect to [27]). Although deeper investigation would be required, our results tend to confirm that these effects originate from combined mid-IR-assisted nonlinear absorption and thermal effects.

5. Beam characterization

The spatial beam profile was characterized by a scanning slit beam profiler (NanoScan, Ophir Photonics) integrating a pyroelectric detector and a slit of 5 μm. The spatial profile, measured after a ~50 cm free propagation after OPA3 and before the output telescope, is Gaussian-like, with a ~2.2 mm beam diameter at FWHM (Fig. 5). After collimation by a pair of concave mirrors, the beam was focused by an f = 500 mm lens and the 4σ beam diameter was measured as a function of distance from the waist. Following the method described in ISO-11146, we measured a $M^2 = \sqrt{M_X^2 M_Y^2}$ value <1.3.

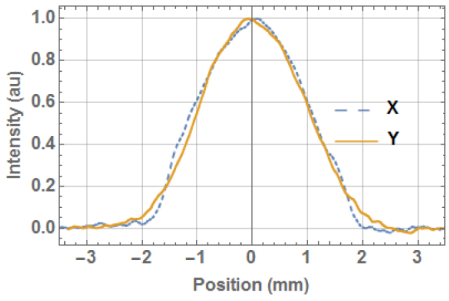

Fig. 5. Near-field spatial profiles along horizontal (X) and vertical (Y) directions

6. Pulse characterization

Fractions of the output beam are sent to a scanning SH-FROG device to characterize the pulse duration and spectral phase and to a 2f-to-f interferometer to monitor the CEP drift. The SH-

Optics EXPRESS

FROG was built from a thin broadband KBr beamsplitter with a reflectivity of 50 ± 5% over the full 2-5 µm bandwidth, a 100-µm silver thiogallate (AgGaS2) crystal oriented for type-I second harmonic generation, and an InGaAs spectrometer (NIRQuest-2.5, OceanOptics). The experimental and reconstructed FROG traces are shown on Fig. 6. The retrieved pulse duration (<0.4% rms error over a 160x160 calculation grid) is 38.3 ± 1 fs at FWHM, which is within 8% of the Fourier-transform limit (35.7 ± 1 fs). The uncertainty on the latter values arises from the limited dynamic range of the FROG measurement and the inevitable choice of a spectral threshold to distinguish signal from background and noise. The spectral barycenter being at 3.1 µm, such a pulse duration corresponds to less than 4 optical cycles (an optical cycle is 10.3 fs at 3.1 µm).

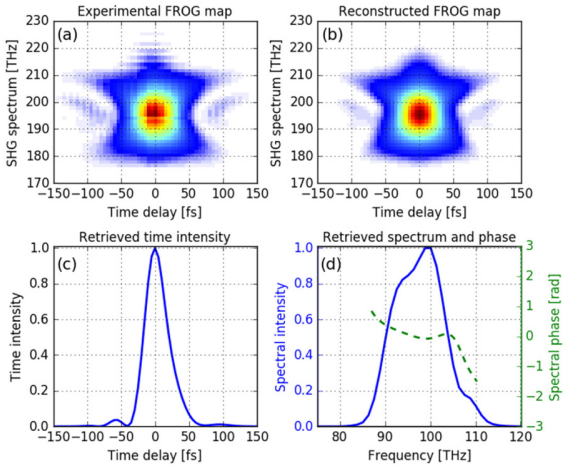

Fig. 6. (a) Experimental FROG trace. (b) Retrieved FROG trace. (c) Reconstructed time-dependent intensity. (d) Reconstructed spectrum and spectral phase.

The stability and drift of the CEP was assessed by nonlinear interferometry. However, unlike previous works, and in particular [24] and [10] which are respectively based on f-to-2f and 2f-to-3f interferometry, we use a 2f-to-f scheme in which the SHG occurs before the spectral broadening step, and all statistical values are calculated from single-shot acquisitions (i.e. not averaged over a large number of shots): the collimated input beam (~10 µJ) first propagates through a thin type-I SHG crystal ($AgGaS_2$) and is then focused in a 4-mm YAG crystal to generate a stable continuum extending to the visible. The spectral beating around 1.55 µm, which arises from the interference between the second harmonic of the input pulse and the continuum, is recorded by a fast spectrometer with onboard calculation capabilities ([25], Fringeezz, Fastlite). In this 2f-to-f scheme, the optical delay between the two components at 1.55 µm is directly related to the thickness of the YAG crystal, which allows a straightforward optimization of this delay in order to match the spectral resolution of the spectrometer. The latter device consists of a slit, a high-efficiency transmission grating, a pair of AR-coated lenses and an InGaAs linear array with a minimum integration time of 3 µs. All components are selected to minimize the optical losses and maximize the signal-to-noise ratio on the detector. As a result, the detector could be saturated even at the minimal integration time (i.e. for single-shot acquisition). The analog beating signal is recorded and the phase drift of the interferogram is computed and stored at 10 kHz. With this setup, the CEP drift between isolated pulses is sub-sampled at 10 kHz (single-shot every ten pulses). As a result, noise contributions above 5 kHz are aliased.

A digital output is used to feed back at 10 kHz the CEP drift to the AOPDF and correct for the CEP fluctuations. The feedback loop is a simple proportional correction with a damping factor of 0.5 (damping factor was limited to $1/2^N$ values by the hardware), time-

Optics EXPRESS

delayed with a latency time of ~60 µs, meaning that the phase correction applied to the pulses from N + 6 to N + 16 is 50% of the phase shift measured for the pulses N-10 to N.

An example of CEP fluctuations over ~80 s without feedback is shown on Figs. 7(a) and 7(b). As the number of acquired values exceeds 800 000 points, Fig. 7(a) represents the probability density function (PDF) as a function of time rather than the values directly. On Fig. 7(b), the distribution of the values is mostly Gaussian with a standard deviation of 255 mrad.

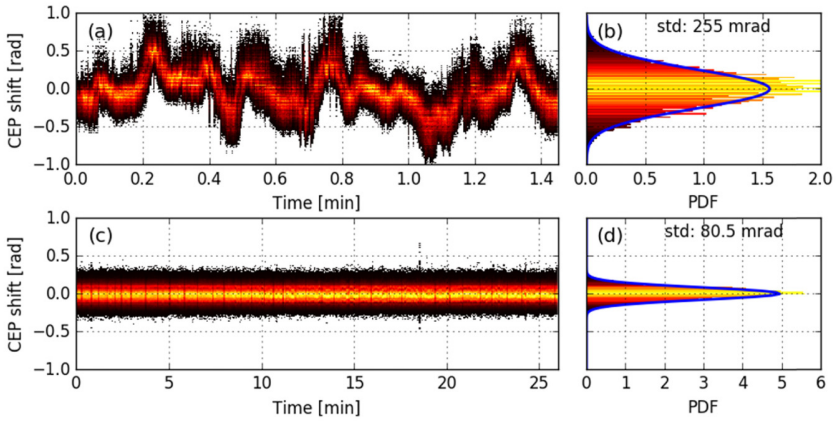

Fig. 7. (a) open-loop CEP noise PDF as a function of time, (b) open-loop CEP noise histogram, the standard deviation is 255 mrad, the blue curve is a Gaussian function with a σ parameter corresponding to the histogram standard deviation, (c) close-loop CEP noise PDF as a function of time, (d) close-loop CEP noise histogram, the standard deviation is 80.5 mrad, the blue curve is a Gaussian function with a σ parameter corresponding to the histogram standard deviation. Colors from dark to bright denote the probability density from low to high, respectively.

In closed-loop operation (Figs. 7(c) and 7(d)), the CEP in-loop fluctuations are below 81 mrad rms with a peak-to-peak variation below 1 rad over 25 min, which corresponds to $15 \cdot 10^6$ samples at 10 kHz or $150 \cdot 10^6$ successive pulses (i.e. equivalent to ~42 h at 1 kHz). h at 1 kHz) Fig. 8(a) shows the comparison of the power spectral densities in open- and closed-loop operations. This figure and Fig. 8(b), representing the integrated phase noise, show a complete noise canceling at all contributing frequencies below ~1 kHz and a residual noise in the 2-5 kHz range, which is in accord with the Nyquist frequency of the measurement device (5 kHz) and the damping factor (0.5) used for the feedback. Further analysis of the noise content requires a better understanding of the resolution of the detector and signal-to-noise ratio of the InGaAs linear array (estimated to be ~100), but also of the intensity-to-CEP coupling effects in the continuum generation [24].

Optics EXPRESS

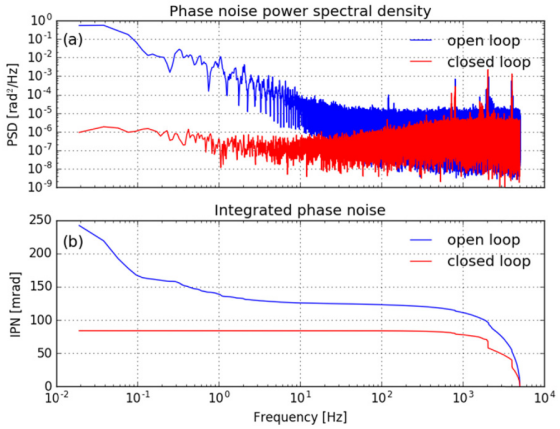

Fig. 8. (a) Phase noise power spectral densities for open and closed loops, (b) integrated phase noise (IPN) for open and closed loops.

7. Conclusion and prospects

The OPCPA system presented here shows an excellent long term power stability with power fluctuations of 0.4% rms over 2 hours, thanks to its collinear geometry, self-seeded design and all-bulk dispersion management. The mid-IR wavelength, centered at 3.1 µm, coupled to <4-cycle pulse duration and pulse energy of 40 µJ, should allow for the HHG in the soft-x-ray regime. From the measured data, a peak intensity of $>10^{14}$ W/cm^2 is at reach with a focal spot of 25 µm FWHM. The long-wavelength operation and a record low CEP fluctuations of 81 mrad rms, combined with a proper post-compression setup, would also form an ideal tool to generate isolated attosecond pulses in the water window.

With the addition of another OPA stage, pumped with the remaining 145 W of pump power, an output pulse energy of 150 µJ is targeted, which would raise the output average power from 4 W to 15 W and pave the route to high flux HHG sources in the water window.

Funding

ELI-HU Non-Profit Ltd and the European Union's Horizon 2020 research and innovation program under the Marie Sklodowska Curie grant agreement No. 641; Fond unique interministériel (FUI AAP17 – projet STAR).

Acknowledgments

The publication reflects only the author's view. The Research agency of the European Union is not responsible for any use that may be made of the information it contains. We also acknowledge the early-stage participation and subsequent fruitful discussions with Alexandre Thai.

Research Article | Vol. 26, No. 21 | 15 Oct 2018 | OPTICS EXPRESS 26907
Optics EXPRESS

Highly stable, 15 W, few-cycle, 65 mrad CEP-noise mid-IR OPCPA for statistical physics

NICOLAS THIRÉ,[1,*] RAMAN MAKSIMENKA,[1] BÁLINT KISS,[2] CLÉMENT FERCHAUD,[1] GRÉGORY GITZINGER,[1] THOMAS PINOTEAU,[1] HERVÉ JOUSSELIN,[1] SEBASTIAN JAROSCH,[3] PIERRE BIZOUARD,[1] VITTORIO DI PIETRO,[1] ERIC CORMIER,[2] KÁROLY OSVAY,[2] AND NICOLAS FORGET[1]

[1]*Fastlite, 165 route des cistes 06600, Antibes, France*
[2]*ELI-HU Non-Profit Ltd, Dugonics tér 1 6720 Szeged, Hungary*
[3]*Imperial College London, South Kensington Campus, London SW7 2AZ, UK*
**nicolas.thire@fastlite.com*

Abstract: We demonstrate a 100 kHz optical parametric chirped-pulse amplifier delivering under 4-cycle (38 fs) pulses at ~3.2 µm with an average power of 15.2 W with a pulse-to-pulse energy stability <0.7% rms and a single-shot CEP noise of 65 mrad RMS over 8h. This source is continuously monitored, by using a fast 100 kHz data acquisition device, and presents an extreme stability, in the short and long terms.

1. Introduction

The advent of diode-pumped ytterbium-doped solid-state lasers has revolutionized femtosecond technologies [1] and strong-field physics not only because of their compactness and power scaling capabilities, but also because of versatile repetition rates and unmatched energy stability. The latter results from a combination of multiple favorable factors, either linked to the physical properties of ytterbium ions (long lifetime, simple electronic structure, relatively large gain bandwidth and small quantum defects) or to the technological aspects (compatibility with large set of host materials into fiber, bulk, slab, and thin-disk architectures and direct pumping by cost-effective laser diodes), allowing efficient and powerful laser amplification at multi-kHz to MHz repetition rates under steady-state pumping conditions. This technology, couple to the work on parametric amplification of ultrashort pulses [2], has set off the development of high-repetition rate optical parametric chirped-pulse amplifiers (OPCPA), especially in the mid-infrared range [3–11] where high repetition rate helps to counteract the rather low count rate of strong-field physics experiments such as COLTRIMS [12], reaction microscope [13], or conversion yield (X-UV generation [14]).

Energy stabilities well below the ~1% threshold, both shot-to-shot and long-term, unravel the potential of nonlinear optics to broaden bandwidths, shift wavelengths, generate or amplify light, without sacrificing the necessary prerequisites of deterministic experimental science: reproducibility and control of physical parameters. High-repetition rate sources also open the path to statistical analysis of large sets of data, an approach seldom used in strong-field physics so far because of the insufficient reproducibility of the intensity and/or electric field of short pulses.

In this paper, we exemplify such an approach by demonstrating an Ytterbium-pumped 100-kHz OPCPA generating few-cycle pulses at ~3.2 µm with a pulse energy of 152-µJ, a duration of 40-fs and a Strehl ratio >0.8. Compared to our previous publication [10], the output energy/power was increased by a factor >4 while maintaining or improving the other optical characteristics. Apart from this power upgrade, we present a complete long-term characterization of the output beam: a shot-to-shot energy stability of 0.7% RMS, a pointing stability of ~10 µrad RMS, and a carrier-envelope phase (CEP) noise of ~65 mrad over more than ~3 billion successive shots (>8h). To date, this is the best recorded non-averaged CEP

#341720 https://doi.org/10.1364/OE.26.026907
Journal © 2018 Received 7 Aug 2018; revised 6 Sep 2018; accepted 6 Sep 2018; published 1 Oct 2018

Optics EXPRESS

stability for an amplified system, independently of the wavelength, pulse duration or repetition rate. This OPCPA also delivers the highest reported peak power (152 µJ/38.2 fs with 92% in the main peak ~3.7 GW) at 100 kHz within the 2-4 µm wavelength range without post-compression.

2. Architecture

The OPCPA is pumped by an Yb^{3+}-YAG, thin-disk, regenerative amplifier (Dira-200, Trumpf Scientific Lasers) seeded by a 40 MHz oscillator (Amplitude Systèmes) and a fiber pre-amplifier (Fastlite). This regenerative amplifier delivers 2 mJ pulses at the repetition rate of 100 kHz (average power of 200 W). The pulse duration at 1030 nm is 1.1 ps full-width at half-maximum (FWHM). Beam profile is close to Gaussian (measured M^2<1.3) and the typical pulse-to-pulse energy stability is ~1% rms. The scheme of the optical setup is represented on Fig. 1.

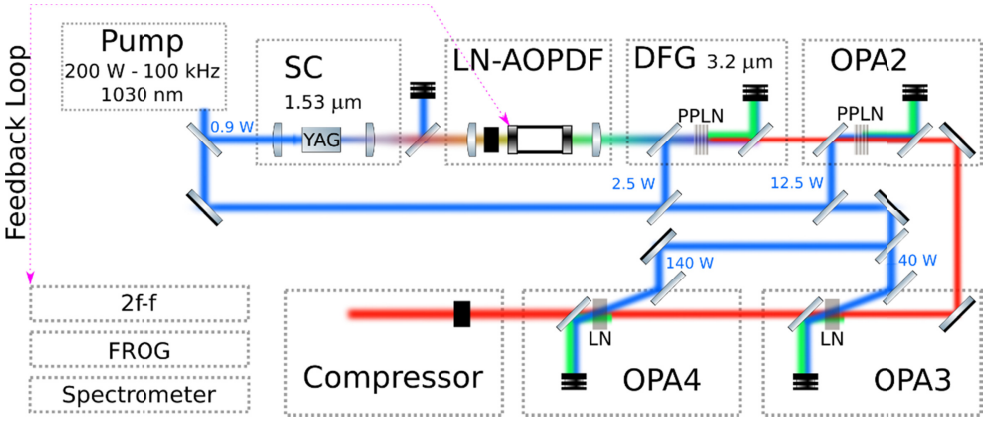

Fig. 1. Optical setup. SC: supercontinuum generation. LN-AOPDF: $LiNbO_3$ acousto-optic programmable dispersive filter. DFG: difference-frequency generation. OPA: optical parametric amplifier. 2f-f: collinear "2f-to-f" interferometer (CEP noise measurement). FROG: scanning second-harmonic frequency-resolved optical gating. PPLN: periodically poled MgO:$LiNbO_3$ crystal. LN: bulk $LiNbO_3$ crystal. Blue: 1.03 µm. Green: <2.06 µm. Red: >2.06 µm.

As already described with more details in [10], about 1 W is split from the main pump beam and spectrally-broadened up to ~2 µm in a 10 mm thick YAG crystal through filamentation. The 1.3-1.9 µm part of the supercontinuum is shaped by Lithium Niobate (LiNbO3) acousto-optic programmable dispersive filter (AOPDF, Dazzler, Fastlite) triggered at 100 kHz. The AOPDF is the heart of the dispersion scheme and cumulates five tasks: spectral selection, pulse-stretching to match the pump duration in the subsequent OPA stages, pre-compensation of the high-order spectral phase introduced along the entire system, CEP stabilization and control. In order to manage pulse duration at each stage, materials of different dispersion are used (Si with positive GDD, and CaF2 with negative GDD). This shaped seed is then amplified in a 1-mm MgO-doped Periodically Poled Lithium Niobate (PPLN) crystal (named DFG in Fig. 1). The generated idler pulse at ~3.2 µm, is selected and successively amplified in the subsequent OPA stages OPA2 (type-0, 0.7-mm MgO-PPLN crystal), OPA3 and OPA4 (both non-collinear, type-I, 1.5-mm, bulk LiNbO3 crystals). All the crystals are heat up to 120 °C. Doping level of MgO is 5% for the PPLNs. LNs are not doped. OPA3 and OPA4 are pumped by ~40 W (peak pump intensity of ~30 GW/cm2) and ~140 W (peak pump intensity of ~90 GW/cm2) respectively with an external angle of ~10°. The noncollinear geometry in the last two OPAs avoids the use of dichroic mirrors and helps to minimize nonlinear effects at these stages, sum frequency generations in particular. At the output of OPA4, the average power at ~3.2 µm is 16.5 W and the global quantum conversion

Optics EXPRESS

(including optical losses) of OPA4 is ~28%. In all OPA stages pump-seed synchronization is passive. The output beam is then expanded to ~10 mm FWHM and sent to a compressor made of 20 mm of bulk Silicon. The usable output power for experiments is 15.2W after the compressor. A 1-mm Sapphire plate serves as both output window and beam sampler (R = 7% from 2.5 to 4 µm on one side, R<1% on the other side. The reflected beam is divided and sent to embedded diagnostics for parallel monitoring of the shot-to-shot energy fluctuations (MCT photodiode), pulse duration (FROG, Frozzer, Fastlite), spectrum (1-5 µm scanning acousto-optic spectrometer, Mozza, Fastlite [15]) and CEP stability (2f-to-f interferometer equipped with a fast fringe detector, Fringeezz, Fastlite [16]). The output average power is measured behind the output window by a large-area water-cooled powermeter. To characterize the spatial beam profile, the output beam is attenuated by a set of reflections on AR-coated Silicon windows and sent to a thermal-infrared camera. Spatial phase is measured by a wavefront sensor (SWIR-SID4, Phasics) and the Strehl ratio is assessed by measuring the focal spot at the focus of a CaF2 lens (f = 500 mm at 3.2 µm). All measurements are done at full power and on the same day for the sake of completeness and comparison.

3. Spectrum

Figure 2(a) shows the output spectrum, acquired at the rate of one spectrum every minute over more than 8h. The spectrum extends from ~2.8 µm to 3.65 µm with a shape typical of saturated OPAs containing a dip at ~3.3 µm showing the onset of the back-conversion process. Spectral modulations in the 2.8-2.9 µm reveal absorption by water vapor and/or –OH contents in coatings and/or optics. Figure 2(a) is an overlay of 500 spectra. Given the very small fluctuations of the spectral intensity we compute and plot the probability density function of the spectral intensity rather than direct values. Note that the color scale is logarithmic and spans over several orders of magnitude. Figure 2(b) shows in a more conventional way the stability of the spectral shape over more than 8h.

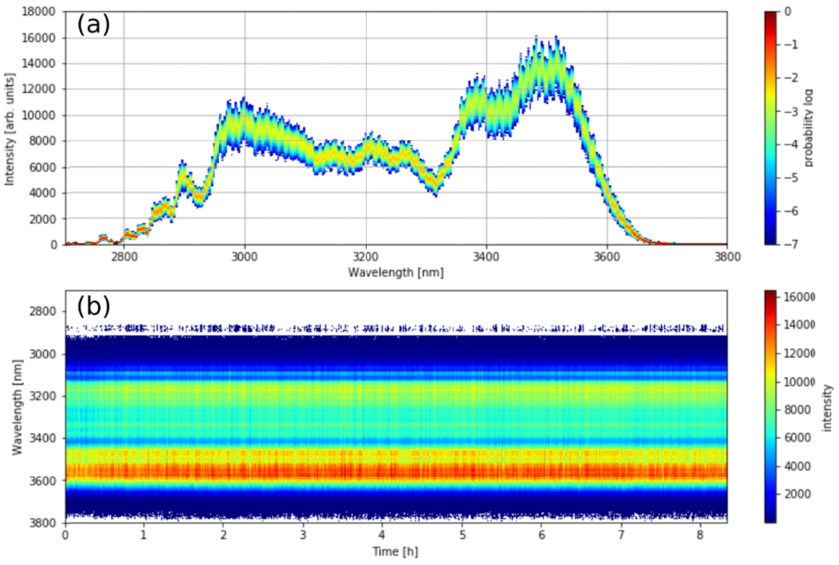

Fig. 2. (a): Overlay of 500 output spectra taken during 8 hours. Each column is a histogram of intensity computed for a particular wavelength. (b): Output spectrum as a function of time.

The system is optimized for 3.2 µm, but it is also important to notice its capability to be tuned from 2.5 µm (9.4 W – 85 fs FTL) to 3.8 µm (7.7 W – 140 fs FTL).

Optics EXPRESS

4. Pulse duration

Second-harmonic frequency-resolved optical gating (SH-FROG) is used to characterize the output pulses temporal profile [17]. A description of the optical setup can be found in [10]. A 1-mm Sapphire plate is inserted in the beam before the SH-FROG to take into account the dispersion of the output window. The retrieved pulse duration is 38.2 fs FWHM, for a Fourier-transform limit of 35.5 fs FWHM. The accuracy of the pulse reconstruction is assessed by computing the RMS reconstruction error (<1%, 160x160 calculation grid). Since the duration of an optical cycle at 3.2 µm is 10.7 fs, the pulses duration is less than four optical cycles.

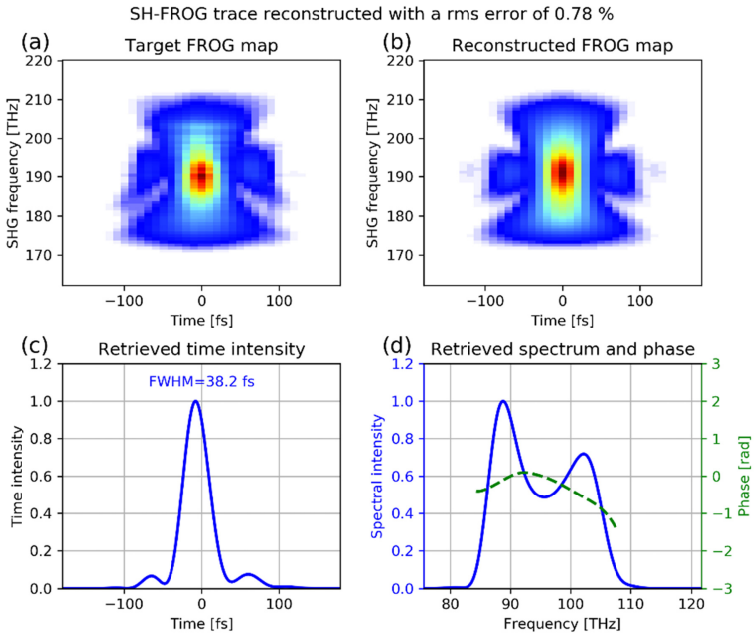

Fig. 3. (a) Experimental FROG trace. (b) Retrieved FROG trace. (c) Reconstructed time-dependent intensity. (d) Reconstructed spectrum and spectral phase.

5. Beam profile and Strehl ratio

The spatial beam profile at the output of the OPCPA is characterized by a customized uncooled micro-bolometer array (Pyroview, DIAS). The detector array is 640 x 480 pixels with a pixel pitch of 17 µm. The near-field beam profile (~1 m after the output window) is shown in Fig. 4. The beam is approximately Gaussian, with a diameter of ~14 mm at $1/e^2$. A fraction of the beam is sampled, attenuated and focused by a + 500 mm AR-coated plano-convex CaF_2 lens. The beam profile, at focus, is shown in Fig. 4, bottom left. To characterize the deviation from an ideal, diffraction limited beam, we compare the measured far field with the one computed from the near-field measurement assuming a perfectly flat spatial phase. Because of the unavoidable presence of a thermal background, a threshold at 5% (of peak counts) is applied to all measured beam profiles. Besides, a numerical filter equivalent to a physical round aperture of 29 mm is applied on the near-field profile to remove spurious contributions (halo from steering optics). Measured and computed widths at $1/e^2$ are 145 µm x 168 µm and 148 µm x 155 µm respectively, which indicate that the beam is actually close to its Fourier-transform limit. More quantitatively, the experimental peak fluence (far-field measurement) is 1.62 J/cm^2, whereas the theoretical peak fluence (deduced from the near-

Optics EXPRESS

field beam profile) is 1.97 J/cm^2. Defining the Strehl ratio as the relative loss of peak fluence at focus induced by spatial phase aberrations, provides a value of ~0.82. Another measurement of the Strehl ratio is performed with a wavefront sensor (SID4, Phasics) leading to a calculated value of 0.87, in good agreement with our experiment. The related M^2 value, also deduced from the wavefront measurements is ~1.40.

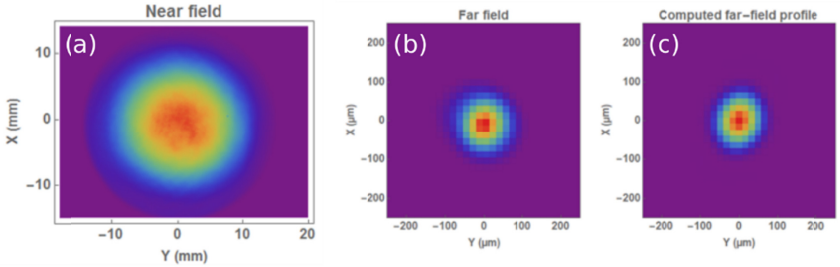

Fig. 4. Beam profile measured in near field (a) and far field (b). Computed far field (c).

Beam pointing fluctuation is defined as the RMS displacement of the beam barycenter in the far-field and was also measured over 8h. The RMS beam deviation is 3.1 µm along the X-direction and 4.8 µm along the Y-direction. The deduced beam pointing stability is ~0.02 times the beam divergence in the X- and ~0.03 in the Y-direction. Given the focal length of the focusing lens (500 mm), the beam pointing stability is <10 µrad RMS in both directions.

6. CEP fluctuations

Fluctuations of the carrier-envelope phase are characterized by "2f-to-f" interferometry [10,18]. Here, a collimated beam of 6 µJ first propagates through a thin type-I SHG crystal ($AgGaS_2$) and consequently generates a second harmonic beam that interferes with a stable continuum produced by focusing the beam in a YAG crystal. A 45° polarizer couples the polarizations of 2f and f. The spectral beating at ~1.55 µm between the continuum and the second harmonic is recorded by a fast fringe detector [16] during 8 hours at 10 kHz (integration time of 2 µs), meaning that an interferogram is acquired for one laser shot every ten pulses, for a total of 2.9 10^8 data points. A digital output (resolution of ~25 mrad: 8 bits digitalization over 2π) is used to feed back the CEP offset to the AOPDF at 10 kHz and correct for CEP fluctuations. The feedback loop is a simple proportional correction with a damping factor of 0.5. Figure 5 demonstrates the CEP stability measured for 8h. The CEP noise is 65 mrad RMS over the entire measurement. This extreme long-term stability and ultra-low noise of the CEP are result of the combination of the intrinsic passive stability of the "self-seeded DFG" process and the active feedback loop. As visible on Fig. 5, the discretization levels of the feedback (~25 mrad) starts to show up.

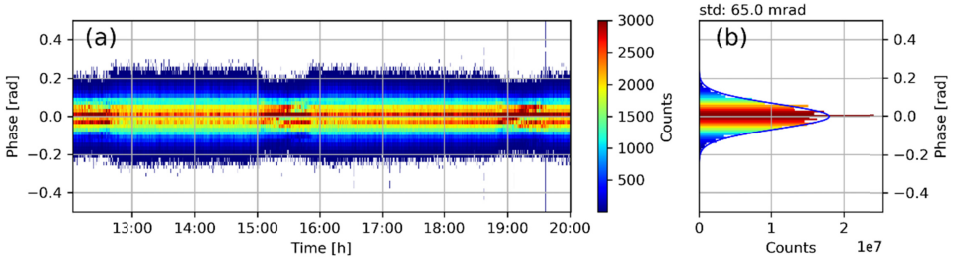

Fig. 5. Measured CEP noise over 8h (closed-loop). (a) Temporal evolution of CEP fluctuations: each column is a histogram of measured CEP offsets for 20000 shots (2 s at 10 kHz); (b) histogram of the total distribution of measured CEP offsets.

Optics EXPRESS

This excellent CEP stability and the capability to manipulate the electric field over a 25 mrad resolution is essential for controlling molecular systems with IR field [19] or, after a post compression stage, optoelectronics experiments [20].

7. Long-term power stability, shot-to-shot energy fluctuations

Average output power is measured every 10 s by a water-cooled, large area powermeter, with an integration time of 2 s. Figure 6 shows the output power after compression as a function of time, for a period of 12 hours. The time axis is local time in order to correlate these results with the CEP measurement (Figs. 5 and 8). The average power value is 15.2 W with a RMS stability of ± 0.7% over the full measurement. The break in the measurement at ~11:50 was caused by an external interlock event. After only a few minutes the full system was restarted and got back to the initial values within a few seconds.

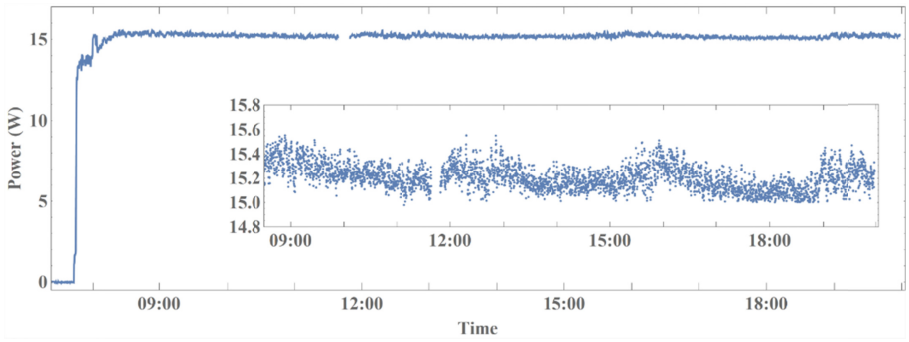

Fig. 6. Average power at the output of the OPCPA after the compression stage. Same data are shown with two scales: [7:20-20:00, 0-17 W] and inset: [8:30-20:00, 14.8-15.8 W].

In parallel, a large-area, TE-cooled, HgCdTe photodiode is used to monitor the output pulse-to-pulse energy. Given the high repetition rate and the high vertical resolution required to resolve low level of the energy fluctuations, an acquisition system has been specifically developed to acquire and log data values at 100 kHz with a dynamic range >40 dB. The combination of these two features allows the computation of statistical figures, and in particular energy fluctuations, with a precision well below 0.1%. This acquisition system (BigBrozzer, Fastlite) is designed to record the data from sixteen input channels simultaneously. Embedded in the OPCPA, it monitors continuously the pump beam position (4-quadrant detector) as well as the energies of pump, continuum, DFG and output beams.

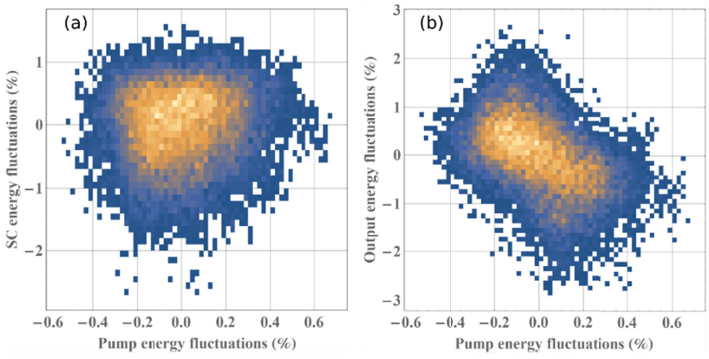

Fig. 7. (a) Supercontinuum (SC) energy fluctuations as a function of pump energy fluctuation (fluctuations relative to the average pulse energies). (b) Output energy fluctuations in function of pump energy fluctuations. Both plots are density functions corresponding to 20 000 successive pulses.

Optics EXPRESS

Figure 7 shows an example of the statistical approach. On Fig. 7(a) the relative fluctuations of the SC energy are plotted against the relative fluctuations of the pump energy. There is no clear correlation between these two data sets. One can still note that the SC energy looks clamped toward the highest energy values. This feature can probably be related to the self-stabilization regime reported in [21]. Figure 7(b) correlates similarly the fluctuations of the output energy versus the pump energy. There is a clear anti-correlation with a slope of approximately −4 showing that OPA4 operates in the saturation regime. In order to be able to save data for a long-period (around a month on a 32 Gb memory card), four parameters are computed and saved every second (i.e. calculated over 100 000 consecutive shots) for all input channels: the average value, the RMS value, the minimum value and the maximum value. Figure 8 compares over 8h the RMS CEP noise (closed-loop) with the following data: relative output pulse energy, relative pump energy, OPCPA RMS energy noise and pump RMS energy noise. The Spearman's rank correlation (or Spearman's rho) coefficients between the RMS CEP and the latter data are, respectively: + 0.48, −0.32, + 0.46 and −0.33. CEP appears to be mostly correlated to the output pulse energy rather than to the pump energy. Interestingly, the CEP noise is not only related to the RMS fluctuations (i.e. the best CEP stability is achieved when the system is the most stable) but also to the average pulse energy. This phenomenon may be explained by an intensity-phase coupling induced by the white-light generation stage of the 2f-to-f interferometer: as described in the section IV of [22], the strength of this intensity-phase coupling actually depends on the input energy level. This measurement also shows a weaker correlation between the pump energy and CEP noise. Beyond the correlation coefficient, a common periodic variation (cycle of 10-15 mn) is clearly visible. For the sake of completeness, it has to be mentioned than the abrupt drops of the output energy are linked to the start/stop of the cooling unit of the system.

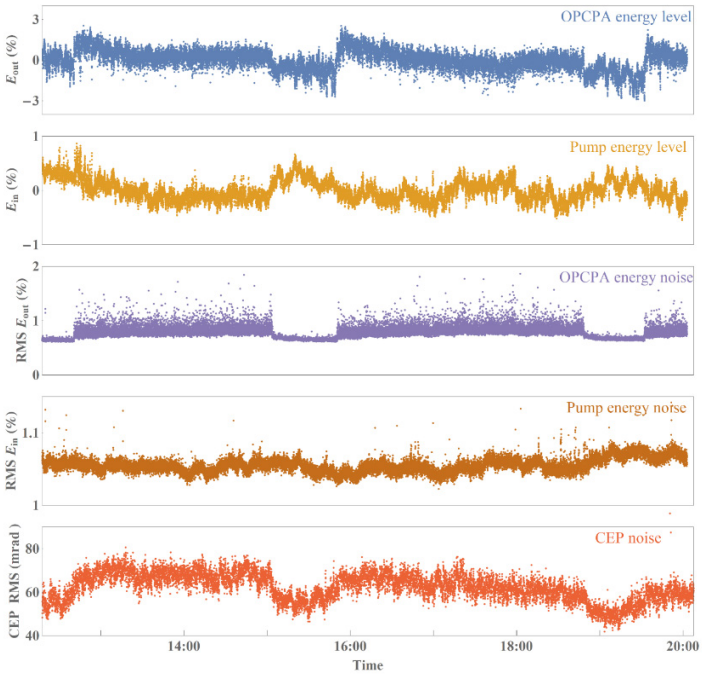

Fig. 8. From top to bottom, long term measurements of: relative OPCPA output energy, relative pump energy, RMS OPCPA energy fluctuations, RMS pump energy fluctuations, CEP noise (RMS). All data were acquired single-shot at 100 kHz (pump energy, OPCPA energy) or 10 kHz (CEP). The OPCPA and pump variations are relative to the average value computed over 8h.

Optics EXPRESS

Although the information deduced from Figs. 7 and 8 was predictable, the interest of the fast data acquisition device lies in the fact that for each shot, several experimental values can be correlated, both shot-to-shot and on the long-term. This is not only useful for understanding the physics of this OPCPA system, but also for analyzing the effect of laser parameters on scientific results. In the present case, this study tends to show that the stability of the CEP is ultimately limited by the stability of white-light generation stage of the 2f-to-f device through intensity-phase coupling. To a lesser extent, another contribution, linked to the pump energy, can be detected. This feature could also be a signature of an intensity-phase coupling but at the SC or DFG level.

8. Conclusion and prospects

We have characterized a 100-kHz, 3.2-µm, 15.2-W, 4-cycle OPCPA with an RMS energy/power stability < 0.7% and an RMS carrier-envelope phase noise of 65 mrad with no drift over eight consecutive hours, which corresponds to almost three billion pulses. We demonstrated that a peak intensity of 10^{15} W/cm^2 with a focal spot of 20 µm FWHM is reachable, making this source suitable to drive nonlinear strong-field processes like HHG up to keV energy level [23]. Coupled to the embedded multi-channel data acquisition device, this system is suitable for performing ultra-stable shot-to-shot measurements over a long-term, promising data accumulation difficult to reach with other sources demonstrated so far.

Funding

European Regional Development Fund (2.3.6-15-2015-00001); H2020 Marie Skłodowska-Curie Actions (641272).

References

1. H. Fattahi, H. G. Barros, M. Gorjan, T. Nubbemeyer, B. Alsaif, C. Y. Teisset, M. Schultze, S. Prinz, M. Haefner, M. Ueffing, A. Alismail, L. Vámos, A. Schwarz, O. Pronin, J. Brons, X. T. Geng, G. Arisholm, M. Ciappina, V. S. Yakovlev, D.-E. Kim, A. M. Azzeer, N. Karpowicz, D. Sutter, Z. Major, T. Metzger, and F. Krausz, "Third-generation femtosecond technology," Optica **1**(1), 45–63 (2014).
2. A. Dubietis, G. Jonušauskas, and A. Piskarskas, "Powerful femtosecond pulse generation by chirped and stretched pulse parametric amplification in BBO crystal," Opt. Commun. **88**(4–6), 437–440 (1992).
3. B. M. Luther, K. M. Tracy, M. Gerrity, S. Brown, and A. T. Krummel, "2D IR spectroscopy at 100 kHz utilizing a Mid-IR OPCPA laser source," Opt. Express **24**(4), 4117–4127 (2016).
4. A. Thai, M. Hemmer, P. K. Bates, O. Chalus, and J. Biegert, "Sub-250-mrad, passively carrier-envelope-phase-stable mid-infrared OPCPA source at high repetition rate," Opt. Lett. **36**(19), 3918–3920 (2011).
5. B. W. Mayer, C. R. Phillips, L. Gallmann, and U. Keller, "Mid-infrared pulse generation via achromatic quasi-phase-matched OPCPA," Opt. Express **22**(17), 20798–20808 (2014).
6. U. Elu, M. Baudisch, H. Pires, F. Tani, M. H. Frosz, F. Köttig, A. Ermolov, P. St.J. Russell, and J. Biegert, "High average power and single-cycle pulses from a mid-IR optical parametric chirped pulse amplifier," Optica **4**(9), 1024 (2017).
7. B. W. Mayer, C. R. Phillips, L. Gallmann, M. M. Fejer, and U. Keller, "Sub-four-cycle laser pulses directly from a high-repetition-rate optical parametric chirped-pulse amplifier at 3.4 µm," Opt. Lett. **38**(21), 4265–4268 (2013).
8. M. Mero, F. Noack, F. Bach, V. Petrov, and M. J. J. Vrakking, "High-average-power, 50-fs parametric amplifier front-end at 1.55 µm," Opt. Express **23**(26), 33157–33163 (2015).
9. P. Rigaud, A. Van de Walle, M. Hanna, N. Forget, F. Guichard, Y. Zaouter, K. Guesmi, F. Druon, and P. Georges, "Supercontinuum-seeded few-cycle mid-infrared OPCPA system," Opt. Express **24**(23), 26494–26502 (2016).
10. N. Thiré, R. Maksimenka, B. Kiss, C. Ferchaud, P. Bizouard, E. Cormier, K. Osvay, and N. Forget, "4-W, 100-kHz, few-cycle mid-infrared source with sub-100-mrad carrier-envelope phase noise," Opt. Express **25**(2), 1505–1514 (2017).
11. M. Neuhaus, H. Fuest, M. Seeger, J. Schötz, M. Trubetskov, P. Russbueldt, H. D. Hoffmann, E. Riedle, Z. Major, V. Pervak, M. F. Kling, and P. Wnuk, "10 W CEP-stable few-cycle source at 2 µm with 100 kHz repetition rate," Opt. Express **26**(13), 16074–16085 (2018).
12. R. Dörner, V. Mergel, O. Jagutzki, L. Spielberger, J. Ullrich, R. Moshammer, and H. Schmidt-Böcking, "Cold Target Recoil Ion Momentum Spectroscopy: a 'momentum microscope' to view atomic collision dynamics," Phys. Rep. **330**(2-3), 95–192 (2000).
13. J. Ullrich, R. Moshammer, A. Dorn, R. Dörner, L. Ph. H. Schmidt, and H. Schmidt-Böcking, "Recoil-ion and electron momentum spectroscopy: reaction-microscopes," Rep. Prog. Phys. **66**(9), 1463–1545 (2003).

Optics EXPRESS

14. A. D. Shiner, C. Trallero-Herrero, N. Kajumba, H.-C. Bandulet, D. Comtois, F. Légaré, M. Giguère, J.-C. Kieffer, P. B. Corkum, and D. M. Villeneuve, "Wavelength Scaling of High Harmonic Generation Efficiency," Phys. Rev. Lett. **103**(7), 073902 (2009).
15. G. Gitzinger, V. Crozatier, R. Maksimenka, S. Grabielle, N. Forget, S. Alisauskas, A. Pugzlys, A. Baltuska, B. Monoszlai, C. Vicario, and C. P. Hauri, "Multi-octave acousto-optic spectrum analyzer for mid-infrared pulsed sources," in CLEO: 2014, paper STh1N.5, OSA Technical Digest (2014).
16. F. Lücking, V. Crozatier, N. Forget, A. Assion, and F. Krausz, "Approaching the limits of carrier-envelope phase stability in a millijoule-class amplifier," Opt. Lett. **39**(13), 3884–3887 (2014).
17. D. J. Kane and R. Trebino, "Characterization of Arbitrary Femtosecond Pulses Using Frequency-Resolved Optical Gating," IEEE J. Quantum Electron. **29**(2), 571–579 (1993).
18. M. Kakehata, H. Takada, Y. Kobayashi, K. Torizuka, Y. Fujihira, T. Homma, and H. Takahashi, "Single-shot measurement of carrier-envelope phase changes by spectral interferometry," Opt. Lett. **26**(18), 1436–1438 (2001).
19. V. Wanie, H. Ibrahim, S. Beaulieu, N. Thiré, B. E. Schmidt, Y. Deng, A. S. Alnaser, I. V. Litvinyuk, X. M. Tong, and F. Légaré, "Coherent control of D 2 /H 2 dissociative ionization by a mid-infrared two-color laser field," J. Phys. B **49**(2), 025601 (2016).
20. M. Schultze, E. M. Bothschafter, A. Sommer, S. Holzner, W. Schweinberger, M. Fiess, M. Hofstetter, R. Kienberger, V. Apalkov, V. S. Yakovlev, M. I. Stockman, and F. Krausz, "Controlling dielectrics with the electric field of light," Nature **493**(7430), 75–78 (2012).
21. L. Indra, F. Batysta, P. Hříbek, J. Novák, Z. Hubka, J. T. Green, R. Antipenkov, R. Boge, J. A. Naylon, P. Bakule, and B. Rus, "Picosecond pulse generated supercontinuum as a stable seed for OPCPA," Opt. Lett. **42**(4), 843–846 (2017).
22. A. Baltuska, M. Uiberacker, E. Goulielmakis, R. Kienberger, V. S. Yakovlev, T. Udem, T. W. Hänsch, and F. Krausz, "Phase-controlled amplification of few-cycle laser pulses," IEEE J. Sel. Top. Quantum Electron. **9**(4), 972–989 (2003).
23. T. Popmintchev, M.-C. Chen, D. Popmintchev, P. Arpin, S. Brown, S. Ališauskas, G. Andriukaitis, T. Balčiunas, O. D. Mücke, A. Pugzlys, A. Baltuška, B. Shim, S. E. Schrauth, A. Gaeta, C. Hernández-García, L. Plaja, A. Becker, A. Jaron-Becker, M. M. Murnane, and H. C. Kapteyn, "Bright coherent ultrahigh harmonics in the keV x-ray regime from mid-infrared femtosecond lasers," Science **336**(6086), 1287–1291 (2012).

Chapitre 5

Cristaux pour l'optique ultra-rapide

5.1 Introduction

En 2015, l'équipe Optique et Cristaux Liquides (OCL), de l'Institut Non Linéaire de Nice (ex-INLN, aujourd'hui l'Institut de Physique de Nice ou InPhyNi), et l'entreprise Fastlite ont fondé le laboratoire commun Softlite (financement ANR LABCOM en 2015). Celui-ci a pour objectif d'étudier et de développer des dispositifs dispersifs programmables à base de cristaux liquides épais, dans le but de contrôler la phase d'impulsions ultra-brèves [37] et plus généralement de faisceaux optiques [40, 41, 43]. En tant que membre du comité de pilotage et membre de l'équipe, j'ai également participé au développement d'une valve optique contrôlée thermo-optiquement [44, 51], qui est l'aboutissement de la thèse de Vittorio Di Pietro (co-encadrée avec Aurélie Jullien d'InPhyNi). Ces travaux sont aujourd'hui poursuivis dans le cadre de la thèse CIFRE de Loïc Ramousse. Deux brevets ont été déposés dans ce cadre [137, 141].
J'ai également initié en 2018 un contrat de recherche avec le laboratoire InPhyNi pour explorer un concept de « slant poling » [48] dans les cristaux de niobate de lithium, l'objectif étant de réaliser des cristaux retournés périodiquement (PPLN) d'ouverture centimétrique. Les échantillons produits par Elizaveta Neradovskaia durant sa thèse ont été testés et évalués à Fastlite en 2019.

Cadre	Type	Nom	Date	Direction	Laboratoire
Thèse	ITN HICONO	Vittorio di Pietro	2016-2019	Aurélie Jullien	InPhyNi
Thèse	CIFRE	Loïc Ramousse	2020-	Aurélie Jullien	InPhyNi
Thèse	ITN Smart-X	Benjamin Maingot	2020-	Aurélie Jullien	InPhyNi
Thèse	InPhyNi	Elizaveta Neradovskaiaa	2018-2019	Marc de Michelis, Vladimir Shur	InPhyNi
Stage	M2	Omar Boughdad	2016	Nicolas Forget	Fastlite

Table 5.1 – Thèses co-encadrées et stages dirigés.

Type	Acronyme	Laboratoire/entreprise	Rôle	Date
Collaboration	ANR LABCOM	InPhyNi	PI	2015-
Contrat	Slant poling	InPhyNi	PI	2018-2019
Collaboration	THERMOPTIX	InPhyNi	PI	2019-2021
ITN	Smart-X	-	PI	2019-2023

TABLE 5.2 – Contrats et collaborations.

5.2 Cristaux de PPLN

5.2.1 Cartes d'efficacité

La plupart des OPCPA décrits dans le chapitre 4 utilisent des cristaux de PPLN de relativement grande ouverture : 3 mm suivant la direction de poling et une dizaine de mm suivant l'autre direction. Les réalisations expérimentales ont mis en évidence de larges variations d'efficacité d'un cristal de PPLN à l'autre. Afin de comprendre l'origine de ces variations, un banc de cartographie a été mis en place. Pour cela on utilise deux faisceaux, l'un à 1030 nm et l'autre à 1.55 µm, focalisés sur un cristal test lui-même installé dans un four et placé sur deux platines de translation motorisées. La différence de fréquence à ≃3 µm est filtrée et mesurée par un détecteur MCT amplifié. Un programme pilote les platines afin de mesurer la différence de fréquence, point par point, sur toute la surface du cristal. Sans surprise, les résultats de mesure montrent que le processus de retournement de domaines n'est pas homogène sur l'épaisseur du cristal. Concrètement, les cristaux les plus homogènes sont identifiés (figure 5.1) et les autres écartés. Ce banc de test de cristaux a été réalisé par Omar Boughdad durant son stage de M2 (Télécom Saint-Etinenne, Université Jean Monnet) en 2016.

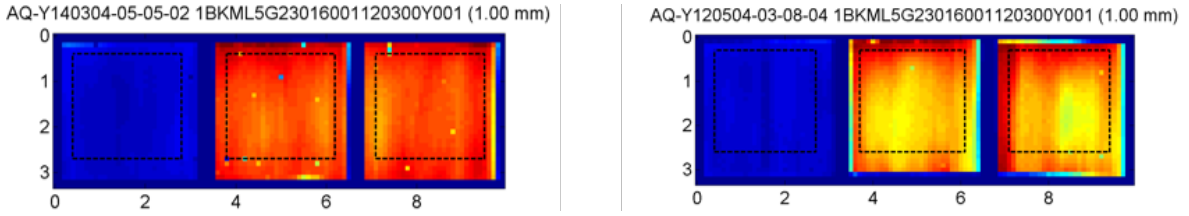

FIGURE 5.1 – Efficacité de conversion spatialement résolue pour deux cristaux (à gauche et à droite). Chaque cristal présente trois zones où les domaines ont été retournés périodiquement. Chacune des zones correspond à une période différente. Ce sont les zones rouges ou bleu clair. On note de fortes différences entre les deux cristaux.

5.2.2 Slant poling

Les cristaux de niobate de lithium retournés périodiquement (PPLN) possèdent des propriétés exceptionnelles (coefficient non linéaire élevé, bande de gain large, absence de walk-off, possibilité de structurer le matériau...) et sont les milieux non linéaires de prédilection dans les OPCPA infrarouges. L'ouverture actuelle maximale (3 mm) ne permet cependant pas leur utilisation dans les étages de puissance, ce qui serait pourtant désirable. Dans ce but, la société Fastlite a conclu en 2017-2018 un contrat de d'étude de 18

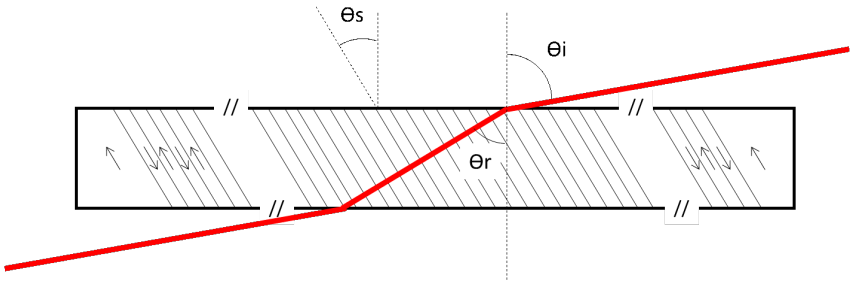

FIGURE 5.2

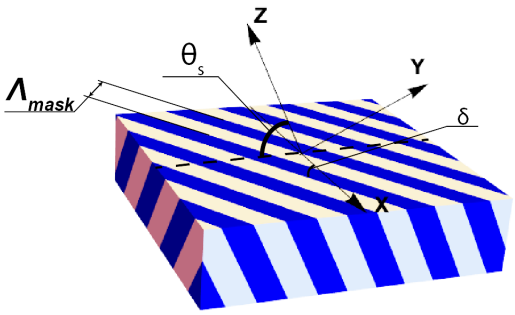

FIGURE 5.3 – Orientation cristalline par rapport aux surfaces des wafers de niobate de lithium. Les zones hachurées correspondent aux domaines ferroélectriques retournés.

mois avec le CNRS et l'Université Nice Sophia-Antipolis pour développer une technique de retournement de domaine compatible avec la fabrication de cristaux de PPLN et de PPSLT d'ouverture centimétrique. La réalisation des PPLN (Ural Federal University, Ekaterinburg, Russie) et leur étude (à Fastlite) ont été réalisées par Elizaveta Neradovskaia lors de sa thèse (co-dirigée par Valdimir Schur et Marc de Micheli [1]).

L'idée maîtresse du programme de recherche est de réaliser une inversion de domaines ferroélectriques suivant une direction non orthogonale à la grande surface du composant (« slant-poling » ou poling en biais). Étant donné que les domaines croissent préférentiellement suivant la direction polaire, il est nécessaire de partir de cristaux dont l'axe polaire (axe z ou [001]) forme un angle avec la normale à la surface du composant (angle de « slant »). Ce choix de géométrie est également intéressant pour des raisons pratiques car compatible avec une incidence égale à celle de Brewster (pour éviter les traitements anti-reflets par exemple). Pour le $LiNbO_3$ et le $LiTaO_3$, on trouve alors les angles de slant optimaux suivants : 65.9° et 64.4°. Malheureusement, la réalisation de tels PPLN n'est pas simple car les wafers de niobate de lithium avec la bonne orientation ne sont pas disponibles commercialement, du moins pour de faibles quantités. Nos tentatives d'approvisionnement ayant échoué, nous nous sommes tournés vers les wafers commerciaux acoustiques possédant l'orientation la plus proche de celle désirée. Ce choix introduit de nombreuses complications car la coupe cristalline (64° Y-cut) est doublement en biais (figure 5.3).

Les échantillons étudiés sont des wafers (galettes) de 0,5 mm d'épaisseur orientés de manière à ce que l'angle entre la normale à la surface et l'axe Y forme un angle de 36° (un

1. ainsi que Pascal Baldi, suite au décès de Marc de Micheli.

des standards pour les wafers destinés à des application acoustiques). Une couche de résine positive de 3 mm d'épaisseur est déposée sur la surface correspondant à la direction positive de la projection polaire (surface Z_s). Une partie de la résine photosensible est ensuite retirée par photolithographie de manière à former un motif. Pour caractériser la cinétique de croissance des domaines, le premier motif réalisé représente quatre cercles vides de diamètre 300 µm situés à proximité du centre de l'échantillon. L'échantillon est ensuite pressé contre une surface en plastique plane et décollé rapidement, ce qui a pour effet de former de nombreux trous à l'échelle du micron dans la couche de résine photosensible. En présence d'un électrolyte liquide, ces trous jouent le rôle d'électrodes locales. La distribution des diamètres est mesurée puis un champ électrique externe est appliqué à l'échantillon en utilisant une solution aqueuse saturée de chlorure de lithium comme électrolyte de part et d'autre de l'échantillon. L'inversion de polarisation en champ constant a été étudiée en analysant l'évolution de la fraction de domaines inversés en fonction du temps. Ces résultats ont fait l'objet d'une publication [73].

Des échantillons de 4 mm×4 mm×0.5 mm avec une masque de 18.3 µm (figure 5.3) ont ensuite été réalisés Elizaveta Neradovskaia sur des wafers Y-cut à 64° (pour des questions d'approvisionnement et de qualité de wafer). Ce cristaux ont ensuite été caractérisés à Fastlite sur un OPCPA à 100 kHz (pompe à 1030 nm et signal à 1.65 µm). Des mesures

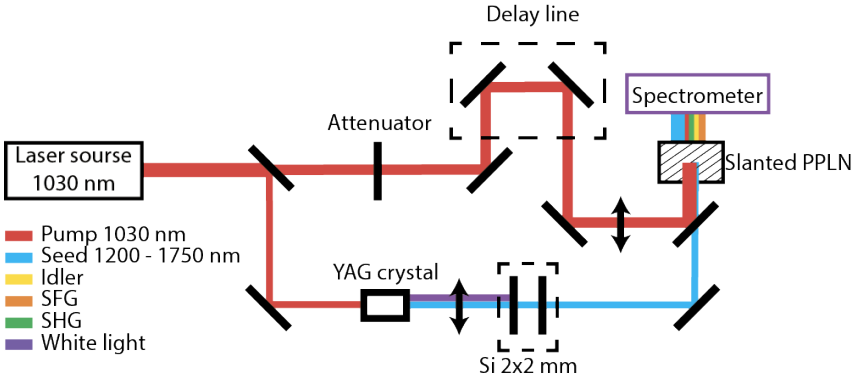

FIGURE 5.4 – Gain paramétrique des cristaux de PPLN réalisés.

de gain paramétrique (figure 5.4) indiquent que des gains importants sont atteints malgré la faible épaisseur du cristal (0.5 mm) et que le seuil de dommage du cristal demeure très élevé. La valeur de d_{eff} trouvée (2 pm/V) est bien plus faible qu'attendue, ce qui peut s'expliquer par un rapport cyclique de poling imparfait (<50%) mais aussi par l'angle de 64° (qui est beaucoup moins favorable). L'homogénéité transverse du poling reste aussi un point à améliorer. C'est toutefois une preuve de principe convaincante qui mériterait d'être poursuivie avec des moyens plus conséquents. Des substrats de meilleure qualité coupés suivant une orientation plus favorable (36°) conduiraient à des résultats nettement plus proches des PPLNs classiques. La surface de 4 mm×4 mm n'est pas limitée par la technologie et des ouvertures de 50 mm sont à portée de main.

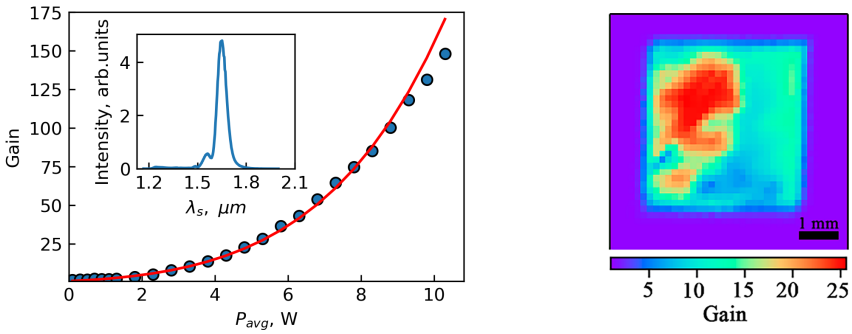

FIGURE 5.5 – Gain paramétrique des cristaux de PPLN réalisés.

5.3 Cristaux liquides

5.3.1 Softlite

Le contexte scientifique et technique est celui du laboratoire commun Softlite (combinaison de « soft matter » et de « Fastlite »), dont l'activité vise à développer des dispositifs à base de cristaux liquides pour la manipulation d'impulsions femtosecondes. Il est bien connu que les cristaux liquides présentent des propriétés optiques extrêmement intéressantes : une grande biréfringence, une large plage spectrale de transparence, et surtout la possibilité de modifier leurs propriétés optiques à travers une réorientation moléculaire induite par un champ électrique, magnétique, ou un contrôle en température. Les cristaux liquides sont, en particulier, très largement utilisés pour la manipulation de la lumière visible ou proche infrarouge (SLM, Spatial Light Modulators). Jusqu'à Softlite, l'application des cellules de cristaux liquides à la manipulation d'impulsions ultra-brèves se cantonnait, pour l'essentiel, aux SLM placés dans le plan de Fourier de lignes 4f. L'idée principale de Softlite est que les cristaux liquides en cellules épaisses (>50 µm) peuvent fournir des solutions technologiques nouvelles et complémentaires pour le contrôle de la phase spectrale des sources femtosecondes, grâce à leur indice optique élevé et à leurs propriétés configurables.

Les recherches menées dans ce cadre ont d'ores et déjà permis de démontrer l'efficacité de cellules nématiques épaisses dans des dispositifs optiques originaux de manipulation de la lumière et de mettre en place des diagnostics innovants pour l'étude de la dynamique des cristaux liquides. Les résultats obtenus sont particulièrement nombreux et résultent de la participation, au fil du temps, d'un collectif assez large de chercheurs, ingénieurs, post-docs ou étudiants. Parmi ces derniers figurent notamment Vittorio Di Pietro (thèse financée par l'ITN HICONO via Fastlite), Loïc Ramousse (thèse CIFRE avec Fastlite) et Benjamin Maingot (thèse financée par l'ITN Smart-X via Fastlite), dont les thèses ont été ou sont dirigées par Aurélie Jullien et que j'ai contribué à encadrer du côté Fastlite. Pour résumer très rapidement, l'utilisation de ces cellules, seules ou en cascade, a permis à Softlite de réaliser les dispositifs suivants :

- une ligne à délai colinéaire adapté aux impulsions femtosecondes, pour le contrôle indépendant de la vitesse de phase et de groupe avec une résolution temporelle sub-cycle optique [74]

- un instrument d'imagerie hyperspectrale colinéaire, offrant une résolution de 6nm sur la gamme spectrale 400 nm-1000 nm [75],
- un prisme accordable pour l'interférométrie spatiale à décalage [76],
- un réseau de biréfringence en volume,
- un SLM contrôlé thermo-optiquement et son application au façonnage d'impulsions brèves [77].

En parallèle, Softlite a déterminer les indices optiques de certains cristaux liquides [78], également mis en évidence plusieurs des limites liées à l'adressage électrique des cristaux liquides, découlant toutes de l'électrode transparente utilisée (ITO, oxyde d'étain et d'indium) :

- inadéquation des dispositifs dans la gamme spectrale infrarouge (>1 µm) [79],
- seuil de dommage de l'électrode (300 mJ/cm^2) [80]
- pertes par diffusion optique liées à la transition de phase de Fréederisczk [81],
- pertes par diffusion liées à la réorientation moléculaire.

Je ne détaille ici qu'un seul des dispositifs étudiés : la valve thermo-optique.

5.3.2 Valve thermo-optique

L'élévation locale de la température combinée au caractère thermotrope des nématiques modifie les indices de réfraction. Si le caractère thermotrope des nématiques est établi depuis quelques décennies, la plupart des applications requièrent d'utiliser le cristal liquide loin de la température critique. Quelques publications font état d'effets non linéaires (automodulation de phase, auto-diffraction) d'origine thermique. Dans ce cas, l'échauffement des cristaux liquides provient de l'absorption de la lumière dans le cristal liquide lui-même grâce à l'ajout d'un agent de dopage. Récemment, nous avons démontré la non-linéarité thermique induite optiquement dans une cellule épaisse nématique, par absorption partielle de la lumière (20%) par le revêtement ITO de la cellule, dans le domaine spectral infrarouge [79]. Nous avons ainsi pu contrôler de manière réversible toute la dynamique des indices extraordinaires et ordinaires jusqu'à la température critique, ce qui correspond à une augmentation de la température locale de 40°. Le gradient thermique bien confiné permet une mise en forme spatiale significative du laser femtoseconde (figure 5.6 et figure 5.7). L'idée est ensuite venue d'exploiter cet effet pour former un masque de phase programmable au moyen d'un faisceau optique d'écriture totalement ou partiellement absorbé par l'un des composants de la cellule de cristal liquide figure 5.8. Plutôt que d'utiliser le cristal liquide lui-même ou l'ITO comme milieu absorbant, on choisit ici une absorption par une couche mince réflective - une couche d'or en l'occurrence. Les longueurs d'onde <500 nm étant fortement absorbées, un faisceau d'écriture bleu échauffe directement la couche d'or et ainsi le cristal liquide. Ceci permet de travailler en réflexion sur la valve optique, de doubler ainsi le déphasage, et de bien séparer les faisceaux de lecture (le faisceau mis en forme) et de lecture (le faisceau de mise en forme). Le terme de « valve optique » fait référence aux SLMs contrôlés optiquement via des photoconducteurs, lequels partagent cette terminologie. Le contrôle thermo-optique évite les contraintes liées à l'électrode (adaptabilité en longueur d'onde, seuil de dommage) mais aussi les pertes, défauts et inhomogénéités des cristaux liquides lors des réarrangements moléculaires. Enfin, cette architecture a l'avantage d'être compatible de substrats transparents dans l'infra-

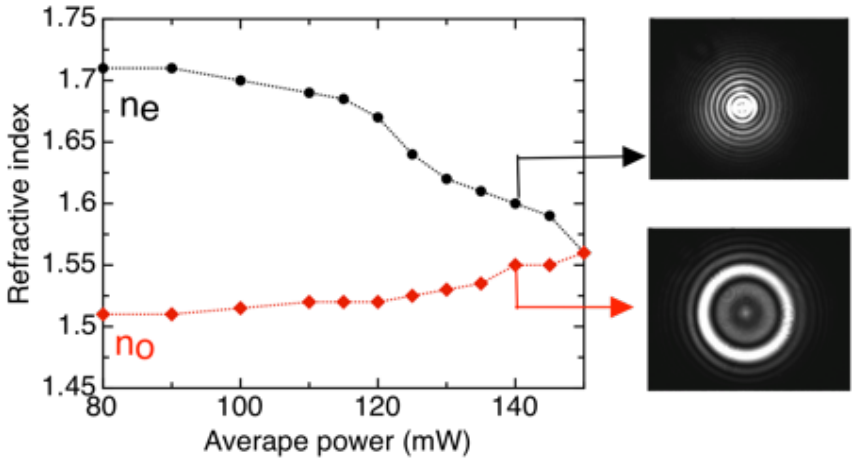

FIGURE 5.6 – Évolution de l'indice de réfraction d'un nématique induite optiquement par l'absorption d'un laser infra-rouge dans le substrat (ITO)].

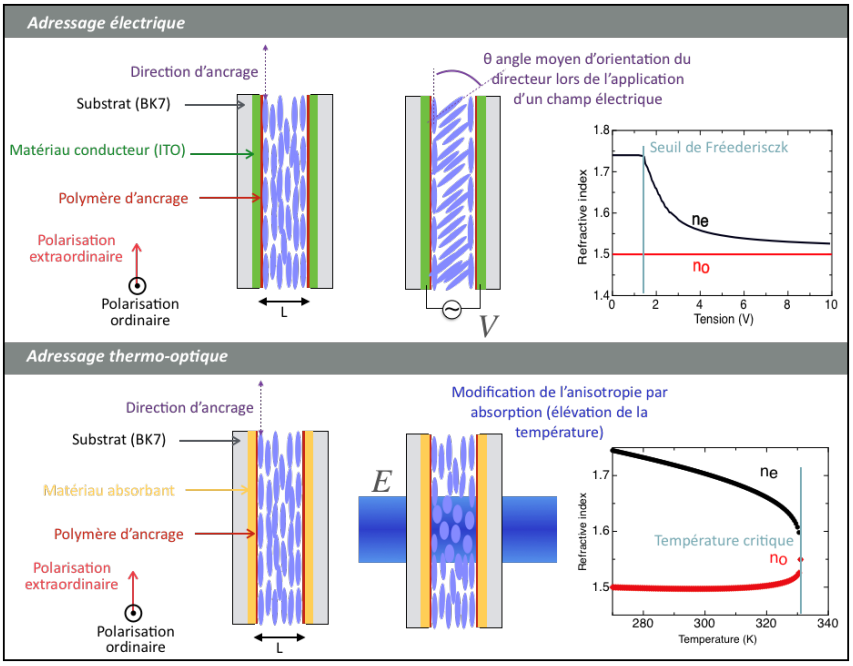

FIGURE 5.7 – En haut : contrôle électrique traditionnel de cellules nématiques par adressage électrique : schéma de principe et courbes de biréfringence. En bas : adressage thermo-optique : schéma de principe et courbes de biréfringence.

rouge moyen et donc d'étendre la gamme spectrale d'utilisation des cellules. Compte tenu de son épaisseur, la valve est caractérisée par une relativement grande variation du chemin optique, correspondant à un déphasage de 2π même aux grandes longeurs d'onde. Suite aux premières démonstrations durant le travail de thèse de Vittorio di Pietro, un brevet a été déposé en co-propriété CNRS-Fastlite. L'un des premières applications de cette valve est le façonnage d'impulsions de spectre très large (de 540 nm à 2500 nm) [77], comme détaillé dans la publication jointe. L'étude de la valve s'est poursuivie avec le projet THERMOPTIX (financement IDEX UCA JEDI).

L'un des objectifs de la thèse de Loïc Ramousse (CIFRE) est de lever différents verrous scientifiques et technologiques sur la valve optique :

- achromaticité du dispossitif : les expériences préliminaires ont été réalisées à λ =1.5 µm. Les applications visées nécessitent d'établir le fonctionnement du modulateur pour les gammes spectrales suivantes : 500 nm – 950 nm (sources impulsionnelles dites au cycle optique) ; 1.030 µm (lasers femtosecondes Yb) ; 1 µm-2 µm (sources paramétriques optiques) :
- efficacité de l'adressage thermo-optique pour réduire la puissance optique nécessaire
- obtention d'une haute résolution spatiale (<100 µm)
- optimisation du temps de réponse et du temps de rafraîchissement
- établissement des conditions de stabilité et réversibilité du déphasage induit.

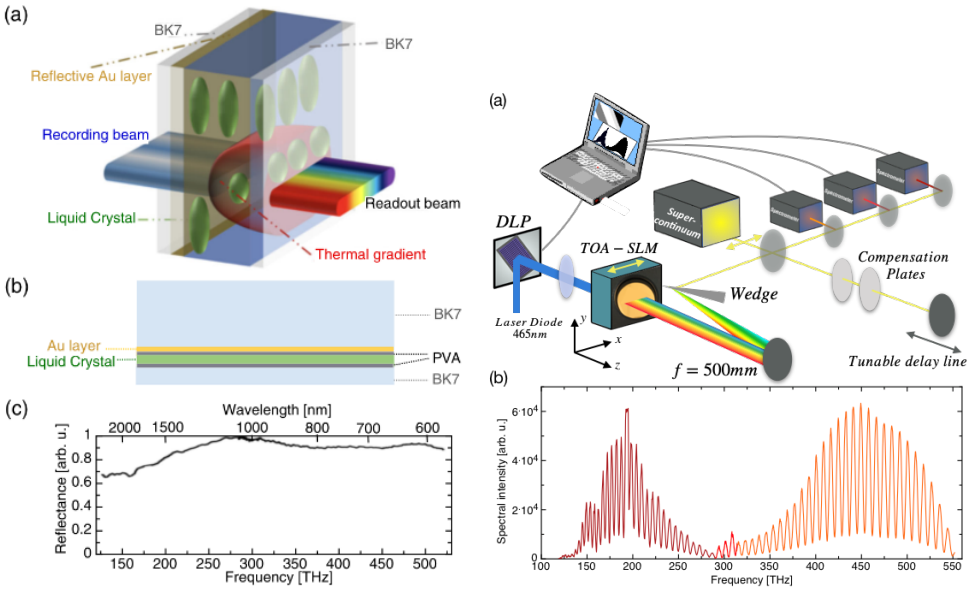

FIGURE 5.8 – A gauche : schéma de principe de la valve optique (a) et (b), réflectivité de la valve (c). A droite : application au façonnage d'impulsions courtes.

Continuously tunable femtosecond delay-line based on liquid crystal cells

Aurélie Jullien,[1,*] **Umberto Bortolozzo,**[1] **Stéphanie Grabielle,**[2] **Jean-Pierre Huignard,**[3] **Nicolas Forget,**[2] **and Stefania Residori**[1]

[1]*Institut Non Linéaire de Nice, Université de Nice Sophia-Antipolis, CNRS UMR 7335, 1361 route des Lucioles, 06560 Valbonne, France*
[2]*Fastlite, Les collines de Sophia, 1900 route des cretes, 06560 Valbonne, France*
[3] *Jphopto, 20 Rue Campo Formio, 75013 Paris, France*
[*]*Aurelie.Jullien@inln.cnrs.fr*

Abstract: We introduce a new device for group and phase delay steering of femtosecond pulse trains that makes use of cascaded, electrically driven, nematic liquid-crystal cells. Based on this approach we demonstrate a continuously tunable optical delay line. The simple collinear implementation with no moving parts enables to shape the achievable temporal range with sub-femtosecond accuracy. By appropriately choosing the bias voltages applied to the cascaded cells, the imparted group delay can be made either positive or negative and precisely adjusted. Moreover, independent control of the group delay and the phase of femtosecond pulses is demonstrated.

OCIS codes: (140.7090) Ultrafast lasers; (320.5540) Pulse shaping; (230.3720) Liquid-crystal devices.

References and links

1. A. M. Weiner, "Ultrafast optical pulse shaping: A tutorial review," Opt. Comm. **184,** 3669-3692 (2011).
2. F. Krausz and M. Ivanov, "Attosecond physics," Rev. Mod. Phys. **81**, 163-234 (2009).
3. I. A. Walmsley and C. Dorrer, "Characterization of ultrashort electromagnetic pulses," Adv. of Opt. and Phot. **1,** 308-437 (2009).
4. A. Börzsönyia, A.P. Kovacs, M. Gorbe and K. Osvay, "Advances and limitations of phase dispersion measurement by spectrally and spatially resolved interferometry," Opt. Comm. **281,** 3051-3061 (2008).
5. P. Tian, D. Keusters, Y. Suzaki and W. S. Warren, "Femtosecond Phase-Coherent Two-Dimensional Spectroscopy," Science **300,** 1553 (2003).
6. T. Brixner, I. V. Stiopkin and G. R. Fleming, "Tunable two-dimensional femtosecond spectroscopy," Opt. Lett. **29,** 884-886 (2004).
7. J. Rehault, M. Maiuri, A. Oriana and G. Cerullo "Two-dimensionnal electronic spectroscopy with birefringent wedges," Rev. of Sci. Inst. **85,** 123107 (2014).
8. A. Kolomenskii, J. Strohaber, N. Kaya, G. Kaya, A. V. Sokolov and H. A. Schuessler "White-light generation control with crossing beams of femtosecond laser pulses," Opt. Express **24,** 282-293 (2016).
9. S. Zhou, F. W. Wise and D. G. Ouzounov, "Divided-pulse amplification of ultrashort pulses," Opt. Lett. **32,** 871-873 (2007).
10. M. Hanna, F. Guichard, Y. Zaouter, D. N Papadopoulos, F. Druon and P. Georges, "Coherent combination of ultrafast fiber amplifiers," Journ. of Phys. B **49,** 062004 (2016).
11. D. Brida, C. Manzoni and G. Cerullo, "Phase-locked pulses for two-dimensional spectroscopy by a birefringent delay line," Opt. Lett. **37,** 3027-3029 (2012).
12. H. Jacqmin, A. Jullien, B. Mercier, M. Hanna, F. Druon, D. Papalopoulos and R. Lopez-Martens, "Passive coherent combining of CEP-stable few-cycle pulses from a temporally divided hollow fiber compressor," Opt. Lett. **40,** 709-711 (2015).
13. H. Jacqmin, A. Jullien, B. Mercier and R. Lopez-Martens, "Temporal pulse division in hollow fiber compressors," J. Opt. Soc. Am. B, **32,** , 1901-1909 (2015).
14. D.-K. Yang and S.-T. Wu, *Fundamentals of Liquid Crystal Devices* Wiley (2012).

#263766 Received 21 Apr 2016; revised 7 Jun 2016; accepted 10 Jun 2016; published 17 Jun 2016

15. I.-C. Khoo, Liquid crystals, *Physical Properties and Nonlinear Optical Phenomena* Wiley (1995).
16. S.-T. Wu, U. Efron and L. D. Hess, "Birefringence measurements of liquid crystals," App. Opt. **23,** 3911-3915 (1984).
17. U. Bortolozzo, S. Residori and J.-P. Huignard, "Transmissive liquid crystal light-valve for near-infrared applications," App.Opt. **52,** E73-E77 (2013).
18. S. Residori, U. Bortolozzo and J.-P. Huignard, "Slow and Fast Light in Liquid Crystal Light Valves," Phys. Rev. Lett. **100,** 203603 (2008).
19. T. Kuki, H. Fujikake, T. Nomoto and Y. Utsumi, "Design of a Microwave Variable Delay Line Using Liquid Crystal, and a Study of Its Insertion Loss," Electron. Comm. in Japan **85,** 90-96 (2002).
20. D. Dolfi, M. Labeyrie, P. Joffre and J.-P. Huignard, "Liquid Crystal microwave phase shifter," Electron. Lett. **29,** 926-928 (1993).
21. C.-S. Yang, T.-T. Tang, P.-H. Chen, R.-P. Pan, P. Yu and C.-L. Pan, "Voltage-controlled liquid-crystal terahertz phase shifter with indium-tin-oxide nanowhiskers as transparent electrodes," Opt. Lett. **39,** 2511-2513 (2014).
22. C.-Y. Chen, C.-F. Hsieh, Y.-F. Lin, R.-P. Pan and C.-L. Pan, "Magnetically tunable room-temperature 2 pi liquid crystal terahertz phase shifter," Opt. Exp. **12,** 2625-2630 (2004).
23. N. Sanner, N. Huot, E. Audouard, C. Larat, J.-P. Huignard and B. Loiseaux, "Programmable focal spot shaping of amplified femtosecond laser pulses," Opt. Lett. **30,** 1479-1481 (2005).
24. L. Cattaneo, M. Savoini, I. Muševič, A. Kimel and T. Rasing, "Ultrafast all-optical response of a nematic liquid crystal," Opt. Exp. **23,** 14010-14017 (2015).
25. L. Song, S.E Fu, Y. Liu, J. Zhou, V. G. Chigrinov and I. C. Khoo, "Direct femtosecond pulse compression with miniature-sized Bragg cholesteric liquid crystal," Opt. Lett. **38,** 5040-5042 (2013).
26. J. Li, C.-H. Wen, S. Gauza, R. Lu and S.-T. Wu, ''Refractive Indices of Liquid Crystals for Display Applications," J. Display Techno. **1,** 51-61 (2005).
27. I. C. Khoo, "Nonlinear optics, active plasmonics and metamaterials with liquid crystals," Progress in Quantum Electronics **38,** 77-117 (2014).
28. R. Dabrowski, P. Kula and J. Herman, "High Birefringence Liquid Crystals," Crystals **3,** 44-4823 (2013).
29. L. Lepetit, G. Chériaux and M. Joffre , "Linear techniques of phase measurement by femtosecond spectral interferometry for applications in spectroscopy," J. Opt. Soc. Am. B **12,** 2467–2474 (1995).
30. S.-T. Wu and C.-S. Wu, "High speed liquid crystal modulators using transient nematic effect," Journ. of App. Phys. **65,** 527-532 (1989).
31. M. Görbe, K. Osvay, C. Grebing and Günter Steinmeyer, "Isochronic carrier-envelope phase-shift compensator," Opt. Lett. **33,** 2704-2706 (2008).
32. O. Gobert, G. Mennerat, C. Cornaggia, D. Lupinski, M. Perdrix, D. Guillaumet, F. Lepetit, T. Oksenhendler and M. Comte, "Electro-optic prism-pair setup for efficient high bandwidth isochronous CEP phase shift or group delay generation," Opt. Comm. **366,** 45-49 (2016).

1. Introduction

Ultrafast optical waveforms propagating in any dispersive medium experience different group and phase velocities. Controlling these quantities is the basis of temporal manipulation and shaping of ultrafast pulses, while stabilizing the slippage between them (carrier-to-envelope phase, CEP) has paved the way to attosecond physics [1, 2]. Group delay manipulation, among other pulse shaping objectives, provides tools for temporal division of femtosecond pulses. Devices for temporal division are widely employed for measurement and characterization of ultrashort pulses [3], self-referenced spectral interferometry [4], ultrafast spectroscopy [5, 6, 7], nonlinear optics [8] and temporal multiplexing [9, 10]. For most of these applications, accurate tunability and sub-fs resolution of the introduced delay are required. As a complement to mechanical delay lines, collinear setups based on birefringent elements ensure simplicity, compactness and robustness. However, the achievable delays are discrete and characterized by little tunability. A couple of elegant solutions mixing collinearity and continuous tunability have been recently proposed : birefringent wedges for electronic spectroscopy [11] and tilting birefringent plates with out-of-axis orientation for coherent combining of ultrashort pulses [12, 13]. Both schemes are based on crystallographic material and require mechanical action on it, which could result in a certain numbers of drawbacks due to the moving parts.

In this paper, we propose to exploit the large and electrically-controllable birefringence of nematic liquid crystals for precise control of the group and phase delays of femtosecond pulses. To that purpose, liquid crystals intrinsically present very interesting optical features : a much

#263766 Received 21 Apr 2016; revised 7 Jun 2016; accepted 10 Jun 2016; published 17 Jun 2016

higher birefringence than crystals, together with the ability to change their optical properties through molecular reorientation in response to a low voltage or weak magnetic field. Extensively studied for light manipulation and control [14, 15], liquid-crystals have been, for instance, demonstrated as tunable phase-shifter for optical laser frequencies [16], nonlinear optical Kerr elements in light-valve configuration [17, 18], tunable delay line or phase-shifter in the microwave band [19, 20], or efficient phase-shifters for THz radiation, with either voltage [21] or magnetic control [22]. However, even though liquid crystals are transparent and highly birefringent over a broad spectral range [15], application to the manipulation of ultrashort pulses has been quite occasional so far. Apart from spectral or spatial shaping by spatial-light-modulators in the Fourier plane [1, 23], only a very few studies report on the use of liquid-crystals for direct manipulation of ultrafast pulses, either via a coherently excited nonlinear response in nematics [24] or by exploiting the Bragg resonance in a cholesteric cell [25].

Here, we demonstrate an innovative and efficient device to control the group and phase delay of femtosecond pulses, which is realized by appropriately addressing one or two electrically-driven nematic liquid-crystal cells. Based on this approach, we first focus on the group delay tuning with a single nematic cell and demonstrate a simple, collinear, continuously tunable optical delay line suitable for ultrafast pulse trains. The tested devices afford various group delay ranges, from $\sim$10fs to $\sim$100fs, with an applied voltage between 0V and 10V. The response time evolves between second to millisecond time-scale. Electrically-controlled temporal resolution can be chosen between 2.3 fs and $<$0.1fs. Then, two cascaded liquid crystal cells are shown to provide temporal division with a delay tunable between -50fs and +50fs, and sub-fs precision. By appropriately choosing the couple of bias voltages applied to the cascaded cells, the introduced group delay can be made either positive or negative and finely adjusted around the chosen value. Finally, we highlight an additional possibility. Adequate electrical control of two cells with different thicknesses is shown to afford independent tuning of the phase and group delays. Altogether, these results demonstrate that nematic liquid-crystals cells enable the high-precision manipulation of optical pulses in the femtosecond regime. The setup is simple and offers many advantageous features, such as compactness, continuous tunability, collinearity and no moving parts.

2. Femtosecond continuously tunable delay line with a single liquid crystal cell

We first implement temporal division and group delay control of femtosecond pulses by using a single liquid-crystal cell. The tunable delay line is realized by using as the birefringent medium the nematic liquid crystal (LC) mixture E7, inserted in between two 0.7mm-thick fused-silica substrates. Both of them include a conductive layer of ITO (Indium-tin oxyde) for electrical control of the molecular director. A thin film of polyvinyl alcohol (PVA) is spin-coated on the ITO layer with subsequent rubbing to favor initial alignment of the molecules in a plane parallel to the substrate (splay geometry). Four samples with different thickness ranging from 25 μm to 130 μm were prepared. The experiment is set up as shown in Fig. 1(a). The laser system is a Femtofiber PRO IRS (Toptica Photonics) oscillator delivering 40 fs pulses, at 1570 nm, with 200 mW average power. The repetition rate is 80 MHz. The pulses are frequency-doubled in a 0.25 mm BBO crystal to produce about 30 fs pulses, with a spectrum centered at 770 nm. A half-waveplate and a polarizer set the linear polarization direction to 45° with respect to the nematic director of the LC cell, so that two sub-pulses, respectively P and S polarized, propagate through the LC cell. An analyzer, a broadband thin film polarizer parallel to the first one, projects the two cross-polarized sub-pulses onto the same polarization direction. They finally interfere in a spectrometer (Avantes). If the two sub-pulses propagate with different group delay, the interference spectrum presents fringes with a period inversely proportional to the relative delay.

#263766 Received 21 Apr 2016; revised 7 Jun 2016; accepted 10 Jun 2016; published 17 Jun 2016

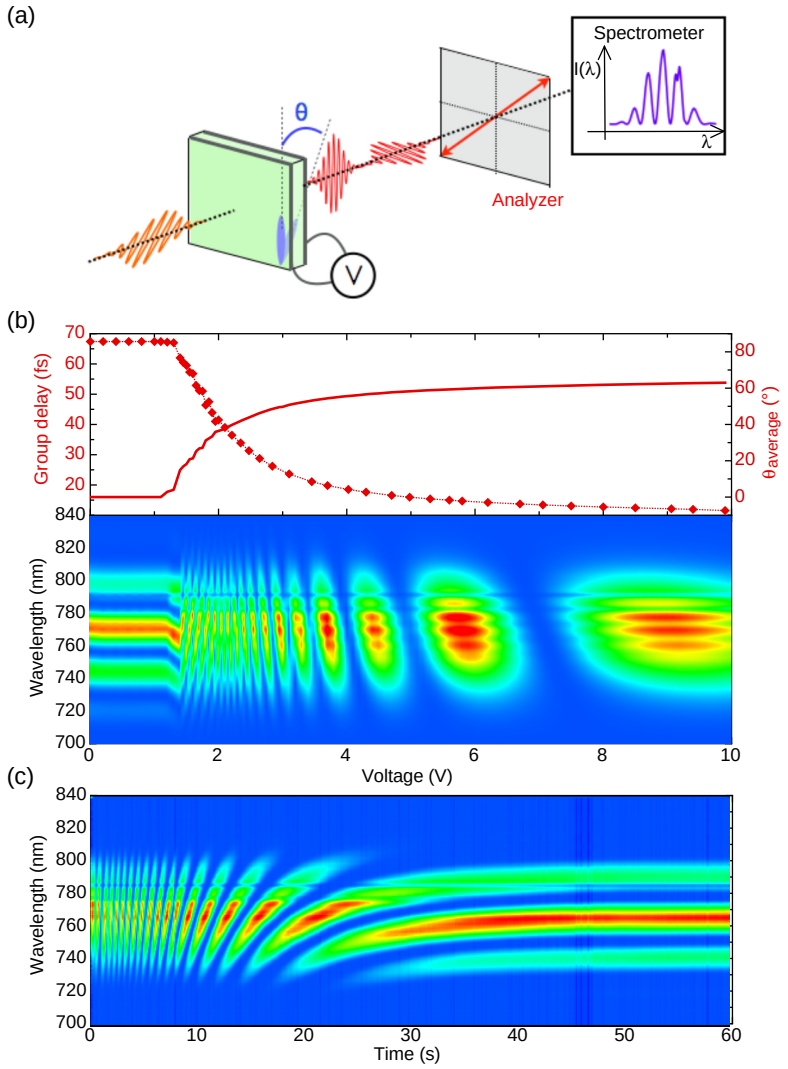

Fig. 1. (a) Principle of the experiment. Green : LC cell, blue : initial molecular orientation. (b) (colormap) Analyzed interference spectrum measured as a function of the voltage, for the 88 μm - thick LC cell. The upper graph shows the retrieved group delay (points) and corresponding tilt angle θ (solid line) averaged over the cell thickness. (c) Analyzed interference spectrum recorded regularly (2 ms) as a function of time, for the 88 μm - thick LC cell. The bias voltage of 10V is shut down at $t = 0$.

#263766 Received 21 Apr 2016; revised 7 Jun 2016; accepted 10 Jun 2016; published 17 Jun 2016

Phase and group delays acquired in the LC mixture for each polarization directions are respectively defined as :

$$\tau_{(\phi)o,e} = n_{o,e}\frac{L}{c} \tag{1}$$

$$\tau_{(g)o,e} = n_{(g)o,e}\frac{L}{c} \quad \text{with} \quad n_{(g)o,e} = n_{o,e} + \omega_0 \frac{dn_{o,e}}{d\omega} \tag{2}$$

n_o (resp. n_e) is the ordinary (resp. extraordinary) refractive index of the LC mixture, $n_{(g)o}$ (resp. $n_{(g)e}$) is the ordinary (resp. extraordinary) group index, L is the LC thickness and ω_0 the central laser frequency. In the following, group index, group delay and group delay dispersion (GDD) are calculated for $\lambda_0 = 770nm$.

The LC cells, at normal incidence, were first characterized with no voltage applied. The orientation of the nematic director is then determined by the anchoring conditions. The S-polarized pulse propagates through a purely extraordinary medium. The refractive index difference with the P-polarized ordinary wave, which is related to the birefringence of the LC mixture, is maximum and can be expressed as $\Delta n_{o-e} = n_e - n_o$. For nematic E7, in the considered spectral range, the group index difference $\Delta n_{(g)o-e}$ is 0.23 [26]. The two sub-pulses consequently emerge out of the cell with a temporal spacing proportional to the LC thickness. Simple Fourier Transform of the interference spectrum enables to recover the introduced group delay and thus to deduce the sample thickness. Cells $LC_{1,2,3}$ induce an initial group delay of 104 ± 0.2 fs, 67 ± 0.2 fs and 41 ± 0.2 fs, respectively. Uncertainty is here related to the Fourier transformation. The delay is also likely to vary by ± 1 fs on a day-to-day basis because of alignment or temperature changes. Respective thicknesses are $136 \pm 2\,\mu$m, $88 \pm 2\,\mu$m and $55 \pm 1\,\mu$m, as summarized in Table 1. A thinner cell, LC_4, leading to a delay smaller than the pulse width, was calibrated with respect to the other samples : Fourier transform of the interference spectrum produced by two successive cells with parallel orientation provides the additional group delay. LC_4 is found to be $26 \pm 1\,\mu$m-thick.

GDD introduced by E7 is $\phi_o^{(2)}$ = 120 fs^2/mm and $\phi_e^{(2)}$ = 320 fs^2/mm. Table 1 presents the total GDD for each cell, mainly originating from the substrates. Whatever the cell thickness, the transmission is 75%, limited by Fresnel losses on the uncoated substrates and absorption in the ITO layers. AR-coating and thinner ITO would raise this value.

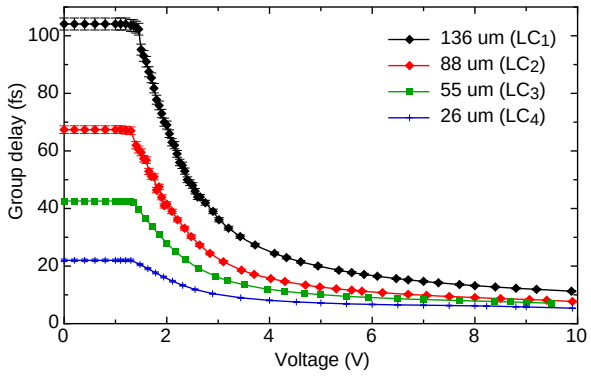

Fig. 2. Measured group delay as a function of the applied voltage, according to the liquid crystal cell thickness.

When an external electric field is applied, its interaction with the LC induces molecular reorientation [14]. As E7 presents a positive dielectric anisotropy, the molecules tend to reorient

#263766 Received 21 Apr 2016; revised 7 Jun 2016; accepted 10 Jun 2016; published 17 Jun 2016

Table 1. **Liquid crystal cells thickness, GDD ($\lambda_0 = 770nm$) in both polarization directions and properties as a tunable delay line for several bias voltages. δ_t is the temporal tunability and τ is the response time.**

		LC_1	LC_2	LC_3	LC_4
Thickness (μm)		136	88	55	26
	$\phi_o^{(2)}(fs^2)$	69	64	60	56
	$\phi_e^{(2)}(fs^2)$	95	81	71	61
2V	$\delta_t(fs/50mV)$	2.3	1.3	0.75	0.35
	$\tau(s)$	20	10	5	2
4V	$\delta_t(fs/100mV)$	0.7	0.4	0.25	0.1
	$\tau(s)$	3	1	0.7	0.1
6V	$\delta_t(fs/100mV)$	0.3	0.2	0.07	0.03
	$\tau(s)$	0.1	0.01	0.001	0.001
8V	$\delta_t(fs/100mV)$	0.1	0.07	0.04	0.03
	$\tau(s)$	0.001	0.001	0.001	0.001

along the applied electric field direction [27, 28]. A waveform generator produces a sinusoidal AC voltage (frequency 1 kHz) with an amplitude between 0V and 10V. The interference spectrum is registered as the voltage regularly increases (step : 50 mV between 1.3V and 3V, 100 mV otherwise) for each LC cell. The integration time is 1 ms and the spectrum is monitored until stability is reached. The resolution of the spectrometer is 0.3 nm, well below the narrowest fringes spacing (19 nm for a relative group delay of 100 fs). For a given bias voltage in static conditions, the stability of the interference pattern is found to lie within the spectrometer resolution. The resulting spectra are plotted as a 2D map, as shown in Fig. 1(b) for LC_2 (88 μm thick). The initial interference spectrum remains constant up to the Freedericksz transition voltage (1.2 V for E7), above which the molecules start to reorient. In the current implementation, the extraordinary index is then progressively changed according to the following law :

$$n_e(\theta) = \frac{n_o n_e}{\sqrt{cos^2\theta\ n_o^2 + sin^2\theta\ n_e^2}} \tag{3}$$

with θ the local angle formed between the nematic director and the original alignment axis. Note that θ depends on the voltage and is not uniform across the LC thickness, as reorientation occurs mostly in the middle of the cell, while closer to the substrates the anchoring conditions dominate [14]. Anyway, the average tilt angle increases with the voltage, therefore the average extraordinary index decreases as the voltage increases, inducing narrowing of the temporal spacing between the pulses and significant changes of the interference pattern. Important reorientation between 2V and 4V is followed by a saturated behavior with progressive constructive and destructive interferences. The spectrogram is analyzed with Fourier Transform Spectral Interferometry methods (FSTI, [29]) and enables to recover the introduced group delay as a function of the voltage, as shown in the upper graph of Fig. 1(b). The average refractive index, and thus the average value of θ, according to the applied voltage can be deduced from the experimental group delay. Measured reorientation as a function of the field, plotted in Fig. 1(b),

#263766 Received 21 Apr 2016; revised 7 Jun 2016; accepted 10 Jun 2016; published 17 Jun 2016

presents a typical trend [14].

Figure 2 summarizes the group delay dependence with the voltage, measured for the four considered LC cells. The group delay is easily tunable over several tens of femtosecond, depending on the initial delay fixed by the LC properties and thickness. At 10V, the medium is not purely ordinary in the S-polarization direction, as the molecular reorientation is less effective close to the substrates because of the strong anchoring conditions. The delay for this maximum voltage only slightly varies with the sample and is $\sim$10fs. The temporal tunability per voltage step is deduced from the spectrograms and is reported in Table 1. It depends on the cell thickness and the bias voltage, and is ranging from a few fs per 50mV to less than 0.1fs per 100mV. The highest resolution is reached for a high bias voltage. Under this condition, as 0.1 fs corresponds to a 250 mrad phase-shift ($\lambda_0 = 770nm$), the change is visible in the spectrogram as a shift of the interference pattern of a few nm, above the resolution of the spectrometer.

The optical response to the electric field is governed by collective motion of the molecules and rotational viscosity of the medium, and again depends on the cell thickness and the applied voltage. The response time indicated in Table 1 is measured for small voltage increment (50 mV or 100 mV) for different bias voltages (2V, 4V, 6V, 8V). The results are in good agreement with previous publications [30]. The optical response is rather slow for the larger tunability settings (a few seconds) but is significantly reduced at higher bias voltage, enabling kHz adjustment rate. Furthermore, the remanence of the molecules orientation can be used for faster acquisition of the full delay range of thick cells. As an illustration, Fig. 1(c) shows the analyzed spectrum regularly logged (every 2 ms over 1 minute, thanks to the spectrometer software), for LC_2, when the voltage is shut down from 10V to 0V at $t = 0$. The full delay range in this transient nematic state can be acquired in less than 1 minute with a temporal resolution of 0.1 fs per acquisition step. These properties may contribute to the eligibility of such devices to ultrafast pulse train manipulation.

Given these observations, applications such as ultrafast spectroscopy or coherent combining, which require fast and precise control of the group delay and/or phase delay, could benefit of the combination of two LC cells. A thick one would introduce a variable main delay while a thiner one would provide nearly real-time (for kHz or sub-kHz repetition rate laser systems), tunable, precise adjustment. Furthermore, we underline that thin LC cells can be adapted to phase-delay control and could advantageously complete bulk thin wedges currently used for CEP stabilization.

3. Cascaded liquid crystal cells

In this section, by cascading two LC cells, we realize a delay line where the relative group delay of the femtosecond pulses can be made either positive or negative depending on the values of the bias voltages.Such tunable delay line presents interesting prospects for temporal measurement purposes. In that case, both positive and negative delays are required (e.g. for an autocorrelation measurement) and controllable delay around the temporal overlap of the two sub-pulses is needed.

We performed this experiment by cascading two LC cells with crossed orientations and independent voltage control, as shown in Fig. 3(a). Under the action of the electric field, the two nematic directors are rotated by an angle θ_1 and θ_2, respectively. Two nearly identical cells are employed, presenting a thickness of 88 μm. The measurements reported in Fig. 1(b) enable to extrapolate the delay introduced by the cascaded crossed cells scheme. Figure 3(b) shows the calculated output group delay between the two sub-pulses as a function of the two voltages. For couples of identical voltages, the delay is nearly zero. The widest temporal range around the overlap is provided by increasing one voltage while decreasing symmetrically the second one.

Both cells are aligned close to auto-collimation. When no voltage is applied, the temporal

#263766 Received 21 Apr 2016; revised 7 Jun 2016; accepted 10 Jun 2016; published 17 Jun 2016

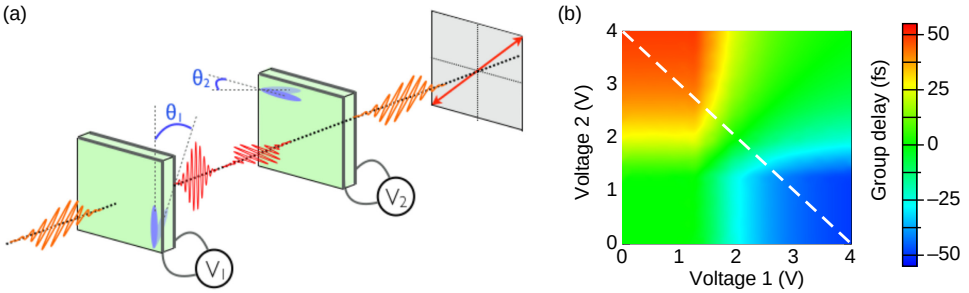

Fig. 3. (a) Tunable delay line with two cascaded LC cells with crossed orientation. (b) Extrapolated dependence of the introduced group delay as a function of the voltage applied on both cells, considering two identical birefringent media (88 μm - thick). The white line indicates the couples of bias voltages applied in the experiment.

overlap is supposed to be achieved at the output of the second cell, meaning that the two sub-pulses can be coherently added. In that case, the analyzed spectrum is identical to the input one and the transmitted energy through the analyzer is maximum. Because of a small thickness discrepancy between the two cells, a slight horizontal tilt of the second one is needed to achieve this condition. The voltage on the first cell is then increased from 0V to 4V, while the voltage on the second cell is simultaneously decreased from 4V to 0V. The increment step is 10 mV for both voltages. The interference spectra are registered after the analyzer following the procedure described in the previous section. The resulting group delay evolution issued from FTSI analysis is shown in Fig. 4.

The achievable group delay is tunable over -50fs / +50fs temporal range, with a linear dependence with the voltage between $V_1 \sim 1.5V$ and $V_1 \sim 2.5V$. The analyzed spectrum map for $1.6V < V_1 < 2.4V$ is plotted in Fig. 4(b). One can see wavelength-dependent constructive and destructive interferences, as a function of the two applied voltages. As the voltages tune the relative delay, the map is a spectrally-resolved correlation of the fields of the two sub-pulses. When the temporal overlap is reached (envelopes and carrier waves), all the spectral components are coherently added and transmitted through the analyzer. The overlap is indicated on the spectrogram ($V_1 = 2.06V$, $V_2 = 2.05V$) and the input laser spectrum is then fully recovered after the analyzer, as shown in Fig. 4(c). The spectral shift of the interference pattern between each acquisition step provides the achievable temporal resolution in this portion : 0.5 fs per acquisition step. Higher resolution can be achieved by reducing the voltage increment or by choosing other couples of voltage values, according to Fig. 3(b).

This experiment demonstrates the eligibility of the proposed setup for collinear coherent combining of femtosecond pulses. Furthermore, this crossed LC cells device is a simple, achromatic delay line suitable for autocorrelation-based temporal measurements of ultrashort pulses. GDD is here $\sim$145 fs^2 and can be reduced by using thinner substrates and combining the cells so as to remove one interface. The overall temporal range can be simply extended by using other liquid crystal material or increasing the cell thickness.

4. Independent control of the phase and group delay

To further emphasize the pulse shaping skills of the proposed device, we also demonstrate the ability to independently control the group delay or the phase of the propagating pulse. Such features are of interest for CEP-controlled ultrafast laser or OPA systems. Furthermore, changing the phase with no modification of the delay (e.g. timing) or changing the relative

#263766 Received 21 Apr 2016; revised 7 Jun 2016; accepted 10 Jun 2016; published 17 Jun 2016

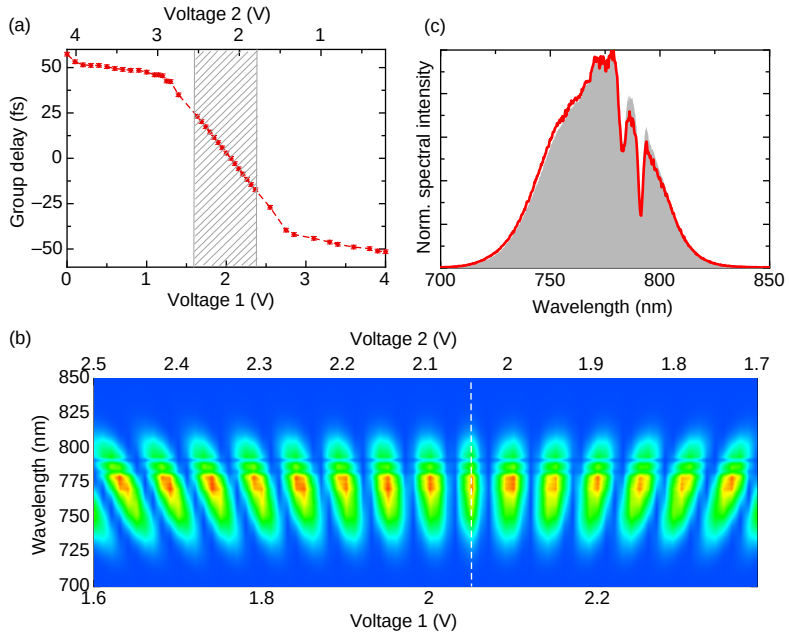

Fig. 4. (a) Group delay measured at the output of the cascaded cells as presented in Fig. 3(a), as a function of the voltages (V_1 and V_2, two x-axis graduations) applied on the two cells. The cells present nearly identical thickness (88 μm). Their initial director orientations are crossed. (b) Measured output spectrum for a narrower voltage range (hatched area in (a)). A white line indicates the temporal overlap (see text). (c) Corresponding output spectrum (red, $V_1 = 2.06V$, $V_2 = 2.05V$) compared to the initial laser spectrum (shaded).

spacing between two pulses with constant relative phase might provide an additional insight in high-resolution pump-probe experiments. So far, such capabilities have been demonstrated with bulk prism pairs : thin wedges made from carefully chosen optical material [31] and electro-optic prisms of RTP crystal [32]. Both methods require accurate sizing and angular orientation of the prisms.

The principle relies on the different evolution of the group index (resp. group delay) and the refractive index (resp. phase delay) in the LC as a function of θ, for the wave polarized in the rotation plane of the molecular director under the action of the electric field. In order to achieve independent control of the phase and group delay of this wave, two cascaded cells with separate voltage control are needed. Furthermore, the capability to produce very thin LC cells ($< 10\mu m$) eases the experimental realization.

Figure 5(a) shows the tested implementation : two cells are positioned at normal incidence with parallel orientations. They present different thicknesses : LC_1 (136 μm) is used together with a fifth cell, whose measured LC (E7) thickness is 8.2 μm . For such a cell, the maximum relative group delay introduced when no voltage is applied is 6.3 fs. In the discussed setup, the relative group delay and the relative phase between the two sub-pulses can be simply expressed as :

$$\Delta t = \frac{1}{c}[n_{(g)e}(\theta_1)L_1 + n_{(g)e}(\theta_2)L_2 - n_{(g)o}(L_1 + L_2)] \tag{4}$$

$$\Delta\phi = \frac{2\pi}{\lambda}[n_e(\theta_1)L_1 + n_e(\theta_2)L_2 - n_o(L_1 + L_2)] \tag{5}$$

#263766 Received 21 Apr 2016; revised 7 Jun 2016; accepted 10 Jun 2016; published 17 Jun 2016

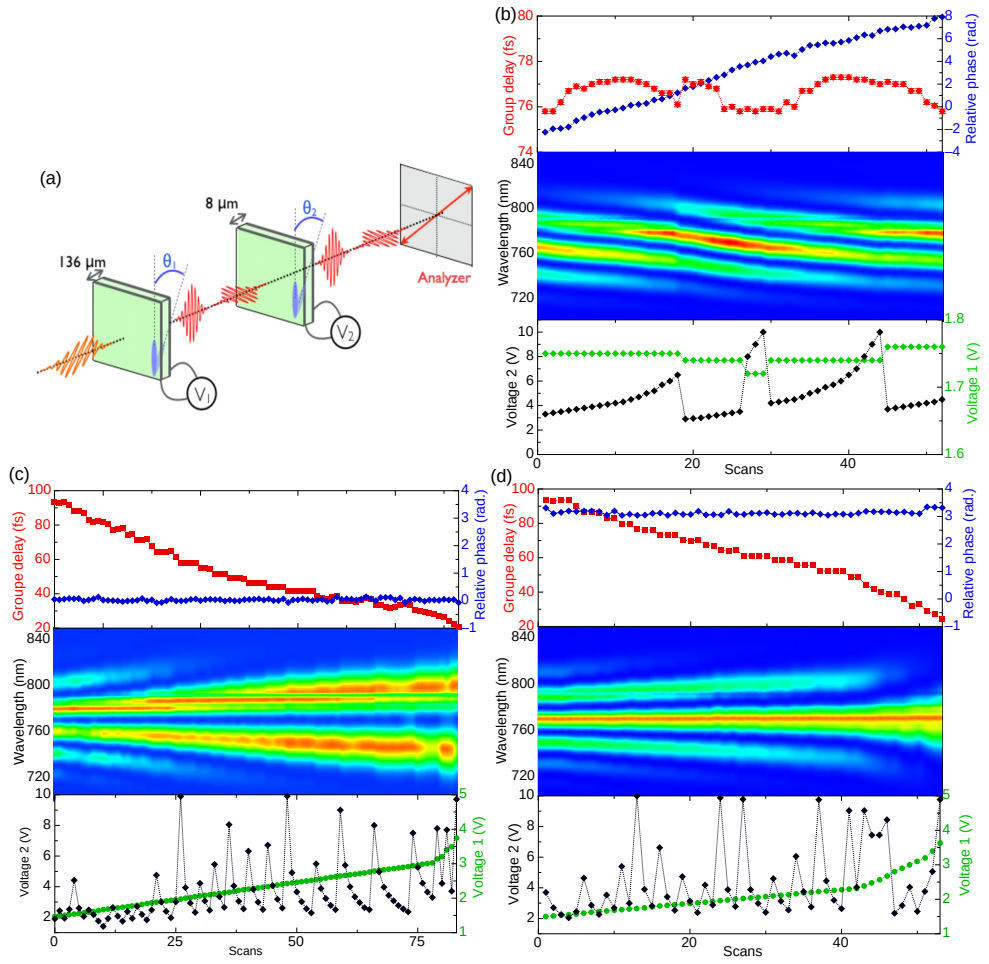

Fig. 5. (a) Cascaded LC cells with parallel orientations for independent control of the phase and group delay. Phase control (b) and group delay control for two different phase values (c,d) : measured group delay and relative phase (upper graphs) and corresponding spectra registered after the analyzer (middle graphs). The data are successfully recorded for different couples of voltage values indicated on the lower graphs.

where $L_1 = 136\mu m$, $L_2 = 8.2\mu m$, $n_{(g)e}(\theta)$ and $n_e(\theta)$ are defined according to Eq. (2) and Eq. (3). θ_1 and θ_2, the molecular orientations in each cell, are the two tunable parameters, through the applied voltages V_1 and V_2.

Given the respective cell thicknesses, the first one mainly manages the relative group delay, while full voltage excursion on the second enables to adjust the relative phase. Finally, in this setup, the ordinary wave (P-polarized) can be seen as a reference beam, as its propagation is not affected by the molecular reorientation. The extraordinary wave alone undergoes group delay and phase changes. The interference spectrum between the two waves measured after the analyzer enables to monitor and analyze those changes.

The two voltages are first tuned to change the phase continuously, while keeping constant the group delay. Measured group delay, phase and the resulting spectrogram are shown in Fig. 5(b). In this case, the voltage rise on the thin cell affords phase excursion while minor voltage varia-

#263766 Received 21 Apr 2016; revised 7 Jun 2016; accepted 10 Jun 2016; published 17 Jun 2016

tions on the thick one enables to maintain the group delay nearly constant. The required voltage increments are 100 mV for V_2 and 10 mV for V_1. As a result, the phase can be adjusted over 2.5π with a precision of 200 mrad while the group delay excursion is reduced to 1.5 fs.

Symmetrically, the group delay can be tuned while the phase is maintained to an arbitrary chosen value. This is illustrated in Fig. 5(c,d) for two different phase values. To do so, the voltage on the first cell is progressively increased (20 mV step) from 1V to 4V to initiate significant group delay changes. The second cell, whose voltage oscillates between 2V and 10V, enables to precisely adjust the phase to the desired value. 10 mV precision is then required. In both cases, the phase is constant with 70 mrad RMS noise and the group delay evolves between 90 fs and 20 fs. The temporal resolution is better than 2 fs and could be minimized by the use of a thinner second LC cell.

The proposed simple setup composed of two cascaded LC cells offers precise pulse manipulation capabilities. The alignment is straightforward. Furthermore, the device is static, requires only low-voltage electrical control and is easily scalable in its lateral dimensions.

5. Conclusion

To conclude, we have demonstrated a femtosecond, continuously tunable, optical delay-line based on one or two cascaded nematic liquid-crystal cells. The proposed setup is versatile. The introduced group delay, response time and temporal resolution are adjustable depending on the desired application. Cascaded cells enable to shape the achievable temporal range as well as the temporal accuracy. Both the phase and group delay can be controlled with such devices, independently if needed. The experimental implementation is straightforward, no mechanical action is required as low voltage control is only needed. The proposed performances can be tuned by modifying the cascaded cells architecture, the cells thickness, the material, and the voltage increment. This scheme is suited to higher pulse energy as the lateral dimensions of the liquid-crystal cell are easily scalable. Furthermore, it can be adapted to typical wavelengths of femtosecond sources, from the visible to mid-IR. The presented results disclose an innovative approach in the manipulation of femtosecond pulse trains. Near-future applications include temporal division for pulse measurement as well as carrier-to-envelope phase control of ultrafast pulses.

Acknowledgments

The work is supported by the ANR (Agence Nationale de la Recherche) under the project Labcom SOFTLITE (ANR 15-LCV1-0002-01).

#263766 Received 21 Apr 2016; revised 7 Jun 2016; accepted 10 Jun 2016; published 17 Jun 2016

Optics Letters

Phase-only pulse shaper for multi-octave light sources

VITTORIO MARIA DI PIETRO,[1,2] SIMONE BUX,[2] NICOLAS FORGET,[2] AND AURÉLIE JULLIEN[1,*]

[1]Institut de Physique de Nice, CNRS, Université Cote d'Azur, UMR 7010, 1361 route des Lucioles, 06560 Valbonne, France
[2]Fastlite, 165 route des Cistes, 06600 Antibes, France
*Corresponding author: Aurelie.Jullien@inphyni.cnrs.fr

Received 17 October 2019; revised 10 December 2019; accepted 12 December 2019; posted 16 December 2019 (Doc. ID 380712); published 13 January 2020

Continuous spectral phase shaping is demonstrated over a spectral bandwidth spanning from 540 nm to 2500 nm (450 THz) with a modulation dynamic large enough to shape single-cycle pulses or even transient electric fields in the near infrared.

https://doi.org/10.1364/OL.380712

The phase relationship between optical components plays a crucial role in controlling the electric field of broadband transient optical radiations [1], and a large number of devices have been proposed to shape the spectral phase: bulk media, prisms, grating and prism pairs [2,3], acousto-optic dispersive programmable filters (AOPDFs) [4], zero-dispersion lines [5], and dispersive mirrors [6]. The growing development of light sources delivering pulses as short as a few optical cycles [7–11], based on either nonlinear post-compression or parametric amplification, has triggered the development of innovative pulse shaping or pulse compression devices, capable of handling bandwidths spanning over multiple optical octaves. Such spectral widths raise specific challenges: maximal spectral acceptance, minimal internal dispersion, and high throughput are mandatory properties that tend to rule out most of the aforementioned techniques with the exception of thin wedges, thin plates, and dispersive mirrors. To date, one of the most broadband and extreme pulse shaping devices is an assembly of super-octave chirped mirrors used to compress and coherently combine up to four adjacent optical bandwidths ranging from the ultraviolet to the near-infrared [12]. Once manufactured, sets of dispersive mirrors are, however, characterized by a very small number of degrees of freedom and can hardly be compared to programmable shapers such AOPDFs or spatial light modulators (SLMs) inserted in zero-dispersion lines, in terms of shaping capability and flexibility.

SLMs usually consist of segmented elements, individually controlled by an electrical signal. Reflective SLMs are particularly suited, as the zero-dispersion line may be folded while light propagates twice in the modulating layer, which, in turn, increases the dynamic range. Within the context of pulse shaping, two major classes of reflective SLMs have been considered so far: deformable mirrors (such as micro-electro mechanical (MEMs) mirrors [13] or thermally deformable surfaces [14]) and liquid crystal (LC) on silicon (LCoS) [15]. In general, such devices provide independent control of the reflected light over a limited number of points, equal roughly to the number of actuators. Apart from inactive gaps between adjacent segments, a drawback of the LCoS technology is the presence of an unsegmented top electrode (indium tin oxyde, ITO, transparent over 0.3–1 μm, with partial transmission up to ≃2 μm), which strongly reduces the spectral bandwidth and damage threshold of the device, by comparison with the LC mixture itself. This electrode is, however, mandatory, as an oscillating electric field has to be maintained across the LC layer to control the average orientation of the molecular director.

Optical addressing solves the pixelation issue and ensures continuous phase modulation [16]. In so-called light valve modulators, a biased photo-conductive substrate replaces the segmented electrode, and the voltage across the LC layer is locally controlled by an ancillary absorbed beam, often referred to as the "recording" beam, as opposed to the "readout" beam, which is the (reflected) modulated beam. Here again, the top electrode limits the spectral bandwidth and maximum power of the readout beam. Another strong limitation is the stringent requirement for an isolation layer to prevent crosstalk between the recording and readout beams.

Independent of the addressing technique, the thickness of the LC layer is <20 μm in most SLMs, and results from a balance between the phase modulation range, maximum control voltage, molecular disorder issues [17], and dynamic response time. As the phase modulation range scales with the optical frequency, extending the spectral range towards the infrared tends to require thicker LC layers, which, in turn, constrains the electric addressing scheme.

In this Letter, we propose an ultra-broadband reflective SLM, whose design is issued from our previous investigations on the use of thick cells of thermotropic nematic LCs [18–20]. The device, referred to as a thermo optically addressed SLM (TOA-SLM), is optically addressed and circumvents most previous technical issues by eliminating the need for electrodes: the electrical addressing is replaced by an optically induced control of the local temperature. The optical isolation between the recording and readout beam is performed by a single gold layer that supports three additional functions: partial absorption

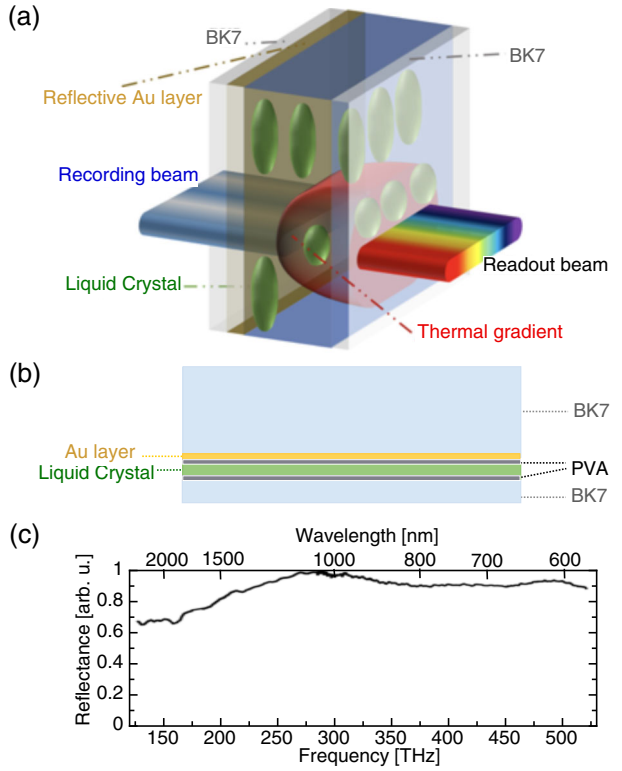

Fig. 1. Design of the TOA-SLM. (a) Illustration and (b) cross-section of the multilayer structure. (c) Spectral reflectivity.

of the recording beam, local heating of the LC, and the reflection of the readout beam.

In previous studies, thermal control of the refractive index of glass slabs has been exploited for phase shaping [21]. The thermotropicity of LCs is much higher than glass and, as a matter of fact, thermo-optical valves were investigated widely in the 1980s in the context of displays [22]. The underlying physical mechanism was, however, different and relied on thermotropic LCs in the smectic mesophase with homeotropic organization. The local temperature was elevated via laser absorption and the smectic-to-isotropic phase transition then provided amplitude modulation through the nucleation of static diffusion centers. The proposed TOA-SLM radically differs from the latter device by the modulated parameter (phase versus amplitude), the mesophase (nematic versus smectic), and the dynamic of the modulation (transient versus steady state).

The spectral bandwidth of the TOA-SLM is, in principle, delimited by the reflectivity of the gold layer and the transmission of LC and/or top substrate. By inserting a TOA-SLM in a zero-dispersion line, we experimentally demonstrate arbitrary phase shaping over an ultra-broad spectral bandwidth of 450 THz (540–2500 nm), this value being limited on the infrared side by the light source. The modulation range exceeds one wave number, even at the longest wavelengths.

The TOA-SLM [Figs. 1(a) and 1(b)] is composed of: (i) a thick BK7 window (6 mm), coated on one side by a 100-nm gold layer and by an AR coating at 465 nm on the other side, and (ii) a thin BK7 window (1 mm) AR-coated on one side and uncoated on the other side. A thin film of polyvinyl alcohol (PVA) is spin-coated on both the gold layer and the uncoated BK7 surface, and then rubbed to anchor the molecules in a plane parallel to the substrate. Finally, a layer of 50 μm of the nematic mixture E7 (Merck) is inserted between the substrates, in contact with the PVA layers. The gold layer achieves simultaneous partial absorption ($\simeq 60\%$) of a recording beam at 465 nm and the reflection of the broadband readout light. The transverse dimensions are 25 mm per 25 mm. As depicted in Fig. 1(a), thermo-optical addressing is applied from the back of the TOA-SLM, through the thick substrate, with a 465-nm fiber-coupled laser diode (600 mW). The beam is partially absorbed by the gold layer, generates heat, and establishes a localized thermal gradient in the LC layer by diffusion. The LC being thermotropic and birefringent, both the ordinary and extraordinary optical refractive indices are locally modulated. Arbitrary modulation is achieved with a digital light processing (DLP) mirror. The spectral reflectivity of the TOA-SLM is shown in Fig. 1(c) and spans from, at least, 120 THz (2.5 μm) to 555 THz (540 nm) with $R > 80\%$ between 200 THz and 555 THz, and $R > 60\%$ between 120 THz and 200 THz. The measurement is limited by the test source and should extend in the infrared to the transparency edge of E7, i.e., 110 THz (2700 nm) [23].

The TOA-SLM is placed in the Fourier plane of a folded $4f$-line: a BK7 glass wedge with an apex angle of 11° disperses the optical frequency components in the horizontal plane, a $f = 500$ mm concave silver mirror images the glass wedge on the TOA-SLM in a "$2f - 2f$" configuration, and the TOA-SLM reflects the beam backward. The spatial extension of the spectrum is $\simeq 5$ mm on the TOA-SLM [see Fig. 3(c)], and the laser polarization direction matches that of the extraordinary axis of the LC. The resulting setup is inserted in a Michelson interferometer [Fig. 2(a)] and characterized by

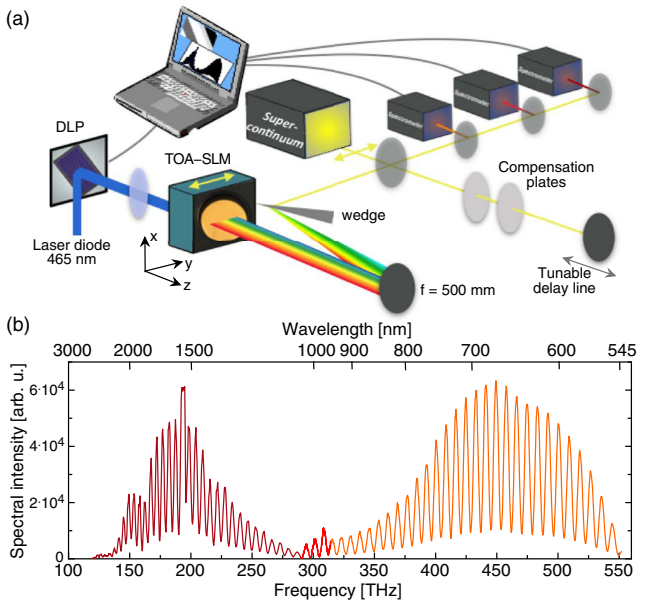

Fig. 2. (a) Experimental setup: the ultra-broadband light source seeds a Michelson interferometer for referenced phase-shaping measurement. The TOA-SLM is inserted in a $4f$-line in a folded configuration. Yellow arrows indicate the laser polarization direction and the extraordinary axis of the LC layer. Three different spectrometers are used to collect the full spectral bandwidth (Avantes 550–1000 nm, Avantes 900–1100 nm, NIRQuest 900–2600 nm). (b) Typical acquired spectra. Different color lines refer to the three different spectrometers.

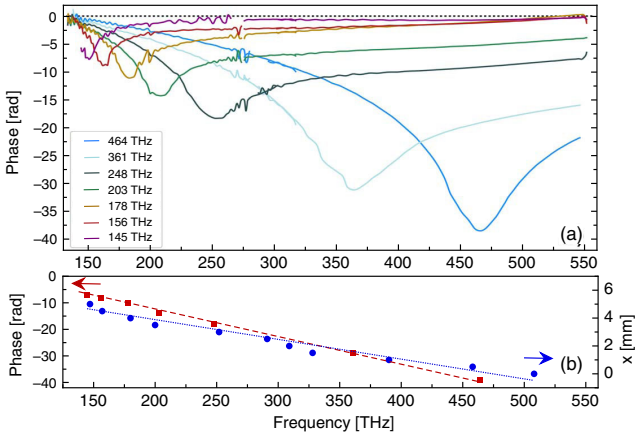

Fig. 3. Calibration of the TOA-SLM (a) Spectrally resolved phase shifts as a function of lateral positions of the recording beam. (b) Maximum phase shift (red squares) and spatial position (blue dots) as a function of the central frequency. (c) Calibration of the $4f$-line design: central frequency ν_n as a function of x.

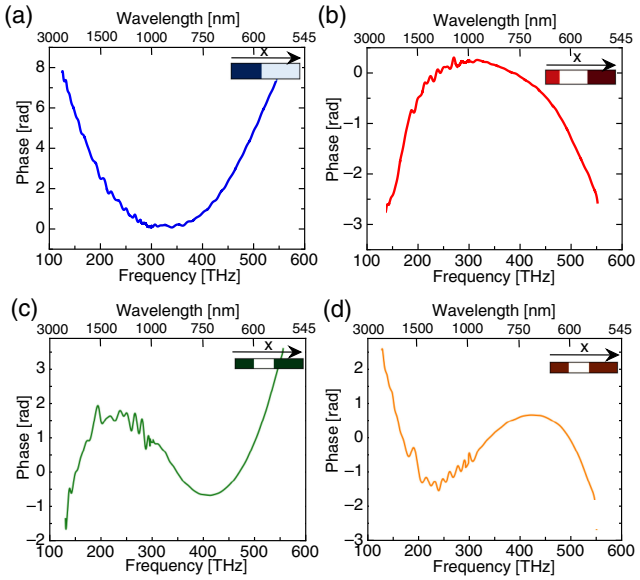

Fig. 4. Spectral phase modulation introduced by the 50-μm-thick TOA-SLM: (a) positive GDD (+8.2 fs^2), (b) negative GDD (−2.5 fs^2), (c) negative TOD (−13 fs^3), and (d) positive TOD (13 fs^3). Top right corner figures: spatial pattern loaded on the DLP to reach the targeted phase. The peak to valley temperature in the LC layer is respectively estimated to (a) 12 K, (b) 7 K, (c) 4 K, and (d) 15 K.

Fourier transform spectral interferometry. The test source is a super-continuum laser (ElectroVisir 250, Leukos) delivering 600 mW over the spectral bandwidth 120–550 THz. The reference arm includes compensation plates and a translation stage for tunable delay. The interference pattern is recorded by three different spectrometers, and the corresponding spectra are stitched to cover the full spectral bandwidth [Fig. 2(b)]. The relative spectral phase is extracted by numerical filtering in the Fourier space. The phase without any recording beam is considered as the reference phase and is subtracted to subsequent measurements. For this proof-of-concept experiment, the spectral phase of the wedge is balanced by the additional dispersion in the other arm of the interferometer and is thus not taken into account.

A first calibration is performed by focusing the blue laser diode on the gold layer of the TOA-SLM and by laterally displacing the beam in order to address different parts of the dispersed spectrum. The beam size on the gold layer is ∼200 μm, and the intensity is kept below 50 W/cm^2. The measured spectral phase is plotted in Fig. 3(a) for seven different positions of the blue focal spot. This experiment demonstrates the ability to continuously address the full spectral range (>450 THz, ∼2000 nm), with a maximum phase shift as high as 35 rad in the visible range (456 THz), and of 7 rad for the infrared edge of the spectrum (130 THz). The introduced phase scales inversely with λ, which is compatible with a constant change in the extraordinary index ($\Delta n_e = 0.1$) over the full spectral bandwidth. The spectral profile of the phase shift indicates a thermal gradient with a Lorentzian-like distribution. This shape could be reproduced by solving numerically the heat equation by taking into account the physical properties of the complete TOA-SLM structure and by assuming a steady state (e.g., thermal equilibrium). In practice, a few seconds are needed to reach the equilibrium. As can be seen in Fig. 3(a), the extension of the thermal gradient limits the spatial resolution to several hundreds of micrometers, thus limiting the spectral resolution. Here the resolution is sufficient to address slowly evolving phase orders, up to five, after our calculations. The thermal evolution of the extraordinary index of E7 is written as

$$n_e(T) = A - BT + \frac{2\Delta n_0}{3}\left(1 - \frac{T}{T_c}\right)^{\beta}, \tag{1}$$

where $T_c = 331$ K is the clearing point (nematic-isotropic phase transition), and A, B, β, Δn_0 some fitting coefficients ($A = 1.7546$, $B = 5.36 * 10^{-4}$, $\beta = 0.2391$, $\Delta n_0 = 0.3768$) [24].

Based on these properties, the performed calibration, and the calculation of extension and shape of the thermal gradient, the blue laser beam was patterned with a linear combination of step-like functions, in order to apply a targeted spectral phase modulation: second-order (e.g., quadratic) or third-order (e.g., cubic) spectral phase (central frequency: 350 THz). A gallery of experimental examples of ultra-broadband phase shaping is shown in Figs. 4(a)–4(d). A purely positive (resp. negative) quadratic phase with more than 8 rad (resp. 2.5 rad) [Figs. 4(a) and 4(b)] is recorded. The asymmetry between the positive and negative cases comes from the fact that it is more difficult to realize a temperature profile with positive curvature than a negative one, given the wide extension of Lorentzian-like distributions. In terms of phase coefficients, the total group delay dispersion (GDD) span of ±10 fs^2 is large enough to triple the pulse duration of a single-cycle Fourier-transform-limited pulse at 1 μm (≃ 3 fs). A purely positive (resp. negative) cubic phase is generated up to ±5 rad, corresponding to a third-order phase coefficient (TOD) of ±13 fs^3 [Figs. 4(c) and 4(d)]. Simple tuning of the phase coefficients is achieved by keeping a constant pattern on the DLP and by increasing/decreasing the average power of the blue diode. A power scan is plotted in Figs. 5(a) and 5(b), demonstrating independent tunability of the GDD and TOD, over the full accessible range.

To assess the shaping scalability of TOA-SLM with the thickness of the LC layer, the same experiments were reproduced with

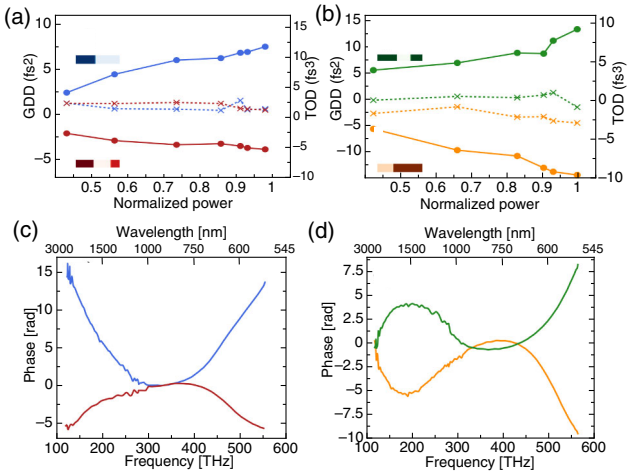

Fig. 5. (a), (b) Spectral phase coefficients as a function of the normalized power of the blue light for the 50-μm-thick TOA-SLM: (a) GDD (solid) and TOD (dotted) evolution for two different patterns (line and pattern colors match); (b) TOD (solid) and GDD (dotted) evolution for two different patterns (line and pattern colors match). (c), (d) Spectral phase modulation introduced by the 110-μm-thick TOA-SLM: (c) positive GDD in blue (+19 fs^2), and negative GDD in red (−7 fs^2); (d) negative TOD in green (−19 fs^3), and positive TOD in yellow (18 fs^3).

a LC layer of 110 μm. Experimental results show that the shaping capability is more than doubled [Figs. 4(c) and 4(d)]. The chirp span reaches ±25 fs^2 in the latter case. These values could still be increased with a more powerful recording laser, since the induced temperature (∼305 K, corresponding to $\Delta n_e = 0.04$) is still well below the clearing point (331 K, $\Delta n_e = 0.2$) [24]. A recording laser with higher power together with a thick LC layer should enable to compensate for the wedge dispersion while preserving the TOA-SLM shaping capabilities. It must be noted that, although the current specifications are comparable to some electromagnetic deformable mirrors, the TOA-SLM is characterized by a larger versatility and a higher damage threshold (limited by the immersed gold surface). Combined with the almost unlimited aperture of LC devices, these features open the way to low-cost, large-aperture, programmable ultra-broadband spectral phase shapers.

To conclude, we have developed a new phase shaper that overcomes the typical limitations of LC SLMs. Thermo-optical addressing enables to control the optical index of the LC without electrodes, making the device broadband and un-segmented. TOA-SLM is compatible with thick LC layers (at least 110 μm) and the modulation range exceeds three wave numbers, even at the longest wavelengths. The optical dephasing can be easily controlled by tuning the average power of the recording laser beam. When inserted in a 4f-line, purely quadratic or purely cubic phases are produced over a multi-octave spectral bandwidth (>450 THz). The total introduced chirp span is large enough to provide a many-fold (up to seven) increase in duration of a single-cycle Fourier-transform-limited pulse at ∼1 μm (3 fs). Forthcoming devices may include a silver layer deposited on the gold layer to further extend the spectral acceptance in the visible part of the spectrum. With an aluminum reflective layer, shorter wavelengths might be addressed as well, as long as above the first absorption bands of carbon bonds (e.g., around 250 nm). In that case, an aluminum reflective layer is required. Higher spatial resolution is expected from optimization of the multilayer structure, currently under study. These results open the way to unprecedented temporal shaping capabilities of few-cycle and single-cycle pulses.

Funding. Agence Nationale de la Recherche (ANR 15-LCV1- 0002-01, ANR-15-IDEX-0001); Research Agency of the European Union (641272).

Disclosures. The authors declare no conflicts of interest.

REFERENCES

1. A. M. Weiner, Opt. Commun. **284**, 3669 (2011).
2. E. B. Treacy, IEEE J. Quantum Electron. **5**, 45408 (1969).
3. P. Tournois, C. R. Acad. Sci. **269**, 455 (1969).
4. P. Tournois, Opt. Commun. **140**, 245 (1997).
5. C. Froehly, B. Colombeau, and M. Vampouille, Prog. Opt. **20**, 63 (1983).
6. V. Pervak, S. Naumov, F. Krausz, and A. Apolonski, Opt. Express **15**, 13768 (2007).
7. A. Kessel, V. E. Leshchenko, O. Jahn, M. Krüger, A. Münzer, A. Schwarz, V. Pervak, M. Trubetskov, S. A. Trushin, F. Krausz, Z. Major, and S. Karsch, Optica **5**, 434 (2018).
8. M. Ouillé, A. Vernier, F. Boehle, M. Bocoum, M. Lozano, J. P. Rousseau, Z. Cheng, D. Gustas, A. Blumenstein, P. Simon, S. Haessler, J. Faure, T. Nagy, and R. Lopez-Martens, ArXiv1907:01239 (2019).
9. Q. Wang, J. Zhang, A. Kessel, N. Nagl, V. Pervak, O. Pronin, and K. F. Mak, Opt. Lett. **44**, 2566 (2019).
10. M. Seidel, *A New Generation of High-Power, Waveform Controlled, Few-Cycle Light Sources* (Springer, 2019).
11. S. Vasilyev, I. Moskalev, V. Smolski, J. Peppers, M. Mirov, A. Muraviev, K. Vodopyanov, S. Mirov, and V. Gapontsev, Opt. Express **27**, 16405 (2019).
12. O. Razskazovskaya, F. Krausz, and V. Pervak, Optica **4**, 129 (2017).
13. M. Hacker, G. Stobrawa, R. Sauerbrey, T. Buckup, M. Motzkus, M. Wildenhain, and A. Gehner, App. Phys. B. **76**, 711 (2003).
14. M. Kasprzack, B. Canuel, F. Cavalier, R. Day, E. Genin, J. Marque, D. Sentenac, and G. Vajente, Appl. Opt. **52**, 2909 (2013).
15. A. M. Weiner, D. E. Leaird, J. S. Patel, and J. R. Wullert, Opt. Lett. **15**, 326 (1990).
16. C. Dorrer, F. Salin, F. Verluise, and J. P. Huignard, Opt. Lett. **23**, 709 (1998).
17. V. M. DiPietro, A. Jullien, U. Bortolozzo, N. Forget, and S. Residori, Opt. Express **26**, 10716 (2018).
18. A. Jullien, U. Bortolozzo, S. Grabielle, J.-P. Huignard, N. Forget, and S. Residori, Opt. Express **24**, 14483 (2016).
19. A. Jullien, R. Pascal, U. Bortolozzo, N. Forget, and S. Residori, Optica **4**, 400 (2017).
20. V. M. di Pietro, A. Jullien, U. Bortolozzo, N. Forget, and S. Residori, Laser Phys. Lett. **16**, 015301 (2018).
21. K. Osvay, K. Varju, and G. Kurdi, App. Phys. B **89**, 565 (2007).
22. A. G. Dewey, Opt. Eng. **23**, 230 (1984).
23. S. T. Wu, Opt. Eng. **26**, 262120 (1987).
24. J. Li, "Refractive indices of liquid crystals and their applications in display and photonic devices," Electronic Theses and Dissertations (University of Central Florida, 2005).

Conclusion

Il est difficile de conclure tant les sujets abordés sont vastes. Une première conclusion concerne la place des technologies femtosecondes aujourd'hui : les femtosecondes ne sont plus des curiosités de laboratoire et ont réellement essaimé à travers des domaines extrêmement variés. Je crois que la large palette d'applications des AOPDFs, en spectroscopie notamment, en est une preuve suffisante. Une seconde conclusion est que le degré d'intégration technologique des sources ultra-brèves (composants fibrés, thin disks, slabs, OPCPAs...) a probablement atteint un seuil et que les investissements financiers et humains nécessaires pour faire progresser les performances nécessitent une « masse critique » importante. L'écosystème économique de l'« ultrafast » se consolide à grande vitesse à l'heure ou j'écris ces lignes et les petites entreprises s'effacent devant les plus grandes. Le même mouvement s'observe d'ailleurs dans les laboratoires de recherche académiques : le coût des sources de troisième génération de forte puissance opère de fait une sélection qui amplifie les disparités nationales et internationales. Les promesses des sources de troisième génération et, en particulier, la production « table top » de rayonnements X-UV à haut flux, sont néanmoins en bonne voie de réalisation et leurs applications n'en sont qu'au commencement.

Il reste bien entendu de beaux espaces de créativité, comme en témoigne le succès du laboratoire commun Softlite. La valve optique adressée thermo-optiquement est, à ce titre, un exemple remarquable de réussite collective. Au delà des résultats scientifiques et des inventions, Softlite est aussi un lieu de formation et de liberté - et je dois saluer ici le dynamisme et l'engagement total d'Aurélie Jullien dans ce laboratoire commun. L'autre pan de mes recherches actuelles se trouve à l'interface entre les OPCPAs et la spectroscopie non linéaire avec, d'une part, le contrat FEDER « SAVOIRS » et, d'autre part, la collaboration avec le groupe d'Hervé Rigneault à l'Institut Fresnel. Si l'objectif technique principal de SAVOIRS est la réalisation d'un OPA accordable à très haute cadence (40 MHz), le cœur scientifique du projet est l'étude du RIN et plus généralement des sources de bruit dans les sources de 3^{e} génération - un sujet encore peu exploré. Plus largement, il ne s'agit pas seulement de mettre au point une source femtoseconde de plus mais une source dédiée à la spectroscopie non linéaire, combinant puissance moyenne, accordabilité, bas bruit et balayage de délai ultra-rapide - la synthèse de 15 ans de recherche en somme !

Bibliographie

[1] N. Forget, M. Joffre, and T. Ruchon, "Ultrashort Light Sources," in *Laser : 50 Years of Discoveries. Edited by BRETENAKER FABIEN ET AL. Published by World Scientific Publishing Co. Pte. Ltd*, pp. 73–91, 2015.

[2] H. Fattahi, H. G. Barros, M. Gorjan, T. Nubbemeyer, B. Alsaif, C. Y. Teisset, M. Schultze, S. Prinz, M. Haefner, M. Ueffing, A. Alismail, L. Vámos, A. Schwarz, O. Pronin, J. Brons, X. T. Geng, G. Arisholm, M. Ciappina, V. S. Yakovlev, D.-E. Kim, A. M. Azzeer, N. Karpowicz, D. Sutter, Z. Major, T. Metzger, and F. Krausz, "Third-generation femtosecond technology," *Optica, OPTICA*, vol. 1, pp. 45–63, July 2014.

[3] R. L. Fork, B. I. Greene, and C. V. Shank, "Generation of optical pulses shorter than 0.1 psec by colliding pulse mode locking," *Appl. Phys. Lett.*, vol. 38, pp. 671–672, May 1981.

[4] W. Dietel, E. Döpel, D. Kühlke, and B. Wilhelmi, "Pulses in the femtosecond range from a cw dye ring laser in the colliding pulse mode-locking (CPM) regime with down-chirp," *Optics Communications*, vol. 43, pp. 433–436, Nov. 1982.

[5] W. Dietel, J. J. Fontaine, and J.-C. Diels, "Intracavity pulse compression with glass : A new method of generating pulses shorter than 60 fsec," *Opt. Lett., OL*, vol. 8, pp. 4–6, Jan. 1983.

[6] J. A. Valdmanis, R. L. Fork, and J. P. Gordon, "Generation of optical pulses as short as 27 femtoseconds directly from a laser balancing self-phase modulation, group-velocity dispersion, saturable absorption, and saturable gain," *Opt. Lett., OL*, vol. 10, pp. 131–133, Mar. 1985.

[7] W. H. Knox, M. C. Downer, R. L. Fork, and C. V. Shank, "Amplified femtosecond optical pulses and continuum generation at 5-kHz repetition rate," *Opt. Lett., OL*, vol. 9, pp. 552–554, Dec. 1984.

[8] C. Rolland and P. B. Corkum, "Amplification of 70 fs pulses in a high repetition rate XeCl pumped dye laser amplifier," *Optics Communications*, vol. 59, pp. 64–68, Aug. 1986.

[9] P. F. Moulton, "Spectroscopic and laser characteristics of Ti :Al_2O_3," *J. Opt. Soc. Am. B, JOSAB*, vol. 3, pp. 125–133, Jan. 1986.

[10] E. Sorokin, S. Naumov, and I. Sorokina, "Ultrabroadband infrared solid-state lasers," *IEEE Journal of Selected Topics in Quantum Electronics*, vol. 11, pp. 690–712, May 2005.

[11] D. Strickland and G. Mourou, "Compression of amplified chirped optical pulses," *Optics Communications*, vol. 56, pp. 219–221, Dec. 1985.

[12] F. Krausz and M. Ivanov, "Attosecond physics," *Rev. Mod. Phys.*, vol. 81, pp. 163–234, Feb. 2009.

[13] G. A. Mourou, T. Tajima, and S. V. Bulanov, "Optics in the relativistic regime," *Rev. Mod. Phys.*, vol. 78, pp. 309–371, Apr. 2006.

[14] S. Gales, K. A. Tanaka, D. L. Balabanski, F. Negoita, D. Stutman, O. Tesileanu, C. A. Ur, D. Ursescu, I. Andrei, S. Ataman, M. O. Cernaianu, L. D'Alessi, I. Dancus, B. Diaconescu, N. Djourelov, D. Filipescu, P. Ghenuche, D. G. Ghita, C. Matei, K. Seto, M. Zeng, and N. V. Zamfir, "The extreme light infrastructure—nuclear physics (ELI-NP) facility : New horizons in physics with 10 PW ultra-intense lasers and 20 MeV brilliant gamma beams," *Rep. Prog. Phys.*, vol. 81, p. 094301, Aug. 2018.

[15] J. H. Sung, H. W. Lee, J. Y. Yoo, J. W. Yoon, C. W. Lee, J. M. Yang, Y. J. Son, Y. H. Jang, S. K. Lee, and C. H. Nam, "4.2 PW, 20 fs Ti :sapphire laser at 0.1 Hz," *Opt. Lett., OL*, vol. 42, pp. 2058–2061, June 2017.

[16] W. Li, Z. Gan, L. Yu, C. Wang, Y. Liu, Z. Guo, L. Xu, M. Xu, Y. Hang, Y. Xu, J. Wang, P. Huang, H. Cao, B. Yao, X. Zhang, L. Chen, Y. Tang, S. Li, X. Liu, S. Li, M. He, D. Yin, X. Liang, Y. Leng, R. Li, and Z. Xu, "339 J high-energy Ti :sapphire chirped-pulse amplifier for 10 PW laser facility," *Opt. Lett., OL*, vol. 43, pp. 5681–5684, Nov. 2018.

[17] T. Oksenhendler, S. Coudreau, N. Forget, V. Crozatier, S. Grabielle, R. Herzog, O. Gobert, and D. Kaplan, "Self-referenced spectral interferometry," *Applied Physics B*, vol. 99, no. 1, pp. 7–12, 2010.

[18] A. Moulet, S. Grabielle, C. Cornaggia, N. Forget, and T. Oksenhendler, "Single-shot, high-dynamic-range measurement of sub-15 fs pulses by self-referenced spectral interferometry," *Optics letters*, vol. 35, no. 22, pp. 3856–3858, 2010.

[19] V. Loriot, G. Gitzinger, and N. Forget, "Self-referenced characterization of femtosecond laser pulses by chirp scan," *Optics express*, vol. 21, no. 21, pp. 24879–24893, 2013.

[20] N. Forget, M. Joffre, S. Coudreau, and T. Oksenhendler, "Toward programmable ultrashort pulse characterization," in *Conference on Lasers and Electro-Optics*, p. CFO7, Optical Society of America, 2007.

[21] N. Forget, "Shaping up," *Nature Photonics*, vol. 4, no. 3, pp. 154–155, 2010.

[22] J. Xu, *Acousto-Optic Devices : Principles, Design, and Applications*. Wiley Series in Pure and Applied Optics, Wiley, 1992.

[23] F. Verluise, V. Laude, Z. Cheng, C. Spielmann, and P. Tournois, "Amplitude and phase control of ultrashort pulses by use of an acousto-optic programmable dispersive filter : Pulse compression and shaping," *Opt. Lett., OL*, vol. 25, pp. 575–577, Apr. 2000.

[24] D. Kaplan and P. Tournois, "Theory and performance of the acousto optic programmable dispersive filter used for femtosecond laser pulse shaping," *J. Phys. IV France*, vol. 12, pp. 69–75, June 2002.

[25] S. Coudreau, D. Kaplan, and P. Tournois, "Ultraviolet acousto-optic programmable dispersive filter laser pulse shaping in KDP," *Opt. Lett., OL*, vol. 31, pp. 1899–1901, June 2006.

[26] R. Maksimenka, P. Nuernberger, K. F. Lee, A. Bonvalet, J. Milkiewicz, C. Barta, M. Klima, T. Oksenhendler, P. Tournois, D. Kaplan, and M. Joffre, "Direct mid-infrared femtosecond pulse shaping with a calomel acousto-optic programmable dispersive filter," *Opt. Lett., OL*, vol. 35, pp. 3565–3567, Nov. 2010.

[27] N. Uchida, "Optical Properties of Single-Crystal Paratellurite (Te${\mathrm{O}}_{2}$)," *Phys. Rev. B*, vol. 4, pp. 3736–3745, Nov. 1971.

[28] G. Georgiev, D. A. Glenar, and J. J. Hillman, "Spectral characterization of acousto-optic filters used in imaging spectroscopy," *Applied optics*, vol. 41, no. 1, pp. 209–217, 2002.

[29] J. G. Berny, J. P. Bourgoin, and B. Ayrault, "Dispersion des indices de refraction du molybdate de plomb (PbMoO4) et de la paratellurite (TeO2)," *Optics Communications*, vol. 6, pp. 383–387, Dec. 1972.

[30] S. Grabielle, *Manipulation et caractérisation du champ électrique optique : applications aux impulsions femtosecondes*. PhD thesis, Ecole Polytechnique X, Dec. 2011.

[31] T. Fuji, N. Ishii, C. Y. Teisset, X. Gu, T. Metzger, A. Baltuska, N. Forget, D. Kaplan, A. Galvanauskas, and F. Krausz, "Parametric amplification of few-cycle carrier-envelope phase-stable pulses at 21 Mm," *Opt. Lett.*, vol. 31, p. 1103, Apr. 2006.

[32] O. D. Mücke, A. Pugžlys, P. Dombi, S. Ališauskas, V. Smilgevičius, N. Forget, J. Pocius, L. Giniūnas, R. Danielius, and A. Baltuška, "10-mJ Few-Cycle OPCPA at 1.5 Mm,"

[33] O. D. Mücke, S. Ališauskas, A. J. Verhoef, A. Pugžlys, A. Baltuška, V. Smilgevičius, J. Pocius, L. Giniūnas, R. Danielius, and N. Forget, "Self-compression of millijoule 1.5 Mm pulses," *Optics letters*, vol. 34, no. 16, pp. 2498–2500, 2009.

[34] O. D. Mücke, D. Sidorov, P. Dombi, A. Pugžlys, A. Baltuška, S. Ališauskas, V. Smilgevičius, J. Pocius, L. Giniūnas, and R. Danielius, "Scalable Yb-MOPA-driven carrier-envelope phase-stable few-cycle parametric amplifier at 1.5 Mm," *Optics letters*, vol. 34, no. 2, pp. 118–120, 2009.

[35] O. D. Mücke, D. Sidorov, P. Dombi, A. Pugžlys, S. Ališauskas, V. Smilgevičius, N. Forget, J. Posius, L. Giniūnas, and R. Danielius, "10-mJ optically synchronized CEP-stable chirped parametric amplifier at 1.5 Mm," *Optics and Spectroscopy*, vol. 108, no. 3, pp. 456–462, 2010.

[36] O. D. Mücke, S. Ališauskas, A. J. Verhoef, A. Pugžlys, A. Baltuška, V. Smilgevičius, J. Pocius, L. Giniūnas, R. Danielius, and N. Forget, "Toward TW-peak-power single-cycle IR fields for attosecond physics and high-field science," *Advances in Solid-State Lasers : Development and Applications*, pp. 279–300, 2010.

[37] S. Ališauskas, V. Smilgevičius, A. P. Piskarskas, O. D. Mücke, A. J. Verhoef, A. Pugžlys, A. Baltuška, J. Pocius, L. Giniunas, R. Danielius, and N. Forget, "Efficient 4-fold

self-compression of millijoule pulses from a 1.5-Mm optical parametric chirped-pulse amplifier," *Lithuanian Journal of Physics*, vol. 50, no. 1, pp. 111–120, 2010.

[38] L. Canova, X. Chen, A. Trisorio, A. Jullien, A. Assion, G. Tempea, N. Forget, T. Oksenhendler, and R. Lopez-Martens, "Carrier-envelope phase stabilization and control using a transmission grating compressor and an AOPDF," *Optics Letters*, vol. 34, no. 9, pp. 1333–1335, 2009.

[39] A. Jullien, L. Canova, N. Forget, X. Chen, R. Lopez-Martens, L. Canova, X. Chen, A. Jullien, and R. Lopez-Martens, "Closed-loop carrier-envelope phase stabilization with an acousto-optic programmable dispersive filter," *Optics Letters*, vol. 34, no. 23, pp. 3647–3649, 2009.

[40] S. Grabielle, N. Forget, H. Jacqmin, A. Jullien, B. Mercier, J.-P. Rousseau, A. Ricci, F. Böhle, and R. Lopez-Martens, "Carrier-envelope-phase stable, high-contrast, double chirped-pulse-amplification laser system," *Optics Letters*, vol. 39, no. 13, p. 3774, 2014.

[41] L. Canova, *Generation and Shaping of Ultra-Short, Ultra-High Contrast Pulses for High Repetition Rate Relativistic Optics*. These de doctorat, Palaiseau, Ecole polytechnique, Jan. 2009.

[42] A. J. Ricci, *Développement d'une Source Laser Ultra-Brève, Stabilisée En Phase et à Haut Contraste Pour l'optique Relativiste Haute Cadence*. These de doctorat, Palaiseau, Ecole polytechnique, Jan. 2013.

[43] H. Jacqmin, *Coherent Combining of Few-Cycle Pulses for the next Generation of Terawatt-class Laser Sources Devoted to Attosecond Physics*. These de doctorat, Université Paris-Saclay (ComUE), Oct. 2016.

[44] F. Lücking, V. Crozatier, N. Forget, A. Assion, and F. Krausz, "Approaching the limits of carrier-envelope phase stability in a millijoule-class amplifier," *Opt. Lett., OL*, vol. 39, pp. 3884–3887, July 2014.

[45] V. Crozatier, N. Forget, and T. Oksenhendler, "Towards single shot carrier-envelope phase stabilization for multi kHz ultrafast amplifiers," in *The European Conference on Lasers and Electro-Optics*, p. CF1_4, Optical Society of America, 2011.

[46] N. Forget, V. Crozatier, and P. Tournois, "Transmission Bragg-grating grisms for pulse compression," *Applied Physics B*, vol. 109, no. 1, pp. 121–125, 2012.

[47] P. Tournois and N. Forget, *Time Dispersion Compensating Device Applied to the Generation of Ultra-Short Light Pulses*. US Patent App. 14/078,721, 2014.

[48] J. Tan, N. Forget, A. Borot, D. Kaplan, P. Tournois, A. Muschet, and L. Veisz, "Dispersion control for temporal contrast optimization," *Optics express*, vol. 26, no. 19, pp. 25003–25012, 2018.

[49] A. Jullien, R. Lopez-Martens, A. Ricci, N. Forget, V. Crozatier, and P. Tournois, "Grism compressor for carrier-envelope phase-stable millijoule-energy chirped pulse amplifier lasers featuring bulk material stretcher," *Optics Letters*, vol. 37, p. 1196, Mar. 2012.

[50] G. Gitzinger, V. Crozatier, R. Maksimenka, S. Grabielle, N. Forget, S. Alisauskas, A. Pugzlys, A. Baltuska, B. Monoszlai, and C. Vicario, "Multi-octave acousto-optic analyzer for spectral measurement in the mid-infrared spectral range," in *Mid-Infrared Coherent Sources*, p. MTh3C. 3, Optical Society of America, 2013.

[51] J. A. Myers, K. L. M. Lewis, P. F. Tekavec, and J. P. Ogilvie, "Two-color two-dimensional Fourier transform electronic spectroscopy with a pulse-shaper," *Opt. Express, OE*, vol. 16, pp. 17420–17428, Oct. 2008.

[52] J. A. de la Paz, A. Bonvalet, and M. Joffre, "Frequency-domain two-dimensional infrared spectroscopy using an acousto-optic programmable dispersive filter," *Opt. Express, OE*, vol. 27, pp. 4140–4146, Feb. 2019.

[53] P. Tyagi, J. I. Saari, B. Walsh, A. Kabir, V. Crozatier, N. Forget, and P. Kambhampati, "Two-color two-dimensional electronic spectroscopy using dual acousto-optic pulse shapers for complete amplitude, phase, and polarization control of femtosecond laser pulses," *The Journal of Physical Chemistry A*, vol. 117, no. 29, pp. 6264–6269, 2013.

[54] H. Seiler, B. Walsh, S. Palato, A. Thai, V. Crozatier, N. Forget, and P. Kambhampati, "Kilohertz generation of high contrast polarization states for visible femtosecond pulses via phase-locked acousto-optic pulse shapers," *Journal of Applied Physics*, vol. 118, no. 10, 2015.

[55] O. Schubert, M. Eisele, V. Crozatier, N. Forget, D. Kaplan, and R. Huber, "Rapid-scan acousto-optical delay line with 34 kHz scan rate and 15 as precision," *Optics letters*, vol. 38, no. 15, pp. 2907–2910, 2013.

[56] B. Urbanek, M. Möller, M. Eisele, S. Baierl, D. Kaplan, C. Lange, and R. Huber, "Femtosecond terahertz time-domain spectroscopy at 36 kHz scan rate using an acousto-optic delay," *Appl. Phys. Lett.*, vol. 108, p. 121101, Mar. 2016.

[57] O. Schubert, M. Eisele, V. Crozatier, N. Forget, D. Kaplan, and R. Huber, "Acousto-optic Fastscan Delay for Ultrabroadband THz Photonics with sub-20-Attosecond Precision and Scan Rates exceeding 30 kHz," p. 1.

[58] I. Znakovskaya, E. Fill, N. Forget, P. Tournois, M. Seidel, O. Pronin, F. Krausz, and A. Apolonski, "Dual frequency comb spectroscopy with a single laser," *Optics letters*, vol. 39, no. 19, pp. 5471–5474, 2014.

[59] N. Forget, D. E. Leaird, M. S. Alshaykh, C.-S. Liao, O. E. Sandoval, J.-X. Cheng, G. Gitzinger, and A. M. Weiner, "High-speed stimulated hyperspectral Raman imaging using rapid acousto-optic delay lines," *Optics Letters*, vol. 42, no. 8, p. 1548, 2017.

[60] X. Audier, N. Forget, and H. Rigneault, "Shot noise limited high speed stimulated Raman microscopy," *arXiv preprint arXiv :1905.11953*, 2019.

[61] X. Audier, N. Forget, and H. Rigneault, "High-speed chemical imaging of dynamic and histological samples with stimulated Raman micro-spectroscopy," *Opt. Express, OE*, vol. 28, pp. 15505–15514, May 2020.

[62] D. Raanan, X. Audier, S. Shivkumar, M. Asher, M. Menahem, O. Yaffe, N. Forget, H. Rigneault, and D. Oron, "Sub-second hyper-spectral low-frequency vibrational imaging via impulsive Raman excitation," *Optics letters*, vol. 44, no. 21, pp. 5153–5156, 2019.

[63] X. Audier, *Spectroscopie Raman Stimulée Rapide et Imagerie Spectrale*. These de doctorat, Aix-Marseille, Dec. 2018.

[64] A. Dubietis, G. Jonušauskas, and A. Piskarskas, "Powerful femtosecond pulse generation by chirped and stretched pulse parametric amplification in BBO crystal," *Optics Communications*, vol. 88, pp. 437–440, Apr. 1992.

[65] I. N. Ross, P. Matousek, M. Towrie, A. J. Langley, and J. L. Collier, "The prospects for ultrashort pulse duration and ultrahigh intensity using optical parametric chirped pulse amplifiers," *Optics Communications*, vol. 144, pp. 125–133, Dec. 1997.

[66] A. Van de Walle, M. Hanna, F. Guichard, Y. Zaouter, A. Thai, N. Forget, and P. Georges, "Spectral and spatial full-bandwidth correlation analysis of bulk-generated supercontinuum in the mid-infrared," *Optics letters*, vol. 40, no. 4, pp. 673–676, 2015.

[67] A. Van de Walle, M. Hanna, P. Georges, A. Thai, N. Forget, Y. Zaouter, T. Ruchon, and B. Carre, "High repetition rate mid-IR few-cycle source based on optical parametric chirped pulse amplification (MIR OPCPA project)," 2015.

[68] P. Rigaud, A. Van de Walle, M. Hanna, N. Forget, F. Guichard, Y. Zaouter, K. Guesmi, F. Druon, and P. Georges, "Supercontinuum-seeded few-cycle mid-infrared OPCPA system," *Optics express*, vol. 24, no. 23, pp. 26494–26502, 2016.

[69] N. Thiré, R. Maksimenka, B. Kiss, C. Ferchaud, P. Bizouard, E. Cormier, K. Osvay, and N. Forget, "4-W, 100-kHz, few-cycle mid-infrared source with sub-100-mrad carrier-envelope phase noise," *Optics express*, vol. 25, no. 2, pp. 1505–1514, 2017.

[70] N. Thiré, R. Maksimenka, B. Kiss, C. Ferchaud, G. Gitzinger, T. Pinoteau, H. Jousselin, S. Jarosch, P. Bizouard, V. Di Pietro, E. Cormier, K. Osvay, and N. Forget, "Highly stable, 15 W, few-cycle, 65 mrad CEP-noise mid-IR OPCPA for statistical physics," *Opt. Express*, vol. 26, p. 26907, Oct. 2018.

[71] N. Forget, "Generator of short optical pulses having a very high temporal contrast," 2017.

[72] A. van de Walle, M. Hanna, F. Guichard, Y. Zaouter, A. Thai, N. Forget, and P. Georges, "Spectral and spatial shot-to-shot correlation analysis of bulk supercontinuum in the mid-infrared," in *The European Conference on Lasers and Electro-Optics*, p. CF_P_27, Optical Society of America, 2015.

[73] E. A. Neradovskaia, M. M. Neradovskiy, A. A. Esin, M. A. Chuvakova, A. R. Akhmatkhanov, P. Baldi, M. P. De Micheli, N. Forget, and V. Y. Shur, "Forward domain growth in 36° Y-cut congruent lithium niobate," *Ferroelectrics*, vol. 541, no. 1, pp. 115–122, 2019.

[74] J.-P. Huignard, A. Jullien, S. Grabielle, U. Bortolozzo, N. Forget, and S. Residori, "Continuously tunable femtosecond delay-line based on liquid crystal cells," *Optics Express*, vol. 24, no. 13, p. 14483, 2016.

[75] A. Jullien, R. Pascal, U. Bortolozzo, N. Forget, and S. Residori, "High-resolution hyperspectral imaging with cascaded liquid crystal cells," *Optica*, vol. 4, no. 4, pp. 400–405, 2017.

[76] R. Laberdesque, A. Jullien, U. Bortolozzo, N. Forget, and S. Residori, "Tunable angular shearing interferometer based on wedged liquid crystal cells," *Applied optics*, vol. 56, no. 31, pp. 8656–8662, 2017.

[77] V. M. di Pietro, S. Bux, N. Forget, and A. Jullien, "Phase-only pulse shaper for multi-octave light sources," *Opt. Lett., OL*, vol. 45, pp. 543–546, Jan. 2020.

[78] V. M. di Pietro and A. Jullien, "Broadband Spectral Domain Interferometry for Optical Characterization of Nematic Liquid Crystals," *Applied Sciences*, vol. 10, p. 4701, Jan. 2020.

[79] V. M. Di Pietro, A. Jullien, U. Bortolozzo, N. Forget, and S. Residori, "Thermally-induced nonlinear spatial shaping of infrared femtosecond pulses in nematic liquid crystals," *Laser Physics Letters*, vol. 16, no. 1, p. 015301, 2018.

[80] L. Ramousse, L. Ramousse, G. Chériaux, C. Claudet, and A. Jullien, "Femtosecond laser-induced damage threshold of nematic liquid crystals at 1030 nm," *Appl. Opt., AO*, vol. 60, pp. 8050–8056, Sept. 2021.

[81] V. M. Di Pietro, A. Jullien, U. Bortolozzo, N. Forget, and S. Residori, "Dynamical optical response of nematic liquid crystal cells through electrically driven Fréedericksz transition : Influence of the nematic layer thickness," *Optics express*, vol. 26, no. 8, pp. 10716–10728, 2018.

Liste des publications

Bibliométrie, tirée de Google Scholar, en janvier 2022

	Toutes	Depuis 2016
Citations	2298	1062
Indice h[1]	28	19
Indice g[2]	44	
Indice i10[3]	46	

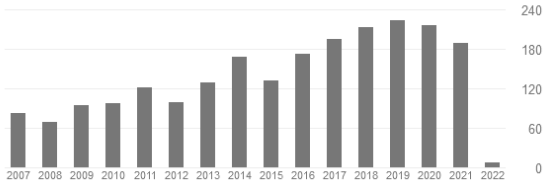

Répartition des articles de la bibliographie

Revue	Facteur d'impact 2019	Nombre de publications
Nature Photonics	31.241	1
Optica	9.778	1
Physical Review Letters	8.385	1
Optics Letters	3.714	23
Opt. Express	3.669	8
Journal of Physical Chemistry	2.600	1
Journal of Applied Physics	2.286	1
J. Opt. Soc. Am. B	2.180	2
Appl. Optics	1.961	1
IEEE Journal of Quantum Elctronics	1.887	1
Laser Physics Letters	1.884	1
Appl. Phys. B	1.782	4
Review of Scientific Instruments	1.480	1
Autres journaux		5

[1] https://fr.wikipedia.org/wiki/Indice_h
[2] https://en.wikipedia.org/wiki/G-index
[3] Nombre de publications avec plus de 10 citations.

Publications dans des journaux à comité de lecture

1. R. Haïdar, N. Forget, and E. Rosencher, "Optical parametric oscillation in microcavities based on isotropic semiconductors: a theoretical study," IEEE journal of quantum electronics **39**, 569–576 (2003).

2. R. Haïdar, N. Forget, P. Kupecek, and E. Rosencher, "Fresnel phase matching for three-wave mixing in isotropic semiconductors," Journal of the Optical Society of America B **21**, 1522–1534 (2004).
3. N. Forget, A. Cotel, E. Brambrink, P. Audebert, C. Le Blanc, A. Jullien, O. Albert, and G. Chériaux, "Pump-noise transfer in optical parametric chirped-pulse amplification," Optics Letters **30**, 2921 (2005).
4. I. Jovanovic, C. G. Brown, C. A. Ebbers, C. P. J. Barty, N. Forget, C. L. Blanc, and C. Le Blanc, "Generation of high-contrast millijoule pulses by optical parametric chirped-pulse amplification in periodically poled KTiOPO4," Optics Letters **30**, 1036–1038 (2005).
5. A. Cotel, A. Jullien, N. Forget, O. Albert, C. L. Blanc, J. Etchepare, G. Chériaux, N. Minkovski, and S. M. Saltiel, "Nonlinear temporal pulse cleaning for high-energy petawatt-class lasers," J. Phys. IV France **133**, 713–715 (2006).
6. A. Cotel, A. Jullien, N. Forget, O. Albert, G. Chériaux, and C. Le Blanc, "Nonlinear temporal pulse cleaning of a 1-μm optical parametric chirped-pulse amplification system," Appl. Phys. B **83**, 7–10 (2006).
7. N. Forget, S. Bahbah, C. Drag, F. Bretenaker, M. Lefèbvre, and E. Rosencher, "Actively mode-locked optical parametric oscillator," Optics Letters **31**, 972 (2006).
8. T. Fuji, N. Ishii, C. Y. Teisset, X. Gu, Th. Metzger, A. Baltuska, N. Forget, D. Kaplan, A. Galvanauskas, and F. Krausz, "Parametric amplification of few-cycle carrier-envelope phase-stable pulses at 2.1 μm," Optics Letters **31**, 1103 (2006).
9. V. Bagnoud, J. D. Zuegel, N. Forget, and C. Le Blanc, "High-dynamic-range temporal measurements of short pulses amplified by OPCPA," Opt. Express **15**, 5504 (2007).
10. E. Rosencher, J.-M. J. J.-M. Melkonian, C. Drag, F. Bretenaker, M. Lefebvre, N. Forget, F. Bretenaker, C. Drag, M. Lefebvre, and E. Rosencher, "Active mode locking of continuous-wave doubly and singly resonant optical parametric oscillators," Optics Letters **32**, 1701–3 (2007).
11. L. Canova, O. Albert, N. Forget, B. Mercier, S. Kourtev, N. Minkovski, S. M. Saltiel, and R. Lopez Martens, "Influence of spectral phase on cross-polarized wave generation with short femtosecond pulses," Appl. Phys. B **93**, 443–453 (2008).
12. L. Canova, X. Chen, A. Trisorio, A. Jullien, A. Assion, G. Tempea, N. Forget, T. Oksenhendler, and R. Lopez-Martens, "Carrier-envelope phase stabilization and control using a transmission grating compressor and an AOPDF," Optics Letters **34**, 1333–1335 (2009).
13. A. Jullien, L. Canova, N. Forget, X. Chen, R. Lopez-Martens, L. Canova, X. Chen, A. Jullien, and R. Lopez-Martens, "Closed-loop carrier-envelope phase stabilization with an acousto-optic programmable dispersive filter," Optics Letters **34**, 3647–3649 (2009).
14. O. D. Mücke, D. Sidorov, P. Dombi, A. Pugžlys, A. Baltuška, S. Ališauskas, V. Smilgevičius, J. Pocius, L. Giniūnas, and R. Danielius, "Scalable Yb-MOPA-driven carrier-envelope phase-stable few-cycle parametric amplifier at 1.5 μm," Optics Letters **34**, 118–120 (2009).
15. O. D. Mücke, S. Ališauskas, A. J. Verhoef, A. Pugžlys, A. Baltuška, V. Smilgevičius, J. Pocius, L. Giniūnas, R. Danielius, and N. Forget, "Self-compression of millijoule 1.5 μm pulses," Optics Letters **34**, 2498–2500 (2009).
16. S. Ališauskas, V. Smilgevičius, A. P. Piskarskas, O. D. Mücke, A. J. Verhoef, A. Pugžlys, A. Baltuška, J. Pocius, L. Giniunas, R. Danielius, and N. Forget, "Efficient 4-fold self-compression of millijoule pulses from a 1.5-μm optical parametric chirped-pulse amplifier," Lithuanian Journal of Physics **50**, 111–120 (2010).
17. N. Forget, "Shaping up," Nature Photonics **4**, 154–155 (2010).

18. N. Forget, V. Crozatier, and T. Oksenhendler, "Pulse-measurement techniques using a single amplitude and phase spectral shaper," JOSA B **27**, 742–756 (2010).
19. A. Moulet, S. Grabielle, C. Cornaggia, N. Forget, and T. Oksenhendler, "Single-shot, high-dynamic-range measurement of sub-15 fs pulses by self-referenced spectral interferometry," Optics Letters **35**, 3856–3858 (2010).
20. O. D. Mücke, D. Sidorov, P. Dombi, A. Pugžlys, S. Ališauskas, V. Smilgevičius, N. Forget, J. Posius, L. Giniūnas, and R. Danielius, "10-mJ optically synchronized CEP-stable chirped parametric amplifier at 1.5 μm," Optics and Spectroscopy **108**, 456–462 (2010).
21. T. Oksenhendler, S. Coudreau, N. Forget, V. Crozatier, S. Grabielle, R. Herzog, O. Gobert, and D. Kaplan, "Self-referenced spectral interferometry," Applied Physics B **99**, 7–12 (2010).
22. S. L. Cousin, N. Forget, A. Grün, P. K. Bates, D. R. Austin, and J. Biegert, "Few-cycle pulse characterization with an acousto-optic pulse shaper," Optics Letters **36**, 2803–2805 (2011).
23. S. Grabielle, A. Moulet, N. Forget, V. Crozatier, S. Coudreau, R. Herzog, T. Oksenhendler, C. Cornaggia, and O. Gobert, "Self-referenced spectral interferometry cross-checked with SPIDER on sub-15 fs pulses," Nuclear Instruments and Methods in Physics Research Section A: Accelerators, Spectrometers, Detectors and Associated Equipment **653**, 121–125 (2011).
24. S. L. Cousin, J. M. Bueno, N. Forget, D. R. Austin, and J. Biegert, "Three-dimensional spatiotemporal pulse characterization with an acousto-optic pulse shaper and a Hartmann–Shack wavefront sensor," Optics Letters **37**, 3291–3293 (2012).
25. N. Forget, V. Crozatier, and P. Tournois, "Transmission Bragg-grating grisms for pulse compression," Applied Physics B **109**, 121–125 (2012).
26. A. Jullien, R. Lopez-Martens, A. Ricci, N. Forget, V. Crozatier, and P. Tournois, "Grism compressor for carrier-envelope phase-stable millijoule-energy chirped pulse amplifier lasers featuring bulk material stretcher," Optics Letters **37**, 1196 (2012).
27. A. Trisorio, S. Grabielle, M. Divall, N. Forget, and C. P. Hauri, "Self-referenced spectral interferometry for ultrashort infrared pulse characterization," Optics Letters **37**, 2892–2894 (2012).
28. M. Durand, A. Jarnac, A. Houard, Y. Liu, S. Grabielle, N. Forget, A. Durécu, A. Couairon, and A. Mysyrowicz, "Self-Guided Propagation of Ultrashort Laser Pulses in the Anomalous Dispersion Region of Transparent Solids: A New Regime of Filamentation," Phys. Rev. Lett. **110**, 115003 (2013).
29. V. Loriot, G. Gitzinger, and N. Forget, "Self-referenced characterization of femtosecond laser pulses by chirp scan," Optics express **21**, 24879–24893 (2013).
30. O. Schubert, M. Eisele, V. Crozatier, N. Forget, D. Kaplan, and R. Huber, "Rapid-scan acousto-optical delay line with 34 kHz scan rate and 15 as precision," Optics Letters **38**, 2907–2910 (2013).
31. P. Tyagi, J. I. Saari, B. Walsh, A. Kabir, V. Crozatier, N. Forget, and P. Kambhampati, "Two-color two-dimensional electronic spectroscopy using dual acousto-optic pulse shapers for complete amplitude, phase, and polarization control of femtosecond laser pulses," The Journal of Physical Chemistry A **117**, 6264–6269 (2013).
32. S. Grabielle, N. Forget, H. Jacqmin, A. Jullien, B. Mercier, J.-P. Rousseau, A. Ricci, F. Böhle, and R. Lopez-Martens, "Carrier-envelope-phase stable, high-contrast, double chirped-pulse-amplification laser system," Optics Letters **39**, 3774 (2014).
33. F. Krausz, N. Forget, F. Lücking, V. Crozatier, and A. Assion, "Approaching the limits of carrier-envelope phase stability in a millijoule-class amplifier," Optics Letters **39**, 3884 (2014).
34. I. Znakovskaya, E. Fill, N. Forget, P. Tournois, M. Seidel, O. Pronin, F. Krausz, and A. Apolonski, "Dual frequency comb spectroscopy with a single laser," Optics Letters **39**, 5471–5474 (2014).
35. H. Seiler, B. Walsh, S. Palato, A. Thai, V. Crozatier, N. Forget, and P. Kambhampati, "Kilohertz generation of high contrast polarization states for visible femtosecond pulses via phase-locked acousto-optic pulse shapers," Journal of Applied Physics **118**, (2015).
36. A. Van de Walle, M. Hanna, F. Guichard, Y. Zaouter, A. Thai, N. Forget, and P. Georges, "Spectral and spatial full-bandwidth correlation analysis of bulk-generated supercontinuum in the mid-infrared," Optics Letters **40**, 673–676 (2015).

37. J.-P. Huignard, A. Jullien, S. Grabielle, U. Bortolozzo, N. Forget, and S. Residori, "Continuously tunable femtosecond delay-line based on liquid crystal cells," Optics Express **24**, 14483 (2016).
38. P. Rigaud, A. Van de Walle, M. Hanna, N. Forget, F. Guichard, Y. Zaouter, K. Guesmi, F. Druon, and P. Georges, "Supercontinuum-seeded few-cycle mid-infrared OPCPA system," Optics express **24**, 26494–26502 (2016).
39. N. Forget, D. E. Leaird, M. S. Alshaykh, C.-S. Liao, O. E. Sandoval, J.-X. Cheng, G. Gitzinger, and A. M. Weiner, "High-speed stimulated hyperspectral Raman imaging using rapid acousto-optic delay lines," Optics Letters **42**, 1548 (2017).
40. A. Jullien, R. Pascal, U. Bortolozzo, N. Forget, and S. Residori, "High-resolution hyperspectral imaging with cascaded liquid crystal cells," Optica **4**, 400–405 (2017).
41. R. Laberdesque, A. Jullien, U. Bortolozzo, N. Forget, and S. Residori, "Tunable angular shearing interferometer based on wedged liquid crystal cells," Applied optics **56**, 8656–8662 (2017).
42. N. Thiré, R. Maksimenka, B. Kiss, C. Ferchaud, P. Bizouard, E. Cormier, K. Osvay, and N. Forget, "4-W, 100-kHz, few-cycle mid-infrared source with sub-100-mrad carrier-envelope phase noise," Optics express **25**, 1505–1514 (2017).
43. V. M. Di Pietro, A. Jullien, U. Bortolozzo, N. Forget, and S. Residori, "Dynamical optical response of nematic liquid crystal cells through electrically driven Fréedericksz transition: influence of the nematic layer thickness," Optics Express **26**, 10716–10728 (2018).
44. V. M. Di Pietro, A. Jullien, U. Bortolozzo, N. Forget, and S. Residori, "Thermally-induced nonlinear spatial shaping of infrared femtosecond pulses in nematic liquid crystals," Laser Physics Letters **16**, 015301 (2018).
45. G. Jargot, N. Daher, L. Lavenu, X. Delen, N. Forget, M. Hanna, and P. Georges, "Self-compression in a multipass cell," Optics Letters **43**, 5643–5646 (2018).
46. J. Tan, N. Forget, A. Borot, D. Kaplan, P. Tournois, A. Muschet, and L. Veisz, "Dispersion control for temporal contrast optimization," Optics express **26**, 25003–25012 (2018).
47. N. Thiré, R. Maksimenka, B. Kiss, C. Ferchaud, G. Gitzinger, T. Pinoteau, H. Jousselin, S. Jarosch, P. Bizouard, V. Di Pietro, E. Cormier, K. Osvay, and N. Forget, "Highly stable, 15 W, few-cycle, 65 mrad CEP-noise mid-IR OPCPA for statistical physics," Opt. Express **26**, 26907 (2018).
48. E. A. Neradovskaia, M. M. Neradovskiy, A. A. Esin, M. A. Chuvakova, A. R. Akhmatkhanov, P. Baldi, M. P. De Micheli, N. Forget, and V. Y. Shur, "Forward domain growth in 36° Y-cut congruent lithium niobate," Ferroelectrics **541**, 115–122 (2019).
49. D. Raanan, X. Audier, S. Shivkumar, M. Asher, M. Menahem, O. Yaffe, N. Forget, H. Rigneault, and D. Oron, "Sub-second hyper-spectral low-frequency vibrational imaging via impulsive Raman excitation," Optics Letters **44**, 5153–5156 (2019).
50. X. Audier, N. Forget, and H. Rigneault, "High-speed chemical imaging of dynamic and histological samples with stimulated Raman micro-spectroscopy," Opt. Express, OE **28**, 15505–15514 (2020).
51. V. M. di Pietro, S. Bux, N. Forget, and A. Jullien, "Phase-only pulse shaper for multi-octave light sources," Optics Letters, OL **45**, 543–546 (2020).

B. Maingot, G. Cheriaux, N. Forget, and A. Jullien, "Spectral coherence properties of continuum generation in bulk crystals", submitted to Optics Letters (2022).

Autres publications (chapitres)

52. B. Chatel and N. Forget, "Sources ultra-courtes accordables: état de l'art," in *Lasers et Technologies Femtoseconde*, Vol. 6, p. 207 (Université de Saint-Etienne, 2005). Ouvrage Réalisé à La Suite de La deuxième école des technologies, sources et systèmes femtosecondes, 21-24 Septembre 2004, Île-de-Porquerolles, Var.
53. N. Forget and T. Oksenhendler, "Pulse Measurement Techniques Using an Acousto-Optic Programmable Dispersive Filter," in *Advances in Solid State Lasers: Development and Applications*,

p. 319 (2010).

54. O. D. Mücke, S. Ališauskas, A. J. Verhoef, A. Pugžlys, A. Baltuška, V. Smilgevičius, J. Pocius, L. Giniūnas, R. Danielius, and N. Forget, "Toward TW-peak-power single-cycle IR fields for attosecond physics and high-field science," in *Advances in Solid State Lasers: Development and Applications*, p279 (2010).
55. N. Forget, M. Joffre, and T. Ruchon, "Ultrashort Light Sources," in *Laser: 50 Years of Discoveries.* Edited by F. Bretenacker et al. Published by World Scientific Publishing Co, pp. 73–91 (2015).
56. Y. Pertot, N. Thiré, R. Maksimenka, O. Albert, and N. Forget, "100 kHz tunable mid-IR ultrafast sources for high intensity applications". *Emerging Laser Technologies for High-Power and Ultrafast Science* (2021).

Conférences (présentations, posters)

57. C. Le Blanc, C. Felix, J. C. Lagron, N. Forget, P. Hollander, A. M. Sautivet, C. Sauteret, F. Amiranoff, and A. Migus, "The petawatt laser glass chain at LULI: from the diode-pumped front end to the new generation of compact compressors," in *Proceedings of Third International Conference on Inertial Fusion Sciences and Applications* (American Nuclear Society, 2004), pp. 608–611.
58. V. Bagnoud, J. Puth, I. Begishev, M. Guardalben, J. D. Zuegel, N. Forget, and C. Le Blanc, "A multiterawatt laser using a high-contrast , optical parametric chirped-pulse preamplifier," in *2005 Quantum Electronics and Laser Science Conference* (IEEE, 2005), pp. 2003–2005.
59. A. Cotel, N. Forget, C. Brach, F. Bonnemason, E. Baynard, C. Le Bris, and C. Le Blanc, "Characterisation of Multilayer Dielectric Grati ngs for Petawatt-class Lasers," in *Conference on Lasers and Electro-Optics* (Optical Society of America, 2005), p. JFB6.
60. I. Jovanovic, C. C. Brown, C. A. Ebbers, C. P. J. Barty, N. Forget, and C. Le Blanc, "Millijoule pulses from a double-passed, quasi-phase-matched optical-parametric chirped-pulse amplifier," in *2005 Quantum Electronics and Laser Science Conference* (IEEE, 2005), Vol. 3, pp. 2009–2011.
61. A. Baltuška, N. Ishii, T. Fuji, X. Gu, N. Forget, D. Kaplan, A. Galvanauskas, and F. Krausz, "Few-cycle chirped-pulse parametric amplification," in *Quantum Electronics and Laser Science Conference* (Optical Society of America, 2006), p. JThE1.
62. A. Cotel, N. Forget, A. Jullien, O. Albert, G. Chériaux, and C. Le Blanc, "High-efficiency temporal pulse cleaning for a 1 μm front end on a Petawatt-class laser," in *Conference on Lasers and Electro-Optics* (Optical Society of America, 2006), p. CMA7.
63. A. Cotel, A. Jullien, N. Forget, O. Albert, C. Le Blanc, J. Etchepare, G. Cheriaux, N. Minkovski, and S. M. Saltiel, "Nonlinear temporal pulse cleaning for high-energy petawatt-class lasers," in *Journal de Physique IV (Proceedings)* (EDP sciences, 2006), Vol. 133, pp. 713–715.
64. N. Forget, S. Bahbah, J.-M. Melkonian, C. Drag, F. Bretenaker, M. Lefebvre, and E. Rosencher, "Direct Active Mode-Locking of an Optical Parametric Oscillator," in *2006 Conference on Lasers and Electro-Optics and 2006 Quantum Electronics and Laser Science Conference* (IEEE, 2006), pp. 1–2.
65. S. Noailles, G. Deschaseaux, J. Neauport, N. Forget, A. Mingus, C. Rullière, E. Freysz, N. Loustalet, G. Marre, P. Vivini, E. Couturier, H. Coïc, E. Hugonnot, A. Cotel, L. Videau, J. Luce, S. Mousset, C. Rouyer, C. Sauteret, S. Montant, C. Le Blanc, N. Blanchot, and E. Bignon, "Multi-petawatt high-energy laser project on the LIL facility in Aquitaine," in *Topical Problems of Nonlinear Wave Physics* (International Society for Optics and Photonics, 2006), Vol. 5975, pp. 59750C-59750C–16.
66. L. Canova, M. Merano, A. Jullien, G. Chériaux, R. L. Martens, O. Albert, N. Forget, S. Kourtev, N. Minkovsky, S. M. Saltiel, R. Lopez Martens, O. Albert, N. Forget, S. Kourtev, N. Minkovski, and S. M. Saltiel, "Coherent contrast improvement by cross-polarized wave generation," in *Conference on Lasers and Electro-Optics/Quantum Electronics and Laser Science Conference and Photonic Applications Systems Technologies* (Optical Society of America, 2007), p. JThD131.
67. J. P. Chambaret, F. Canova, R. L. Martens, G. Cheriaux, G. Mourou, A. Cotel, C. L. Blanc, F. Druon,

P. Georges, N. Forget, F. Ple, and M. Pittman, "ILE 25PW single laser beamline: The French step for the European Extreme Light Infrastructure (ELI)," in *2007 Quantum Electronics and Laser Science Conference* (2007), pp. 1–2.

68. N. Forget, A. Cotel, T. Oksenhendler, C. Le Blanc, D. Kaplan, and P. Tournois, "Picosecond to Nanosecond Pulse Shaping via a Chirp-Transform Scaling Technique," in *The European Conference on Lasers and Electro-Optics* (Optical Society of America, 2007), p. CG6_6.
69. N. Forget, A. Cotel, T. Oksenhendler, C. L. Blanc, D. Kaplan, and P. Tournois, "Wideband to narrowband pulse shaping via a chirp-transform scaling technique," in *2007 Quantum Electronics and Laser Science Conference* (2007), pp. 1–2.
70. N. Forget, S. Coudreau, F. Lepetit, O. Albert, and T. Oksenhendler, "Achromatic and single-beam pulse characterization technique for visible-UV pulses based on direct UV pulse shaping and cross-polarized wave generation," in *2007 Conference on Lasers and Electro-Optics (CLEO)* (IEEE, 2007), pp. 1–2.
71. N. Forget, M. Joffre, S. Coudreau, and T. Oksenhendler, "Toward programmable ultrashort pulse characterization," in *Conference on Lasers and Electro-Optics* (Optical Society of America, 2007), p. CFO7.
72. T. Oksenhendler, N. Forget, D. Garzella, O. Gobert, R. Herzog, P. Hollander, and F. Lepetit, "Direct UV pulse shaping applied to 3ps square and parabolic pulses," in *Conference on Lasers and Electro-Optics* (Optical Society of America, 2007), p. CFO5.
73. L. Canova, O. Albert, A. Trisorio, R. L. Martens, N. Forget, T. Oksenhendler, S. Kourtev, N. Minkovski, and S. M. Saltiel, "Systematic study of the Influence of the high orders spectral phase on XPW generation," in *2008 Conference on Lasers and Electro-Optics and 2008 Conference on Quantum Electronics and Laser Science* (IEEE, 2008), pp. 1–2.
74. L. Canova, N. Minkovski, S. Kourtev, O. Albert, N. Forget, T. Oksenhendler, R. L. Martens, and S. M. Saltiel, "Highly efficient cross-polarized wave generation in the UV region," in *2008 Conference on Lasers and Electro-Optics and 2008 Conference on Quantum Electronics and Laser Science* (IEEE, 2008), pp. 1–2.
75. O. D. Mücke, A. Pugžlys, P. Dombi, A. Baltuška, S. Ališauskas, N. Forget, J. Pocius, L. Giniunas, R. Danielius, and A. Baltuška, "10-mJ few-cycle chirped pulse parametric amplification at 1.5 μm," in *Conference Proceedings - Lasers and Electro-Optics Society Annual Meeting-LEOS* (IEEE, 2008), pp. 559–560.
76. O. D. Mücke, A. Pugžlys, P. Dombi, S. Ališauskas, V. Smilgevičius, N. Forget, J. Pocius, L. R. Giniunas, R. Danielius, and A. Baltuška, "10-mJ few-cycle OPCPA at 1.5 μm," in *2008 IEEE PhotonicsGlobal at Singapore, IPGC 2008* (IEEE, 2008), pp. 1–4.
77. O. D. Mücke, D. Sidorov, P. Dombi, A. Pugžlys, A. Baltuška, S. Ališauskas, J. Pocius, L. Giniūnas, and R. Danielis, "Multimillijoule Optically Synchronized and Carrier-Envelope-Phase-Stable Chirped Parametric Amplification at 1.5 μm," in *Advanced Solid-State Photonics* (Optical Society of America, 2008), p. MG1.
78. L. Canova, X. Chen, B. Mercier, O. Albert, R. L. Martens, N. Forget, and T. Oksenhendler, "Automated optimization of the temporal duration of a 21 fs, 4 mJ CPA laser system with high B-integral," in *The European Conference on Lasers and Electro-Optics* (Optical Society of America, 2009), p. CF_P5.
79. L. Canova, A. Jullien, X. Chen, A. Trisorio, R. Lopez-Martens, A. Assion, G. Tempea, N. Forget, T. Oksenhendler, and D. Kaplan, "Carrier-envelope phase control using a transmission grating compressor and an AOPDF," in *International Quantum Electronics Conference* (Optical Society of America, 2009), p. JFA3.
80. L. Canova, A. Trisorio, X. Chen, B. Mercier, O. Albert, R. L. Martens, N. Forget, and T. Oksenhendler, "Closed-loop optimization of the temporal duration of a 21fs, 4 mJ CPA laser system with high B-integral," in *International Quantum Electronics Conference* (Optical Society of America, 2009), p. JTuD38.
81. N. Forget, P. M. Paul, C. Hauri, T. Oksenhendler, and P. Tournois, "Efficient chirped-matched third

harmonic generation of long UV pulses," in *The European Conference on Lasers and Electro-Optics* (Optical Society of America, 2009), p. CD1_3.
82. S. Grabielle, N. Forget, S. Coudreau, T. Oksenhendler, D. Kaplan, J.-F. Hergott, and O. Gobert, "Local spectral compression method for cpa lasers," in *The European Conference on Lasers and Electro-Optics* (Optical Society of America, 2009), p. CF_P17.
83. O. D. Mücke, A. J. Verhoef, A. Pugžlys, A. Baltuška, S. Ališauskas, V. Smilgevičius, J. Pocius, L. Giniūnas, R. Danielius, and N. Forget, "Multi-mJ single-filament supercontinuum generation from IR OPCPA," in *The European Conference on Lasers and Electro-Optics* (Optical Society of America, 2009), p. CF5_3.
84. O. D. Mücke, A. J. Verhoef, A. Pugžlys, A. Baltuška, S. Ališauskas, V. Smilgevičius, J. Pocius, L. Giniūnas, R. Danielius, and N. Forget, "Toward Terawatt-Peak-Power Single-Cycle Infrared Fields," in *Nonlinear Optics: Materials, Fundamentals and Applications* (Optical Society of America, 2009), p. NFA3.
85. O. D. Mücke, A. Verhoef, A. Pugžlys, A. Baltuška, S. Ališauskas, V. Smilgevičius, J. Pocius, L. Gini\=unas, R. Danielius, and N. Forget, "10-mJ Infrared Phase-Stable Parametric Amplification Based on a Femtosecond Yb-MOPA," in *Advanced Solid-State Photonics* (Optical Society of America, 2009), p. WD5.
86. O. D. Mücke, A. J. Verhoef, A. Pugžlys, A. Baltuška, S. Ališauskas, V. Smilgevičius, J. Pocius, L. Giniūnas, R. Danielius, and N. Forget, "Infrared Multimillijoule Single-Filament Supercontinuum Generation," in *Conference on Lasers and Electro-Optics/International Quantum Electronics Conference* (2009), p. JWD6.
87. T. Oksenhendler, S. Coudreau, N. Forget, S. Grabielle, D. Kaplan, and O. Gobert, "Self-referenced spectral interferometry," in *Conference on Lasers and Electro-Optics* (Optical Society of America, 2009), p. CThW4.
88. P. M. Paul, A. Bonvalet, N. Forget, T. Okshendler, and C. Hauri, "Two-color chirped pulse amplification with AOPGCF for self-stabilized mid-infrared radiation generation," in *The European Conference on Lasers and Electro-Optics* (Optical Society of America, 2009), p. CF_P10.
89. A. Moulet, N. Forget, R. Herzog, S. Coudreau, and T. Oksenhendler, "Characterization and optimization of a femtosecond laser by self-referenced spectral interferometry," in *Conference on Lasers and Electro-Optics* (Optical Society of America, 2010), p. JThE81.
90. H.-S. Chan, N. Forget, and A. H. Kung, "Ultrabroad band acousto-optic programmable dispersive filters for five discrete harmonics spanning the blue to mid-infrared frequencies," in *Conference on Lasers and Electro-Optics/Pacific Rim* (Optical Society of America, 2011), p. C654.
91. S. L. Cousin, J. M. Bueno, N. Forget, D. R. Austin, and J. Biegert, "Compact spatio-temporal ultrashort pulse characterisation using a pulse shaper and a wavefront sensor," in *CLEO 2011 Laser Science to Photonic Applications* (ICFO-Institut de Ciencies Fotoniques, Mediterranean Technology Park, 08860 Castelldefels (Barcelona), Spain, 2011), Vol. 2, pp. 1–2.
92. S. L. Cousin, J. M. Bueno, N. Forget, D. R. Austin, and J. Biegert, "Pulse-shaper-assisted spatio-temporal ultrashort pulse characterisation," in *2011 Conference on Lasers and Electro-Optics Europe and 12th European Quantum Electronics Conference (CLEO EUROPE/EQEC)* (IEEE, 2011), pp. 1–1.
93. V. Crozatier, N. Forget, and T. Oksenhendler, "Towards single shot carrier-envelope phase stabilization for multi kHz ultrafast amplifiers," in *The European Conference on Lasers and Electro-Optics* (Optical Society of America, 2011), p. CF1_4.
94. S. Grabielle, S. Coudreau, V. Crozatier, N. Forget, F. Lepetit, O. Gobert, and T. Oksenhendler, "Self-referenced spectral interferometry in the UV domain," in *CLEO: Science and Innovations* (Optical Society of America, 2011), p. CTuO3.
95. S. Grabielle, A. Moulet, N. Forget, V. Crozatier, S. Coudreau, O. Gobert, C. Cornaggia, and T. Oksenhendler, "Sub-12 fs pulses characterization by self-referenced spectral interferometry," in *CLEO: Applications and Technology* (Optical Society of America, 2011), p. JWA77.
96. A. Moulet, S. Grabielle, N. Forget, C. Cornaggia, O. Gobert, and T. Oksenhendler, "Single-shot

Characterization of sub-15fs Pulses with 40dB Dynamic Range," in *High Intensity Lasers and High Field Phenomena* (Optical Society of America, 2011), p. HFB6.
97. A. Ricci, F. Silva, A. Jullien, S. Cousin, N. Forget, D. Austin, J. Biegert, and R. Lopez-Martens, "Generation of high-fidelity few-cycle pulses at 2 μm via XPW," in *CLEO: Science and Innovations* (Optical Society of America, 2012), p. CM1B. 8.
98. P. Tyagi, J. I. Saari, V. Crozatier, N. Forget, and P. Kambhampati, "Multiparticle correlations in semiconductor quantum dots using two-quantum 2DFT electronic spectroscopy," in *ABSTRACTS OF PAPERS OF THE AMERICAN CHEMICAL SOCIETY* (AMER CHEMICAL SOC 1155 16TH ST, NW, WASHINGTON, DC 20036 USA, 2012), Vol. 244.
99. G. Gitzinger, V. Crozatier, R. Maksimenka, S. Grabielle, N. Forget, S. Alisauskas, A. Pugzlys, A. Baltuska, B. Monoszlai, and C. Vicario, "Multi-octave acousto-optic analyzer for spectral measurement in the mid-infrared spectral range," in *Mid-Infrared Coherent Sources* (Optical Society of America, 2013), p. MTh3C. 3.
100. R. Huber, O. Schubert, D. Kaplan, M. Eisele, V. Crozatier, N. Forget, D. Kaplan, and R. Huber, "Acousto-optic Fastscan Delay for Ultrafast Photonics with sub-20-Attosecond Precision and Scan Rates exceeding 30 kHz," CLEO: Science and Innovations, CLEO_SI 2013 6–7 (2013).
101. O. Schubert, M. Eisele, V. Crozatier, N. Forget, D. Kaplan, and R. Huber, "Acousto-optic fastscan delay with scan rates exceeding 30 kHz and sub-20-attosecond precision," in *2013 Conference on Lasers and Electro-Optics Europe and International Quantum Electronics Conference, CLEO/Europe-IQEC 2013* (2013).
102. A. Trisorio, S. Grabielle, M. Divall, N. Forget, and C. P. Hauri, "XPW based Self-Referenced Spectral Interferometry for few-cycle pulse characterization in the short wavelength IR," in *International Quantum Electronics Conference* (Optical Society of America, 2013), p. CFIE_P_21.
103. R. Maksimenka, C. P. Hauri, A. Baltuska, G. Gitzinger, S. Alisauskas, B. Monoszlai, V. Crozatier, S. Grabielle, A. Pug¡zlys, C. Vicario, and N. Forget, "Multi-octave acousto-optic spectrum analyzer for mid-infrared pulsed sources," in *Cleo* (researchgate.net, 2014), Vol. 2014-Janua, p. STh1N.5.
104. A. Ricci, A. Jullien, F. Böhle, J.-P. Rousseau, S. Grabielle, N. Forget, P. Tournois, and R. Lopez-Martens, "High-contrast, CEP-controlled double-CPA laser," in *2014 Conference on Lasers and Electro-Optics (CLEO)-Laser Science to Photonic Applications* (IEEE, 2014), pp. 1–2.
105. T. Kanai, P. Malevich, G. Gitzinger, R. Maksimenka, N. Forget, A. Baltuška, and A. Pugžlys, "Broadband 6-μm Parametric Amplification Driven by a Sub-ps Ho: YAG Chirped Pulse Amplifier," in *The European Conference on Lasers and Electro-Optics* (Optical Society of America, 2015), p. CF_2_4.
106. P. Malevich, T. Kanai, G. Gitzinger, R. Maksimenka, N. Forget, A. Baltuška, and A. Pugžlys, "Broadband ZGP OPA pumped by femtosecond Ho: YAG chirped pulse amplifier," in *CLEO: Science and Innovations* (Optical Society of America, 2015), p. SM1P. 3.
107. V. Shumakova, P. Malevich, S. Ališauskas, A. Voronin, A. M. Zheltikov, D. Faccio, D. Kartashov, G. Gitzinger, R. Maksimenka, and N. Forget, "Self-compressed to sub-three optical cycles multi-millijoule mid-IR pulses: balancing between solitonic self-compression and spatial collapse," in *The European Conference on Lasers and Electro-Optics* (Optical Society of America, 2015), p. CF_3_5.
108. V. Shumakova, P. Malevich, S. Alisauskas, A. Voronin, A. Zheltikov, D. Faccio, D. Kartashov, R. Maksimenka, G. Gitzinger, and N. Forget, "250-GW sub-three-cycle multi-millijoule mid-IR pulses self-compressed in a YAG plate," in *CLEO: QELS_Fundamental Science* (Optical Society of America, 2015), p. FTu4D. 1.
109. A. van de Walle, M. Hanna, F. Guichard, Y. Zaouter, A. Thai, N. Forget, and P. Georges, "Spectral and spatial shot-to-shot correlation analysis of bulk supercontinuum in the mid-infrared," in *The European Conference on Lasers and Electro-Optics* (Optical Society of America, 2015), p. CF_P_27.
110. P. Rigaud, A. van de Walle, M. Hanna, A. Thai, N. Forget, F. Guichard, Y. Zaouter, and P. Georges, "Femtosecond-pumped mid-infrared few-cycle optical parametric chirped pulse amplifier source (orale)," in *7th EPS-QEOD Europhoton Conference" Solid State, Fibre, and Waveguide Cohernt Light Sources"* (2016).

111. A. Thai, E. Gontier, C. Ferchaud, P. M. Paul, F. Falcoz, and N. Forget, "High contrast CEP-stable OPCPA front-end for PW-class Ti: Sapphire system," in *International Conference on Ultrafast Phenomena* (Optical Society of America, 2016), p. UTh4A. 25.
112. A. Thai, R. Maksimenka, C. Ferchaud, N. Thiré, and N. Forget, "Few-cycle mid-IR OPCPA front-end at 100 kHz with sub-50 mrad CEP-stability," in *International Conference on Ultrafast Phenomena* (Optical Society of America, 2016), p. UTh4A. 24.
113. A. Jullien, U. Bortolozzo, J.-P. Huignard, S. Grabielle, N. Forget, and S. Residori, "Liquid crystal cells for phase and group delay control of femtosecond pulses–Application to hyperspectral imaging," in *The European Conference on Lasers and Electro-Optics* (Optical Society of America, 2017), p. CF_10_5.
114. A. Jullien, U. Bortolozzo, S. Residori, S. Grabielle, N. Forget, and J.-P. Huignard, "Phase and group delay control of femtosecond pulses with liquid crystal cells and application to hyperspectral imaging," in *Slow Light, Fast Light, and Opto-Atomic Precision Metrology X* (International Society for Optics and Photonics, 2017), Vol. 10119, p. 101191B.
115. P. Rigaud, A. Van de Walle, M. Hanna, N. Forget, F. Guichard, Y. Zaouter, K. Guesmi, F. Druon, and P. Georges, "High power mid-IR OPCPA system pumped by a femtosecond Yb-doped fiber amplifier," in *Proceedings of SPIE - The International Society for Optical Engineering* (2017), Vol. 10094, p. 100941I.
116. N. Thiré, R. Maksimenka, B. Kiss, C. Ferchaud, P. Bizouard, E. Cormier, K. Osvay, and N. Forget, "Multi-W, 100-kHz, few-cycle mid-infrared source with sub-100-mrad single-shot carrier-envelope phase noise," in *The European Conference on Lasers and Electro-Optics* (Optical Society of America, 2017), p. CF_4_1.
117. X. Audier, N. Balla, N. Forget, and H. Rigneault, "Ultra-fast stimulated Raman scattering (SRS) hyper-spectral imaging with an acousto-optic delay line," in *SPIE Photonics West 2018* (2018).
118. A. Jullien, R. Pascal, U. Bortolozzo, N. Forget, and S. Residori, "High-resolution hyperspectral imaging based on liquid-crystal cells," in *2018 Conference on Lasers and Electro-Optics (CLEO)* (IEEE, 2018), pp. 1–2.
119. E. A. Neradovskaia, M. M. Neradovskiy, A. A. Esin, M. A. Chuvakova, P. Baldil, M. P. De Micheli, A. R. Akhmatkhanov, N. Forget, and V. Y. Shur, "Domain kinetics during polarization reversal in 36 Y-cut congruent lithium niobate," in *IOP Conference Series: Materials Science and Engineering* (IOP Publishing, 2018), Vol. 443, p. 012024.
120. N. Thiré, V. Di Pietro, C. Ferchaud, N. Forget, S. Jarosch, K. Osvay, E. Cormier, B. Kiss, P. Bizouard, and R. Maksimenka, "A 15 W, Few-Cycle and Ultra-Stable Mid-infrared Parametric Source for ELI-ALPS," in *High-Brightness Sources and Light-Driven Interactions* (Optical Society of America, 2018), Vol. Part F86-H, p. HW4A.4.
121. V. M. di Pietro, A. Jullien, U. Bortolozzo, N. Forget, and S. Residori, "Thermally-induced nonlinear spatial shaping of femtosecond pulses in nematic liquid crystals," in *CLEO: Applications and Technology* (Optical Society of America, 2019), pp. JW2A--35.
122. N. Forget, N. Thiré, R. Maksimenka, Y. Pertot, O. Albert, B. Kiss, E. Cormier, and K. Osvay, "High-average-power Mid-infrared Sources for Spectroscopy and Strong-field Physics at 100 kHz," in *2019 Conference on Lasers and Electro-Optics (CLEO)* (IEEE, 2019), pp. 1–2.
123. N. Forget, P. Tournois, N. Thiré, R. Maksimenka, B. Kiss, E. Cormier, and K. Osvay, "A 100-kHz tunable femtosecond source for spectroscopy from the X-UV to the mid-IR (Conference Presentation)," in *Frontiers in Ultrafast Optics: Biomedical, Scientific, and Industrial Applications XIX* (International Society for Optics and Photonics, 2019), Vol. 10908, p. 1090814.
124. G. Jargot, N. Daher, L. Lavenu, X. Delen, N. Forget, M. Hanna, and P. Georges, "Soliton compression in a multipass cell," in *2019 Conference on Lasers and Electro-Optics Europe & European Quantum Electronics Conference (CLEO/Europe-EQEC)* (IEEE, 2019), pp. 1–1.
125. A. Jullien, V. M. Di Pietro, S. Bux, and N. Forget, "A phase-only pulse shaper for multi-octave light sources," in *Ultrafast Optics XII* (SPIE, 2019).
126. E. A. Neradovskaia, M. M. Neradovskiy, M. A. Chuvakova, A. R. Akhmatkhanov, P. Baldi, R.

Maksimenka, N. Forget, and V. Y. Shur, "Periodical poling in congruent lithium niobate with slanted polar axis," in *Scanning Probe Microscopy. Russia-China Workshop on Dielectric and Ferroelectric Materials.—Ekaterinburg, 2019* (Ural Federal University, 2019), pp. 113–114.

127. R. Maksimenka, G. Jargot, G. Jargot, N. Thiré, Y. Pertot, and N. Forget, "Ultra-stable OPCPA at 2 µm, 16 fs, sub 100 mrad CEP noise," in *OSA High-Brightness Sources and Light-Driven Interactions Congress 2020 (EUVXRAY, HILAS, MICS) (2020), Paper MM1C.3* (Optical Society of America, 2020), p. MM1C.3.
128. V. M. D. Pietro, S. Bux, N. Forget, and A. Jullien, "A phase-only liquid-crystal based pulse shaper for multi-octave light sources," in *Conference on Lasers and Electro-Optics (2020), Paper SM1H.2* (Optical Society of America, 2020), p. SM1H.2.
129. S. Shivkumar, D. Raanan, X. Audier, M. Asher, M. Menahem, O. Yaffe, N. Forget, D. Oron, and H. Rigneault, "Sub-second low frequency vibrational SRS imaging using a fast acousto-optic delay line," in *Advanced Chemical Microscopy for Life Science and Translational Medicine 2021* (International Society for Optics and Photonics, 2021), Vol. 11656, p. 116560.
130. V. M. Di Pietro, S. Bux, L. Ramousse, C. Claudet, G. Chériaux, N. Forget, and A. Jullien, "A liquid-crystal based phase-shaper for multi-octave light sources," in 2021 Conference on Lasers and Electro-Optics Europe and European Quantum Electronics Conference, OSA Technical Digest (Optical Society of America, 2021), paper cf_7_5.
131. N. Thiré, R. Maksimenka, Y. Pertot, J. Villanueva, T. Pinoteau, and N. Forget, Nicolas "CEP-stable infrared OPCPA sources", *European Optical Society annual meeting*, p. TOM13 – S03 (2021).
132. O. Albert, V. Femy, M. Neradovskiy, T. Pinoteau, J. Villanueva, and N. Forget, "A µJ-level parametric source tunable from 3 to 10µm by direct difference-frequency-generation in LGS at 250kHz", *European Optical Society annual meeting*, p. TOM13 – S05 (2021).
133. N. Thiré, R. Maksimenka, Y. Pertot, J. Villanueva, T. Pinoteau, and N. Forget, "CEP-stable Infrared OPCPA Sources," in *Frontiers in Optics + Laser Science 2021*, C. Mazzali, T. (T.-C.) Poon, R. Averitt, and R. Kaindl, eds., Technical Digest Series (Optical Society of America, 2021), paper JTu1A.26.
134. V. Femy, M. Neradovskiy, T. Pinoteau, J. Villanueva, O. Albert, and N. Forget, "Microjoule-level Femtosecond Pulses from 3 to 10 µm by DFG in LiGaS2 at 250 kHz," in *Frontiers in Optics + Laser Science 2021*, C. Mazzali, T. (T.-C.) Poon, R. Averitt, and R. Kaindl, eds., Technical Digest Series (Optical Society of America, 2021), paper FTh4B.4.

Brevets

135. EP-2011200-B1, « Dispositif pour la programmation en amplitude et en phase d'impulsions lumineuses longues a bande spectrale étroite à partir d'un modulateur d'impulsions lumineuses brèves à large bande spectrale », Fastlite, Nicolas Forget & Pierre Tournois (2006).
136. EP-2075556-B1, « Procédé et dispositif pour la mesure de la phase spectrale ou de phase spectrale et spatiale combinées d'impulsions lumineuses ultra brèves », Fastlite, Daniel Kaplan, Thomas Oksenhendler & Nicolas Forget (2007).
137. EP-2733530-B1, « Dispositif pour la compensation de dispersion temporelle appliqué à la génération d'impulsions lumineuses ultra brèves », Fastlite, Pierre Tournois & Nicolas Forget (2012).
138. FR-3013857-A1, « Système pour générer des impulsions optiques courtes de durée inférieure à la période de la porteuse optique utilisant le principe de l'amplification paramétrique », Fastlite, Nicolas Forget (2013).
139. EP-2981860-B1, « Dispositif pour la mise en forme temporelle en amplitude et en phase d'impulsions lumineuses ultra-brèves », Fastlite, Pierre Tournois & Nicolas Forget (2013)
140. EP-3074816-B1, « Générateur d'impulsions optiques courtes a très haut contraste temporel », Fastlite, Nicolas Forget (2014).
141. WO2021064326A1, « Modulateur spatial de lumière adresse thermo-optiquement », Fastlite-CNRS,

Nicolas Forget, Vittorio Di Pietro, Aurélie Jullien.
142. WO2021064045A1, « Génération de faisceau unique et sans compression d'une impulsion optique stable en phase à enveloppe porteuse », Fastlite, Nicolas Forget